

THERMOELECTRIC TRANSPORT IN SEMICONDUCTING HETEROSTRUCTURES

Dissertation

zur Erlangung des akademischen Grades
doctor rerum naturalium (Dr. rer. nat.)

vorgelegt von

NICKI FRANK HINSCHKE

geboren am 07.08.1982 in Halle/Saale



Martin-Luther-Universität Halle-Wittenberg

Institut für Physik
der Naturwissenschaftlichen Fakultät II
Fachgruppe Quantentheorie des Festkörpers
Von-Seckendorff-Platz 1, 06120 Halle/Saale

Halle (Saale), den 13.11.2012

Erstgutachterin: Prof. Dr. Ingrid Mertig
Zweitgutachter: PD Dr. Arthur Ernst
Drittgutachter: Prof. Dr. Kornelius Nielsch

Tag der Abgabe: 13.11.2012
Tag der öffentlichen Verteidigung: 28.05.2013
Vorsitzender der Promotionskommission: Prof. Dr. Jochen Balbach

*“An expert is someone who knows some of the worst mistakes that can be made
in his subject and who manages to avoid them.”*

WERNER HEISENBERG in *“Der Teil und das Ganze”*, 1969

Contents

1	Introduction	1
2	Thermoelectric concepts	5
2.1	IOFFE's theory of thermoelectrics	5
2.2	Low-dimensional thermoelectrics	6
2.3	Phonon glass - electron crystal	7
2.4	Phonon-blocking and electron-transmitting superlattices	9
3	Electronic structure	11
3.1	Density functional theory	11
3.1.1	Theorem of HOHENBERG & KOHN	11
3.1.2	Exchange-correlation functional	13
3.2	Band structure methods	15
3.2.1	KORRINGA-KOHN-ROSTOKER method	15
3.2.2	The plane-wave pseudopotential method	18
3.3	The DIRAC equation	22
3.4	Evaluation of surface integrals	24
4	BOLTZMANN transport theory	27
4.1	Distribution function	27
4.2	Linearisation and relaxation time approximation	28
4.3	Transport coefficients	31
4.3.1	Decoupled processes	33
4.3.2	Coupled processes	34
4.4	Lattice thermal conductivity	37
4.5	Beyond relaxation time approximation	40
4.5.1	Electron-impurity scattering	40
4.5.2	Electron-phonon scattering	42
5	Selected results	45
5.1	Bi ₂ Te ₃ /Sb ₂ Te ₃ heterostructures	45
5.2	Silicon/Germanium heterostructures	71
6	Summary & outlook	99
	List of publications	i
	Bibliography	iii

List of Figures

1.1	Schematics of a thermoelectric cooler, a thermoelectric generator and a thermoelectric device.	1
1.2	Thermoelectric conversion efficiency for different values of ZT	2
2.1	Evolution of the thermoelectric figure of merit ZT for semiconductors in the years 1950 to 2010.	5
2.2	Dependence of thermoelectric transport properties on the charge concentration.	6
2.3	Complex thermoelectric materials within the phonon glass - electron crystal approach.	8
2.4	Transmission electron microscopy graphs of $\text{Bi}_2\text{Te}_3/\text{Sb}_2\text{Te}_3$ and Si/Ge superlattices.	9
3.1	Schematic presentation of different potential shapes.	16
3.2	Nonlocal part of the relativistic pseudopotential and wavefunctions for atomic bismuth.	19
3.3	Phonon dispersion relation $\omega(q)$ for bulk silicon	22
3.4	Band structure of Bi_2Te_3 with and without spin-orbit coupling. Visualization of the band inversion.	23
3.5	Schematic of a tetrahedron for the approximation of the FERMI surface and the related properties.	25
3.6	FERMI surface of electron-doped bulk silicon determined with different k -meshes.	26
4.1	Schematic view of the distribution functions under applied electrical and thermal gradient	30
4.2	Sketch of OHM's law, the SEEBECK effect and the THOMSON effect.	31
4.3	FERMI surfaces and transport distribution function for Bi_2Te_3	33
4.4	Electronic thermal conductivity and LORENZ function for a spherical two band model and for bulk Bi_2Te_3	34
4.5	Anisotropic thermopower and THOMSON coefficient for Bi_2Te_3	37
4.6	Phonon thermal conductivity, specific heat, and group velocities for bulk silicon.	38
4.7	Experimental temperature-dependent thermal conductivity of bulk silicon.	39
4.8	Anisotropy of the electron-impurity relaxation time in BORN approximation for electron-doped bulk Bi_2Te_3	41
4.9	Electron-phonon coupling properties of bulk aluminium.	43
5.1	Electrical conductivity anisotropy of bulk Bi_2Te_3 and Sb_2Te_3 . Topology of the conduction band of bulk Bi_2Te_3	45
5.2	Unit cells and directional anisotropies of lattice thermal conductivity and electrical conductivity for different $\text{Bi}_2\text{Te}_3/\text{Sb}_2\text{Te}_3$ -SL.	46
5.3	Calculated anisotropic thermoelectric transport properties of $\text{Bi}_2\text{Te}_3/\text{Sb}_2\text{Te}_3$ -SL.	47
5.4	FERMI surfaces of electron-doped silicon and anisotropic thermopower under biaxial 001-strain.	71
5.5	Effective masses of 111-strained bulk Si and cross-plane thermoelectric transport properties of an Si/Ge-SL grown on 111-Si.	72

List of abbreviations

AE	all-electron	19
ASA	atomic-sphere approximation	16
BZ	BRILLOUIN zone	10
CBM	conduction band minimum	41
DFPT	density functional perturbation theory	21
DFT	density functional theory	3
DOS	density of states	7
E-PH	electron-phonon	42
GF	GREEN's function	3
GGA	generalized gradient approximation	13
IBZ	irreducible part of the BRILLOUIN zone	25
IFC	interatomic force constants	21
KKR	KORRINGA-KOHN-ROSTOKER	3
L(S)DA	local (spin) density approximation	13
LDOS	local density of states	41
PBET	phonon-blocking and electron-transmitting	9
PGEC	phonon glass-electron crystal	7
PGV	phonon group velocity	7
PHDOS	phonon density of states	24
PP	pseudopotential	3
QDSL	quantum-dot superlattice	10
RTA	relaxation time approximation	3
SKKR	screened KORRINGA-KOHN-ROSTOKER	18
SL	superlattice	3
SOC	spin-orbit coupling	23
TDF	transport distribution function	24
TE	thermoelectric	1
TEC	thermoelectric cooler	1
TEG	thermoelectric generator	1
USPP	ultra-soft pseudopotential	24

INTRODUCTION

Thermoelectrics are solid-state materials that convert heat into electricity or electrical power directly into cooling or heating [Row06]. The physical effects on which thermoelectricity foot, are known since the early 19th century. In the 1820s SEEBECK [See26] found that the electrochemical potential and the temperature couple with each other. Applying a temperature gradient ∇T on a materials produces a chemical potential gradient or an electrical field $\mathcal{E} = S\nabla T$. Here, S is the SEEBECK coefficient or thermopower. In a closed circuit an electrical current \mathbf{j} will flow. Few years later, PELTIER [Pel34] became aware of the reversion of this phenomenon, when he demonstrated the emergence of a heat flux \mathbf{Q} via coupling to an electrical current, as $\mathbf{Q} = \Pi\mathbf{j}$. The proportionality of both currents is the PELTIER coefficient. The classical theory of thermoelectrics was then generalized by THOMSON [God11], the later LORD KELVIN, who showed that the SEEBECK and PELTIER effects are not independent and can be related by the THOMSON coefficient \mathfrak{K} .

With this considerations it is obvious that thermoelectric (TE) effects are able to convert thermal energy into electrical energy (thermoelectric generator (TEG)) and vice versa (thermoelectric cooler (TEC)). These two concepts of TE energy conversion are sketched in figure 1.1.

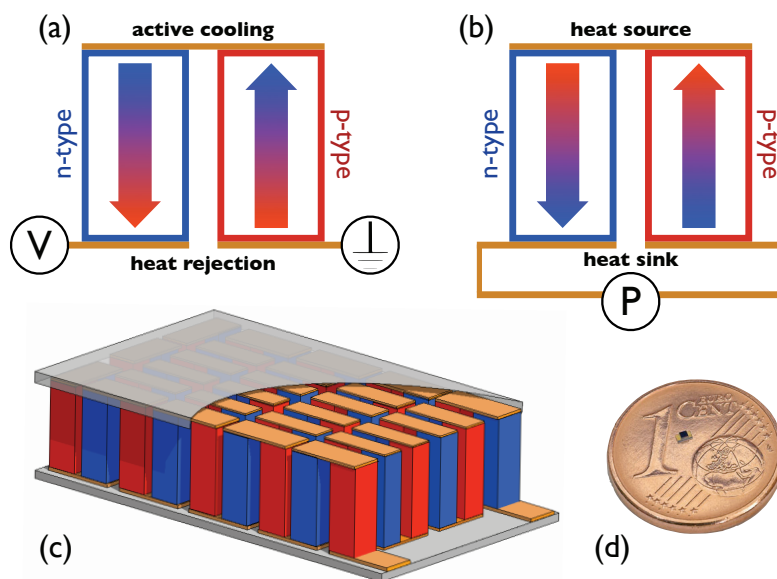
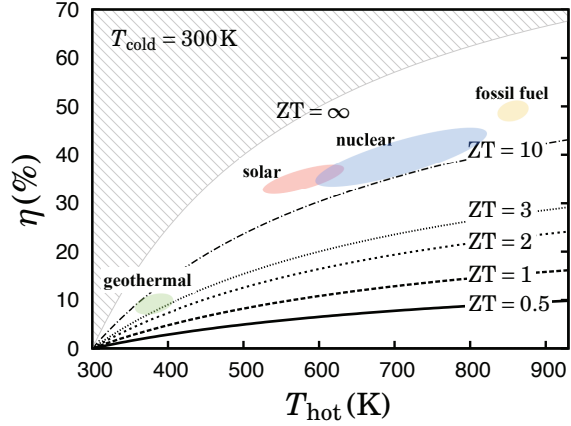


Figure 1.1: Schematics of a thermoelectric cooler, a thermoelectric generator and a thermoelectric device based on n - and p -type semiconductors. (a) Scheme of a thermoelectric cooler (TEC). (b) Scheme of a thermoelectric generator (TEG). The arrows in the segments illustrate the electric current flow (blue: low temperature, red: high temperature). (c) Sketch of a thermoelectric device built of several thermocouples connected in series. (d) The thin-film TEC MPC-D305 from MICROPELT company on a one euro cent coin [BNSV07].

Nowadays, modern thermocouples are not made of two metals, but are rather formed by heavily doped n - and p -type semiconducting materials. The segments of n - and p -type semiconductors are then connected by a good conductor, i.e. a metal. An applied voltage will now drive an electrical current through the circuit. Depending on the direction of the electrical current one side will be cooled (heated) and the other heated (cooled) [Bel08]. The method of a TEC shown in figure 1.1(a). Within a TEG, the TE processes are reversed. Active cooling or heating of one side of the thermocouple will result in an electrical field, forcing an electrical current to flow (cf. figure 1.1(b)). Conventional TE

Figure 1.2: Thermoelectric conversion efficiency calculated by equation (1.1) for different values of ZT . For $ZT = \infty$ the CARNOT limit is reached. The cold side of the thermocouple is fixed to 300K, while the temperature for the hot side is varied. Colored shaded regions show the efficiency range of common conventional heat-electricity conversion methods.



devices, as shown in figure 1.1(c), are built of hundreds of n - and p -type thermocouples connected in series. To state some numbers, MICROPELTs TEG MPG-D751 [Mic12] consists of 540 segments producing an electrical power output of $P_{el} \approx 12\text{mW}$ and a voltage $U \approx 3\text{V}$ at a heat load of $P_{th} \approx 2\text{W}$ and a temperature difference of $\Delta T \approx 30\text{K}$.

The energy conversion efficiency η of a TEG is given by [Iof57]

$$\eta = \frac{T_{hot} - T_{cold}}{T_{hot}} \cdot \frac{\sqrt{1 + Z\bar{T}} - 1}{\sqrt{1 + Z\bar{T} + \frac{T_{cold}}{T_{hot}}}} \quad \text{with} \quad Z\bar{T} = \frac{\sigma S^2}{\kappa_{el} + \kappa_{ph}} \bar{T} \quad (1.1)$$

\bar{T} is the average temperature of the TE device, and ZT is the average thermoelectric figure of merit that expresses the possible conversion efficiency of the material. Obviously, Z depends only on the material's electronic and vibronic transport properties: σ is the electrical conductivity, S is the thermopower, κ_{el} is the electronic part of the thermal conductivity, while κ_{ph} is the lattice part of the thermal conductivity. The numerator σS^2 is referred to as the power factor. The TE conversion efficiency for different values of ZT is shown in figure 1.2. From equation (1.1) and figure 1.2 one obtains that for infinite values of ZT the CARNOT efficiency will be reached. For conventional bulk thermoelectrics, e.g. Bi_2Te_3 , $ZT \approx 0.5 - 1$, and thus the conversion efficiency will be well below 20% even at large temperature differences. However, due to its desirable nature of being highly reliable, stable, compact, and integrable TE devices are extensively used in outer-space missions, energy-autarkic sensor systems, and waste-heat recovery within the last 50 years [Nie07, Bel08, ST08, Vin09]. Increasing ZT would extend these niche areas and lead to new potential TE applications which could compete with conventional geothermal, solar, fossil and nuclear energy conversion methods (cf. figure 1.2) and serve as a new alternative energy source.

In the last years, state-of-the-art concepts and experiments enabled nanostructured TEs which gave a considerable leap forward in reaching higher values of ZT . Most remarkable results were presented by HARMAN [HWLT05] for a PbSeTe/PbTe quantum-dot superlattice (QDSL) with $ZT = 3.5$ and VENKATASUBRAMANIAN [VSC01] for a $\text{Bi}_2\text{Te}_3/\text{Sb}_2\text{Te}_3$ -SL with $ZT = 2.4$. Both systems are built of alternating epitaxially grown material layers. This introduces new artificial interfaces which are expected to block phonons and to transmit electrons. From this separation it is expected that the lattice part of the thermal conductivity κ_{ph} will be suppressed, while the electronic transport properties, mainly the power factor σS^2 , might be enhanced compared to those of the bulk constituents. Consequently, the figure of merit would be enhanced.

The scope of this thesis is to understand the microscopic origin of TE transport in semiconduct-

ing heterostructures and to identify and elucidate mechanisms which could lead to enhanced TE conversion efficiency. Based on first-principles calculations the electronic structure and the related TE transport properties of bulk Bi_2Te_3 , Sb_2Te_3 , Si, and Ge, as well as their heterostructures $\text{Bi}_2\text{Te}_3/\text{Sb}_2\text{Te}_3$ and Si/Ge are determined and discussed. The focus is on the influence of bulk and interfacial strain, varying charge carrier concentration, temperature and superlattice (SL) periods on the TE transport properties.

This thesis is organized in four parts. First, the reader is introduced to conventional and novel concepts of TE material design. In the second part the basis for the electronic structure calculations is given. The concept of density functional theory (DFT) is introduced (section 3.1) and the band structure methods of choice, a KORRINGA-KOHN-ROSTOKER (KKR) GREEN's function (GF) method (section 3.2.1) and a method based on plane waves and pseudopotentials (PPs) (section 3.2.2) are described. The third part consists of a detailed derivation of the TE transport coefficients for the BOLTZMANN transport theory within the relaxation time approximation (RTA) (section 4). This is done for electrons (section 4.3) and for phonons (section 4.4). The impact of microscopic scattering, beyond a RTA, is accounted for in section 4.5. In the last part, four publications are chosen to present the obtained results. After a brief summary two publications each, for heterostructures based on the chalcogenides Bi_2Te_3 and Sb_2Te_3 (section 5.1) and for heterostructures based on Si and Ge (section 5.2), are attached. A summary and outlook will conclude this thesis.

THERMOELECTRIC CONCEPTS

In the last sixty years, strong efforts were made to improve the TE figure of merit ZT . In figure 2.1 this development is summarized by showing the optimal ZT values for different materials together with their original reference. While a huge amount of concepts were developed, only a few of them had reasonable impact on the TE research and will be reviewed in the following sections. Three of the presented concepts already showed their reliability and contributed significantly to the enhancement of ZT . Those are, marked by red arrows in figure 2.1, IOFFE's work on TE semiconductors [Iof57] (section 2.1), HICKS' & DRESSELHAUS' introduction of low-dimensional TES [HD93] (section 2.2), and SLACK's proposal of materials that are glass- and crystal-like at the same time for phonons and electrons, respectively. [Sla95] (section 2.3).

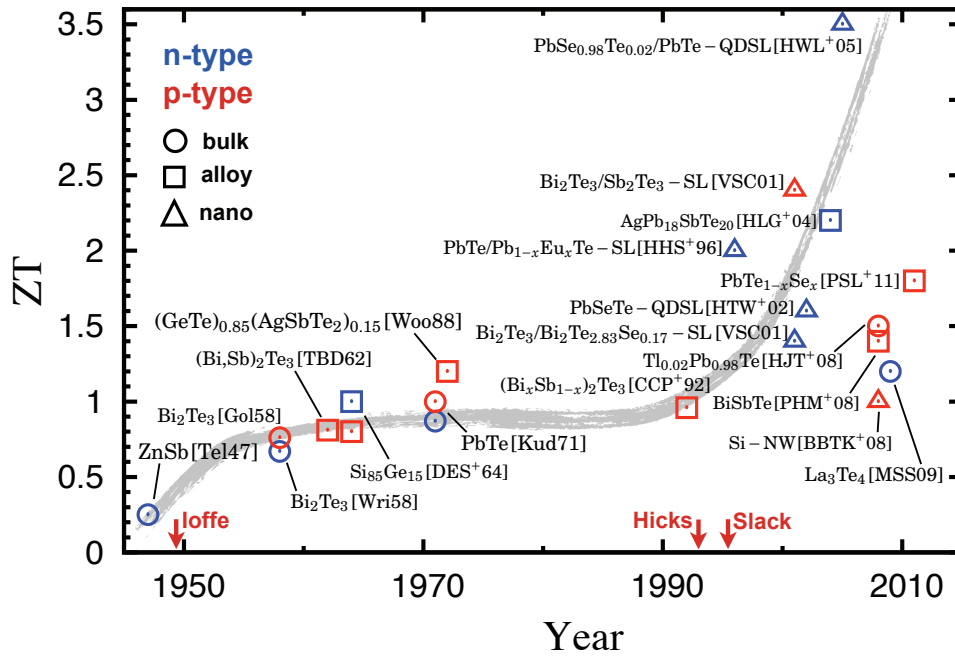


Figure 2.1: Evolution of the thermoelectric figure of merit ZT for semiconductors in the years 1950 to 2010. Circles indicate single crystalline bulk materials, squares alloyed bulk materials, and triangles nanostructured materials, e.g. nanowires, heterostructures or quantum-dots. Blue and red colors indicate n - and p -type materials, respectively. Given to each symbol is the original reference, which can be found at page iii et seqq.

2.1 IOFFE's theory of thermoelectrics

In the 1950s, Abram Fedorovich IOFFE set the basis for the modern theory of thermoelectricity. He focused on studies of electrical and thermal transport properties of a new class of solids that he later called semiconductors [VI98]. IOFFE recognized semiconductors as potential materials with high thermoelectric conversion efficiency. Materials of interest were particularly bulk PbS, PbTe, PbSe, ZnSb, Bi_2Te_3 , and Sb_2Te_3 . By introducing and analyzing the figure of merit ZT , he rapidly realized that ZT cannot be optimized by optimizing its constituents [Iof58]. The interdependence of the key transport properties σ , S , and κ is a challenge for thermoelectrics till today. In figure 2.2 this interdependence is highlighted for bulk p -type Bi_2Te_3 at room temperature. The heavy dependence of

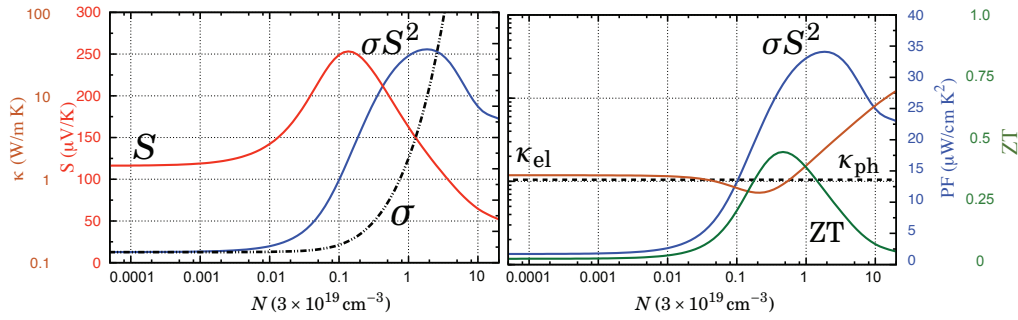


Figure 2.2: Dependence of thermoelectric transport properties on the charge concentration on the example of bulk p -type Bi_2Te_3 at room temperature. Shown are the electrical conductivity σ (black dash-dotted line), the thermopower S (red line), the power factor σS^2 (blue line), the electronic part of thermal conductivity κ_{el} (orange line), the lattice part of the thermal conductivity κ_{ph} (black dashed line) and the related figure of merit ZT (green line). Results are taken from [E5].

the TE transport on the charge-carrier concentration as well as the interdependence of the single transport properties is obvious. Assuming pure spherical band conduction, i.e. in a highly degenerate semiconductor, it is $\sigma \propto N$ and $S \propto N^{-2/3}$ [Mot67, CM69], thus the electrical conductivity and the thermopower are directly related by $S \propto \sigma^{-2/3}$ [E8]. The electronic part of the thermal conductivity κ_{el} scales directly with the electrical conductivity σ , as proposed by the WIEDEMANN-FRANZ law [Zim60]. Thus, the conversion efficiency of a semiconducting TE is highly dependent on the charge carrier concentration N and should be optimized by doping [VI98]. IOFFE was one of the first who claimed that N should be in the order of $1 \times 10^{19} \text{ cm}^{-3}$ for an optimal semiconducting TE. While IOFFE and his co-workers also developed the concept of reducing the lattice thermal conductivity κ_{ph} by alloying and by the introduction of point defects, it was IOFFE's generalized theory on optimizing ZT by varying the amount of doping, which boosted TEs from 1950 on (cf. figure 2.1). His work on semiconducting TES culminated in his classic book [Iof57] which sets a standard for understanding bulk TES up to now.

Despite the remarkable impact of IOFFE's theory, it is worth noting that, expectedly, other scientists contributed to the then young field of semiconducting TEs, too. The works of TELKES, GOLDSMID and PRICE on ZnSb , Bi_2Te_3 and Sb_2Te_3 and their alloys should be quoted representatively [Tel47, Pri56a, Gol56, Pri56b, GSW58, Wri58, SKS62]

2.2 Low-dimensional thermoelectrics

In 1993, the pioneering work of HICKS & DRESSELHAUS [HD93, HHD93] renewed interest in TES, becoming the inspiration for most of the recent developments in the field of low-dimensional TES [Sha11]. The basic idea was that quantum confinement of electrons and holes would dramatically increase ZT by independently increasing the power factor. Quantum confinement is available in low-dimensional geometries as quantum dots (0D), nanowires (1D), as well as quantum wells and SLs (2D).

While infinite enhancements on the in-plane figure of merit were predicted at vanishing geometry size [HD93, HHD93, DDS+99], HICKS & DRESSELHAUS neglected electron tunnelling and thermal currents between the layers by introducing infinite potential barriers at zero width. Later on it was shown that for realistic barrier heights and widths the enhancement is rather moderate, predicting ZT values that at their best are a few percent larger than corresponding bulk materials [BR95a, BR95b, CR11]. Indeed, a few groups found evidently large enhancements of the thermopower in SLs based on PbTe [HHS96, KHCD99, HTSW00, HTWL02, HWLT05] and on SrTiO_3 [Oht07, OKM+07,

OMK⁺08, JS10]. However, the determination of the 2D charge carrier concentration is sophisticated and leads in at least two of the previous experiments [HTSW00, HHLT05] to a way to large estimates for the thermopower [VHC⁺08]. In some of other cases, the carriers had to be confined in delta-doped like layers with a maximum width of a unit cell to show an enhancement upto $ZT \approx 2$ [Oht07, OKM⁺07, OMK⁺08], while otherwise ZT would have been only marginally enhanced [KDL09].

Several experiments have been performed on processing and characterizing TE 1D nanowires [LWK⁺03, ZJS⁺05, BBTK⁺08, CHM⁺08, HCDL08, TZG08, YBP⁺09]. Confinement effects on the electronic TE transport properties, say σS^2 , were negligible [LD03, CR11]. While at very low wire diameters, $d \ll 15$ nm, enhancements of the power factor could be reached [CR11], the main gain in ZT for nanowires came from a dramatical reduction of the lattice thermal conductivity. Here, phonon boundary scattering is the reason [ZJS⁺05]. Unfortunately, at small diameters the latter effect causes a reduction of the phonon-drag effect and by that also of the thermopower [WLG92]. If both, phonon boundary scattering and phonon drag, could be retained, promising values of ZT were found for TE nanowires, too [BBTK⁺08].

Adding up the previous ideas, MAHAN & SOFO [MS96] argued that sharp features in the density of states (DOS) alone could lead to enhancements of the thermopower and the power factor. Recent experimental proofs of principle, showed this assumption to be achievable already in bulk materials by the introduction of a resonant defect level near the FERMI level [HJT⁺08, JKH09, LWG10, KNG⁺11].

2.3 Phonon glass - electron crystal

Obviously, the TE efficiency (1.1) is dictated by the figure of merit ZT . The latter can be optimized by enhancing either the power factor σS^2 or by decreasing the thermal conductivity $\kappa_{\text{el}} + \kappa_{\text{ph}}$. For long time, the concept of alloying allowed for the lowest thermal conductivities [Iof57]. The reduction of κ_{ph} was due to scattering of phonons by atomic substitutions and limited by the so-called *alloy limit*. Unfortunately, the introduction of impurities leads also to electron-impurity scattering which most often lowers the power factor.

At the best, TE electronic and vibronic properties are decoupled, allowing for both, maximizing the power factor and minimizing the lattice contribution to the thermal conductivity. Having this in mind, SLACK proposed 1995 the concept of a phonon glass-electron crystal (PGEC) [Sla95, Sla79]. The best TE material should possess thermal properties similar to that of a glass ($\kappa_{300\text{K}} \lesssim 1$ W/mK [CP87]) and electrical properties similar to that of a perfect single-crystal material [NMT99]. Up to now, several experimental and theoretical studies support the PGEC concept but differ in their approach.

Archetypical examples of bulk PGEC materials are the skutterudites ((Co,Ni,Fe)(As,Sb)₃ and related compounds) [NSM⁺96, NCS98, NMT99, SKL⁺08] and the clathrates (e.g. Ba₈Ga₁₆Si₃₀) [Vin08b, NCSS98, DSM01, BCB⁺04, SYB⁺10]. The latter carry the TE approach within their name, as *clathrates* is Latin for *within a cage*. As shown in figure 2.3(a), the typical crystal of skutterudites and clathrates is cagelike (blue atoms), holding *guest* atoms inside the cages (purple and orange atoms). The idea is that the cage atoms form a regular periodic crystal lattice along which electrons (or holes) can move fairly freely, ideally approaching the so-called electron crystal [NPK06]. The enclosed *guest* atom (often *rattler*) is commonly bigger, heavier and more loosely bound compared with the cage atoms. The *rattlers* are believed to have independent oscillations that scatter the acoustic phonons of the cage. This causes an avoided crossing of the acoustic phonon branches, leading to a diminished phonon group velocity (PGV) and a drastically reduced κ_{ph} . One then speaks of a phonon glass, even though strictly speaking the long-range ordering is maintained in all cases [CAC⁺08].

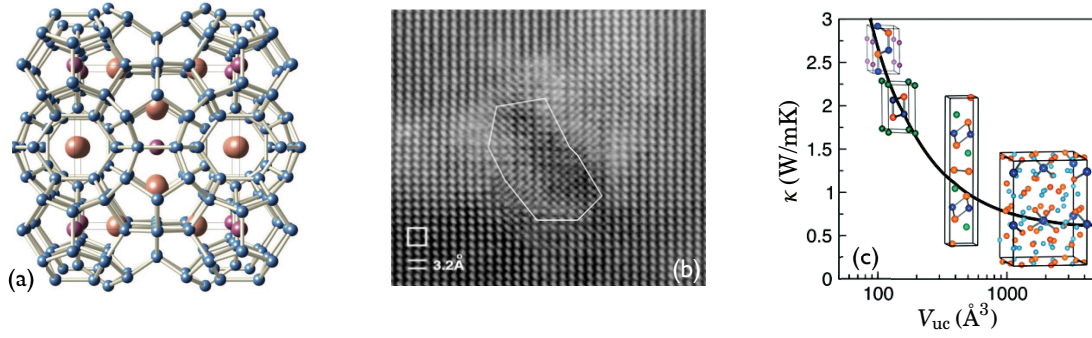


Figure 2.3: Complex thermoelectric materials within the phonon glass - electron crystal approach. (a) Crystal structure of the type I clathrate. Cage atoms are shown in blue, guest atoms inside the tetrakaidecahedra are orange, and guest atoms inside the pentagonal dodecahedra are purple. Figure adapted from [NPK06]. (b) TEM image of a $\text{AgPb}_{18}\text{SbTe}_{20}$ sample showing a nanodot enclosed in the periodic crystal structure. Figure adapted from [HLG⁺04]. (c) Lattice thermal conductivity in dependence on the unit cell volume for different Zintl-antimonides. For increasing unit cell volume and number of atoms in the unit cell, the lattice thermal conductivity rapidly decreases. Figure after [TMS09].

Similar findings, although not in cage-like crystal structures, were recently reported for heavily doped Zn_4Sb_3 [CFB97, ZTIY03, SCNC04]. While showing a stable single-crystal structure with sufficiently high power factor, significant disorder is introduced, with zinc atoms diffusing over multiple void positions. These glass-like interstitial sites uncovered a highly effective mechanism for reducing thermal conductivity, which is comparable to the rattling modes mentioned before. Total thermal conductivities of $\kappa \approx 0.5 \text{ W/mK}$ and a figure of merit of $ZT \approx 1.3$ were found at 400 K [SCNC04].

An other concept of *guest domains* in a *host matrix* was recently provided by HSU [HLG⁺04] and others [KZG⁺06, BBG⁺09]. Here, the samples reveal compositional nano-modulations caused by precipitation and strain relaxation [SW01]. Exemplary, in figure 2.3(b) the transmission electron microscopy TEM image of an endotaxially dispersed nano-array within a $\text{AgPb}_{18}\text{SbTe}_{20}$ host crystal is shown. The very high number of *guest domain-host matrix* interfaces provides a formidable barrier to phonons in the bulk sample [NPK06], enabling thermal conductivity values as low as $\kappa_{\text{ph}} = 0.45 \text{ W/mK}$ [HLG⁺04]. Moreover, the nano-inclusions occur to be highly conducive for the electronic transport, thus backing-up the idea of a PGEC.

Introducing porous or holey materials to TEs did not give a considerable leap forward [Gol09, TWL⁺10, LG09, E4]. Here, high-density nanoscopic holes are created in the material and can even be filled with various gases to control the lattice thermal conductivity [Gol09]. At first sight, one would not expect porosity to affect the TE performance, as the holes will not contribute significantly to neither the electronic nor the vibronic transport; thus, their ratio is constant. However, it was found that the increased surface to volume ratio most probably leads to an enhanced phonon-surface scattering reducing κ by almost two orders of magnitude compared to the bulk value [TWL⁺10, E4]. Unfortunately, these surfaces cause non-homogeneous charge carrier concentrations in the sample and, moreover, act as electron scattering centers, thereby decreasing the charge carrier mobility. Summing up, this leads to disappointing electronic transport properties and, hence, only to moderate numbers for ZT .

Different approaches to the PGEC concept were recently contributed by the group of SNYDER. TOBERER *et al.* suggested that the lattice thermal conductivity scales inversely with the number of atoms in the unit cell [TCB⁺08, TMS09, ZZP⁺]. A support of this proposal is given in figure 2.3(c), where the lattice thermal conductivity in dependence on the unit cell volume is shown for different antimonides. With increasing unit cell volume, the number of atoms N increases, too. It is well known that in a three-dimensional crystal only three acoustic phonon branches, but $3(N - 1)$ optical branches exist and hence for complex crystals with high number of atoms per unit cell, optical

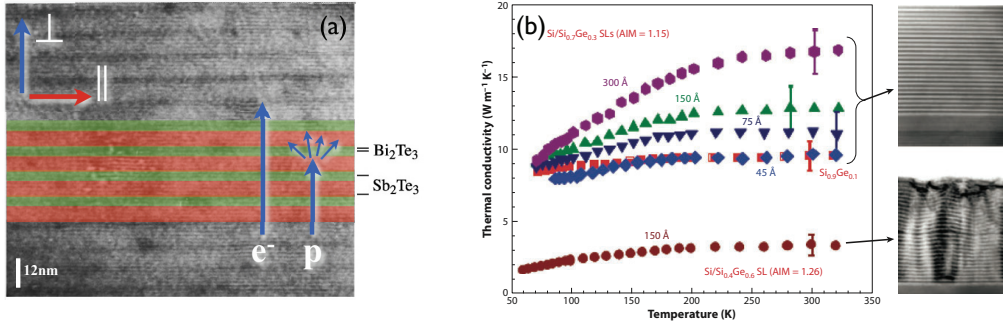


Figure 2.4: Transmission electron microscopy graphs (TEM) of $\text{Bi}_2\text{Te}_3/\text{Sb}_2\text{Te}_3$ and Si/Ge superlattices. (a) TEM of a $10\text{\AA}/50\text{\AA}$ $\text{Bi}_2\text{Te}_3/\text{Sb}_2\text{Te}_3$ -SL. Red and green areas highlight the layered structure. For cross-plane transport (\perp) phonons (p) are expected to be scattered at the artificial interfaces, while electrons (e^-) transmit without losses. In the in-plane direction (\parallel) quantum confinement effects for electrons are expected. Figure modified from [VCO⁺99]. (b) Cross-plane thermal conductivity (left frame) of several Si/Ge based superlattices with different superlattice periods. TEM images for different interface roughness of the superlattices are shown on the right. Decreasing the superlattice period leads to smaller thermal conductivity and less pronounced temperature dependence. Figure adapted from [Sha11].

phonons dominate. In the argumentation of TOBERER *et al.* the bandwidth of the acoustic phonons thus reduces to $\Delta\omega_{\text{acoustic}} = N^{1/3}\omega_{\text{max}}$. They note that the $3(N-1)$ optical modes have very small PGVs and thus are summed to account only for a constant, small, glass-like contribution to κ_{ph} within a DEBYE model [TMS09,RK73]. The latter assumption is rather crude. As will be shown later (cf. figure 4.6(b) and section 4.4), optical phonon modes can have PGVs in the same order as the acoustic modes and consequently contribute to κ [Tiw78,ZB01]. However, the experimental results of SNYDER *et al.* [TMS09,TCB⁺08,ZZP⁺] for complex ZINTL-phases showed a tremendous reduction of $\kappa_{\text{ph}} \approx 0.2\text{W/mK}$ along with $ZT \approx 1.3$ at high temperatures. Nevertheless, the intrinsically low κ_{ph} might be more connected with the complex crystal structures than with the proposed reduction of the optical mode's PGVs.

The newest, maybe most appropriate, member in the zoo of PGEC materials is bulk p -type Cu_{2-x}Se [LSX⁺12]. Most interestingly, the Se atoms form a rigid face-centred cubic lattice providing a crystalline pathway for semiconducting holes, while the copper ions are highly disordered around the Se sublattice and show liquid-like mobility [LSX⁺12]. As a result, Cu_{2-x}Se can be seen as an archetypical PGEC material. The Se sublattice forms the electron crystal and dictates the electronic transport properties, while the highly disordered, liquid-like copper ions represent the phonon glass and reduce the thermal conductivity. Both transport regimes appear to be decoupled. This combination leads to a remarkable figure of merit $ZT = 1.5$ together with $\kappa = 0.8\text{W/mK}$ at 1000K.

2.4 Phonon-blocking and electron-transmitting superlattices

The very sophisticated TE concept of phonon-blocking and electron-transmitting (PBET) superlattices combines the PGEC approach (section 2.3) and the idea of quantum confinement in low-dimensional systems (section 2.2). Made available by state-of-the art heteroepitaxy [BCV06,VCW⁺97,TZVG01,KWB⁺11,WLK⁺11,WLK⁺12], SLs consist of alternating thin layers of different materials stacked periodically. Most prominent applications of TE SLs are $\text{Bi}_2\text{Te}_3/\text{Sb}_2\text{Te}_3$ [VCWH96,Ven97,VSC01,KWB⁺11,WLK⁺11], Si/Ge [LCV97,BT00,YLWC01] and SLs based on PbTe and PbSe [HTSW00,HTWL02,HWLT05,BNB⁺02a,BNB⁺02b,JNC⁺11]. Other SLs based on Bi/Sb [CKY⁺01] or skutterudites [CSS⁺01] showed no or only small enhancements of the TE efficiency.

Even though being inspired by the approaches of a PGEC and the idea of quantum confinement in low-dimensional systems, the *ansatz* of a phonon-blocking and electron-transmitting SL is very

different. First, they differ in their quantum confinement. In low-dimensional 1D, 2D structures proposed by HICKS & DRESSELHAUS, the transport is mostly perpendicular to the confinement, i.e. in the in-plane direction of the SLS, and can be assumed almost free-electron-like. In a phonon-blocking and electron-transmitting SL the thermal gradient is preferably applied parallel to the confinement, i.e. electron and phonon transport occur in cross-plane direction of the superlattice. The latter is emphasized in figure 2.4(a).

With no obvious enhancement of the cross-plane electronic transport to be expected due to quantum confinement effects, the desired increase in ZT has to stem entirely from a distinct reduction of the cross-plane lattice thermal conductivity $\kappa_{\text{ph},\perp}$. Indeed, exceptionally low thermal conductivities were found for phonon-blocking and electron-transmitting SLS [LCV97, Ven00, CKH⁺03, HAT02, HTWL02, EGR⁺07]. VENKATASUBRAMANIAN reported $\kappa_{\text{ph},\perp} = 0.22 \text{ W/mK}$ for $\text{Bi}_2\text{Te}_3/\text{Sb}_2\text{Te}_3$ -SL with a period of 50\AA , which is about five times smaller than the bulk values and significantly below the alloy limit [Ven00]. Those values add up to the lowest room-temperature thermal conductivities in crystalline materials reported so far ¹.

The physical reason for the low cross-plane thermal conductivity is still under intense debate using two model pictures [BCV06]. In the first, the phonons are expected to be quasiparticles that are scattered specularly or diffusively at the interfaces [Che98]. Experimental results from TOUZEL-BAEV seem to support this picture, as decreasing lattice thermal conductivity was found for an increased interface roughness [TZVG01]. In the second, the phonons are expected to behave as coherent waves across the interfaces. Reduction of the thermal conductivity then comes purely from band structure effects, like BRILLOUIN zone (BZ) downfolding, leading to decreased PGVS and thermal conductivities [HM97, TTM99]. This picture alone is not sufficient to explain the magnitude of the thermal conductivity reduction perpendicular to the film plane, and it fails completely to explain the observed in-plane thermal conductivity reduction [BCV06]. VENKATASUBRAMANIAN proposed that coherent backscattering of phonons at *mirror-like* interfaces could lead to standing phonon waves which do not contribute to the thermal transport [Ven00]. Depending on the SL period l , this leads to a localization of certain phonon modes with wavelength $\lambda \leq l/2$ [Ven00]. The goal of SL engineering is to choose the SL period in such a way that low-frequency acoustic modes are localized and κ_{ph} most probably becomes diminished.

To the best, a phonon-blocking and electron-transmitting (PBET) SL shows power factors similar to that of the bulk, albeit at different optimal carrier concentrations. As will be shown in the results of this thesis (section 5) these assumptions are per se rather optimistic but achievable under certain conditions. Summing up, TE transport in the cross-plane direction of SLS shows the highest numbers for the figure of merit so far. $ZT = 2.4$ and 1.5 were predicted for p -type and n -type $\text{Bi}_2\text{Te}_3/\text{Sb}_2\text{Te}_3$ -SLS at room temperature [VCO⁺99], while $ZT = 1.6 - 3.5$ was reported for n -type PbSeTe-based quantum-dot superlattices (QDSLs) at $T = 300 - 600 \text{ K}$ [HTSW00, HTWL02, HWLT05] ².

This chapter presents without any claim of completeness some important concepts of modern thermoelectricity and should give the unbiased reader some insight into the developments in the last 60 years. Unintentionally, some alternative approaches to thermoelectricity like thermionic emission [Sha11, VS07, SB97, MW98] and solar thermal energy conversion [TBC08] are not discussed and the reader is referred to the cited publications.

¹Note, that $\kappa_{\text{ph},\perp} \approx 0.05 \text{ W/mK}$ was reported for intrinsically layered WSe_2 [CCN⁺07, CCHL08, Goo07]. The very poor electronic transport properties render WSe_2 as an insufficient TE material.

²Some of the measurements for the PbSeTe-based QDSLs have been corrected after publication by the authors [VHC⁺08]. The maximum value of $ZT = 3.5$ is highly unlikely, $ZT \gg 1$ is expected for all the samples.

ELECTRONIC STRUCTURE

Describing the TE transport properties of an electronic ensemble requires full knowledge of the electronic structure. According to quantum mechanics, the interaction of electrons at site \mathbf{r} and nuclei at site \mathbf{R} is determined by the HAMILTONIAN

$$\mathcal{H} = \mathcal{T}_n(\mathbf{R}) + \mathcal{U}_{nn}(\mathbf{R}) + \mathcal{T}_e(\mathbf{r}) + \mathcal{U}_{ee}(\mathbf{r}) + \mathcal{V}_{en}(\mathbf{r}, \mathbf{R}), \quad (3.1)$$

describing the physics of about 10^{26} particles. To find a ground state of this HAMILTONIAN by solving the corresponding SCHRÖDINGER or DIRAC equation is numerically impossible. An expedient to this problem was given in 1965 by KOHN, HOHENBERG, and SHAM by describing the many-body problem by means of a real-space charge density related to independent one-particle problems [HK64, KS65]. This was the origin to the most popular and successful quantum mechanical approaches to matter: density functional theory (DFT) [Koh99].

In the first part of this chapter, the theoretical background of DFT will be elucidated, starting with the theorems of HOHENBERG & KOHN (section 3.1.1). In the second part, the numerical implementation of DFT in order to obtain the electronic structure of the system of interest will be introduced. The band structure methods of choice are the KORRINGA-KOHN-ROSTOKER (KKR) GREEN's function (GF) approach (section 3.2.1), as well as a method based on plane waves and pseudopotentials (section 3.2.2). The importance of relativistic effects is discussed in section 3.3. The chapter closes by some introductory remarks on the determination of forces within DFT and the numerical determination of FERMI surface integrals (section 3.4).

3.1 Density functional theory

The fundamental problem in modern solid state physics is the determination of the ground state energy E and the local spin-densities $n_\uparrow(\mathbf{r})$, $n_\downarrow(\mathbf{r})$ for a huge number of electrons interacting among themselves and with an external potential \mathcal{V}_{ext} . The HAMILTONIAN \mathcal{H} of such a many-body system consists of several contributions. Here, the total kinetic energy is represented by \mathcal{T} , \mathcal{U}_{ee} is the electron-electron COULOMB repulsion and \mathcal{V}_{ext} represents the interaction with an external, in principle spin-dependent potential. The latter can be regarded as the COULOMB interaction of electrons with the localized nuclei, assuming an adiabatic decoupling of the motion of the electrons and nuclei. This assumption introduced by BORN & OPPENHEIMER is valid as the characteristic kinetic energies of electrons and nuclei differ by several orders of magnitude. The low nuclei mobility leads to the fact, that the electrons respond to an almost stationary potential. Hence, a product *ansatz* of the total wavefunction enables a separation of the system into two independent parts, where the electronic HAMILTONIAN in atomic units reads

$$\mathcal{H}_{el} = \mathcal{T}_{ee} + \mathcal{U}_{ee} + \mathcal{V}_{ext} = -\frac{1}{2} \sum_i^N \nabla_i^2 + \frac{1}{2} \sum_{i \neq j}^N \frac{1}{|\mathbf{r}_i - \mathbf{r}'_j|} + \sum_i^N v_{ext}^\sigma(\mathbf{r}). \quad (3.2)$$

3.1.1 Theorem of HOHENBERG & KOHN

Unfortunately, a precise determination of the ground state energy of the many-electron problem by solving the SCHRÖDINGER equation $\mathcal{H}_{el}\Psi = E\Psi$ is still impossible. This is due to the mere fact

that the presence of the two-electron operator \mathcal{U}_{ee} of the electron-electron interaction prevents a decoupling of the many-electron system. An expedient for this problem was provided by the idea of replacing the many-electron wavefunction with the free-electron charge density, as proposed in 1927 by THOMAS [Tho27] and FERMI [Fer27, Fer28]. The latter lead to the so-called THOMAS-FERMI approach to electronic structure. DIRAC improved the theory by adding a term describing the exchange energy [Dir30]. However, it took nearly forty years until the complementing theorems of HOHENBERG & KOHN [HK64], VON BARTH & HEDIN [vBH72] as well as LEVY [Lev82] introduced a convenient and effective way to describe the many-electron problem in terms of the one-electron charge density. Today, modern DFT is based on the following theorems. They propose the ground state energy of a spin-polarised many-electron system to be a proper and unique functional of the ground state spin-dependent electron densities $n_\sigma(\mathbf{r})$ ¹:

$$E_0 = E[n_\sigma(\mathbf{r})]. \quad (3.3)$$

The total electron density $n(\mathbf{r})$ and magnetization density $m(\mathbf{r})$ read

$$n \equiv n(\mathbf{r}) = n_\uparrow(\mathbf{r}) + n_\downarrow(\mathbf{r}), \quad (3.4)$$

$$m \equiv m(\mathbf{r}) = n_\uparrow(\mathbf{r}) - n_\downarrow(\mathbf{r}). \quad (3.5)$$

From equation (3.3) it is obvious that a unique energy can be assigned to each electron density, for which the variational principle

$$E_0 = E[n_\sigma^0] \leq E[n_\sigma] \quad (3.6)$$

holds. Therefore, the energy of the many-electron system takes its global minimum at the ground state density. Consequently, the variation of the energy with respect to the electron density has to vanish:

$$\delta E[n_\sigma]_{n=n^0} = 0. \quad (3.7)$$

With that the HOHENBERG-KOHN theory arrives at an equation which only involves a functional or derivatives of functionals of the charge density alone. However, there is still the obstacle of the unknown interdependence of the ground state energy and the electron density. Without further knowledge only the functional dependence for the potential of the nuclei \mathcal{V}_{ext} is given.

Kohn-Sham equations

Therefore, a subsequent approach was suggested partially going back to a wavefunction-like description. KOHN & SHAM remedied the HOHENBERG-KOHN problem by mapping the interacting electronic system onto a fictitious system of noninteracting quasiparticles moving in an effective potential [KS65]. In the representation of non-interacting one-electron wavefunctions $\psi_{\alpha\sigma}$, the electron density becomes

$$n_\sigma = \sum_\alpha \Theta(\mu - \epsilon_{\alpha\sigma}) |\psi_{\alpha\sigma}(\mathbf{r})|^2. \quad (3.8)$$

The HEAVISIDE-function $\Theta(\mu - \epsilon_{\alpha\sigma})$ in (3.8) ensures all KOHN-SHAM-orbitals with $\epsilon_{\alpha\sigma} < \mu$ to be completely occupied and those with $\epsilon_{\alpha\sigma} > \mu$ being unoccupied. The chemical potential μ coincides with the FERMI energy at vanishing temperature.

The functional of the kinetic energy can now be decomposed into a part of non-interacting elec-

¹Hereinafter the abbreviation $\mathcal{A}[n_\uparrow^\alpha(\mathbf{r}), n_\downarrow^\alpha(\mathbf{r})] \equiv \mathcal{A}[n_\sigma^\alpha]$ will be used. Here $\sigma = \uparrow, \downarrow$ are the z -components of the spin and α is the basis of the remaining quantum numbers.

trons and an unknown exchange-correlation part T_{xc}

$$T[n_\sigma] = -\frac{1}{2} \sum_{\alpha} \Theta(\mu - \epsilon_{\alpha\sigma}) \langle \psi_{\alpha\sigma} | \nabla^2 | \psi_{\alpha\sigma} \rangle + T_{xc}[n_\sigma]. \quad (3.9)$$

The interaction potential \mathcal{U}_{ee} consists of contributions due to the classical electrostatic interaction and an unknown exchange-correlation correction E_{xc} . The total energy functional referring to the HAMILTONIAN (3.2) can now be rewritten as

$$E[n_\sigma] = T[n_\sigma] + \int d^3\mathbf{r} v(\mathbf{r}) n_\sigma(\mathbf{r}) + U[n_\sigma] + E_{xc}[n_\sigma]. \quad (3.10)$$

Here, $U[n_\sigma]$ constitutes the HARTREE interaction among the electrons, as well as their self-interaction:

$$U[n_\sigma] = \frac{1}{2} \int d^3\mathbf{r} \int d^3\mathbf{r}' \frac{n(\mathbf{r})n(\mathbf{r}')}{|\mathbf{r} - \mathbf{r}'|}. \quad (3.11)$$

Under the constraints of particle conservation,

$$\int_{-\infty}^{\mu} d^3\mathbf{r} n(\mathbf{r}) = N, \quad (3.12)$$

and the normalization of the wavefunctions $\psi_{\alpha\sigma}(\mathbf{r})$, the variation of equation (3.10) with respect to the electron density n_σ leads directly to the KOHN-SHAM-equations:

$$\left(-\frac{1}{2} \nabla^2 + v(\mathbf{r}) + u[n_\sigma] + v_{xc}[n_\sigma] \right) \psi_{\alpha\sigma}(\mathbf{r}) = \epsilon_{\alpha\sigma} \psi_{\alpha\sigma}(\mathbf{r}). \quad (3.13)$$

The potential $u[n_\sigma]$ in equation (3.13) states a HARTREE-like repulsion

$$u[n_\sigma] = \int d^3\mathbf{r}' \frac{n_\sigma(\mathbf{r}')}{|\mathbf{r} - \mathbf{r}'|}. \quad (3.14)$$

The exchange-correlation potential $v_{xc}[n_\sigma]$ reads as

$$v_{xc}[n_\sigma] = \frac{\delta E_{xc}[n_\sigma]}{\delta n_\sigma}. \quad (3.15)$$

The term $E_{xc}[n_\sigma]$ represents corrections to the kinetic energy $T_{xc}[n_\sigma]$, as well as those to the interaction potential \mathcal{U}_{ee} . Hereinafter, the potentials $v(\mathbf{r})$, $u(\mathbf{r})$ and $v_{xc}(\mathbf{r})$ are summarized as \mathcal{V}_{eff} .

3.1.2 Exchange-correlation functional

In principle, the KOHN-SHAM equations are exact within the framework of the BORN-OPPENHEIMER approximation. Nevertheless, the exchange-correlation potential is unknown and prevents to solve equation (3.13) exactly. Nowadays the main challenge within DFT is to find reliable approximations for the exchange-correlation potential $v_{xc}[n_\sigma]$ [HCTH98, SS05]. The two most common parametrizations, also applied within this thesis, are the local (spin) density approximation (L(S)DA) and the generalized gradient approximation (GGA) and present the first two rungs of “Jacob’s ladder” towards the divine functional as introduced by PERDEW [Mat02, TPSS03].

Historically, the most important and till today the most widely used density functional approximation for the exchange-correlation energy is the L(S)DA, first suggested by KOHN and SHAM

[KS65]:

$$E_{xc}^{\text{LSDA}}[n_\sigma] = \int d^3\mathbf{r} n_\sigma \epsilon_{xc}^{\text{uniform}} = \frac{3}{4} \left(\frac{3}{\pi} \right)^{1/3} \int d^3\mathbf{r} (n_\sigma)^{4/3}. \quad (3.16)$$

Within, $\epsilon_{xc}^{\text{uniform}}$ is the exchange-correlation energy per electron in a uniform electron gas of local density n_σ [vL94]. This quantity is known exactly in the limit of high density and is often computed using Monte Carlo techniques for varying densities [Cep80, CA86, AM98]. In practice, the latter results are then parametrized within a certain accuracy to present the exchange-correlation energy analytically. In this thesis, the parametrization of VOSKO, WILK and NUSAIR [VWN80, VW80] was used for the description of the chalcogenide material systems (section 5.1). Besides basing on simple formulas derived in the theory of a uniform electron gas, the L(S)DA delivers very good results on the electronic structure for typical crystals.

A fundamental requirement of the L(S)DA is an almost homogeneous density, that is, n_σ only slowly varies in space. If this cannot be guaranteed, the spatial change of the density has to be taken into account, too. A first straight-forward attempt at doing this were the so-called gradient-expansion approximations (GEA). Here, one tried to add a first-order gradient of the density to the THOMAS-FERMI-DIRAC approximation [Tho27] [Fer27, Fer28] [Dir30], resulting in the WEIZSÄCKER correction to L(S)DA [Wei35]. In practice, the inclusion of low-order gradient corrections almost never improves on the L(S)DA and often even worsens it [Cap06]. The calculation of higher-order corrections is exceedingly sophisticated. Therefore, climbing a step further on “*Jacob’s ladder*”, the GGA [PJP⁺92] includes the functional f of the first derivative of the density and the density itself:

$$E_{xc}^{\text{GGA}}[n_\sigma] = \int d^3\mathbf{r} f[n_\sigma, \nabla n_\sigma]. \quad (3.17)$$

In comparison with the L(S)DA, the GGA tends to improve total energies, ionization energies, and geometrical energy differences. Additionally, the GGA expands and softens bonds, an effect that sometimes corrects and sometimes over-corrects the predictions of the L(S)DA ([PBE96] and references within). Obviously, the GGA favours density inhomogeneity more than the L(S)DA can. Contrary to L(S)DA, for which all parametrizations have to lead to the only possible correct expression for $\epsilon_{xc}^{\text{uniform}}$, different flavours of the GGA can give very different expressions for the functional $f(n_\sigma, \nabla n_\sigma)$. For the silicon-based materials presented in this thesis, the PERDEW-BURKE-ERNZERHOF flavour of the exchange-correlation functional was chosen [PBE96].

A general drawback of the L(S)DA and GGA is the underestimation of the electronic band gap in semiconductors and insulators [Per85]. Applying advanced approaches, as LDA+U [AAL97] and self-interaction corrections (SIC) [Per81, LED⁺05] to L(S)DA, as well as the usage of special semi-local exchange-correlation potentials [TB09] and self-energy corrections (GW) [AG98] give zero temperature band gap widths comparable to experiment. However, within parts of this thesis (section 5.2), the temperature dependence of the band gap is important. Hence, a temperature-dependent scissors-operator based on the representation of GODBY [GSS88] and VARSHNI [Var67] was included to correct the temperature dependence of the band gaps [E3, E4, E8].

Despite the success of the L(S)DA and GGA, the quest for more precise and powerful functional goes ever on. With orbital functionals, like the SIC, the step on the third rung of “*Jacob’s ladder*” is already made. Further state-of-the art exchange-correlation functionals include e.g. hybrid functionals [Bec93], which attempt to include the exact exchange of HARTREE-FOCK theory to the L(S)DA, and meta-GGAs [TPSS03], which additionally introduce the KOHN-SHAM kinetic energy density.

3.2 Band structure methods

In the preceding, it has been shown that the complex many-particle problem (3.2) can be mapped onto an effective one-particle problem for the electronic ground-state. In fact, the KOHN-SHAM equations (3.13) are understood as effective one-particle SCHRÖDINGER equations. Due to the fact of equations (3.13) and (3.8) being coupled, the KOHN-SHAM equations can only be solved by iteration to self-consistency. The goal of various band structure methods is now to determine the charge density for a given effective potential by iteratively solving the KOHN-SHAM equations. In this section, the band structure methods used within this thesis, namely the KORRINGA-KOHN-ROSTOKER (KKR) approach and a method based on plane waves and pseudopotentials (PPS), will be introduced.

3.2.1 KORRINGA-KOHN-ROSTOKER method

An elegant way to solve the KOHN-SHAM equations by principles of a multiple-scattering approach was first described in 1947 by KORRINGA [Kor47] and in 1954 by KOHN & ROSTOKER [KR54]. The great advantage of the method is to separate the scattering properties of the single potentials from the geometry of the system. Although KOHN & ROSTOKER already used GREEN's functions (GFs) to calculate the electronic structure of materials, DUPREE [Dup61], BEEBY [Bee67], and HOLZWARTH [Hol75] proposed more efficient ways to solve differential equations, like (3.13), by applying the method of GFs. Meanwhile, the KKR method is perpetually improved and for deeper reading I refer to [MMZ87], [PZD02, MP06, DLZ06] and [EBB⁺10, EKM11].

By using GFs, one avoids to determine the eigenvalues $\epsilon_{\alpha\sigma}$ and corresponding eigenstates $\psi_{\alpha\sigma}$ directly from the HAMILTONIAN, but rather inverts the differential equation to obtain the GF $G(\mathbf{r}, \mathbf{r}'; E)$ of the system. The latter is linked to the solution of an inhomogeneous SCHRÖDINGER or DIRAC like equation

$$(\mathcal{H} + V_{\text{eff}} - E)G(\mathbf{r}, \mathbf{r}'; E) = -\delta(\mathbf{r}, \mathbf{r}'). \quad (3.18)$$

The LEHMANN spectral representation [Leh54] for the spin-dependent GF for complex energies $Z^\pm = E \pm i\Gamma$ reads

$$G_\sigma^\pm(\mathbf{r}, \mathbf{r}'; Z^\pm) = \sum_\alpha \frac{\psi_{\alpha\sigma}(\mathbf{r})\psi_{\alpha\sigma}^*(\mathbf{r}')}{Z^\pm - \epsilon_{\alpha\sigma}}, \quad (3.19)$$

where the poles are the eigenvalues $\epsilon_{\alpha\sigma}$ of the KOHN-SHAM operator. Comparing with Equation (3.8) and using the DIRAC identity [MMZ87], the spin-dependent electron density n_σ and DOS N_σ on the real axis ($\Gamma \rightarrow 0$) can be calculated as

$$n_\sigma(\mathbf{r}) = \mp \frac{1}{\pi} \int_{-\infty}^{\mu} dE \Im G_\sigma^\pm(\mathbf{r}, \mathbf{r}; E) \quad (3.20)$$

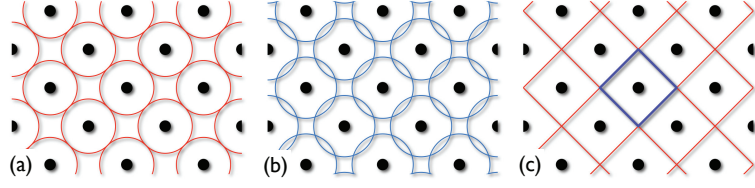
$$N_\sigma(E) = \mp \frac{1}{\pi} \int d^3\mathbf{r} \Im G_\sigma^\pm(\mathbf{r}, \mathbf{r}; E). \quad (3.21)$$

DYSON and LIPPMANN-SCHWINGER equation

The hierarchy of GFs allows for an effective way to determine the GF $G(E)$ of the physical system of interest by relating \mathcal{H} to a known reference HAMILTONIAN \mathcal{H}^0 , represented by $\mathring{G}(E)$. Assuming, that \mathcal{H} can be obtained from \mathcal{H}^0 by adding a perturbation $\Delta\mathcal{V}$, it is $\mathcal{H} = \mathcal{H}^0 + \Delta\mathcal{V}$ and the GFs are related by a DYSON equation

$$G(E) = \mathring{G}(E) + \mathring{G}(E)\Delta\mathcal{V}G(E) = \mathring{G}(E) + \mathring{G}(E)\mathring{T}(E)\mathring{G}(E), \quad (3.22)$$

Figure 3.1: Schematic potential presentation for (a) a muffin-tin approximation, (b) an atomic-sphere-approximation and (c) a full potential description. Adapted from [Dän08].



which in principal has to be solved iteratively for $G(E)$. The definition of the transition operator (often t -matrix) $\tilde{T} = \Delta\mathcal{V} (1 + \hat{G}\tilde{T})$, which sums the infinite perturbation series (3.22), enables to solve the DYSON equation exactly. Using \tilde{T} , a wavefunction ψ referring to the electronic system \mathcal{H} can be related to the corresponding wavefunction $\hat{\psi}$ of the reference system $\hat{\mathcal{H}}$ by a LIPPMANN-SCHWINGER equation [LS50]

$$|\psi\rangle = |\hat{\psi}\rangle + \hat{G}(E)\tilde{T}(E)|\hat{\psi}\rangle = |\hat{\psi}\rangle + \hat{G}(E)\Delta\mathcal{V}|\psi\rangle. \quad (3.23)$$

According to GYÖRFFY & STOTT [GS73], \tilde{T} can be expressed as

$$\tilde{T}(E) = \sum_{nn'} \tau^{nn'}(E), \quad (3.24)$$

where the scattering path operator $\tau^{nn'}$ transfers a wave at site n to a wave at site n' taking into account all possible scattering paths [Gon92, EKM11].

Single-site and multiple scattering

With the previous introduction, it is obvious that all information of the physical system of interest can be obtained by knowledge of the reference GF $\hat{G}(E)$ and the transition operator \tilde{T} . With that, the KOHN-SHAM equations or equivalent differential equations can be solved. Obviously, solving (3.18) for an arbitrary potential is numerically very demanding.

In principle, the effective potential \mathcal{V}_{eff} can be represented by discrete non-overlapping scattering centers. Within this full-potential approach (sketched in figure 3.1(c)), the potential is treated exactly in each WIGNER-SEITZ cell of the system [DWZD91, HZE+98, ASH+99]. It is more practicable to neglect non-spherical potential contributions and to assume a spherically symmetric potential around each atom. The potential within each sphere around the atomic position \mathbf{R}^n then reads

$$\mathcal{V}_{\text{eff}}(\mathbf{r}) = \sum_n \mathcal{V}_0^n(\mathbf{r} - \mathbf{R}^n) \quad \text{with} \quad \mathcal{V}_0^n(\mathbf{r}) = \begin{cases} \mathcal{V}_0^n(r) & r \leq s^n \\ 0 & r > s^n \end{cases} \quad (3.25)$$

s^n is either the muffin-tin radius and the spheres are non-overlapping (muffin-tin approximation (MTA, cf. figure 3.1(a)), or s^n is the WIGNER-SEITZ radius for overlapping spheres accounting for the full cell volume (atomic-sphere approximation (ASA), cf. figure 3.1(b)). The latter approximation was used for all KKR calculations within this thesis. Assuming $\hat{\mathcal{H}} = -\frac{1}{2}\nabla^2$ and applying the ASA, the solution to equation (3.18) reads²

$$G^{nn'}(\mathbf{r}, \mathbf{r}'; E) = -i\sqrt{E}\delta_{nn'} \sum_L R_L^n(r_{<}; E) H_L^n(r_{>}; E) + \sum_{LL'} R_L^n(\mathbf{r}; E) G_{LL'}^{nn'}(E) R_L^{n'}(\mathbf{r}'; E). \quad (3.26)$$

Here, the GF is expressed in terms of the regular and irregular solution to the radial SCHRÖDIN-

²The abbreviation $G^{nn'}(\mathbf{r}, \mathbf{r}'; E) = G(\mathbf{r} + \mathbf{R}^n, \mathbf{r}' + \mathbf{R}^{n'}; E)$ is used here et seq.

GER equation

$$R_L^n(r_<;E) = R_l^n(r;E)Y_L(\hat{e}_r) \quad \text{and} \quad H_L^n(r_>;E) = H_l^n(r;E)Y_L(\hat{e}_r), \quad (3.27)$$

where $Y_L(\hat{e}_r)$ are real spherical harmonics with shorthand index $L = (l, m)$ and $\hat{e}_r = \mathbf{r}/r$, while $r_<$ and $r_>$ are the smaller and larger of r and r' [BZLD84]. Equation (3.26) elucidates the character of the KKR method. The first term is the contribution of a scattering event on an isolated potential in free space. The second term, accenting $G_{LL'}^{nn'}(E)$, accounts for multiple scattering between the atomic spheres. The latter structural GF can be related analytically to the free space structural GF $\hat{g}_{LL'}^{nn'}(E)$ via an algebraic DYSON equation [Dup61]

$$G_{LL'}^{nn'}(E) = \hat{g}_{LL'}^{nn'}(E) + \sum_{n''L''} \hat{g}_{LL''}^{nn''}(E) t_{l''}^{n''}(E) G_{L''L'}^{n''n'}(E). \quad (3.28)$$

The single-site t -matrix $t_{l''}^{n''}$ can be interpreted as the operator connecting an incoming free wave with the waves being scattered at the single-site crystal potential $\mathcal{V}_0^{n''}(r)$ [MP06]. It is worthwhile to remember that the structural GF depends only on the geometry of the lattice and not on the scattering properties.

For the scattering path operator, the equation of motion referring to equation (3.28) reads [Gon92, EKM11]:

$$\tau_{LL'}^{nn'}(E) = t_l^n(E) \delta_{nn'} \delta_{LL'} + t_l^n(E) \sum_{n''L''} \hat{g}_{LL''}^{nn''}(E) \tau_{L''L'}^{n''n'}(E). \quad (3.29)$$

According to FAULKNER [Fau77], the latter can be solved straightforwardly for finite systems, yielding

$$\tau(E) = [t(E)^{-1} - \hat{g}(E)]^{-1} = [\mathcal{M}(E)]^{-1}, \quad (3.30)$$

where $\mathcal{M}(E)$ is the real-space KKR matrix [PBT⁺98]. For a periodic system, it is convenient to use the lattice FOURIER transforms of \hat{g} and τ and to rewrite equation (3.28) as

$$G_{LL'}(\mathbf{k}, E) = \hat{g}_{LL'}(\mathbf{k}, E) + \sum_{L''} \hat{g}_{LL''}(\mathbf{k}, E) t_{l''}(E) G_{L''L'}(\mathbf{k}, E) \quad (3.31)$$

and with that equation (3.30) becomes

$$\tau(\mathbf{k}, E) = [t(E)^{-1} - \hat{g}(\mathbf{k}, E)]^{-1} = [\mathcal{M}(\mathbf{k}, E)]^{-1}. \quad (3.32)$$

The KKR matrix in equation (3.32) is related to the secular equation occurring in the original KKR method [Kor47]. That is, varying the energy E for a fixed wave vector \mathbf{k} , $\mathcal{M}(\mathbf{k}, E)$ will indicate an eigenvalue $E_{\mathbf{k}}$ by a jump of its determinants phase [Gon92, EKM11]. Alternatively, one can also fix the energy and search for the allowed $\mathbf{k}(E)$. If the energy is the FERMI energy, $\mathbf{k}(E)$ defines the FERMI surface.

By knowledge of the GREEN's function (GF) $G_{LL'}(\mathbf{k}, E)$ the electron density can be calculated via equation (3.20), thus establishing a self-consistency loop for \mathcal{V}_{eff} . Using the analytically known free-space GF as a starting point in equation (3.22) is not efficient. First, the free space structural constants decay weakly in space - a huge number of atoms would be necessary for a correct description of the physical system. Second, the free-space solutions $E_{\mathbf{k}} = (\mathbf{k} + \mathbf{G}^n)^2$ determined by \hat{g} , which are in the same energy range as the solutions of the physical system, lead to numerical instabilities in equation (3.30). A DYSON equation with a system of repulsive potentials as reference, instead of free space, avoids these problems.

Screened reference system

As introduced by SZUNYOGH, ZELLER, WILDBERGER and ZAHN [SUWK94, ZDU⁺95, WZD97, Zah98] in the KKR method and originating in an idea of ANDERSEN [AJ84], constant repulsive potentials inside the atomic spheres are chosen as a reference system. Within this thesis, a constant positive height of 8Ry was used, pushing the reference states out of the physical scope. Accordingly, the DYSON equation (3.22) has to be solved in two steps. First, starting with the free electron gas \tilde{g} , the reference system \tilde{g} is determined. Second, from the reference system \tilde{g} the physical system G can be found. With $\Delta t = t - \tilde{t}$ defined as the difference of the single-site t -matrices of real and reference system, one can rearrange equation (3.32) as

$$[\mathcal{M}(\mathbf{k}, E)]^{-1} = [\Delta t(E)^{-1} - \tilde{g}(\mathbf{k}, E)]^{-1}. \quad (3.33)$$

By

$$\det[\mathcal{M}(\mathbf{k}, E) - \lambda(\mathbf{k}, E)\mathbb{1}] = 0 \quad (3.34)$$

the single-particle eigenvalue spectrum, which is interpreted as band structure $E_{\mathbf{k}}$ of the physical system, is well defined by the zeros of the eigenvalues $\lambda(\mathbf{k}, E)$.

Due to the fact that the reference GF $\tilde{g}_{LL}^{nn'}$ decays rapidly in real space this extension to KKR is called screened KORRINGA-KOHN-ROSTOKER (SKKR) or tight-binding KKR (TB-KKR) method. The fully relativistic extension to the SKKR [Cze09, GCF⁺09, Gra10] was used within this thesis and allows for a numerically efficient treatment by sparse matrix techniques.

3.2.2 The plane-wave pseudopotential method

Plane waves are eigenfunctions of the kinetic operator $\mathcal{T} = -1/2\nabla^2$. Thus, presuming that localized states are not dominating, it is plausible to expand the KOHN-SHAM eigenfunctions ψ in terms of plane waves. Demanding periodicity of the system and applying BLOCH's theorem [Blo25], one can write the FOURIER series

$$\psi_{\mathbf{k}}(\mathbf{r}) = \sum_{\mathbf{G}} c_{\mathbf{k}+\mathbf{G}} \cdot e^{i(\mathbf{k}+\mathbf{G})\mathbf{r}} \quad \text{and} \quad \mathcal{V}_{\text{eff}}(\mathbf{r}) = \sum_{\mathbf{G}} \tilde{\mathcal{V}}_{\text{eff}}(\mathbf{G}) \cdot e^{i\mathbf{G}\mathbf{r}}, \quad (3.35)$$

for the wavefunctions and the effective potential, respectively. Here, \mathbf{G} are reciprocal lattice vectors; $c_{\mathbf{k}+\mathbf{G}}$ and $\tilde{\mathcal{V}}_{\text{eff}}(\mathbf{G})$ are the FOURIER expansion coefficients for the effective potential and the wavefunctions, respectively. The application of equations (3.35) allows to solve the KOHN-SHAM equations (3.13) in reciprocal space exactly,

$$\sum_{\mathbf{G}'}^{\infty} (|\mathbf{k} + \mathbf{G}'|^2 \delta_{\mathbf{G}\mathbf{G}'} + \tilde{\mathcal{V}}_{\text{eff}}(\mathbf{G} - \mathbf{G}')) c_{\mathbf{k}+\mathbf{G}} = \epsilon(\mathbf{k}) c_{\mathbf{k}+\mathbf{G}}. \quad (3.36)$$

However, a numerical evaluation of equation (3.36) is impossible due to the infinite sum. Practically, it is reliable to account only for a finite number of \mathbf{G} , which are related to plane waves with energy less than a given cut-off $E_{\text{cut}} \geq |\mathbf{k} + \mathbf{G}|^2$ [FKBK00]. However, core wavefunctions as well as valence wavefunctions nearby the core region, show detailed features and thus need high FOURIER components in equations (3.35), i.e. a large value for E_{cut} .

Ultrasoft norm conserving pseudopotentials

The idea of pseudopotentials (PPs) was originally introduced to simplify electronic structure calculations by eliminating the chemically inert core electrons within a frozen-core approximation

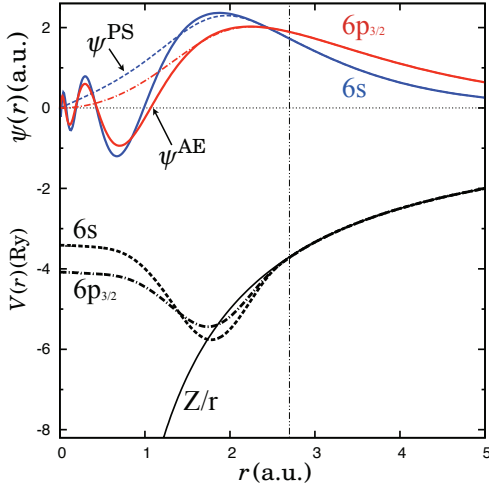


Figure 3.2: Nonlocal part of the relativistic pseudopotential as introduced by equation (3.41) (black dashed line for the 6s state with $l = 0, j = 1/2, \kappa = -1$ and black dash-dotted line for the $6p_{3/2}$ state with $l = 1, j = 3/2, \kappa = -2$) and accompanied nodeless pseudo-wavefunctions ψ^{PS} for atomic bismuth. The effective ionic potential Z/r (black solid line) and the referring all-electron (AE) wavefunctions ψ^{AE} are shown, too. At the cut-off radius $r_C = 2.7$ and beyond, the pseudo-wavefunctions and the AE solutions have to match according to the condition given by equation (3.43). The valence configuration $6s^2 6p^3$ for the pseudopotential was chosen. The exchange-correlation part was accounted for by the GGA [PBE96]. The pseudopotential was generated with the LD1 atomic code [CC05, Gmo09].

[HSC79, vG80] and to account only for the chemically active valence electrons. Often, the structure and properties of a material are then sufficiently determined by the valence electrons.

The essence of the PP approach is to replace the strong core potential, including valence-core interactions, by a PP whose node-less ground state wavefunction ψ^{PS} is identical to the all-electron (AE) wavefunction ψ^{AE} at and beyond a certain core radius r_C [SN06].³

Following the orthogonalized plane wave method (OPW) [Her40], the valence AE wavefunction ψ_v^{AE} is augmented with core AE wavefunctions ψ_c^{AE} to obtain the pseudo-wavefunction in DIRAC notation

$$\langle \psi_v^{\text{PS}} | = \langle \psi_v^{\text{AE}} | + \sum_c \alpha_{cv} \langle \psi_c^{\text{AE}} |. \quad (3.37)$$

Here $i = \{E, l, m\}$ is a composite index representing the dependence on energy E and angular momentum (l, m) . Demanding orthonormality, equation (3.37) becomes [Pic89, Hen09]

$$\langle \psi_v^{\text{PS}} | = \langle \psi_v^{\text{AE}} | + \sum_c |\psi_c^{\text{AE}}\rangle \langle \psi_c^{\text{AE}} | \psi_v^{\text{PS}}\rangle. \quad (3.38)$$

Substituting the latter into the SCHRÖDINGER equation $\mathcal{H} \langle \psi^{\text{AE}} | = \epsilon^{\text{AE}} \langle \psi^{\text{AE}} |$ yields the pseudo-wavefunction to be an eigenstate of the HAMILTONIAN

$$\left(\mathcal{T} + \mathcal{V}_c^{\text{PS}} \right) \langle \psi_i^{\text{PS}} | = \epsilon_i^{\text{PS}} \langle \psi_i^{\text{PS}} |, \quad (3.39)$$

where the pseudopotential $\mathcal{V}_v^{\text{PS}}$ can be obtained by inversion of equation (3.39):

$$\mathcal{V}_v^{\text{PS}} = \mathcal{V}(\mathbf{r}) + \sum_c (\epsilon_v - \epsilon_c) |\psi_c^{\text{AE}}\rangle \langle \psi_c^{\text{AE}} |, \quad (3.40)$$

where $\mathcal{V}(\mathbf{r})$ is the bare COULOMB potential.

The PP was first introduced by PHILLIPS & KLEINMAN [PK59] and causes some consequences. In fact, \mathcal{V}^{PS} is a non-local, energy-dependent operator. As already apparent from the index i , the projector term acts differently on states depending on their angular momentum. According to KLEIN-

³The all-electron (AE) description is obtained by solving the SCHRÖDINGER equation for an isolated atom, yielding the wavefunctions ψ_c^{AE} and eigenenergies ϵ_c^{AE} of the core electrons. The above introduced KKR method is an AE method and thus appropriate for this purpose.

MAN and BYLANDER [KB82, GSS91], one can rewrite equation (3.40) in a semi-local form,

$$\mathcal{V}^{\text{PS}} = \mathcal{V}(\mathbf{r}) + \sum_{l=0}^{l_{\text{max}}} \mathcal{V}_l^{\text{PS}} \mathcal{P}_l, \quad (3.41)$$

in which \mathcal{P}_l is an angular momentum projection operator. The sum, originally over all l , converges fast at increasing l . Thus, $l_{\text{max}} \leq 3$ is most often sufficient to ensure convergence of equation (3.41). Commonly, l_{max} is increased by 1, and the local potential $\mathcal{V}(\mathbf{r})$ accounts for the $l = 0$ component. Additionally, and shown in figure 3.2, the projector term in equations (3.40)-(3.41) is short-ranged and repulsive. Thus, it weakens the dominating COULOMB potential close to the nucleus and cancels the nodal structure of ψ^{AE} , leading to smoother pseudo-wavefunctions ψ^{PS} close to the core. Consequently, a significantly smaller number of plane waves is needed for the FOURIER expansions in equations (3.35) and (3.36) and the main requisite is fulfilled.

Over the last decades, several approaches were introduced to optimize \mathcal{V}^{PS} for application and physical plausibility (see [Pic89, FS99b, SN06] and references therein). For that purpose, the pseudo-wavefunction should fulfill some additional requirements. First, although $\psi^{\text{AE}} \neq \psi^{\text{PS}}$, the charge density inside r_C has to be conserved [HSC79, BHS82], i.e.

$$\int_0^{r_C} dr r^2 |\psi^{\text{PS}}(r)|^2 = \int_0^{r_C} dr r^2 |\psi^{\text{AE}}(r)|^2. \quad (3.42)$$

Second, the scattering properties of ψ^{AE} should be accurately reproduced by ψ^{PS} over a broad energy range. Therefore, the logarithmic derivatives are matched at r_C to account for

$$\frac{1}{\psi_v^{\text{PS}}(r_C)} \frac{d\psi_v^{\text{PS}}(r_C)}{dr} = \frac{1}{\psi_v^{\text{AE}}(r_C)} \frac{d\psi_v^{\text{AE}}(r_C)}{dr}. \quad (3.43)$$

A very good transferability of the PP is then usually obtained by fulfilling equation (3.43) at a palmful of energy points per angular momentum channel, spanning the range of occupied states [Van90, FS99b].

Further progress was done in a seminal work by VANDERBILT [Van90], who introduced so-called ultra-soft pseudopotentials USPP. Here, the normalization condition (3.42) is relaxed, allowing for much smoother ψ^{PS} inside the core radius and, therefore, a tremendous reduction in the number of plane waves in the expansion (3.35). This is done at the price of having to augment the square modulus of the pseudo-wavefunctions with additional contributions Q_{ij} to recover the actual physical charge densities. Thus, the generalized norm-conserving condition reads

$$\langle \psi_i^{\text{AE}} | \psi_j^{\text{AE}} \rangle = \langle \psi_i^{\text{PS}} | \psi_j^{\text{PS}} \rangle + Q_{ij}. \quad (3.44)$$

The only other remaining constraint is then given by the matching condition equation (3.43). In principle, ultra-soft PPs tend to be less transferable than conventional PPs and a higher number of reference energies in equation (3.43) should be taken into account [Van90]. In return, the heavily reduced basis set allows for large-scale calculations. Within this thesis, the fully relativistic expansion ([CC05], cf. section 3.3) to the VANDERBILT scheme [Van90] is applied for the silicon-based materials.

Hellmann-Feynman theorem

For the description of the thermoelectric materials addressed in this thesis, knowledge of the equilibrium lattice configuration, e.g. the atomic positions, is essential. Besides the importance of structural relaxation of the atomic positions for systems involving external or interfacial strain (cf. [E3,E5,E7,E8]), the knowledge also enables access to the vibrational spectra of the systems. The latter are directly connected to the lattice thermal conductivity (see section 4.4) and, with that, to the TE figure of merit.

Within DFT, lattice dynamics is simulated by treating the nuclei as semi-classical particles on the BORN-OPPENHEIMER energy surface. The latter is defined by the nuclei part of equation (3.1). At the equilibrium geometry the force on any individual nucleus α has to vanish⁴,

$$\mathbf{F}_\alpha \equiv -\frac{\partial E(\mathbf{R})}{\partial \mathbf{R}_\alpha} = 0. \quad (3.45)$$

The vibrational modes ω of the lattice are given as eigenvalues of the HESSIAN of the BORN-OPPENHEIMER energy [BGC01,BGI10]

$$\det \left| \frac{1}{\sqrt{M_\alpha M_\beta}} \frac{\partial^2 E(\mathbf{R})}{\partial \mathbf{R}_\alpha \partial \mathbf{R}_\beta} - \omega^2 \right| = 0, \quad (3.46)$$

where M are the nuclei masses at place α, β . From equations (3.45) and (3.46) it is obvious that the determination of the equilibrium lattice configuration of a system demands the computation of the first and second derivatives of the BORN-OPPENHEIMER energy surface. The heart of this description is given by the HELLMANN-FEYNMAN theorem [Hel37, Fey39],

$$\mathbf{F}_\alpha = -\frac{\partial E(\mathbf{R})}{\partial \mathbf{R}_\alpha} = -\langle \Psi | \frac{\partial \mathcal{H}(\mathbf{R})}{\partial \mathbf{R}_\alpha} | \Psi \rangle = -\int n_{\mathbf{R}}(\mathbf{r}) \frac{\partial \mathcal{V}_{\text{en}}(\mathbf{r})}{\partial \mathbf{R}_\alpha} d^3 \mathbf{r} - \frac{\partial \mathcal{U}_{\text{nn}}(\mathbf{R})}{\partial \mathbf{R}_\alpha}, \quad (3.47)$$

where in general \mathbf{R}_α could be any parameter on which \mathcal{H} depends. Here the HAMILTONIAN is related to the nuclei by the electron-nucleus interaction \mathcal{V}_{en} , which couples to the electrons via the electron charge density $n_{\mathbf{R}}(\mathbf{r})$ at the lattice configuration \mathbf{R} .

The HESSIAN in equation (3.46) is obtained straightforward by differentiating the HELLMANN-FEYNMAN forces (3.47) as [BGC01,BGI10,SN06]

$$\frac{\partial^2 E(\mathbf{R})}{\partial \mathbf{R}_\alpha \partial \mathbf{R}_\beta} = -\frac{\partial \mathbf{F}_\alpha}{\partial \mathbf{R}_\beta} = \int n_{\mathbf{R}}(\mathbf{r}) \frac{\partial^2 \mathcal{V}_{\text{en}}(\mathbf{r})}{\partial \mathbf{R}_\alpha \partial \mathbf{R}_\beta} d^3 \mathbf{r} + \int \frac{\partial n_{\mathbf{R}}(\mathbf{r})}{\partial \mathbf{R}_\beta} \frac{\partial \mathcal{V}_{\text{en}}(\mathbf{r})}{\partial \mathbf{R}_\alpha} d^3 \mathbf{r} + \frac{\partial^2 \mathcal{U}_{\text{nn}}(\mathbf{R})}{\partial \mathbf{R}_\alpha \partial \mathbf{R}_\beta}. \quad (3.48)$$

It is usually defined as the matrix of the real-space interatomic force constants (IFC) $C_{\alpha\beta}^{ij}$, with ij being Cartesian components [GGPB91]. Fourier transforming the IFC equation (3.48) and solving the secular equation (3.46) in reciprocal space will give access to the phonon band structure, as shown for bulk silicon in figure 3.3, as well as to integral quantities like the phonon density of states $\mathcal{F}(\omega)$, the lattice specific heat or the lattice thermal conductivity (cf. section 4.4).

Obviously, equations (3.47) and (3.48) depend directly on the ground-state electronic charge density $n_{\mathbf{R}}(\mathbf{r})$ and its linear response to a distortion of the lattice $\frac{\partial n_{\mathbf{R}}(\mathbf{r})}{\partial \mathbf{R}_\beta}$. This result was first stated by JOHNSON & DE CICCIO [DJ69]; it is the basis of modern density functional perturbation theory (DFPT) [BGT87,BGC01,BGI10,Gon95a,Gon95b].

⁴Practically, the forces are minimized to be below some threshold. Within, $\mathbf{F}_\alpha \leq 0.1 \text{ meV/\AA}$ was used.

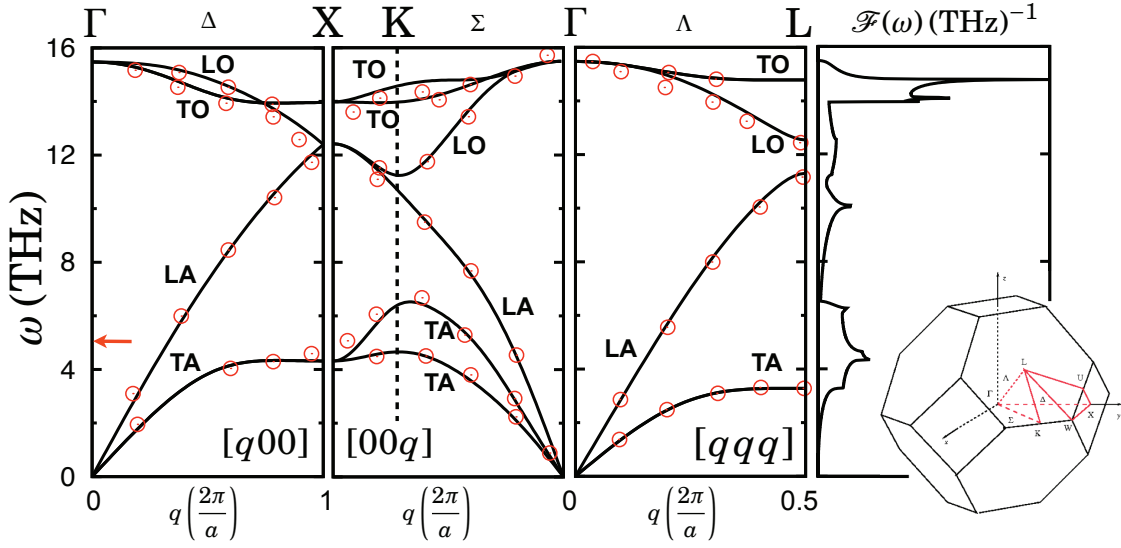


Figure 3.3: Phonon dispersion relation $\omega(q)$ for bulk silicon. The chosen high-symmetry lines are depicted in the inset of the fcc BRILLOUIN zone shown on the right. The phonon density of states $\mathcal{F}(\omega)$ as well as the character of the modes are given. LA=longitudinal acoustic, TA=transversal acoustic, LO=longitudinal optical and TO=transversal optical. Red circles show experimental results from inelastic neutron scattering [TPZ72]. The calculations were done within DFPT, as implemented in the QUANTUMESPRESSO package [Gmo09]. The red arrow on the leftmost axis indicates the energy for which the iso-energy phonon surface is shown in figure 4.6(c).

3.3 The DIRAC equation

As pointed out in section 2, effective thermoelectric materials consist usually of heavy atoms. To account for all relativistic corrections solving the relativistic KOHN-SHAM-DIRAC equation $\mathcal{H}_{\text{KSD}}\psi_k = W_k\psi_k$ is required. The respective HAMILTONIAN then reads [Dir28, Str98]

$$\mathcal{H}_{\text{KSD}} = -ic\alpha_4\nabla_{\mathbf{r}} + \mathbb{1}_4\tilde{\mathcal{V}}_{\text{eff}}(\mathbf{r}) + mc^2\beta_4, \quad (3.49)$$

where the effective potential $\tilde{\mathcal{V}}_{\text{eff}}$ should include the vector field $\mathbf{A}(\mathbf{r})$, i.e. $\tilde{\mathcal{V}}_{\text{eff}}(\mathbf{r}) = -\alpha \cdot \mathbf{A}(\mathbf{r}) + \mathcal{V}(\mathbf{r})$. Omitting diamagnetic effects on the electron's orbital motion, the effective potential simplifies to $\tilde{\mathcal{V}}_{\text{eff}}(\mathbf{r}) = \beta\sigma\mathbf{B}_{\text{eff}} + \mathcal{V}(\mathbf{r})$ [WZB+92]. The effective magnetic field \mathbf{B}_{eff} vanishes in non-magnetic materials, otherwise it depends on the spin magnetization density [HZE+98]. Introducing the PAULI matrices σ , the 4×4 DIRAC matrices are defined as

$$\alpha_4 = \begin{pmatrix} 0 & \sigma \\ \sigma & 0 \end{pmatrix}, \quad \beta_4 = \begin{pmatrix} \mathbb{1}_2 & 0 \\ 0 & -\mathbb{1}_2 \end{pmatrix}, \quad \mathbb{1}_4 = \begin{pmatrix} \mathbb{1}_2 & 0 \\ 0 & \mathbb{1}_2 \end{pmatrix}. \quad (3.50)$$

Within the KKR method the KOHN-SHAM-DIRAC equation replaces the non-relativistic KOHN-SHAM equations (3.13). With some slight extension, the theorems of HOHENBERG and KOHN also apply to the fully relativistic case [MV79, RR79]. Assuming a non-magnetic material, the 4-component solutions to the KOHN-SHAM-DIRAC equation can be expanded into spin-angular functions using the PAULI bi-spinor formalism,

$$\psi_{\mathbf{k}}(\mathbf{r}) = \sum_{Q'} a_{Q'}(\mathbf{k}) \begin{pmatrix} g_{QQ'}(r)\chi_Q(\hat{e}_r) \\ if_{QQ'}(r)\chi_{\tilde{Q}}(\hat{e}_r) \end{pmatrix} \quad \text{with} \quad \begin{matrix} Q = \{+\kappa, \mu\} \\ \tilde{Q} = \{-\kappa, \mu\} \end{matrix} \quad (3.51)$$

Here, $f_{QQ'}(r)$ and $g_{QQ'}(r)$ are the large and the small component of the solution, respectively. The starting point for the DYSON equation (3.28) are now the fully relativistic structure constants

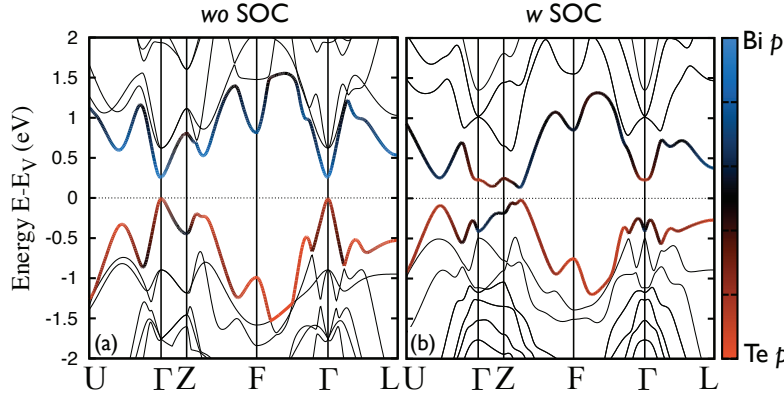


Figure 3.4: Band structure of bulk Bi_2Te_3 in the rhombohedral unit cell (a) without (wo) and (b) with (w) spin-orbit coupling (SOC) included. Superimposed on the highest valence band and lowest conduction band is the site-dependent orbital character ($l = 1$). Accounting for SOC leads to band inversions in some parts of the BZ. Further details are explained in the text.

$\hat{g}_{QQ'}^{nn'}(E)$, which can be obtained from its non-relativistic counterpart, as well as the bi-spinors χ_Q , by a CLEBSCH-GORDON transformation [WZB⁺92]. With that, the fully relativistic band structure $E_k = W_k - mc^2$ is obtained by solving the secular KKR equation (3.33) analogous to the non-relativistic case. For deeper insight into the fully relativistic KKR method I recommend references [FRA83, SESG89, WZB⁺92, HZE⁺98, Kor12]. The implementation used within this thesis is introduced in [Cze09, GCF⁺09, Gra10].

FOLDY-WOUTHOUYSEN representation and spin-orbit coupling

To get more into the physical consequences of DIRAC's equation, it is instructive to rewrite equation (3.49) via the FOLDY-WOUTHOUYSEN transformation [FW50, CM95, SESG89, Ste10] and to separate the solutions of the particle (electron) and antiparticle (positron). For the special case of a non-magnetic spherical potential, the ansatz (3.51) is applied. One obtains a set of four linear first-order differential equations, coupling the small and large components. Describing the eigenvalues W_k up to $\mathcal{O}\left(\frac{1}{c^2}\right)$, equation (3.49) becomes

$$\mathcal{H}_{\text{KSD}} = -\nabla^2 + V(\mathbf{r}) - \underbrace{\frac{(\nabla^2)^2}{2m^2c^2}}_{(i)} - \underbrace{\frac{e}{8m^2c^2}\Delta V(\mathbf{r})}_{(ii)} - \underbrace{\frac{e}{4m^2c^2r}\frac{\partial V(\mathbf{r})}{\partial r}\lambda\mathbf{L}\cdot\mathbf{S}}_{(iii)}; \quad (3.52)$$

it is referred to as PAULI operator [Pau27], which acts on the large components of ψ only. While the first part of equation (3.52) is the SCHRÖDINGER equation for a spherical potential, the accompanied $\left(\frac{1}{c^2}\right)$ corrections can be interpreted as follows: (i) This term includes corrections due to the relativistic mass increase. The so-called DARWIN term (ii) accounts for the uncertainty principle. Due to electron-positron annihilation processes in the electric field of the potential, the position r of the electron is uncertain within an order of $\delta r = \frac{\hbar}{mc}$, which is the COMPTON length [Ste10]. The last term (iii) is related to the coupling of orbital angular momentum $\mathbf{L} = \mathbf{r} \times \mathbf{p}$ and spin $\mathbf{S} = \hbar\boldsymbol{\sigma}/2$, with the total angular momentum given by $\mathbf{J} = \mathbf{L} + \mathbf{S}$. The spin-orbit coupling (SOC) is particularly important for the band formation and related transport processes of the thermoelectric materials within this thesis. The SOC shifts the electron's atomic energy levels due to electromagnetic interaction between the electron's spin and the magnetic field generated by the electron's orbit around the nucleus. Hence, for $l > 0$, the energy levels split according to $j = l \pm 1/2$, known as spin-orbit splitting [SESG89]. For heavy atoms, the spin-orbit coupling strength λ is large [WM74] and the spin-orbit splitting of the valence-states can be in the order of several eV (e.g. for Bi: $E(l = 1, j = 3/2) - E(l = 1, j = 1/2) = 1.97$ eV [CW04]).

Assuming a semiconductor bulk material and the spin-orbit splitting acting on the occupied and unoccupied states near the fundamental band gap, SOC could lead to a shift of the formerly un-

occupied states to energies below the FERMI level E_F and pushing the formerly occupied states to energies above E_F . Thus, the bands are *inverted*. Hybridization between the inverted bands most likely opens the fundamental gap and leaves the electronic structure with reversed orbital character at the band edges [ZLQ⁺09, QZ10, HK10]. Such a situation is illustrated in figure 3.4 for bulk Bi₂Te₃. Here, the band structures without SOC (figure 3.4(a), scalar-relativistic calculation, omitting term (iii) in equation (3.52)) and with SOC (figure 3.4(b), full solution of equation (3.49)) are shown. Neglecting SOC, the unoccupied states near the band gap are formed solely by Bi p states, while the occupied states nearby are formed by Te p states. Switching on the SOC yields a change of the orbital character of the bands at the band gap in certain areas of the BZ, obviously connected with a SOC-induced band inversion, which is most apparent near the Γ high symmetry point [YKML12]. The \mathbf{k} -dependence of the band inversion nicely reflects the \mathbf{k} -dependence of the spin-orbit operator $\mathbf{L} \cdot \mathbf{S}$. If the inverted bands furthermore show up opposite parity eigenvalues, a non-trivial topology of occupied bands arises and the related surface states show intriguing robust metallic properties, while the bulk states remain insulating [ZLQ⁺09, QZ10, HK10]. These topologically non-trivial systems are called topological insulators and include bulk Bi₂Te₃ and Sb₂Te₃ [ZLQ⁺09, HXQ⁺09, KKKI12]. With topological insulators being available by strain engineering [CQK⁺10, SBPP11] and currently under debate [ZCS12], intrinsic SOC seems to be the main origin for the occurrence of topologically projected surface states.

Upon closing this section, some few words on the generation of fully relativistic PP should be said. The basis for a fully relativistic PP is the AE solution of equation (3.49) for a free atom. For a deduction of the non-local part of the PP it is common to solve equation (3.52) and to account only for the large component [Kle80, FS99b]. The derived PP is a scalar function of radius r depending parametrically only on the angular momentum l . However, within this thesis, a more sophisticated approach suggested by DAL CORSO & CONTE [CC05] was used for the silicon-based materials, which applies for the solution of the small and large components and requires the validity of condition (3.43) for the complete set of relativistic quantum numbers (j, s). Consequently, the nonlocal ultrasoft pseudopotential (USPP) has to be a 2×2 matrix of operators acting on the valence electron wavefunctions represented in the two-component spinor form. The local potential can be chosen as a j -averaged USPP [Van90].

This paragraph only gave a rough overview on relativistic electron dynamics. For a more detailed introduction to relativistic quantum mechanics I recommend the books of STRANGE [Str98], ROSE [Ros61], and PYYKKÖ [Pyy88].

3.4 Evaluation of surface integrals

All important ingredients of the thermoelectric transport are based on integrals of constant energy ϵ , written as

$$\mathcal{A}(E) = \oint_{E_{\xi}=E} \frac{d\xi^2}{|\alpha(\xi)|} \beta(\xi). \quad (3.53)$$

As will be shown in detail in section 4.3, the surface integral (3.53) e.g. coincides with the electron density of states if the wave vector \mathbf{k} and the electronic group velocity $\mathbf{v}(\mathbf{k})$ are involved ($\xi = \mathbf{k}, \alpha = \mathbf{v}, \beta = 1$). The phonon density of states (PHDOS) $\mathcal{F}(\omega)$ is given for $\xi = \mathbf{q}$ and the phonon group velocity (PGV) $\mathbf{v}(\mathbf{q})$. If furthermore $\beta = \tau_k \mathbf{v}(\mathbf{k})^2$ an expression for the transport distribution function (TDF) $\Sigma(E)$ (cf. equation (4.23)) is given.

As already pointed out, the KKR method allows for an easy access to the FERMI surface $\mathbf{k}(E_F)$ by solving equation (3.32). However, the numerical evaluation of related surface integrals (3.53) is

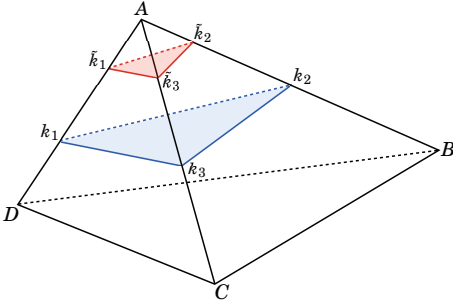


Figure 3.5: Tetrahedron spanned by 4 \mathbf{k} -points (ABCD) within the IBZ. The intersections of the iso-energetic surfaces are slightly above $E_F + \delta E$ (red) and below $E_F - \delta E$ (blue) the Fermi energy. From linear and quadratic interpolations, one numerically determines the group velocity and the effective mass tensor, respectively. Further details are given in the text.

rather complicated, especially concerning the convergence of the integral with respect to FOURIER-space (ξ -space) sampling and the determination of the respective derivatives. In recent calculations of the spin-HALL conductivity (comparable to the expression for the conventional electrical conductivity and originating in strong SOC) it was shown that a large number of \mathbf{k} -points in the BZ, usually in the order of a few to many billion \mathbf{k} for simple to complex systems, were needed to achieve convergence of the surface integral within a few percent [YKM⁺04, YF05, GYN05, WYSV06].

Within this thesis, an extended tetrahedron method [LT72, MMZ87, Zah98] was applied to determine the FERMI surface and related integral properties (3.53). Here, the irreducible part of the BRILLOUIN zone (IBZ) is divided into disjoint tetrahedra, as illustrated in figure 3.5. Each tetrahedron is defined by 4 unique \mathbf{k} -points (ABCD), at which the eigenvalues E_k are determined. Those tetrahedra which contain the FERMI energy $E_k = E_F$ will contribute to the FERMI surface. Performing the iso-energetic surface search for two energies (cf. figure 3.5) slightly around the FERMI energy, i.e. $\mathbf{k}(E_F - \delta E)$ (blue) and $\mathbf{k}(E_F + \delta E)$ (red) allows to determine the FERMI velocity by linear interpolation: $(\tilde{\mathbf{k}}_i - \mathbf{k}_i)\mathbf{v}_F = \delta E$. Obviously, the accuracy of the velocity strongly depends on the size of the tetrahedra, i.e. the number of \mathbf{k} -points. The determination of the velocity for complicated FERMI surfaces involving bands with large curvatures is very demanding. It was found [E6], that for a highly anisotropic BZ for which the group velocity could be highly anisotropic, too, it does matter in which direction the tetrahedron is spanned. If the derivatives are taken along the directions of the reciprocal lattice vectors, the error in the anisotropy ratio of the velocities and with that the conductivities can be substantial. In [E6] we present a detailed analysis how to understand and avoid such problems at the example of bulk Bi_2Te_3 .

Significant efforts have been undertaken to reduce the number of \mathbf{k} -points and to retain the quality of the FERMI velocity. One possibility was recently suggested by GRADHAND [Gra10, GFP⁺11]; it relies on the analytical derivation of the KKR matrix, taking advantage of the energy dependence of the latter. It turns out that this method is not feasible if the analytical derivative is needed for a considerable number of energies. Another approach is to use only a sparse \mathbf{k} -mesh and to determine the corresponding eigenvalues E_k . Afterwards, FOURIER [MS06] or WANNIER [WYSV06] expansions are used to interpolate the bands onto a finer \mathbf{k} -mesh. Such interpolation schemes tend to miscalculate bands with very sophisticated curvatures [E6]; they are very crucial if bands are nearly degenerate, e.g. at points of SOC-induced avoided band crossing. Here, adaptive \mathbf{k} -mesh refinements are advantageous to eliminate these errors [WYSV06].

To do so, an adaptive \mathbf{k} -mesh refinement scheme was also used within this thesis [E6, E7]. Naturally, only tetrahedra which contribute to the isoenergetic surface are refined. Here additional six \mathbf{k} -points are added to the edges of the considered tetrahedra (mid of AB, AC, AD, BC, BD, CD in figure 3.5). This method also allows to determine the effective mass tensor m_{ij} near the band edges via a

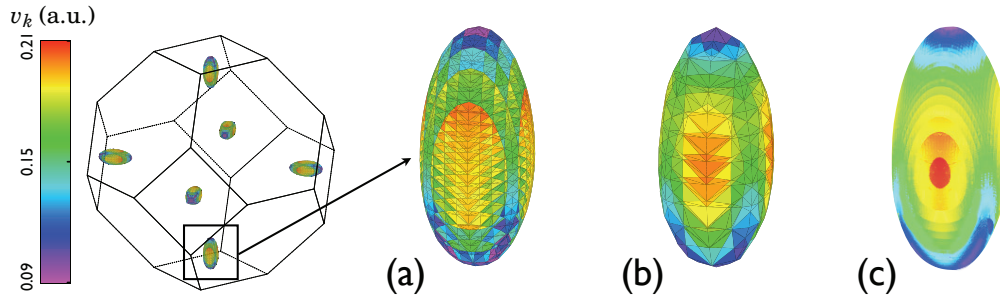


Figure 3.6: FERMI surface of electron-doped bulk silicon determined with different \mathbf{k} -meshes at constant number of about 34000 \mathbf{k} -points. (a) The \mathbf{k} -mesh was not refined and thus, is spread over the whole IBZ. The eigenvalues are determined at the four corners of each tetrahedron. (b) The \mathbf{k} -mesh was not refined, but additional \mathbf{k} -points were added to the tetrahedrons' edges. The eigenvalues are then determined at all ten \mathbf{k} -points of each tetrahedron. (c) After using a sparse mesh of \mathbf{k} -points in the first iteration, all tetrahedra contributing to the FERMI surface were refined according to method (b), thus all 34000 \mathbf{k} -points were used to construct the FERMI surface in a small part of the IBZ. On the left side, the whole BZ of the electron-doped bulk silicon is shown. The FERMI velocity obtained by linear interpolation of the eigenvalues is plotted by a color code onto each FERMI surface.

quadratic interpolation [MMZ87]

$$E_{\mathbf{k}} = E_0 + \mathbf{a}\mathbf{k} + \frac{1}{2}\mathbf{k}M\mathbf{k} \quad \text{with} \quad \frac{1}{2}\frac{\partial^2 E_{\mathbf{k}}}{\partial \mathbf{k}_i \partial \mathbf{k}_j} = M = m_{ij}^{-1}. \quad (3.54)$$

The knowledge of the effective inverse mass tensor m_{ij} can serve as a benchmark to ensure convergence of equation (3.53), as discussed on page 32 and in [E6,E7]. Summarizing, in figure 3.6 the three presented methods are visualized for the example of weakly electron-doped bulk silicon. In all three cases, the exact eigenvalues $E_{\mathbf{k}}$ are determined at approximately 34000 \mathbf{k} -points in the IBZ. The state's FERMI velocity $\mathbf{v}_F(\mathbf{k})$ is plotted onto each surface.

BOLTZMANN TRANSPORT THEORY

Owing knowledge to the microscopic electronic structure of a material, the macroscopic thermoelectric transport properties can be obtained within the BOLTZMANN transport formalism [Zim60, Mer99].

In this chapter, the generalized electronic transport coefficients will be deduced in detail by solving a linearized BOLTZMANN equation (section 4.2). With this, the thermoelectric transport processes will be expressed and discussed by means of generalized forces and fluxes (section 4.3). Solving the BOLTZMANN equation for the BOSE-EINSTEIN distribution function yields insight into the lattice thermal conductivity (section 4.4). To conclude this chapter, a step beyond the relaxation time approximation (RTA) is made, by discussing the microscopic effect of electron-impurity (section 4.5.1) and electron-phonon scattering (section 4.5.2).

4.1 Distribution function

The BOLTZMANN theory is based on a classical distribution function $f(\mathbf{r}, \mathbf{k}, t)$ which gives the number of carriers in a quantum-mechanical state \mathbf{k} . It depends on the position in real space \mathbf{r} , too.

The semiclassical equations of motion of an electron in a solid read [Zim60]

$$\frac{d\mathbf{r}}{dt} = \dot{\mathbf{r}} = \mathbf{v}_v(\mathbf{k}) = \frac{1}{\hbar} \frac{\partial E_v(\mathbf{k})}{\partial \mathbf{k}}, \quad (4.1)$$

$$\frac{d\mathbf{k}}{dt} = \dot{\mathbf{k}} = -\frac{|e|\hbar}{\hbar} \left(\mathcal{E}(\mathbf{r}, t) + \frac{1}{c} \mathbf{v}_v(\mathbf{k}) \times \mathbf{B}(\mathbf{r}, t) \right). \quad (4.2)$$

Here, $E_v(\mathbf{k})$ is the energy eigenvalue for a given band v and wave vector \mathbf{k} . The electron group velocity of this band is hence noted as $\mathbf{v}_v(\mathbf{k})$. The applied external electric and magnetic fields, $\mathcal{E}(\mathbf{r}, t)$ and $\mathbf{B}(\mathbf{r}, t)$, are assumed to be sufficiently weak to ensure the validity of the semiclassical equations (4.1) and (4.2).

One is now interested in more than just a single electron. Without loss of generality, an ensemble of particles can be represented by the distribution function $f_{v\sigma}(\mathbf{r}, \mathbf{k}, t)$, where

$$f_{v\sigma}(\mathbf{r}, \mathbf{k}, t) \frac{d^3 \mathbf{k}}{(2\pi)^3} d^3 \mathbf{r} \quad (4.3)$$

defines the number of electrons with spin σ and band index v confined to the infinitesimal phase space volume $\frac{1}{(2\pi)^3} \frac{d^3 \mathbf{k}}{d^3 \mathbf{r}}$ at time t . To simplify matters, hereinafter the electron spin and the dependence on the band index will be suppressed, giving

$$f_{\mathbf{k}} \equiv f(\mathbf{r}, \mathbf{k}, t) = f_{v\sigma}(\mathbf{r}, \mathbf{k}, t). \quad (4.4)$$

The total number N of particles is given by an integral over the first BRILLOUIN zone (BZ) Ω

$$N = \int_{\Omega} \frac{d^3 \mathbf{k}}{(2\pi)^3} d^3 \mathbf{r} f(\mathbf{r}, \mathbf{k}, t). \quad (4.5)$$

Due to diffusion of charge carriers and the influence of external fields as well as scattering effects, the distribution function changes, giving rise to a net rate of change $\partial f_{\mathbf{k}}/\partial t$. Requiring conservation of the number of particles, it is obvious that the distribution function obeys an extended continuity

equation

$$\left(\frac{\partial f_k}{\partial t}\right) + \nabla \cdot (\mathbf{u} f_k) - \left(\frac{\partial f_k}{\partial t}\right)_{\text{scattering}} = 0, \quad (4.6)$$

where $\nabla = \left(\frac{\partial}{\partial \mathbf{r}}, \frac{\partial}{\partial \mathbf{k}}\right)$ and $\mathbf{u} = (\dot{\mathbf{r}}, \dot{\mathbf{k}})$ are six-dimensional phase space vectors. Because $E(\mathbf{k})$ does depend on \mathbf{k} but not on \mathbf{r} , it is $\nabla \cdot \mathbf{u} = 0$. Thus we can write [Zim60]

$$\begin{aligned} \mathcal{C}_{\mathbf{k}}\{f\} &\equiv \left(\frac{\partial f_k}{\partial t}\right)_{\text{scattering}} = \left(\frac{\partial f_k}{\partial t}\right) + \dot{\mathbf{r}} \cdot \left(\frac{\partial f_k}{\partial \mathbf{r}}\right) + \dot{\mathbf{k}} \cdot \left(\frac{\partial f_k}{\partial \mathbf{k}}\right) \\ &= \left(\frac{\partial f_k}{\partial t}\right) + \left(\frac{\partial f_k}{\partial t}\right)_{\text{diffusion}} + \left(\frac{\partial f_k}{\partial t}\right)_{\text{fields}}, \end{aligned} \quad (4.7)$$

where the terms at the right-hand side account for changes of the distribution function due to an explicit time dependence, due to diffusion, and due to the influence of external fields. All these changes have to be in equilibrium with the changes of the distribution function through scattering [Mer99]. The latter is often referred to as the collision integral $\mathcal{C}_{\mathbf{k}}\{f\}$ and is in general a function of \mathbf{r} , \mathbf{k} , and t , as well as a functional of the distribution function f_k . Equation (4.7) is BOLTZMANN's equation in its general form. Solving for the the distribution function f_k would give complete access to the response of the electronic system in the presence of external force fields and diffusion. However, the generalized BOLTZMANN equation turns out to be a non-linear integro-differential equation of a complicated kind, whereas the non-linearity comes, without further restrictions, from the collision integral $\mathcal{C}_{\mathbf{k}}\{f\}$ [Zim60, Cer88]. In the upcoming section, we will motivate a linearisation of the BOLTZMANN equation and introduce the relaxation time approximation (RTA), which gives an analytical access to the physics described by the BOLTZMANN equation.

4.2 Linearisation and relaxation time approximation

We restrict the following considerations to time-independent external electric and magnetic fields \mathcal{E} and \mathbf{B} , as well as to a temperature gradient ∇T . Applying weak external fields, one can expect that a system in a steady state will only slightly differ from its equilibrium distribution. Reinforcing this, in a conventional free-electron system, an external electrical field of $\mathcal{E} \approx 1 \text{ kV/m}$ leads to an alteration of the FERMI surface in the order of $\delta \mathbf{k} \approx 10^{-6} \mathbf{k}_F$. Here, \mathbf{k}_F is the FERMI wave vector. Hence, it is appropriate that the distribution function f_k in the steady state can be separated into the equilibrium distribution function f_k^0 given by the FERMI-DIRAC distribution at temperature T and a modest perturbation g_k :

$$f_k = f_k^0 + g_k \quad \text{with} \quad f_k^0 = \frac{1}{e^{(E_k - \mu(T))/k_B T} + 1}. \quad (4.8)$$

Applying the perturbation *ansatz* by inserting equation (4.8) in equation (4.7) and by considering equations (4.1) and (4.2), we get after some algebra

$$\mathcal{C}_{\mathbf{k}}\{f\} = \frac{\partial g_k}{\partial t} + \mathbf{v}(\mathbf{k}) \cdot \nabla g_k - \frac{|e|}{\hbar} \left[\mathcal{E} + \frac{1}{c} \mathbf{v}(\mathbf{k}) \times \mathbf{B} \right] \cdot \frac{\partial g_k}{\partial \mathbf{k}} - \mathbf{v}(\mathbf{k}) \left[|e| \mathcal{E} + \nabla \mu + \frac{E_k - \mu}{T} \nabla T \right] \frac{\partial f_k^0}{\partial E}. \quad (4.9)$$

If we further assume both, a weakly chemical potential μ and a homogeneous system $\nabla g_k = 0$, than, to lowest order in g_k , equation (4.9) becomes

$$\mathcal{C}_{\mathbf{k}}\{f\} = \frac{\partial g_k}{\partial t} - \frac{|e|}{\hbar c} [\mathbf{v}(\mathbf{k}) \times \mathbf{B}] \cdot \frac{\partial g_k}{\partial \mathbf{k}} - \mathbf{v}(\mathbf{k}) \left[|e| \mathcal{E} + \frac{E_k - \mu}{T} \nabla T \right] \frac{\partial f_k^0}{\partial E}. \quad (4.10)$$

This time-dependent linearised BOLTZMANN equation describes the steady-state of an electronic ensemble under weak external fields. Without any further restrictions on the collision operator $\mathcal{C}_{\mathbf{k}}$, equation (4.10) is a linear inhomogeneous integral equation for the function $g_{\mathbf{k}}$ [Zim60]. Interestingly, the magnetic field \mathbf{B} is coupled with $\frac{\partial g_{\mathbf{k}}}{\partial \mathbf{k}}$, therefore acting as sort of a scattering term [Zim60]. Indeed, the presence of a magnetic field deflects electrons into complicated real-space trajectories, while preserving their energy [Zim62]. However, for sake of simplicity, we will concentrate to cases without an external magnetic field \mathbf{B} subsequently.

To understand the essence of a steady state $f_{\mathbf{k}}$ in non-equilibrium and the difference from an equilibrium state $f_{\mathbf{k}}^0$, it is useful to consider a simplified *ansatz* to solve for the collision integral $\mathcal{C}_{\mathbf{k}}$ in equation (4.10), before addressing the general theory. We assume that the steady-state distribution function $f_{\mathbf{k}}$ will relax towards the equilibrium distribution $f_{\mathbf{k}}^0$ on a certain time scale τ after switching off the external fields. This relaxation is solely driven by scattering processes. The heart of this approach for the collision integral is the relaxation time approximation (RTA) [Fog63]

$$\mathcal{C}_{\mathbf{k}}\{f\} = -\frac{f_{\mathbf{k}} - f_{\mathbf{k}}^0}{\tau_{\mathbf{k}}} = -\frac{g_{\mathbf{k}}}{\tau_{\mathbf{k}}} \quad \text{and} \quad f_{\mathbf{k}}(t) = f_{\mathbf{k}}^0 + g_{\mathbf{k}} \cdot e^{-\frac{t}{\tau_{\mathbf{k}}}}. \quad (4.11)$$

$\tau_{\mathbf{k}}$ is the relaxation time, which is in principle state-dependent and a tensor of second rank for anisotropic systems. Firstly, $\tau_{\mathbf{k}}$ is considered to be a constant scalar. If one now applies the RTA to the linearised BOLTZMANN equation (4.10), the original integral-differential equation is reduced into an ordinary differential equation with the solution

$$g_{\mathbf{k}} = \tau_{\mathbf{k}} \mathbf{v}(\mathbf{k}) \left[|e| \mathcal{E} + \frac{E_{\mathbf{k}} - \mu}{T} \nabla T \right] \frac{\partial f_{\mathbf{k}}^0}{\partial E}. \quad (4.12)$$

Equation (4.12) yields the perturbation of the equilibrium distribution function $f_{\mathbf{k}}^0$ in the presence of weak external fields and gives, considering equation (4.8), the steady-state distribution function $f_{\mathbf{k}}$, which allows to calculate the transport properties.

Two important facts are apparent from equation (4.12). Firstly, the alteration of the electronic distribution is, as requested, a linear response to the applied electric field \mathcal{E} and the thermal gradient ∇T . Secondly, the factorization with the derivative $\frac{\partial f_{\mathbf{k}}^0}{\partial E}$ of the FERMI-DIRAC distribution indicates that only electrons within an energy shell in the order of $k_B T$ near the FERMI surface can respond to the external forces. Those states have unoccupied states in their vicinity and are redistributed in \mathbf{k} -space.

Beside these similarities, an electric field and a temperature gradient change the equilibrium distribution in very different ways [Zim62, Ask94]. To get insight into the processes, we combine equations (4.8) and (4.12) and apply a TAYLOR expansion in \mathbf{k} , explicitly involving the definition of the group velocity (4.1). In the presence of solely an electric field (equation (4.13)) or a temperature gradient (equation (4.14)), we arrive at

$$f_{\mathbf{k}}(\nabla T = 0) = f_{\mathbf{k}}^0 + \tau_{\mathbf{k}} \left(\frac{|e|}{\hbar} \mathcal{E} \right) \frac{\partial E}{\partial \mathbf{k}} \frac{\partial f_{\mathbf{k}}^0}{\partial E} \approx f^0 \left(\mathbf{k} + \frac{\tau_{\mathbf{k}} |e|}{\hbar} \mathcal{E} \right), \quad (4.13)$$

$$f_{\mathbf{k}}(\mathcal{E} = 0) = f_{\mathbf{k}}^0 + \tau_{\mathbf{k}} \left(\frac{E_{\mathbf{k}} - \mu}{\hbar T} \right) \nabla T \frac{\partial E}{\partial \mathbf{k}} \frac{\partial f_{\mathbf{k}}^0}{\partial E} \approx f^0 \left(\mathbf{k} + \tau_{\mathbf{k}} \left(\frac{E_{\mathbf{k}} - \mu}{\hbar T} \right) \nabla T \right). \quad (4.14)$$

For small electric fields, the stationary distribution function $f_{\mathbf{k}}$ is identical to the equilibrium distribution function $f_{\mathbf{k}}^0$, except for a uniform shift of the FERMI surface in reciprocal space, $f_{\mathbf{k}} \approx f^0(\mathbf{k} + \delta \mathbf{k})$. In figure 4.1(a), the perturbation $g_{\mathbf{k}}$ according to equations (4.8) and (4.13) is shown for a spherical FERMI surface. The shift $\delta \mathbf{k} = \frac{\tau_{\mathbf{k}} |e|}{\hbar} \mathcal{E}$ is not explicitly dependent on the wave vector

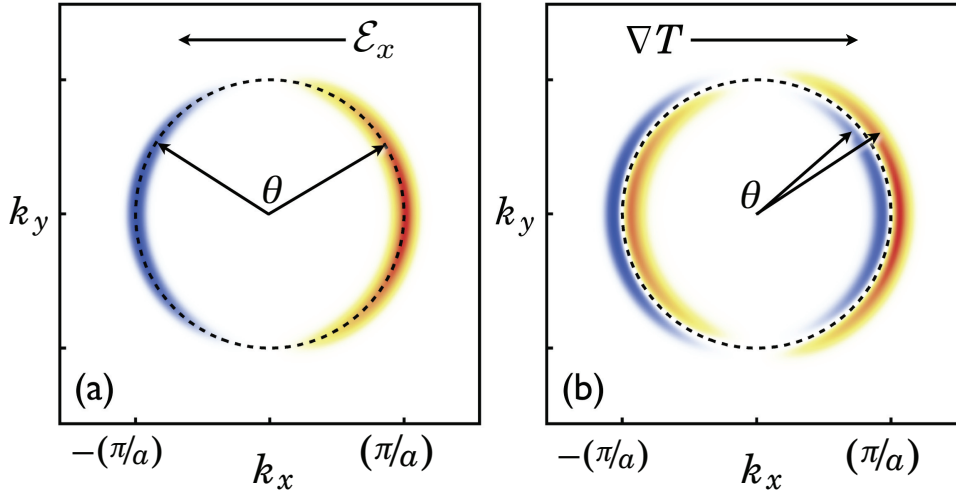


Figure 4.1: Schematic view of the distribution functions $g_{\mathbf{k}}$ on a slice cut through the \mathbf{k} -space ($k_z = 0$) for a spherical Fermi surface. Two situations of electronic transport are considered. In the left panel (a), for an applied electric field along the negative x -direction, in the right panel (b) for a temperature gradient in positive x -direction. The newly populated and depleted BZ areas are marked by red and blue color, respectively. Note the distinction between the large-angle scattering (the so-called horizontal processes) and small-angle scattering connected with a change in the electron's energy (the vertical processes) [Uhe04]. The scattering angle between an initial and a final state is $\theta = \angle(\mathbf{k}, \mathbf{k}')$.

\mathbf{k} ; it scales with the applied electrical field. Hence, the effect of a constant electric field in negative x -direction appears to be like a static shift of the entire distribution function by $\delta\mathbf{k}$ in positive x -direction [Uhe04]. However, one should not speak in terms of a "shifted FERMI surface", but of a redistribution of states enforced by an external electric field. Formerly occupied \mathbf{k} -states nearby the FERMI edge (dashed line) are depleted (blue color), while empty states on the opposite side of the FERMI surface become occupied (red color). After switching off the external electric field, $f_{\mathbf{k}}$ will relax towards $f_{\mathbf{k}}^0$. A priori, it is of minor interest whether $f_{\mathbf{k}}$ relaxes by a single scattering event or by several ones to $f_{\mathbf{k}}^0$. According to ZIMAN's ansatz [Zim60, Zim61, Zah05], large-angle elastic scattering, so called horizontal processes, should be the preferred scattering events, since

$$\frac{1}{\tau} \approx \frac{1}{\tau_C} (1 - \langle \cos\theta \rangle), \quad (4.15)$$

where τ_C is the time between a single scattering event $\mathbf{k} \rightarrow \mathbf{k}'$ and $\langle \cos\theta \rangle$ is the average over the scattering angle $\theta = \angle(\mathbf{k}, \mathbf{k}')$ [Uhe04].

In presence of an external thermal gradient ∇T , the response of the carrier's distribution is different with regard to case of an applied electric field. The perturbation $g_{\mathbf{k}}$ of the equilibrium distribution $f_{\mathbf{k}}^0$ for a degenerate electron gas in the presence of a temperature gradient is schematically drawn in figure 4.1(b). Already from equation (4.14) it is obvious that $g_{\mathbf{k}}$ is a function of wave vector \mathbf{k} . More precisely, for a parabolic dispersion $E_{\mathbf{k}} = \hbar^2 \mathbf{k}_F^2$, we find the change of the equilibrium distribution function $f_{\mathbf{k}}^0$ to

$$\delta\mathbf{k} = \hbar\tau_{\mathbf{k}} (\mathbf{k}^2 - \mathbf{k}_F^2) \nabla T. \quad (4.16)$$

For electrons with $\mathbf{k} > \mathbf{k}_F$ ($\mathbf{k} < \mathbf{k}_F$) the distribution shift is $\delta\mathbf{k} < 0$ ($\delta\mathbf{k} > 0$) if they move along the temperature gradient ∇T and $\delta\mathbf{k} > 0$ ($\delta\mathbf{k} < 0$) if they move against ∇T [Zim60, Ask94]. For electrons resting at the FERMI surface, i.e. $\mathbf{k} = \mathbf{k}_F$, the temperature gradient will not alter their distribution function $f(\mathbf{k}_F) = f^0(\mathbf{k}_F)$. Furthermore, electrons with $\mathbf{k} > \mathbf{k}_F$ moving "down" the thermal gradient, i.e. in the direction of $-\nabla T$, are "hotter" and tend to spread the distribution $f_{\mathbf{k}}$. On the other hand electrons moving "up" the thermal gradient, i.e. in the direction of ∇T , are "colder" and "sharpen"

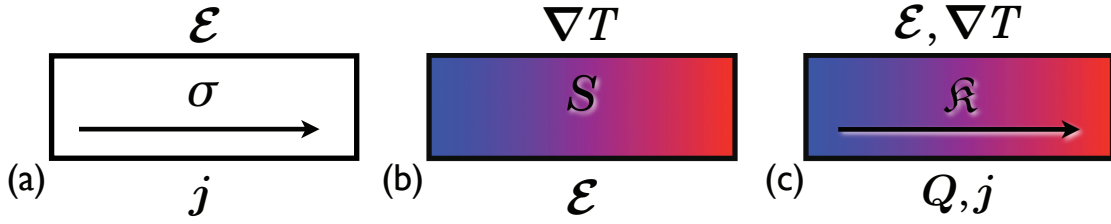


Figure 4.2: Sketch of OHM's law (a), the SEEBECK effect (b), and the THOMSON effect (c). Top and bottom labels show the generalized force and the resulting flux, respectively. In the boxes, the associated direct coupling parameter is shown. Additional arrows symbolize current flows, while colored boxes represent a temperature gradient from hot (red) to cold (blue).

f_k . For electron wave vectors $\mathbf{k} < \mathbf{k}_F$ the opposite holds [Uhe04]. Hence, the asymmetry of g_k with respect to \mathbf{k} , as shown in figure 4.1(b), becomes reasonable.

Comparing figures 4.1(a) and (b), one identifies an alternative electron relaxation mechanism which becomes available for the thermal distribution. While electrons may achieve equilibrium by scattering processes at large angles θ through the FERMI surface in the same way as the electron distribution influenced by an electric field, the thermal gradient allows for small angle scattering, too. As indicated in figure 4.1(b), electrons may relax by collisions from populated states (red color) to depleted states, leaving the wave vector \mathbf{k} almost unchanged, but slightly changing their energy. Following the large angle, horizontal process, this is the so called vertical process, which provides a very effective means to relax a thermally driven electron distribution incorporating thermal conductivity at low temperatures [Zim60, Uhe04]. By definition, vertical scattering processes are inelastic and become less probable at higher temperatures. One reason for this is that at elevated temperatures the maximal energy an electron can absorb or emit is also restricted by the phonon bandwidth of the system, which is usually well below $k_B T$ at room temperature for good thermoelectrics. Associated with the phonon spectrum is the electron-phonon coupling of the thermal driven system, discussed in section 4.5.2. Despite the different probabilities of relaxation mechanisms at different temperatures, one should note that relaxation times in thermally driven systems will be considerably shorter compared to cold systems, since electrons have in the vertical process an additional scattering mechanisms by which they can relax.

Summarizing, even though showing differences in the relaxation mechanisms, in both cases a gradient of a generalized force \mathcal{E} or ∇T causes a violation of the symmetric electron distribution f_k^0 in \mathbf{k} -space and thereby induces a finite current in linear response to the gradients.

4.3 Transport coefficients

While it has been discussed in the last section how a weak electric field and a thermal gradient alter the population of electronic states, one may conclude what currents drive the system to a steady state [Pri56b, Uhe04]. To do so, it is customary to introduce current densities [Zim60]. Considering a flow of particles, a volume element $d^3\mathbf{k}$ around point \mathbf{k} in reciprocal space will contribute a flux of particles of magnitude $\frac{1}{8\pi^3}\mathbf{v}(\mathbf{k})d\mathbf{k}$, where $\mathbf{v}(\mathbf{k})$ is the carrier group velocity [Uhe04]. Since we consider electrons, there are two spin states for each \mathbf{k} -state. Summing over all available states and assigning a charge $-|e|$ to each electron, we obtain the current densities:

$$\mathbf{j} = -\frac{|e|}{2\pi^3} \int \mathbf{v}(\mathbf{k}) f_k d^3\mathbf{k}, \quad (4.17)$$

$$\mathbf{Q} = \frac{1}{2\pi^3} \int \mathbf{v}(\mathbf{k}) (E_k - \mu) f_k d^3\mathbf{k}. \quad (4.18)$$

Considering that $f_k = f_k^0 + g_k$ and that there is no spontaneous net current flow in equilibrium, only g_k of the perturbed distribution function f_k causes a current flow. Substituting equation (4.12) into equations (4.17) and (4.18) yields

$$\mathbf{j} = -\frac{|e|}{2\pi^3} \int \tau_k \mathbf{v}(\mathbf{k}) \circ \mathbf{v}(\mathbf{k}) \cdot \left(|e| \mathcal{E} + \frac{E_k - \mu}{T} \nabla T \right) \frac{\partial f_k^0}{\partial E} d^3 \mathbf{k}, \quad (4.19)$$

$$\mathbf{Q} = \frac{1}{2\pi^3} \int \tau_k \mathbf{v}(\mathbf{k}) \circ \mathbf{v}(\mathbf{k}) \cdot \left(|e| \mathcal{E} + \frac{E_k - \mu}{T} \nabla T \right) \frac{\partial f_k^0}{\partial E} d^3 \mathbf{k}. \quad (4.20)$$

Without loss of generality, the integral expression

$$\mathcal{L}_{\perp, \parallel}^{(n)}(\mu, T) = \frac{1}{(2\pi)^3} \int \tau_k (\mathbf{v}(\mathbf{k})_{(\parallel, \perp)})^2 (E_k - \mu)^n \left(-\frac{\partial f_k^0(\mu, T)}{\partial E} \right)_{E=E_k} d^3 \mathbf{k} \quad (4.21)$$

introduces the generalized conductance moments $\mathcal{L}_{\perp, \parallel}^{(n)}(\mu, T)$, where n is the moments order. Here, $\mathbf{v}(\mathbf{k})_{(\parallel, \perp)}$ denote the group velocities within and perpendicular to the basal plane. For convenience, the integrals over a volume in \mathbf{k} -space can be transformed into integrals over surfaces of constant energy by letting $d^3 \mathbf{k} = d^2 \mathbf{k} d\mathbf{k}_{\perp} = dS d\mathbf{k}_{\perp} = dS dE / (\hbar |\mathbf{v}(\mathbf{k})|)$. Hence, equation (4.21) becomes

$$\mathcal{L}_{(\parallel, \perp)}^{(n)}(\mu, T) = \int \Sigma_{(\parallel, \perp)}(E) \cdot (E - \mu)^n \left(-\frac{\partial f_k^0(\mu, T)}{\partial E} \right) dE, \quad (4.22)$$

involving integrations over surfaces of constant electron energy E in reciprocal space:

$$\Sigma_{(\parallel, \perp)}(E) = \frac{1}{\hbar (2\pi)^3} \oint_{E_k=E} \frac{dS}{|\mathbf{v}(\mathbf{k})|} \tau_k (\mathbf{v}(\mathbf{k})_{(\parallel, \perp)})^2, \quad (4.23)$$

which is the zeroth moment at vanishing temperature $\Sigma_{(\parallel, \perp)}(E) \equiv \mathcal{L}_{(\parallel, \perp)}^{(0)}(E, 0)$ and coincides with the TDF as introduced to thermoelectrics by MAHAN & SOFO [MS96].

The determination of the isoenergetic surface integrals (4.23) requires a thorough integration in \mathbf{k} -space. Especially the anisotropy ratio $\Sigma_{\parallel}/\Sigma_{\perp}$ shows up to be very sensitive if the considered system and the accompanied FERMI surfaces are strongly anisotropic. Different methods to determine the group velocities (cf. section 3.4) can improve the convergence of the surface integral (4.23) [E6]. Additionally, for energies very close to band edges (cf. red crosses in figure 4.3(b)), the concept of effective masses can serve as a benchmark to ensure convergence of the numerical integration schemes [E6, E7].

In figure 4.3(a) the electronic band structure E_k^v for bulk Bi_2Te_3 in the rhombohedral unit cell is shown. Alongside, the anisotropic FERMI surfaces and the related FERMI velocities of each occupied state at two distinct electron- and hole charge carrier concentrations are given. The distribution of occupied states and the related absolute value of the state's velocity $\mathbf{v}(\mathbf{k})$ show quite a spread and do not agree well to those of commonly used free-electron models. As deduced from equation (4.23), surface integrals over all occupied states and their related velocities lead directly to the anisotropic TDF shown in figure 4.3(b). The complex functional behaviour of the TDF ratio $\Sigma_{\parallel}/\Sigma_{\perp}$ can be directly linked to specific topological features of the electronic structure. As an example, the local maxima of $\Sigma_{\parallel}/\Sigma_{\perp}$ at about $E - E_{\text{VBM}} = 0.05 \text{ eV}$ and 0.17 eV originate from saddle points of the dispersion E_k^v (details discussed in [E7]).

Generally the current densities need not to be parallel to the electric field or the thermal gradient. Thus the generalized conductance moments $\mathcal{L}^{(n)}$ and the subsequently related transport coefficients are tensors and we drop the indices (\parallel, \perp) . Using the above definitions and equations (4.19)-(4.22),

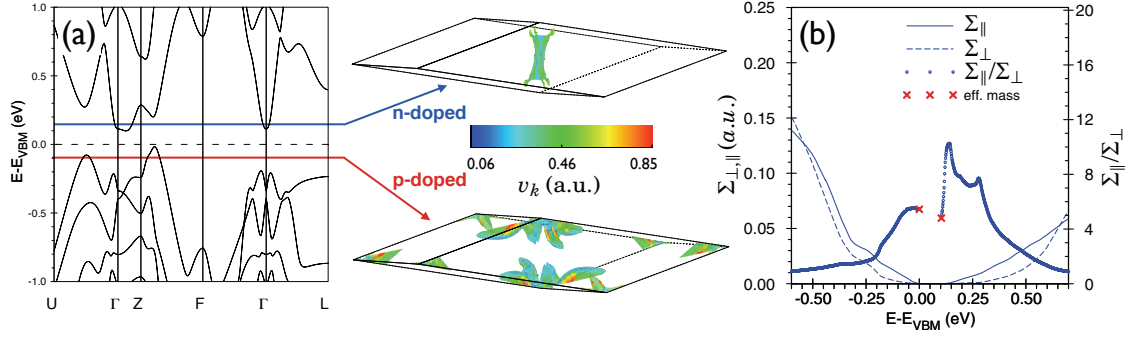


Figure 4.3: (a) Band structure of bulk Bi_2Te_3 on the rhombohedral high-symmetry lines and related Fermi surfaces for electron- (n) and hole-doping (p), respectively. The charge carrier concentrations correspond to $N = 2 \times 10^{19} \text{ cm}^{-3}$ and $N = 1.5 \times 10^{20} \text{ cm}^{-3}$ under n - and p -doping at room temperature, respectively. The color code on the Fermi surfaces shows the state-dependent Fermi velocity in atomic units. In (b) the anisotropic transport distribution function (TDF) for Bi_2Te_3 is shown [E7].

the electric current density (4.19) and heat current density (4.20) can be rewritten in terms of the generalized conductance moments,

$$\mathbf{j} = e^2 \mathcal{L}^{(0)} \boldsymbol{\mathcal{E}} - \frac{e}{T} \mathcal{L}^{(1)} \nabla T, \quad (4.24)$$

$$\mathbf{Q} = e \mathcal{L}^{(1)} \boldsymbol{\mathcal{E}} - \frac{1}{T} \mathcal{L}^{(2)} \nabla T. \quad (4.25)$$

Assuming linear response of the considered ensemble to the influence of any external fields, one finds that the densities of the electrical current \mathbf{j} and the thermal current \mathbf{Q} are always linear functions of the electric field and the temperature gradient along the sample. Per se, the generalized transport coefficients \mathcal{L} are symmetric tensors of second rank, which reduce to scalars in case of cubic systems [Ons31a, Ons31b]. The generalized transport coefficients are, however, no observables. Instead they are combinations of measurable transport properties, as will be discussed in the following [Zim60, Mer99, GSZ⁺11].

4.3.1 Decoupled processes

At a constant temperature, an electrical current \mathbf{j} flows through the material in response to an applied external electrical field $\boldsymbol{\mathcal{E}}$, as sketched in figure 4.2(a). Assuming this, equation (4.24) becomes

$$\mathbf{j} = e^2 \mathcal{L}^{(0)} \boldsymbol{\mathcal{E}}. \quad (4.26)$$

From comparison with OHM's, law one reads

$$\mathbf{j} = \boldsymbol{\sigma} \boldsymbol{\mathcal{E}} \quad \text{with} \quad \boldsymbol{\sigma} = e^2 \mathcal{L}^{(0)}, \quad (4.27)$$

where $\boldsymbol{\sigma}$ is the electrical conductivity tensor. Here, $\sigma_{xx,zz} = \sigma_{\parallel,\perp}$ are the in-plane (CIP) or cross-plane (CPP) component, respectively. The associated electrical resistivity $\boldsymbol{\rho}$ is given by inversion $\boldsymbol{\sigma} = (\boldsymbol{\rho})^{-1}$.

Consider an insulating material in an open circuit. Electrical current flow is not allowed. Focussing on the thermal current flow, equation (4.24) then reads

$$\mathbf{Q} = \frac{1}{T} \left(\frac{(\mathcal{L}^{(1)})^2}{\mathcal{L}^{(0)}} - \mathcal{L}^{(2)} \right) \nabla T. \quad (4.28)$$

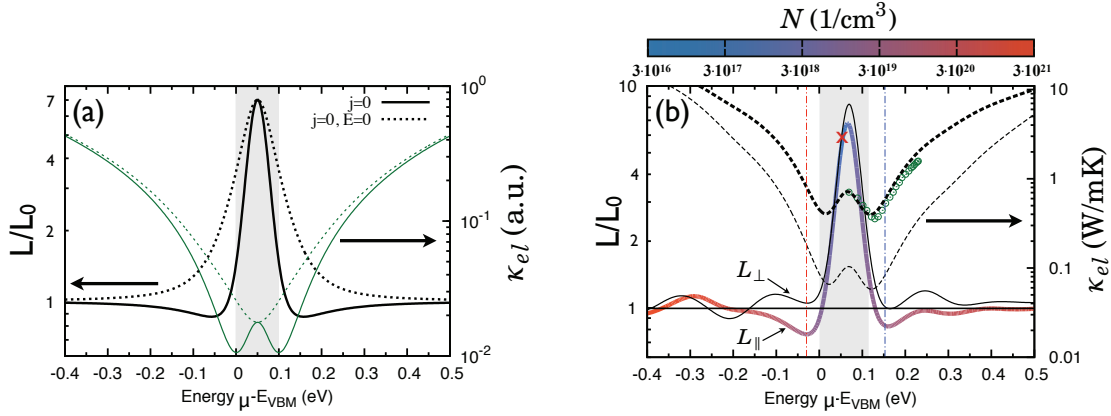


Figure 4.4: Electronic thermal conductivity and LORENZ function for (a) a two band model and (b) for bulk Bi_2Te_3 . (a) LORENZ function L (thick black lines, ref. to left scale) and electronic contribution κ_{el} to the total thermal conductivity (thin green lines, ref. to the right scale) in dependence on position of the chemical potential μ within a spherical two band model. The effective masses of the conduction and the valence band are identical. Dashed lines show results for L in the case of zero electric field in the material ($S = 0$ in equation (4.33)), while solid lines account for the full solution of equation (4.33) and thus include corrections due to bipolar conduction. (b) LORENZ function L presented as in (a) for bulk Bi_2Te_3 for the in-plane (thick lines) and cross-plane (thin lines) transport direction. Superimposed onto the LORENZ function in the in-plane direction is a color code referring to the charge carrier concentration. The red cross emphasizes the change from n to p doping. Thin vertical dash-dotted lines emphasize the position of the chemical potential for a charge carrier concentration of $N = 3 \times 10^{19} \text{ cm}^{-3}$ under n and p doping (blue and red line, respectively). The CBM is located at 0.105 eV . Green open circles show experimental values from Ref. [Gol65] for $\kappa_{el,||}$ for an n -type Bi_2Te_3 single crystal. In (a) and (b) the temperature is fixed to 300 K and the LORENZ function is related to the metallic limit $L_0 = 2.44 \times 10^{-8} \text{ W}\Omega/\text{K}^2$.

Checking against FOURIER's law, we state

$$\mathbf{Q} = -\kappa_{el} \nabla T \quad \text{with} \quad \kappa_{el} = \frac{1}{T} \left(\mathcal{L}^{(2)} - \frac{(\mathcal{L}^{(1)})^2}{\mathcal{L}^{(0)}} \right). \quad (4.29)$$

Here, κ_{el} is the electronic part of the thermal conductivity. The second term in expression (4.29) accounts for a reduction of the thermal conductivity due to an electric field which counteracts the heat flow (cf. figure 4.4). This effect is of high importance in semiconductors with a small band gap [FK54, Gol56, Pri56a, Gol65, UG74] and is discussed in [E1, E2, E5]. Under restriction to a closed circuit at vanishing electric field, it is

$$\mathbf{Q} = -\kappa_{el}^{(0)} \nabla T \quad \text{with} \quad \kappa_{el}^{(0)} = \frac{1}{T} \mathcal{L}^{(2)}. \quad (4.30)$$

Note, assuming a FERMI-DIRAC distribution for the deduction of the transport coefficients, that the lattice part of the thermal conductivity κ_{ph} is neglected up to now. While being of minor importance in metals, its influence in semiconductors is substantial. Hence, the lattice part of the thermal conductivity will be derived and discussed in section 4.4.

4.3.2 Coupled processes

We focus now on processes of thermoelectric coupling, i.e. where electrical and thermal currents coexist under certain external conditions. Assuming an electrical open circuit $\mathbf{j} = 0$ and applying a steady thermal gradient along the sample, as in equation (4.29), but measuring the electric field caused by the thermal gradient, we get

$$\mathcal{E} = \frac{1}{eT} \frac{\mathcal{L}^{(1)}}{\mathcal{L}^{(0)}} \nabla T \quad \text{and} \quad S = \frac{1}{eT} \frac{\mathcal{L}^{(1)}}{\mathcal{L}^{(0)}}. \quad (4.31)$$

The proportionality S of an electric field induced by a thermal gradient was first introduced by SEEBECK in 1821 [See26] and is termed thermopower. Combining the thermopower (4.31) with the electrical conductivity (4.27), for the thermoelectric power factor reads

$$\text{PF} = \sigma S^2 = \frac{1}{T^2} \frac{(\mathcal{L}^{(1)})^2}{\mathcal{L}^{(0)}}, \quad (4.32)$$

which states the electrical power throughput of a material at a given temperature difference. As shown in the second chapter (cf. page 6), the power factor strongly depends on the charge carrier concentration of the thermoelectric material and should be optimized to maximize the figure of merit ZT .

By taking the ratio of electrical conductivity (4.27) and electronic thermal conductivity (4.29), the Lorenz function L is given by

$$L = \frac{\kappa_{el}}{\sigma T} = \frac{\kappa_{el}^{(0)}}{\sigma T} - S^2, \quad (4.33)$$

which becomes the LORENZ number $L_0 = \frac{(\pi k_b)^2}{3e^2}$ in the highly degenerate, metallic limit $S \rightarrow 0$. Nevertheless, slight deviations $L \neq L_0$ are already apparent in this regime for simple metals and semimetals [KPP93]. In semiconductors, the deviations of L from the metallic limit L_0 can be larger than one order of magnitude. Goldsmid [Gol56] and Price [Pri56a] pointed out that the LORENZ function in small gap semiconductors increases to large values $L \gtrsim 10L_0$ in the intrinsic doping regime, when bipolar conduction is dominant and can be reduced to $L \lesssim 0.5L_0$ at almost unipolar conduction and reliable small doping (cf figure 4.4). Indeed, equation (4.33) clearly shows that in the low temperature regime L consists of a constant term and a negative term of order T^2 . To illustrate this behaviour the LORENZ function is shown in figure 4.4 for (a) a parabolic two-band model and (b) for bulk Bi_2Te_3 [E1,E2].

Detailed knowledge of the LORENZ function is particularly important for thermoelectric measurements. Nowadays, the total thermal conductivity κ is determined by the 3ω method [CP87,BTKC01]. Applying the WIEDEMANN-FRANZ law (4.33) provides then a measure to separate the electronic and lattice contributions to the thermal conductivity by $\kappa = \kappa_{ph} + L\sigma T$ [UG74]. Assuming incorrect values for the LORENZ number leads to incorrect values for κ_{el} and κ_{ph} and can even sum up to non-physically negative values for κ_{ph} [SVG01]. In superlattices, additional complex effects, as pronounced oscillations of the Lorenz function in dependence on charge carrier concentration and superlattice period [BZS⁺07,E1] can be present.

If one, as done in equation (4.26), imposes isothermal conditions $\nabla T = 0$ and relates the heat current to a electric current, one gets from equations (4.25) and (4.27)

$$\mathbf{Q} = \Pi \mathbf{j} \quad \text{with} \quad \Pi = \frac{1}{e} \frac{\mathcal{L}^{(1)}}{\mathcal{L}^{(0)}} = ST, \quad (4.34)$$

where Π is the PELTIER coefficient that relates the heat transport in a material to the electric current passing through the material. The second identity in equation (4.34) takes advantage of the second KELVIN relation, equation (4.39). Obviously, the PELTIER effect is linear in the currents and allows for thermoelectric cooling and heating [Uhe04,Bel08].

Finally, I am going to summarize the sources of a general heat flux in presence of an electric field, a thermal gradient, and an electric current \mathbf{j} . Combining equations (4.24) and (4.25), suppressing the directional indices, and eliminating the electric field, the heat flux is rewritten as

$$\mathbf{Q} = \Pi \mathbf{j} - \kappa_{el} \nabla T. \quad (4.35)$$

Applying equations (4.27) and (4.34), the divergence of the heat flux becomes [GSZ⁺11]

$$\begin{aligned}\nabla \cdot \mathbf{Q} &= \nabla \cdot (ST\mathbf{j} - \kappa_{el}\nabla T) \\ &= T\nabla S \cdot \mathbf{j} + \underbrace{\mathbf{j} \cdot S\nabla T}_{\mathbf{j} \cdot \mathcal{E} - \rho j^2} + \nabla \cdot (-\kappa_{el}\nabla T).\end{aligned}\quad (4.36)$$

In equation (4.36) $\nabla \cdot \mathbf{j} = 0$ due to conservation of particles. The second term is due to electrical energy production and dissipation, the latter referred to as JOULE heating. The third term is linked to a change in thermal conduction due to heat production or absorption. The first term is the PELTIER-THOMSON contribution and is of particular interest. Presuming the identity $\Pi = ST$ (see equations (4.34) and (4.39)), one can write [GSZ⁺11]

$$T\nabla S \cdot \mathbf{j} = T\mathbf{j} \cdot \nabla \left(\frac{\Pi}{T} \right) = T\mathbf{j} \cdot \left(\frac{1}{T}\nabla \Pi - \frac{\Pi}{T^2}\nabla T \right) = \mathbf{j} \cdot (\nabla(ST) - S\nabla T). \quad (4.37)$$

Thereby, the classical separation of the PELTIER and THOMSON contribution is artificial, as both effects ground on the gradient of the thermopower [GSZ⁺11]. This can be either the temperature driven gradient $S\nabla T$, or the spatially driven gradient $(\nabla S)T$. At isothermal conditions, equation (4.37) yields the pure PELTIER effect as $\mathbf{j} \cdot \nabla(ST)$. For a homogenous material under a temperature gradient, as sketched in figure 4.2(c),

$$\mathbf{j} \cdot (\nabla \Pi - S\nabla T) = \mathbf{j} \cdot \left(\frac{d\Pi}{dT} - S \right) \nabla T = \mathfrak{K}\mathbf{j}\nabla T \quad (4.38)$$

holds. Here, \mathfrak{K} is introduced as THOMSON coefficient of a material, connected with a THOMSON heat per volume $\mathfrak{K}\mathbf{j}\nabla T$ [STKS12]. The THOMSON coefficient is a measure for the heat absorbed or emitted when the current \mathbf{j} flows in the one or other direction of a temperature gradient.

The THOMSON coefficient \mathfrak{K} is unique among the three main thermoelectric coefficients because it is the only one directly observable for an individual material. The PELTIER coefficient Π and the thermopower S can only be measured for pairs of materials. In 1854, WILLIAM THOMSON (later LORD KELVIN) found important relationships between the three coefficients S, Π and \mathfrak{K} . They are now known as KELVIN or THOMSON relations and imply that only one of them could be considered unique:

$$\mathfrak{K} = \frac{d\Pi}{dT} - S = T \frac{dS}{dT} = \frac{dS}{d \ln T} \quad \text{and} \quad \Pi = ST. \quad (4.39)$$

While THOMSON himself missed a mathematical proof of these relations, it was LARS ONSAGER who first succeeded in giving a convincing theoretical justification of the THOMSON relations by his famous reciprocal relations [Ons31a, Ons31b]. Simultaneously, the experimental support of the interconnectivity of S, Π and \mathfrak{K} was fairly advanced [Mil60].

In metals, the THOMSON coefficient compares to the magnitude of the thermopower and is rather small with values below a few $\mu\text{V/K}$. Hence, the related heat is only of minor relevance. In non-degenerate semiconductors, the thermopower S can take rather large values of above several hundreds $\mu\text{V/K}$. Additionally, the dependence of S on the temperature is strongly non-monotonic, which favours enhanced values of the derivative $\frac{dS}{dT}$. To give some insight on this feature, in figure 4.5 the temperature-dependent anisotropic thermopower and the related THOMSON coefficient are shown for bulk Bi_2Te_3 for an electron and hole doping of $N = 1 \times 10^{19} \text{ cm}^{-3}$, respectively. Here, at operating temperatures between $T = 350 - 400 \text{ K}$ an average THOMSON coefficient of about $490 \mu\text{V/K}$, can be stated under electron doping in the cross-plane transport direction. This number is far below the optimal value of $\mathfrak{K} = 1500 \mu\text{V/K}$, which was suggested for optimally graded materials based on $\text{Bi}_x(\text{SbTe})_{(1-x)}$ [SST⁺12]. This magnitude of the THOMSON coefficient could be even more en-

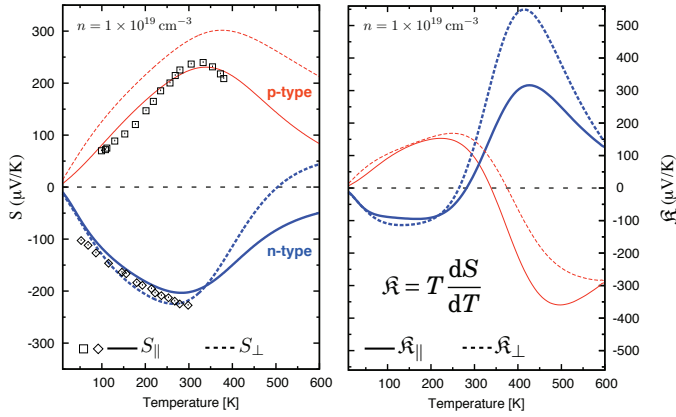


Figure 4.5: (a) Anisotropic thermopower for bulk Bi_2Te_3 . Electron doping refers to the blue (thick) lines, while red (thin) lines refer to hole doping. Solid lines show the in-plane part S_{\parallel} of the thermopower, while dashed lines show the cross-plane part S_{\perp} . The extrinsic charge carrier concentration was fixed to $N = 1 \times 10^{19} \text{ cm}^{-3}$. Experimental data (squares, diamonds) from Ref. [SK75, Kai89] are given for comparison. (b) THOMSON coefficient for Bi_2Te_3 in the same presentation as done for (a).

hanced for wide band gap semiconductors ($E_g > 1\text{eV}$) at very low charge carrier concentrations of $N \leq 1 \times 10^{14} \text{ cm}^{-3}$ (compare e.g. figure 2 in [E8] for bulk silicon). At the same time, bipolar conduction is suppressed and electrical conductivity is small. Consequently, the absorbed or generated heat $\mathcal{R}\mathbf{j}\nabla T$ is tiny and the THOMSON effect is ineligious for cooling applications [STKS12].

Nevertheless, beside the need of sophisticated techniques to measure \mathcal{R} , a large THOMSON coefficient in a broad temperature range could lead to a new kind of thermoelectric coolers based on the THOMSON effect. These would enable solid-state cooling to cryogenic temperatures [STKS12, SST⁺12].

To close this section on the electronic thermoelectric BOLTZMANN transport, I summarize the responses of a system on the generalized forces \mathcal{E} and ∇T by expressing the generalized fluxes (4.24) and (4.25) entirely in terms of physical observables. Therefore, I introduce the general conductivity matrix Ξ [CG52, GC52, GSZ⁺11] as

$$\begin{pmatrix} \mathbf{j} \\ \mathbf{Q} \end{pmatrix} = \underbrace{\begin{pmatrix} \sigma & S\sigma \\ S\sigma T & \kappa^0 \end{pmatrix}}_{\Xi} \cdot \begin{pmatrix} \mathcal{E} \\ -\nabla T \end{pmatrix}. \quad (4.40)$$

Obviously, the thermopower S acts as thermoelectric coupling between the electronic and thermal fields and currents. Hence, for metals and heavily doped semiconductors ($N > 1 \times 10^{21} \text{ cm}^{-3}$), the interaction of charge and heat transport is less pronounced. For vanishing thermopower $S \rightarrow 0$, electronic and thermal transport decouple and the general conductivity matrix Ξ reflects OHM's (4.27) and FOURIER's law (4.30), respectively.

4.4 Lattice thermal conductivity

As mentioned in section 4.1, BOLTZMANN's transport theory can also be applied to phonons by simply taking into account the boson equilibrium distribution function

$$n_q^0 = \frac{1}{e^{\hbar\omega_q/k_B T} - 1}, \quad (4.41)$$

where ω_q is the phonon energy dispersion. Comparable to the path described in section 4.1 and 4.2, one can derive the linearized phonon BOLTZMANN equation in RTA [Cal59, Zim60, GK66, SJ89]. Equivalent to equations (4.6) and (4.7), but with $\mathbf{u} = (\dot{\mathbf{r}}, \dot{\mathbf{q}})$, one has

$$\left(\frac{\partial n_q}{\partial t} \right) + \nabla \cdot (\mathbf{u} n_q) - \left(\frac{\partial n_q}{\partial t} \right)_{\text{scattering}} = 0. \quad (4.42)$$

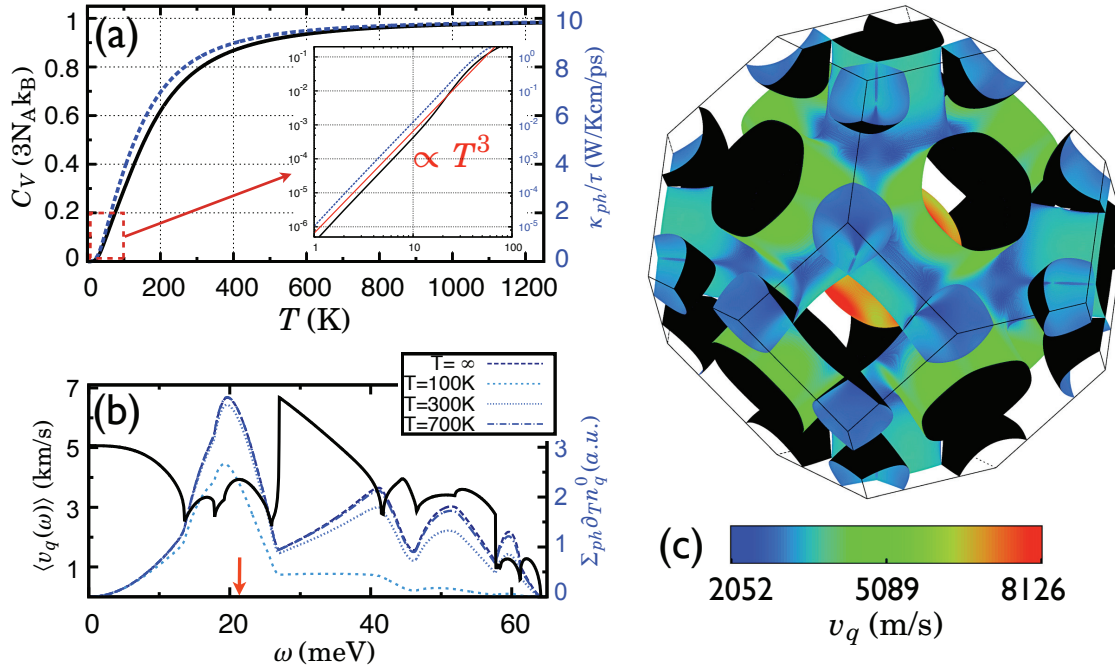


Figure 4.6: Phonon thermal conductivity, specific heat, and group velocities for bulk silicon. (a) Thermal lattice conductivity in RTA calculated by equation (4.48) (blue dashed line, ref. to right scale) and specific heat capacity calculated by equation (4.50) (black solid line, ref. to left scale) in dependence on temperature. As an inset, the T^3 temperature dependence (red thin line) is emphasized. (b) Energy dependence of the average group-velocity (black solid line, ref. to left scale) and the kernel of equation (4.48) at different temperatures (blue lines, ref. to right scale). The latter demonstrates the increasing and saturating contribution of different phonon modes at rising temperatures. (c) Iso-energy phonon surface for an energy of about 21 meV (energy position marked by a red arrow in (b) and figure 3.3). The state's group velocity is depicted onto the phonon iso-energy surface.

Neglecting piezoelectric effects, there is no influence of electric or magnetic fields on the lattice dynamics. As a result, the steady state distribution function n_q and the equilibrium function n_q^0 will only differ by a term g_q which is small in response to the applied thermal gradient ∇T . Revisiting the RTA (4.11) yields

$$\mathcal{L}_q \{n\} \equiv \left(\frac{\partial n_q}{\partial t} \right)_{\text{scattering}} = -\frac{n_q - n_q^0}{\tau_q} = -\frac{g_q}{\tau_q}, \quad (4.43)$$

where τ_q is the condensed relaxation time for all processes, regardless of momentum conservation [Cal59]. From equations (4.42) and (4.43) one then finds

$$g_q = -\tau_q \mathbf{v}(\mathbf{q}) \nabla T \left(\frac{\partial n_q^0}{\partial T} \right), \quad (4.44)$$

which is very similar to the perturbation g_k of an electronic ensemble by a thermal gradient, as derived in equations (4.12) and (4.14). In equation (4.44), $\mathbf{v}(\mathbf{q}) \equiv \mathbf{v}_q = \text{grad}_q \omega_q$ is the phonon group velocity (PGV). The latter is depicted in figures 4.6(b) and (c). In figure 4.6(b) the state-averaged, frequency dependent PGV $\langle \mathbf{v}_q(\omega) \rangle$ is shown. As expected acoustic phonon modes dominate for low frequencies and the PGV is constant (cf. figure 3.3). However, the distribution of the PGV remains complicated with respect to energy and the distribution of the states' PGV in the BZ. As can be seen in figure 4.6(c), the acoustic modes show large absolute values for the PGV near the BZ center, even in energy regions where multiple phonon branches are present.

The heat flux due to a phonon mode \mathbf{q} is the product of the average phonon energy and the PGV. Therefore, the total heat flux carried by all occupied phonon modes at temperature T can be written

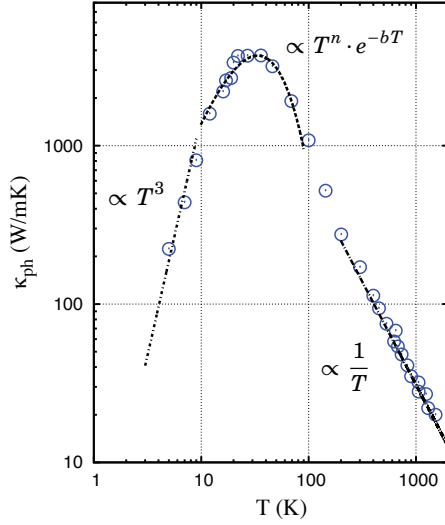


Figure 4.7: Experimental temperature-dependent thermal conductivity of bulk silicon. The black lines represent the temperature dependence of different scattering mechanisms. At low temperature (dotted line), boundary scattering dominates, thus, giving the intrinsic temperature dependence $\kappa \propto T^3$. At intermediate temperature (dashed line), phonons can contribute to the U-scattering, while N-scattering is still dominant, giving $\kappa \propto T^n \cdot e^{-bT}$. At high temperatures (dash-dotted line), U-scattering dominates, yielding a $\kappa \propto T^{-1}$ dependency. Blue open circles are experimental results taken from [GS64]. See text for further explanations.

as

$$\mathbf{Q} = \sum_q n_q \hbar \omega_q \mathbf{v}_q. \quad (4.45)$$

For brevity, the notations for the transport directions (\perp, \parallel) are omitted, but can be included as done for the electronic transport following equation (4.21). Plugging equation (4.44) into equation (4.45) and transforming the sum into an integral, it is

$$\mathbf{Q} = -\frac{1}{8\pi^3} \int \tau_q \hbar \omega_q \mathbf{v}_q^2 \left(\frac{\partial n_q^0}{\partial T} \right) d^3 \mathbf{q} \nabla T. \quad (4.46)$$

From comparison with FOURIER's law (4.29), the lattice part of the thermal conductivity reads

$$\kappa_{ph}(T) = \frac{1}{8\pi^3} \int \tau_q \hbar \omega_q \mathbf{v}_q^2 \left(\frac{\partial n_q^0}{\partial T} \right) d^3 \mathbf{q}. \quad (4.47)$$

Using $\left(\frac{\partial n_q^0}{\partial T} \right) = -\left(\frac{\omega}{T} \frac{\partial n_q^0}{\partial \omega} \right)$ and the explicit expression for the PGV, one can express equation (4.47) as

$$\kappa_{ph}(T) = \int \Sigma_{ph}(\omega) C_V(\omega, T) d\omega, \quad (4.48)$$

involving integrations over surfaces of constant phonon frequency ω ,

$$\Sigma_{ph}(\omega) = \frac{1}{8\pi^3} \oint_{\omega_q=\omega} \frac{dS}{|\mathbf{v}_q|} \tau_q \mathbf{v}_q^2. \quad (4.49)$$

These are analogous to the electronic case in equation (4.23) and include the PHDOS $\mathcal{F}(\omega)$ (cf. equation (3.53)). Furthermore, I define the specific thermal heat at constant volume and temperature T as

$$C_V(\omega, T) = \frac{(\hbar \omega_q)^2}{k_B T^2} n_q^0 (n_q^0 + 1). \quad (4.50)$$

The latter is shown together with the normalized lattice thermal conductivity κ_{ph} , ref. to equation (4.47) and $\tau_q = 1$, in figure 4.6(a). As highlighted in the inset, for both the analytical low-temperature T^3 dependency is reproduced. The specific thermal heat applies furthermore for the expected high-temperature classical limit of $C_V = 3N_A k_B$. However, even by taking into account the full phonon

bandstructure, the experimental temperature dependency of κ_{ph} , as shown for bulk silicon in figure 4.7, cannot be reproduced within the RTA. Obviously, phonon scattering processes are important; they determine the lattice thermal conductivity by temperature- and state dependent expressions for the phonon relaxation time τ_q [WB10, WBSD09, SLT⁺10, STMA10]. Proposed by PEIERLS [Pei29], two kinds of phonon scattering events are important in pure crystals: the momentum-conserving *normal* (often N-) processes and the momentum-dissipating *umklapp* (often U-) processes. Only the latter will contribute to a decrease of the lattice thermal conductivity $\kappa_{ph} \propto \frac{1}{T}$ at high temperatures. In small samples or impure materials, phonon scattering at impurities, grain boundaries or interfaces/surfaces can be of importance, too [Cal59]. Excellent reviews on the origins and variations of the lattice thermal conductivity are given in the books of ZIMAN [Zim60] and TRITT [NG04].

4.5 Beyond relaxation time approximation

As was pointed out at the end of the last paragraph, microscopic scattering effects can affect the macroscopic transport properties considerably. This holds for phonons, as well as for electrons. Introduced by MATTHIESSEN & VOGT [MV64] contributions to the relaxation time τ are manifold and originate from scattering processes with different physical sources. The total relaxation time is then represented by a sum $\frac{1}{\tau} = \sum_i \frac{1}{\tau_i}$ of the single scattering processes τ_i . Two of these, i.e. electron-impurity scattering and electron-phonon scattering, will be introduced hereinafter to emphasize possible influences on the thermoelectric transport.

4.5.1 Electron-impurity scattering

As shown in section 3.2.1 the KKR method provides a very effective way to treat perturbations of crystals. Assuming that full information on the physical system by knowing the GREEN's function (GF) of the unperturbed crystal (cf. equation (3.32)) has been obtained, I introduce a local potential change at position n ,

$$\Delta\mathcal{V}(\mathbf{r}) = \sum_n \mathcal{V}_n(\mathbf{r}) - \mathcal{V}_0(\mathbf{r}), \quad (4.51)$$

which may represent an impurity. It acts as perturbation to the perfect crystal. By solving the DYSON equation starting from the GF of the perfect crystal, the electronic structure of the perturbed system is properly defined by its GF. According to MERTIG [Mer99, MMZ87] and using equations (3.22)-(3.24), the scattering of an unperturbed state k into a state k' by interaction with the local potential is then represented by a t -matrix

$$T_{kk'} = \int d^3\mathbf{r} \psi_k(\mathbf{r}) \Delta\mathcal{V}(\mathbf{r}) \psi_{k'}(\mathbf{r}). \quad (4.52)$$

By applying FERMI's "golden rule", the microscopic transition probability $P_{kk'}$ for an electron in state k being scattered into a state k' on the FERMI surface is given by [MMZ87, ZMRE95]

$$P_{kk'} = \frac{2\pi}{\hbar} cN |T_{kk'}|^2 \delta(E_k - E_{k'}) \quad \text{and} \quad \tau_k^{-1} = \sum_{k'} P_{kk'}, \quad (4.53)$$

where c is the concentration of non-interacting impurities in the dilute limit and cN is the number of perturbed atoms in the system. The electron-impurity scattering time $\tau_{k,\text{imp}}$ is then given by the inverse of the microscopic transition probability summed over all final states. In the presence of SOC the microscopic reversibility is not valid for the scattering probability $P_{kk'} \neq P_{k'k}$, although the systems might be space-inversion invariant [Str98, GFZM10a].

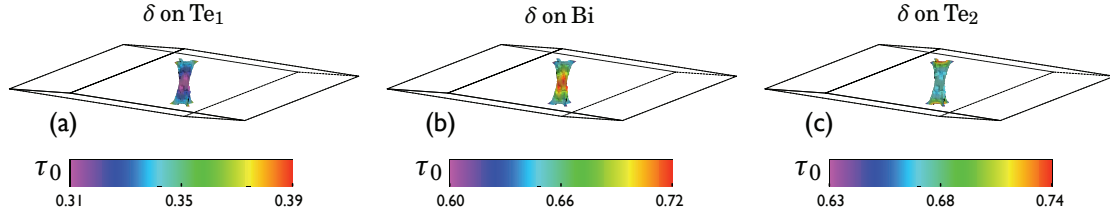


Figure 4.8: Anisotropy of the electron-impurity relaxation time in BORN approximation for electron-doped bulk Bi_2Te_3 calculated via equation (4.55). The chemical potential was set to be about 37 meV above the CBM, corresponding to an electron charge carrier concentration of about $N = 1 \times 10^{19} \text{ cm}^{-3}$ at room temperature. The δ -scatterer was placed on the three (a)-(c) inequivalent sites of the unit-cell. The color code on the FERMI surfaces shows the state-dependent relaxation time in units of τ_0 .

The electron-impurity relaxation time, whose properties depend strongly on the different host-impurity combinations, proved to be important for a proper theoretical description of the giant magnetoresistance (GMR) effect [ZMRE95, ZBM⁺98] and the extrinsic spin HALL effect (SHE) [Gra10, GFZM10a, GFZM10b]. It is worth noting that the relaxation time is in principal energy-dependent and anisotropic with respect to \mathbf{k} , which in turn could lead to anisotropic transport properties in real space (cf. equation (4.23)). In [E5], I proposed the introduction of an anisotropic relaxation time $\tau_{xx}/\tau_{zz} \neq 1$ for bulk Bi_2Te_3 . So far, detailed *ab initio* calculations of the anisotropic relaxation time within the previously presented scheme are unavailable for the complex thermoelectric materials within the scope of this thesis. However, first estimations on a possible directional anisotropy of $\tau_{k,\text{imp}}$ can be made by neglecting details of the scattering potential (4.51), assuming δ -scatterers with weak scattering strength ϑ at site n ,

$$\Delta V(\mathbf{r}_n) = \vartheta \delta(\mathbf{r} - \mathbf{r}_n). \quad (4.54)$$

According to ZAHN [Zah05, ZBM⁺98], the energy- and state-dependent relaxation time τ_{imp} in BORN approximation becomes

$$\tau_{\text{imp}}^{-1}(\mathbf{k}, \mu) = 2\pi c |\hat{\psi}_{\mathbf{k}}(\mathbf{r})|^2 n(\mathbf{r}, \mu) \vartheta^2 + \tau_0^{-1}, \quad (4.55)$$

in which $n(\mathbf{r}, \mu)$ is the local density of states (LDOS) at the chemical potential μ . τ_0 is constant and in the order of the first term in equation (4.55). It is introduced to avoid short-circuit effects due to states with vanishing probability amplitude at the defect site. In terms of multiple scattering theory, the expression for τ_{imp} corresponds to a single-site approximation, neglecting all backscattering effects. The scattering strength ϑ approximates the difference of the t -matrices of the host and the impurity site.

In figure 4.8, the anisotropic relaxation time $\tau_{\text{imp}}^{-1}(\mathbf{k}, \mu)$ is shown for bulk Bi_2Te_3 , with the δ -scatterer placed on the three inequivalent sites of the unit cell (cf. figure (1) in [E7]). The chemical potential was set to be 37 meV above the conduction band minimum (CBM), i.e. an electron charge carrier concentration of about $N = 1 \times 10^{19} \text{ cm}^{-3}$ at room temperature. In figures 4.55(a)-(c) distinct differences in the absolute value and \mathbf{k} -dependence of τ_{imp} can be seen. While the scattering seems to be strongest for a δ -impurity on the Te_1 site leading to a small τ_{imp} , the occurrence of maximal and minimal values of τ_{imp} in dependence on \mathbf{k} is very different for all three impurity positions. A directional anisotropy τ_{xx}/τ_{zz} can be concluded from comparison to the results of equation (4.23) in RTA, where $\tau_{xx}/\tau_{zz} = 1$ by definition. Hence, we find $\tau_{xx}/\tau_{zz} = 0.95$, $\tau_{xx}/\tau_{zz} = 1.04$ and $\tau_{xx}/\tau_{zz} = 0.97$ for the δ -impurity placed on the Te_1 , Bi, and Te_2 sites, respectively. Besides these anisotropies being considerably smaller than the suggested value of $\tau_{xx}/\tau_{zz} = 0.47$ [E5], the model shows a possible impact of electron-impurity scattering on the electronic transport. Neither directional anisotropies

nor orbital anisotropies of $\Delta\mathcal{V}(\mathbf{r})$ were taken into account. Influences of the latter could significantly enhance the effects.

4.5.2 Electron-phonon scattering

Following FRÖHLICH [FT64, Mah90], the HAMILTONIAN for the electron-phonon (E-PH) interaction in second quantization can be written as

$$\mathcal{H}_{\text{e-ph}} = \sum_{\mathbf{k}\mathbf{q}} g_{\mathbf{k}+\mathbf{q},\mathbf{k}}^{\mathbf{q},mn} c_{\mathbf{k}+\mathbf{q}}^{\dagger m} c_{\mathbf{k}}^n (n_{-\mathbf{q}}^{\dagger} + n_{\mathbf{q}}), \quad (4.56)$$

where $c_{\mathbf{k}+\mathbf{q}}^{\dagger m}$ and $c_{\mathbf{k}}^n$ are the creation and annihilation operators for the electronic states $\psi_{\mathbf{k}+\mathbf{q}}^m$ and $\psi_{\mathbf{k}}^n$ with energies $\varepsilon_{\mathbf{k}+\mathbf{q},m}$ and $\varepsilon_{\mathbf{k},n}$ in bands m and n , respectively. The phonon's creation and annihilation operators for frequency $\omega_{\mathbf{q}\nu}$ and wavevector \mathbf{q} are $n_{-\mathbf{q}}^{\dagger}$ and $n_{\mathbf{q}}$. The scheme in figure 4.9(a) emphasizes possible E-PH interactions. The matrix element $g_{\mathbf{k}+\mathbf{q},\mathbf{k}}^{\mathbf{q},mn}$ describes the E-PH coupling and can be obtained, e.g. within density functional perturbation theory (DFPT) [BGC01, WGG05, HEC02, HSRC09] (cf. page 21), by

$$g_{\mathbf{k}+\mathbf{q},\mathbf{k}}^{\mathbf{q},mn} = \sqrt{\frac{\hbar}{2\omega_{\mathbf{q}}}} \langle \psi_{\mathbf{k}+\mathbf{q}}^m | \Delta\mathcal{V}_{\mathbf{q}} | \psi_{\mathbf{k}}^n \rangle \quad \text{with} \quad \Delta\mathcal{V}_{\mathbf{q}} = \sum_{\mathbf{R},i} \frac{\partial \mathcal{V}_{\mathbf{q}}}{\partial \mathbf{u}_{\mathbf{R},i}} \cdot \mathbf{u}_{\mathbf{q},i} \cdot e^{i\mathbf{q}\mathbf{R}}. \quad (4.57)$$

$\Delta\mathcal{V}_{\mathbf{q}}$ is the first-order variation of the KOHN-SHAM potential with respect to the atomic displacement $\mathbf{u}_{\mathbf{R},i}$ for the i -th atom and requires knowledge of the interatomic force constants (IFC) (3.48).

According to ALLEN [All72], the E-PH coupling matrix element (4.57) defines the spectral function

$$\alpha^2 \mathcal{F}(\omega) = \frac{1}{N(\varepsilon_F)} \sum_{mn} \sum_{\mathbf{q}} \delta(\omega - \omega_{\mathbf{q}}) \sum_{\mathbf{k}} |g_{\mathbf{k}+\mathbf{q},\mathbf{k}}^{\mathbf{q},mn}|^2 \times \delta(\varepsilon_{\mathbf{k}+\mathbf{q},m} - \varepsilon_F) \delta(\varepsilon_{\mathbf{k},n} - \varepsilon_F), \quad (4.58)$$

which is the ÈLIASHBERG function [Mig58, Èli60]. It measures the efficiency of an electronic state transition $\psi_{\mathbf{k}}^n \rightarrow \psi_{\mathbf{k}+\mathbf{q}}^m$ by emission or absorption of a phonon with wavevector \mathbf{q} and energy $\hbar\omega_{\mathbf{q}}$. Typical phonon energies are in the order of meV (cf. figure 3.3), while the energies of electrons are of the order of eV. Assuming that E-PH scattering changes mainly the direction of the momentum, but not the energy, corroborates the quasi-elastic assumption $\delta(\varepsilon_{\mathbf{k},n} - \varepsilon_F) \approx \delta(\varepsilon_{\mathbf{k},n} - \varepsilon_F \pm \hbar\omega_{\mathbf{q}})$ [HEC02, HSRC09]. With $\mathcal{F}(\omega)$ defined as the phonon density of states (PHDOS), the dimensionless electron-phonon coupling constant follows from

$$\lambda = 2 \int \frac{\alpha^2 \mathcal{F}(\omega)}{\omega} d\omega. \quad (4.59)$$

The latter is often referred to as *effective mass enhancement factor* $m/m_0 = 1 + \lambda$ and relies on a simplified picture of the averaged electron bands being renormalized by the E-PH interaction.

Knowing the ÈLIASHBERG function allows to calculate the E-PH scattering rate by [Mah90]

$$(\tau_{\text{e-ph}})^{-1} = 2\pi \int_0^{\infty} d\omega \alpha^2 \mathcal{F}(\omega) \times \{f^0(\varepsilon_F + \hbar\omega) - f^0(\varepsilon_F - \hbar\omega) + 2n^0(\omega) + 1\} \stackrel{\varepsilon_F=0}{=} 4\pi \int_0^{\infty} d\omega \frac{\alpha^2 \mathcal{F}(\omega)}{\sinh\left(\frac{\hbar\omega}{k_{\text{B}}T}\right)}. \quad (4.60)$$

Analysing equation (4.60) gives insight into some physical properties of the E-PH relaxation time $\tau_{\text{e-ph}}$, which are moreover shown exemplary in figure 4.9(c) for bulk aluminium. Obviously, at $T = 0$ no phonon modes are occupied, i.e. $n^0(\omega) = 0$ and, hence, $\tau_{\text{e-ph}}(\varepsilon_F) = \infty$. At elevated temperatures, more phonon modes become available for scattering processes and the E-PH relaxation time de-

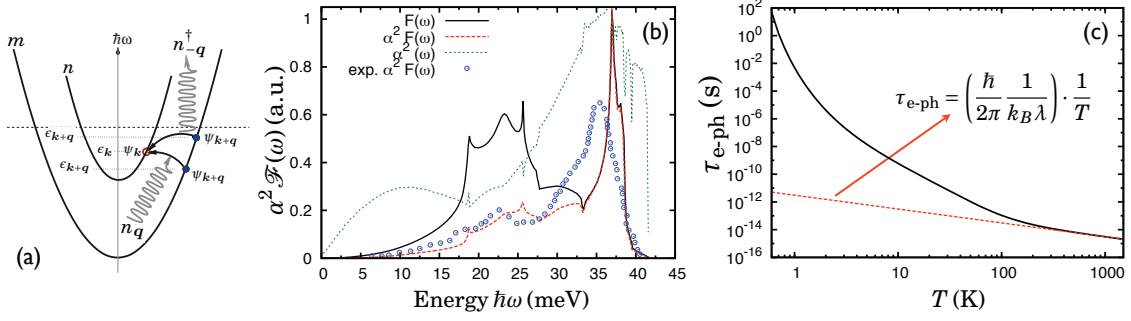


Figure 4.9: Electron-phonon coupling properties of bulk aluminium. (a) Sketch for possible E-PH interactions in a two-band picture. Electronic initial states $\psi_{\mathbf{k}+\mathbf{q}}$ in band m (blue full circles) can relax via emission or absorption of a phonon to a final state $\psi_{\mathbf{k}}$ in band n (red open circle) (figure adapted from [HSRC09]). (b) ÈLIASHBERG function (red dashed line) for bulk aluminium calculated by equation (4.58) as implemented within the QUANTUMESPRESSO package [Gmo09]. Furthermore the PHDOS (black solid line) and the energy dependence of the coupling constants $\alpha(\omega)^2$ (green dotted line) is shown. Blue open circles show results for the ÈLIASHBERG function obtained from tunneling experiments [Sav96]. (c) The thermal E-PH relaxation time obtained via equation (4.60) (solid black line). The red dashed line shows the relation for the high-temperature limit, as explained in the text.

increases strongly. For $\alpha(\omega)^2 = \text{constant}$, it is $\tau_{\text{e-ph}} \propto T^{-3}$, while for the exemplary case of bulk aluminium $\alpha(\omega)^2 \propto \omega$ at small ω leading to $\tau_{\text{e-ph}} \propto T^{-4}$ in the low temperature regime (cf. figures 4.9(b) and (c)). However, due to the finite size of the tetrahedra the determination of the asymptotic low-frequency behaviour is very difficult [CD68, McK76, FS99a]. For frequencies above 5 meV the calculated E-PH coupling $\alpha(\omega)^2$ (cf. green dotted line in figure 4.9(b)) is in excellent agreement to previous published results [Sav96].¹ Once all phonon modes can contribute to the E-PH scattering, i.e. $k_B T \geq \hbar\omega_{\text{max}}$, one readily obtains the relation $\tau_{\text{e-ph}} = \left(\frac{\hbar}{2\pi} \frac{1}{k_B \lambda}\right) \cdot \frac{1}{T}$ from equation (4.60) [FS99a]. It is worthwhile to note that in the high-temperature limit the scattering rate becomes linear in temperature, with a slope determined only by the integral value of the electron-phonon coupling constant (4.59). For bulk aluminium $\lambda = 0.39$, leading to $\tau_{\text{e-ph}} \approx (3.1 \times 10^{-12} \text{ s}) \cdot T^{-1}$. With this, it is obvious that E-PH processes will not contribute noticeably to thermoelectric electron transport at room-temperature and above, as the E-PH scattering rates are at least one order of magnitude higher, than contributions from electron-impurity scattering. However, low temperature E-PH contributions ($T \leq 100 \text{ K}$) can be significant. Here, the phonon-drag effect [Bai67, Zim60, KRR⁺04] can heavily influence the absolute magnitude of the thermopower. As noted before, in a simplified physical picture E-PH coupling directly affects the band formation in the electronic band structure. A large E-PH coupling λ leads to large effective band masses (cf. equation (4.59)) which, at fixed charge carrier concentration, enhances the thermopower as $S/S_0 = 1 + \lambda$ [E3]. A further consequence of E-PH coupling is the failure of the WIEDEMANN-FRANZ law at intermediate temperatures [Uhe04] due to different temperature dependencies of electron-phonon and electron-impurity scattering processes [TPPT07].

¹The ÈLIASHBERG function (4.58) defines the thermal lifetime $\tau_{\text{e-ph}}$, neglecting any backscattering effects. Incorporating the latter, a term $\int_{-\infty}^{\infty} \frac{d\theta}{2\pi} \left(1 - \frac{v_{\mathbf{k}+\mathbf{q}}}{v_{\mathbf{k}}} \cos(\theta_{\mathbf{k}\mathbf{q}})\right)$ enters equation (4.58) and the transport lifetime is defined [Sav96, GKE12]. Hence, for dominating small-angle scattering at low T (see page 31) and $\alpha(\omega)^2 = \text{constant}$, one expects $\tau_{\text{e-ph}} \propto T^{-5}$ [Uhe04].

SELECTED RESULTS

As the present work is a cumulative thesis, some important results are selected to be presented hereinafter by means of peer-reviewed publications. The publications focused on the effect of bulk and interfacial strain on the electronic structure and the anisotropic TE transport properties (see [E5] in section 5.1 and [E8] in section 5.2). They will include detailed discussions on the influence of quantum confinement and the choice of superlattice periods on the TE transport (see [E2] in section 5.1 and [E3] in section 5.2). All results are presented in dependence on temperature and charge carrier concentration. Intentionally, the discussions are tempted to built a strong context to experimental findings.

After a brief introduction and summary for each specific topic, two publications each, for Bi_2Te_3 /- Sb_2Te_3 based superlattices (section 5.1) and for Si/Ge based superlattices (section 5.2), are attached.

5.1 $\text{Bi}_2\text{Te}_3/\text{Sb}_2\text{Te}_3$ heterostructures

The chalcogenides Bi_2Te_3 and Sb_2Te_3 and their solid solutions dominated efficient bulk TEs with $ZT \approx 0.5 - 1$ in the last fifty years [GSW58, Wri58, PHM⁺08]. The intrinsic layered Bi_2Te_3 and Sb_2Te_3 show large anisotropies in their crystal structure and their TE transport properties. At first glance, the anisotropic electronic structure of both materials was studied in detail [E7]. The band structure's topology is very complex, and strong SOC effects dictate the formation of the band edges. To give an example, the conduction band minimum (CBM) of Bi_2Te_3 was found to consist of two valleys, in contrast to the six-valley model proposed by DRABBLE & WOLFE [DGW58]. However, as indicated in figures 5.1(c) and (d), at slightly increased band occupation of about $N = 3 \times 10^{19} \text{ cm}^{-3}$, additional local CBM off the high symmetry lines are occupied, forming the expected six valleys in reciprocal space. Specific details of the band structures topology, like saddle points, were furthermore found to be direct sources of extrema of the electrical conductivity anisotropy [E7]. In [E5] it is shown that the anisotropy of the electrical conductivity surpasses the experimental findings for Bi_2Te_3 , but not for Sb_2Te_3 , implying anisotropic scattering effects in the first (cf. section 4.5.1). By detailed convergence and model studies it was shown, that different numerical methods for the

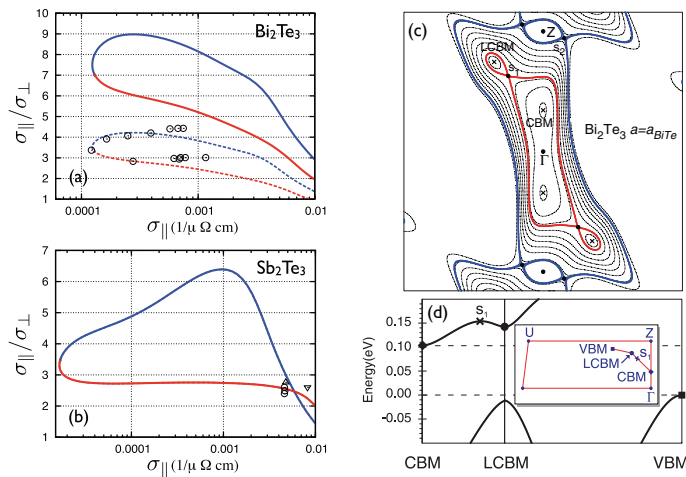


Figure 5.1: Calculated electrical conductivity anisotropy at 300K of bulk (a) Bi_2Te_3 and (b) Sb_2Te_3 . Electron doping refers to blue lines, while red lines refer to hole doping. The dashed lines in panel (a) present the ratio obtained with an anisotropic relaxation time $\tau_{\parallel}/\tau_{\perp} = 0.47$, while all other results are obtained with an isotropic relaxation time. Experimental data (circles and triangles) are given for comparison (further details in [E5]). (c) Energy contour plots for the conduction band in the plane ΓZU for bulk Bi_2Te_3 . 10 isolines for $E - E_{\text{CBM}}$ at 0 to 0.19eV with a constant increment (dotted); additionally, two isolines at $E - E_{\text{CBM}} = 0.05\text{eV}$ and $E - E_{\text{CBM}} = 0.17\text{eV}$ with the saddle points s_1 and s_2 , respectively (bold). The positions of the CBM and the local CBM are marked with crosses. Below in (d) the corresponding band structure near the band gap along the lines shown in the inset are given.

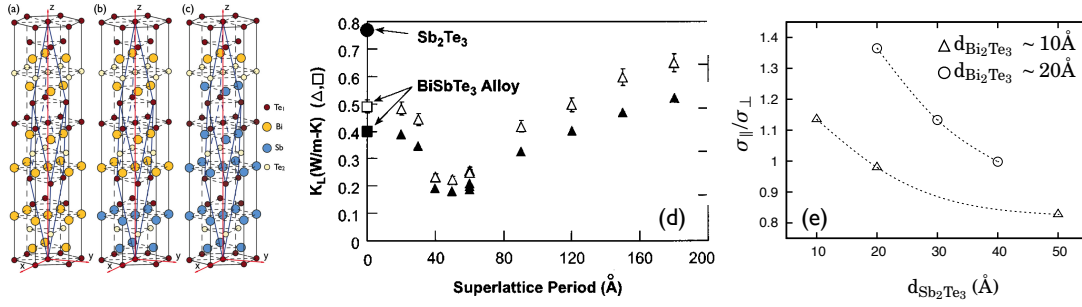


Figure 5.2: Hexagonal unit cells and directional anisotropies for (a) bulk Bi_2Te_3 , (b) $20\text{\AA}\text{Bi}_2\text{Te}_3/10\text{\AA}\text{Sb}_2\text{Te}_3$, and (c) $5\text{\AA}\text{Bi}_2\text{Te}_3/25\text{\AA}\text{Sb}_2\text{Te}_3$ -SLs. (d) Experimental lattice thermal conductivity for epitaxial $\text{Bi}_2\text{Te}_3/\text{Sb}_2\text{Te}_3$ -SL in dependence on their SL period. A distinct minimum can be seen around a SL period of 40-60Å. Figure adapted from [Ven00]. (e) Experimental electrical conductivity anisotropy for different $\text{Bi}_2\text{Te}_3/\text{Sb}_2\text{Te}_3$ -SL. Cross-plane transport was found most preferable for a $10\text{\AA}\text{Bi}_2\text{Te}_3/50\text{\AA}\text{Sb}_2\text{Te}_3$ -SL. Figure modified from [VSC01].

determination of the electrical conductivity anisotropy can give results closer to experiment, hiding the evidence for possible anisotropic scattering effects [E6]. Contrary to earlier experimental assumptions [SH76, Sto80], the anisotropy of the thermopower of both tellurides stems to a large amount, probably entirely, from band structure effects, more precisely from a distinct anisotropy of the transport distribution function (TDF) (see [E5]).

The application of interfacial strain in epitaxially grown Bi_2Te_3 and Sb_2Te_3 in order to optimize the TE transport properties was found to be unsatisfying [E5]. Due to compensation effects of the strain-dependent thermopower and electrical conductivity, the related power factor decreases under applied compressive in-plane strain for Bi_2Te_3 , while being stable for tensile strained Sb_2Te_3 . Thus, growing $\text{Bi}_2\text{Te}_3/\text{Sb}_2\text{Te}_3$ -SLs, a substrate favouring Bi_2Te_3 should be chosen for TE applications, because the transport properties of Sb_2Te_3 are much more robust under applied strain.

In 2001, VENKATASUBRAMANIAN *et al.* made considerable contributions to the field of chalcogenide TE's. These authors introduced the concept of phonon-blocking and electron-transmitting SLs (see section section 2.4), at the pioneering example of $\text{Bi}_2\text{Te}_3/\text{Sb}_2\text{Te}_3$ -SL [VCW⁺97, VSC01]. As shown in figure 5.2(c), they found the cross-plane lattice thermal conductivity to be drastically reduced below the alloy limit [VCWH96, Ven00]. Furthermore, it was found that the electrical conductivity anisotropy $\sigma_{\parallel}/\sigma_{\perp}$ is a function of the SL period and reduces to values smaller than found for bulk, clearly preferring the cross-plane transport $\sigma_{\parallel}/\sigma_{\perp} \leq 1$. Both experimental findings added up to the highest values for the figure of merit so far: $ZT = 2.4$ for a *p*-type $\text{Bi}_2\text{Te}_3/\text{Sb}_2\text{Te}_3$ -SL and $ZT = 1.5$ for a *n*-type $\text{Bi}_2\text{Te}_3/\text{Bi}_2\text{Te}_{2.83}\text{Se}_{0.17}$ at room temperature.

The findings of $\sigma_{\parallel}/\sigma_{\perp} \leq 1$ are contrary to expectations, as $\sigma_{\parallel}/\sigma_{\perp} \sim 2.5 - 5.5$ for bulk Sb_2Te_3 and Bi_2Te_3 (cf. figure 5.1(a),(b) and [E5]). Further carrier confinement in the cross-plane direction due to the heterostructure should be expected. VENKATASUBRAMANIAN *et al.* argued that in the SLs, due to weak confinement and near zero band offset, there is minimal anisotropy between in-plane and cross-plane electrical conductivities. The argumentation of VENKATASUBRAMANIAN concludes that in bulk Bi_2Te_3 and Sb_2Te_3 $\sigma_{\parallel}/\sigma_{\perp} = 1$ since the band offsets in bulk materials are zero by definition. The latter conclusion is obviously wrong. While in [E2] I can confirm that the valence band offset is almost vanishing in all discussed SLs, leading to a bulk-like behaviour (cf. figure 5.3(b)), strong quantum-well effects were found upon electron doping. Here, the electrons tend to localize in Bi_2Te_3 layers, leading to an diminished cross-plane transport (cf. figures 5.3(a,c,d)). The in-plane transport properties, especially under hole doping, only showed a weak dependence on the SL period. However, no enhancement of the in-plane TE transport was found under quantum confinement, as

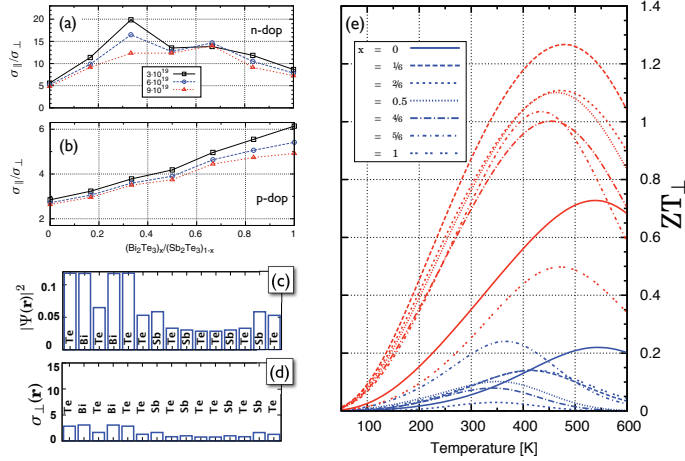


Figure 5.3: (a) and (b) Directional anisotropies of the electrical conductivity for $(\text{Bi}_2\text{Te}_3)_x/(\text{Sb}_2\text{Te}_3)_{1-x}$ SLs in dependence on the superlattice period at 300 K. Results for three different charge carrier concentrations (in units of cm^{-3}) are compared, for (a) electron doping and (b) hole doping. (c) Site-resolved probability amplitude for a $(\text{Bi}_2\text{Te}_3)_x/(\text{Sb}_2\text{Te}_3)_{1-x}$ SLs with $x = 2/6$. In the same manner, the site-resolved cross-plane electrical conductivity [in units of $(\text{cm})^{-1}$] is shown. The temperature is fixed at 300 K, the charge carrier concentration is $N = 3 \times 10^{19} \text{ cm}^{-3}$. (e) Cross-plane figure of merit for different $(\text{Bi}_2\text{Te}_3)_x/(\text{Sb}_2\text{Te}_3)_{1-x}$ SLs at varying temperature and fixed charge carrier concentration of $N = 3 \times 10^{19} \text{ cm}^{-3}$. Here, red and blue lines constitute p - and n -doping, respectively.

suggested within the concept of HICKS & DRESSELHAUS (section 2.2). As an additional result, the LORENZ function of the Bi₂Te₃/Sb₂Te₃-SL and their directional anisotropy were found to be an intricate function of the SL period ([E1] and [E2]). Large deviations from the metallic limit L_0 are evident even in the case of large extrinsic charge carrier concentrations, e.g. $L_{\perp}/L_0 \sim 2$. The latter finding could be important for the community, as usually the lattice thermal conductivity is derived by $\kappa_{\text{ph}} = \kappa - L\sigma T$. With κ being directly measured by 3ω methods [BTKC01], assuming too small or large LORENZ numbers leads to wrong estimations for the lattice part of the thermal conductivity [SVG01].

Concluding, for all Bi₂Te₃/Sb₂Te₃-SLs enhancements of the electronic TE transport properties could not be found. At its best, they behave as being bulk-like, and the enhancement for the figure of merit stems solely from a reduction of the cross-plane thermal conductivity. As shown in figure 5.3 and discussed in [E2], $ZT \approx 1$ for the p -type SLs at 300K; it reaches maximal values of $ZT \approx 1.3$ at 450K for the 5Å Bi₂Te₃/10Å Sb₂Te₃-SL. The latter is the same SL composition for which the largest values of ZT were achieved in experiment, too [Ven00]. While our absolute values for ZT are in contrast to the experimental findings of VENKATASUBRAMANIAN *et al.*, due to the fact that the measured $\sigma_{\parallel}/\sigma_{\perp} \approx 1$ could not be confirmed, we find very good accordance to recent experimental findings in the group of BÖTTNER [KWB⁺11, WLK⁺11, WLK⁺12].

Influence of strain on anisotropic thermoelectric transport in Bi_2Te_3 and Sb_2Te_3

N. F. Hinsche,^{1,*} B. Yu. Yavorsky,¹ I. Mertig,^{1,2} and P. Zahn¹

¹*Institut für Physik, Martin-Luther-Universität Halle-Wittenberg, DE-06099 Halle, Germany*

²*Max-Planck-Institut für Mikrostrukturphysik, Weinberg 2, DE-06120 Halle, Germany*

(Received 25 July 2011; revised manuscript received 14 October 2011; published 28 October 2011; publisher error corrected 13 February 2012)

On the basis of detailed first-principles calculations and semiclassical Boltzmann transport, the anisotropic thermoelectric transport properties of Bi_2Te_3 and Sb_2Te_3 under strain were investigated. It was found that due to compensation effects of the strain-dependent thermopower and electrical conductivity, the related power factor will decrease under applied in-plane strain for Bi_2Te_3 , while being stable for Sb_2Te_3 . A clear preference for thermoelectric transport under hole doping, as well as for the in-plane transport direction was found for both tellurides. In contrast to the electrical conductivity anisotropy, the anisotropy of the thermopower was almost robust under applied strain. The assumption of an anisotropic relaxation time for Bi_2Te_3 suggests that already in the single crystalline system strong anisotropic scattering effects should play a role.

DOI: [10.1103/PhysRevB.84.165214](https://doi.org/10.1103/PhysRevB.84.165214)

PACS number(s): 31.15.A-, 71.15.Mb, 72.20.Pa

I. INTRODUCTION

Thermoelectric (TE) materials are used as solid-state energy devices that convert waste heat into electricity or electrical power directly into cooling or heating.¹⁻³ Telluride-based thermoelectrics, e.g., the bulk materials bismuth (Bi_2Te_3), antimony telluride (Sb_2Te_3), and their related alloys, dominate efficient TE energy conversion at room temperature for the last 60 years.^{4,5} The materials TE efficiency is quantified by the figure of merit

$$ZT = \frac{\sigma S^2}{\kappa_{\text{el}} + \kappa_{\text{ph}}} T, \quad (1)$$

where σ is the electrical conductivity, S the thermopower, κ_{el} and κ_{ph} are the electronic and phononic contributions to the thermal conductivity, respectively. From Eq. (1) it is obvious that a higher ZT is obtained by decreasing the denominator or by increasing the numerator, the latter being called the power factor $\text{PF} = \sigma S^2$. While bulk Bi_2Te_3 and Sb_2Te_3 show ZT values smaller than one and applications have been limited to niche areas, a breakthrough experiment of Venkatasubramanian *et al.* showed a remarkable $ZT = 2.4/1.5$ for p -type/ n -type superlattices (SLs) composed of the two bulk tellurides.⁵⁻⁷ With the availability of high- ZT materials, many new applications will emerge.² The idea of thermoelectric SL follows the idea of phonon blocking and electron transmitting at the same time. It suggests that cross-plane transport along the direction perpendicular to the artificial interfaces of the SL reduces phonon heat conduction while maintaining or even enhancing the electron transport.³ While some effort in experimental research was done,⁸⁻¹³ only a few theoretical works discuss the possible transport across such SL structures.^{14,15} While Park *et al.*¹⁴ discussed the effect of volume change on the in-plane thermoelectric transport properties of Bi_2Te_3 , Sb_2Te_3 , and their related compounds, Li *et al.*¹⁵ focussed on the calculation of the electronic structure for a $\text{Bi}_2\text{Te}_3/\text{Sb}_2\text{Te}_3$ SL, stating changes of the mobility anisotropy estimated from effective masses.

Superlattices are anisotropic by definition and even the telluride bulk materials show intrinsic anisotropic structural and electronic properties. However, investigations of

Venkatasubramanian *et al.* found a strong decrease for the mobility anisotropy and the thermoelectric properties for the $\text{Bi}_2\text{Te}_3/\text{Sb}_2\text{Te}_3$ SLs at certain periods. The reason for this behavior is still under debate and could be related to strain effects, which are induced by the epitaxial growth of the $\text{Bi}_2\text{Te}_3/\text{Sb}_2\text{Te}_3$ SLs. To extend previous works¹⁶⁻¹⁸ and to clarify the open question on the reduced anisotropy, we are going to discuss in this paper the anisotropic electronic transport in bulk Bi_2Te_3 and Sb_2Te_3 and the possible influence of strain in epitaxially grown SL on the TE properties.

For this purpose, the paper will be organized as follows. In Sect. II, we introduce our first-principles electronic structure calculations based on density functional theory and the semiclassical transport calculations based on the solution of the linearized Boltzmann equation. With this, we discuss the thermoelectric transport properties, that is, electrical conductivity, thermopower, and the related power factor of unstrained Bi_2Te_3 and Sb_2Te_3 with a focus on their directional anisotropies. While in epitaxially grown the atoms near the interfaces may be shifted from their bulk positions due to the lattice mismatch and the changed local environment, we modeled Bi_2Te_3 with the experimental lattice parameters and interatomic distances of Sb_2Te_3 and vice versa. We assume that from these two limiting cases, one could estimate the effect of the interface relaxation on the electronic and transport properties in $\text{Bi}_2\text{Te}_3/\text{Sb}_2\text{Te}_3$ SLs. With these structural data we first analyze in Sec. III, the anisotropic thermoelectric properties of the unstrained bulk systems, while in Sec. IV, a detailed view on the influence of strain, which may occur in $\text{Bi}_2\text{Te}_3/\text{Sb}_2\text{Te}_3$ SLs, on the electronic transport of these tellurides is given. Throughout the paper we quote $\text{Bi}_2\text{Te}_3(\text{Sb}_2\text{Te}_3)$ as strained, if it is considered in the lattice structure of $\text{Sb}_2\text{Te}_3(\text{Bi}_2\text{Te}_3)$. As in the SL, p type as well as n type transport was reported, we discuss the concentration dependence for both types of carriers on the transport properties.

II. METHODOLOGY

For both bismuth and antimony telluride, we used the experimental lattice parameters and relaxed atomic positions¹⁹ as provided for the rhombohedral crystal structure with five

atoms, i.e., one formula unit, per unit cell belonging to the space group D_{3d}^5 ($R\bar{3}m$). The related layered hexagonal structure is composed out of three formula units and has the lattice parameters $a_{\text{BiTe}}^{\text{hex}} = 4.384$ Å, $c_{\text{BiTe}}^{\text{hex}} = 30.487$ Å, and $a_{\text{SbTe}}^{\text{hex}} = 4.264$ Å, $c_{\text{SbTe}}^{\text{hex}} = 30.458$ Å, for Bi_2Te_3 and Sb_2Te_3 , respectively. In fact, the main difference between the lattices of Bi_2Te_3 and Sb_2Te_3 is a decrease of the in-plane lattice constant with an accompanied decrease in the cell volume. So, a change between the two lattice constants can be related to either compressive or tensile in-plane strain. This is very similar to the approach by Park *et al.*¹⁴ while omitting computational relaxation of internal atomic positions.

Our electronic structure calculations are performed in two steps. In a first step, the detailed band structures of the strained and unstrained Bi_2Te_3 and Sb_2Te_3 were obtained (see Fig. 1) by first-principles density functional theory calculations (DFT), as implemented in the fully relativistic screened Korrington-Kohn-Rostoker Greens-function method (KKR).²⁰ Within this approach, the Dirac equation is solved self-consistently and with the spin-orbit coupling included. Exchange and correlation effects were accounted for by the local density approximation (LDA) parametrized by Vosco, Wilk, and Nusair.²¹ A detailed discussion on the influence of strain on the band structure topology of Bi_2Te_3 and Sb_2Te_3 is recently published.²²

With the well-converged results from the first step, we obtain the thermoelectric transport properties by solving the linearized Boltzmann equation in relaxation time approximation (RTA) within an in-house developed Boltzmann transport code.^{23–25} Boltzmann transport calculations for thermoelectrics have been carried out for quite a long time and show reliable results for metals^{26–28} as well as for wide- and narrow-gap semiconductors.^{25,29–32} TE transport calculations for bulk Bi_2Te_3 ^{14,18,33,34} and Sb_2Te_3 ^{14,17,35} were presented before. Here, the relaxation time τ is assumed to be constant with respect to wave vector k and energy on the scale of $k_B T$. This assumption is widely accepted for metals and highly doped semiconductors. Most of the presented results are in this high-doping regime. Within the RTA, the transport distribution function $\mathcal{L}_{\perp,\parallel}^{(0)}(\mu, 0)$ (TDF)³⁶ and with this the generalized conductance moments $\mathcal{L}_{\perp,\parallel}^{(n)}(\mu, T)$ are defined as

$$\mathcal{L}_{\perp,\parallel}^{(n)}(\mu, T) = \frac{\tau_{\perp,\parallel}}{(2\pi)^3} \sum_{\nu} \int d^3k (v_{k,(\perp,\parallel)}^{\nu})^2 \times (E_k^{\nu} - \mu)^n \left(-\frac{\partial f_{(\mu,T)}}{\partial E} \right)_{E=E_k^{\nu}}. \quad (2)$$

$v_{k,(\parallel)}^{\nu}$ and $v_{k,(\perp)}^{\nu}$ denote the group velocities in the directions in the hexagonal basal plane and perpendicular to it, respectively. Within, the group velocities were obtained as derivatives along the lines of the Bröchl mesh in the whole Brillouin zone.²² A detailed discussion on implications and difficulties of the numerical determination of the group velocities in highly anisotropic materials is currently published elsewhere.³⁷ As can be seen straightforwardly, the in- and cross-plane electrical conductivity σ is then given by

$$\sigma_{\perp,\parallel} = 2e^2 \mathcal{L}_{\perp,\parallel}^{(0)}(\mu, T) \quad (3)$$

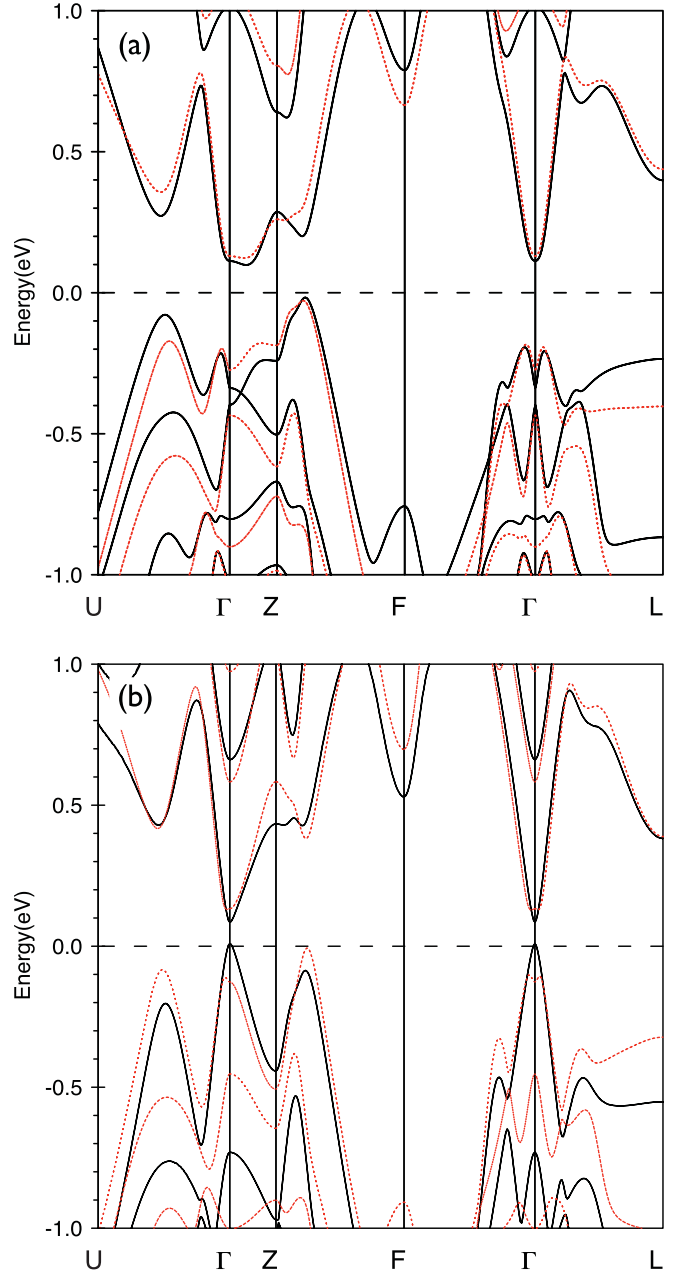


FIG. 1. (Color online) Band structures of (a) Bi_2Te_3 and (b) Sb_2Te_3 along symmetry lines for both unstrained (black solid lines) and strained (red dashed lines) lattices. Energies are given relative to the valence band maximum.

and the temperature- and doping-dependent thermopower states as

$$S_{\perp,\parallel} = \frac{1}{eT} \frac{\mathcal{L}_{\perp,\parallel}^{(1)}(\mu, T)}{\mathcal{L}_{\perp,\parallel}^{(0)}(\mu, T)} \quad (4)$$

for given chemical potential μ at temperature T and extrinsic carrier concentration N determined by an integration over the density of states $n(E)$:

$$N = \int_{\mu-\Delta E}^{\text{VB}^{\text{max}}} dE n(E) [f_{(\mu,T)} - 1] + \int_{\text{CB}^{\text{min}}}^{\mu+\Delta E} dE n(E) f_{(\mu,T)}, \quad (5)$$

where CB^{\min} is the conduction band minimum and VB^{\max} is the valence band maximum (VBM). The energy range ΔE has to be taken sufficiently large to cover the tails of the Fermi-Dirac distribution function $f(\mu, T)$ and to ensure convergence of the integrals in Eqs. (2) and (5).²⁵ The k -space integration of Eq. (2) for a system with an intrinsic anisotropic texture is quite demanding. In previous publications,^{22,37} we stated on the relevance of adaptive integration methods needed to reach convergence of the energy-dependent TDF. Especially in regions close to the band edges, the anisotropy of the TDF requires a high density of the k mesh. Here, convergence tests for the transport properties showed that at least 150 000 k points in the entire BZ had to be included for sufficient high doping rates ($N \geq 1 \times 10^{19} \text{ cm}^{-3}$), while for energies near the band edges, even more than 56 million k points were required to reach the analytical values for the conductivity anisotropies at the band edges. (The analytical value of the ratio $\sigma_{\parallel}/\sigma_{\perp}$ at the band edges was obtained by scanning the energy landscape near the conduction band minimum and valence band maximum fitting the dispersion relation in terms of an effective mass tensor. A detailed description is given in a recent publication by Ref. 22.) Within the RTA, from comparison of the calculated electrical conductivities [Eq. (3)] with experiment it is possible to conclude on the directional anisotropy of τ . For the thermopower S [Eq. (4)], the dependence of the TDF on the energy is essential. That is, not only the slope of the TDF, moreover, the overall functional behavior of the TDF on the considered energy scale has to change to observe an impact on the thermopower. The calculations in this paper aim to cover band structure effects and not scattering-specific impacts by an energy- and state-dependent relaxation time.

III. ANISOTROPIC THERMOELECTRIC PROPERTIES OF UNSTRAINED Bi_2Te_3 AND Sb_2Te_3

In order to understand the experimental findings on the in-plane and cross-plane transport of the $\text{Bi}_2\text{Te}_3/\text{Sb}_2\text{Te}_3$ SLs, in the following section, the anisotropies of the electrical conductivity, the thermopower, and the related power factor of bulk Bi_2Te_3 and Sb_2Te_3 are discussed. Even though the behavior of Sb_2Te_3 is strongly p type with an extrinsic carrier concentration of $N = 1\text{--}10 \times 10^{20} \text{ cm}^{-3}$,³⁸ we also discuss the related n -doped case, as in $\text{Bi}_2\text{Te}_3/\text{Sb}_2\text{Te}_3$ SLs, n as well as p dopings were reported. Bulk Bi_2Te_3 is known to be inherent electron conducting, while hole doping is experimentally achievable for bulk systems.^{4,39–41}

Figure 2 shows the variation of the anisotropic thermopower for unstrained Bi_2Te_3 and Sb_2Te_3 in a wide temperature range. The extrinsic charge carrier concentration of Bi_2Te_3 and Sb_2Te_3 was fixed to $N = 1 \times 10^{19} \text{ cm}^{-3}$ and $N = 1 \times 10^{20} \text{ cm}^{-3}$, respectively. As a reference, experimental values for both single crystalline materials at the same doping conditions are given and an excellent agreement can be stated. It is worth noting that within Eq. (4), the calculation of the thermopower is completely free of parameters. For Bi_2Te_3 , the in-plane thermopower reaches a maximum of $S_{\parallel} \sim -200 \mu\text{V/K}$ at 300 K, while the maximum for the hole-doped case is shifted to slightly higher temperatures of 350 K with a maximum value of $S_{\parallel} \sim 225 \mu\text{V/K}$. We note,

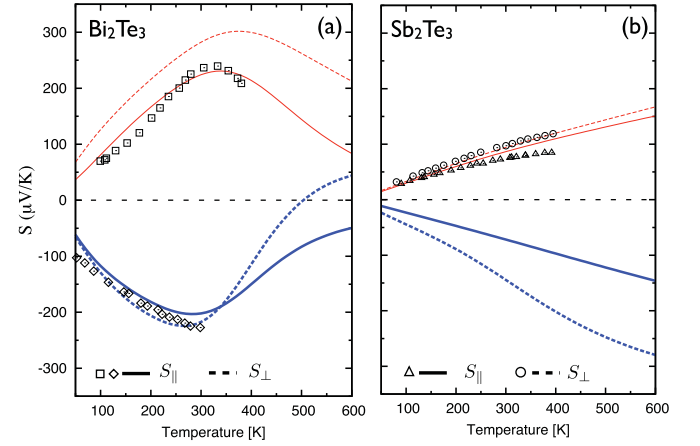


FIG. 2. (Color online) Anisotropic thermopower for bulk (a) Bi_2Te_3 and (b) Sb_2Te_3 in their unstrained bulk lattice constants. Electron doping refers to the blue (thick) lines in the lower part of the figure, while red (thin) lines refer to hole doping and positive values of the thermopower. Solid lines show the in-plane part S_{\parallel} of the thermopower, while dashed lines show the cross-plane part S_{\perp} . The extrinsic charge carrier concentration of Bi_2Te_3 and Sb_2Te_3 was fixed to $N = 1 \times 10^{19} \text{ cm}^{-3}$ and $N = 1 \times 10^{20} \text{ cm}^{-3}$, respectively. Experimental data (squares, diamonds, circles, triangles) from Refs. 41–43 are given for comparison.

that the temperature of the maximum is slightly overestimated. This might be caused by the missing temperature dependence of the energy gap, which was determined as $E_g = 105 \text{ meV}$ for unstrained Bi_2Te_3 . The anisotropy of the thermopower is more pronounced for the p -doped case. Here, the cross-plane thermopower S_{\perp} is, for the given doping, always larger than the in-plane part S_{\parallel} . The anisotropy $\frac{S_{\parallel}}{S_{\perp}}$ is about 0.64 at 100 K, evolving to $S_{\parallel}/S_{\perp} \sim 0.79$ and $S_{\parallel}/S_{\perp} \sim 0.55$ at 300 and 500 K, respectively. The sole available experimental data show no noticeable anisotropy for the thermopower in the hole-doped case.⁴² For the electron-doped case, the situation is more sophisticated. While up to 340 K the overall anisotropy is rather small, with values $S_{\parallel}/S_{\perp} \sim 0.9$, a considerable decrease of S_{\perp} at higher temperatures leads to high values of S_{\parallel}/S_{\perp} for temperatures above 400 K. This tendency could also be revealed by experiments.^{44,45} The crossing point of S_{\parallel} and S_{\perp} near room temperature could explain the fact of varying measured anisotropies for the thermopower at 300 K. Here, anisotropy ratios of $S_{\parallel}/S_{\perp} = 0.97\text{--}1.10$ were reported.^{41,45} The maximum peak of the thermopower near room temperature can be explained by the position of the chemical potential μ as a function of temperature at a fixed carrier concentration. For T much smaller than 300 K, the chemical potential is located in either the conduction or valence band with the tails of the Fermi-Dirac distribution in Eq. (2) only playing a subsidiary role. For rising temperatures, the chemical potential shifts toward the band edges, and S maximizes. At these conditions, the conduction is mainly unipolar. For higher temperatures, the chemical potential shifts into the band gap and conduction becomes bipolar leading to a reduced thermopower. For the case of Sb_2Te_3 , shown in Fig. 2(b), the situation is different. Due to the ten-times-higher inherent doping and the smaller energy gap of

$E_g = 90$ meV, the chemical potential is located deeply in the bands for the whole relevant temperature range. Therefore the functional behavior can be understood in terms of the well-known Mott relation, where Eq. (4) qualitatively coincides with $S \propto T \frac{d \ln \sigma(E)}{dE} |_{E=\mu}$ for the thermopower in RTA.⁴⁶ With increasing temperature, the thermopower increases almost linearly, showing values of $S_{\parallel} \sim 87 \mu\text{V/K}$ and $S_{\perp} \sim -72 \mu\text{V/K}$ at 300 K for p and n doping, respectively. The anisotropy of the thermopower for the hole-doped case is around $S_{\parallel}/S_{\perp} = 0.91$, almost temperature independent and slightly underestimates the available experimental values.^{47,48} While for the electron-doped case the absolute values of the in-plane thermopower are comparable to those of the hole-doped case, the anisotropies are rather large. The anisotropy varies only weakly on temperature, showing $S_{\parallel}/S_{\perp} = 0.48\text{--}0.52$ over the hole temperature range. While bulk Sb_2Te_3 states have a strong p character due to inherent defects, we note here again, that n doping is available in heterostructures combining Bi_2Te_3 and Sb_2Te_3 .⁵

A strongly enhanced cross-plane thermopower S_{\perp} could lead to a strongly enhanced power factor PF_{\perp} , if the cross-plane electrical conductivity σ_{\perp} is maintained at the bulk value.

For this purpose, the anisotropy of the electrical conductivity in dependence on the in-plane conductivity σ_{\parallel} for unstrained Bi_2Te_3 and Sb_2Te_3 is shown in Fig. 3. The temperature is fixed at 300 K, blue and red lines refer to electron and hole doping, respectively. From comparison with experimental data, the in-plane relaxation time is determined to be $\tau_{\parallel} = 1.1 \times 10^{-14}$ and 1.2×10^{-14} s for Bi_2Te_3 and Sb_2Te_3 , respectively. (The calculated dependencies of the electrical conductivity on the thermopower and on the applied doping were matched to fit experiments from Refs. 4, 39, and 48.) With that, we find strong anisotropies for the electrical conductivity $\sigma_{\parallel}/\sigma_{\perp} \gg 1$, clearly preferring the in-plane transport in both bulk tellurides. For the strongly suppressed cross-plane conduction, p -type conduction is more favored than n type. For Bi_2Te_3 , the pure band structure effects [solid lines in Fig. 3(a)] overestimate the measured anisotropy³⁹ of the electrical conductivity. With an assumed anisotropy of the relaxation time of $\tau_{\parallel}/\tau_{\perp} = 0.47$, the experimental values are reproduced very well. This means that scattering effects strongly affect the transport, and electrons traveling along the basal plane direction are scattered stronger than electrons traveling perpendicular to the basal plane. The origin of this assumed anisotropy has to be examined by defect calculations, resulting microscopic transition probabilities, and state-dependent mean free path vectors. It is well known that in Bi_2Te_3 , mainly antisite defects lead to the inherent conduction behavior.^{38,45,50} We have shown elsewhere³⁷ that the integration of the transport integrals (2) in anisotropic k space requires large numerical effort. Tiny regions in k space close to the band gap have to be scanned very carefully, and the texture in k space has a drastic influence on the obtained anisotropy values, if integrals are not converged with respect to the k -point density. As shown, some integration methods tend for the given k -space symmetry to underestimate the ratio $\sigma_{\parallel}/\sigma_{\perp}$ in a systematic manner, and therefore would shift anisotropy closer to the experimental observed values, without representing the real

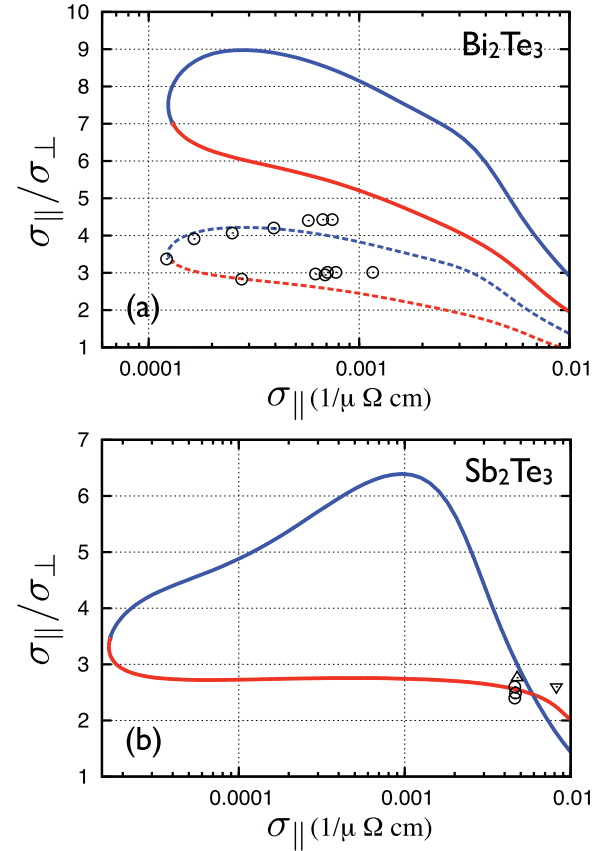


FIG. 3. (Color online) Ratio $\sigma_{\parallel}/\sigma_{\perp}$ of the electrical conductivities at 300 K for unstrained bulk (a) Bi_2Te_3 and (b) Sb_2Te_3 . Electron doping refers to blue lines, while red lines refer to hole doping. The dashed lines in panel (a) present the ratio obtained with an anisotropic relaxation time $\tau_{xx}/\tau_{zz} = 0.47$, while all other results are obtained with an isotropic relaxation time. Experimental data (circles and triangles) from Refs. 39, 49, and 48 are given for comparison.

band structure effects. For unstrained Bi_2Te_3 , the electrical conductivity anisotropy is the highest for low values of σ_{\parallel} , i.e., small amounts of doping and bipolar conduction. For larger charge carrier concentrations, i.e., the chemical potential deeper into either conduction or valence band, the in-plane conductivity σ_{\parallel} increases and the ratio $\sigma_{\parallel}/\sigma_{\perp}$ decreases. Values for $\sigma_{\parallel}/\sigma_{\perp}$ will lower from seven to two for p -type conduction and nine to three for n -type conduction. However, cross-plane electrical transport is always more suppressed for n -type carrier conduction, which also holds for unstrained Sb_2Te_3 . As shown in Fig. 3(b), $\sigma_{\parallel}/\sigma_{\perp}$ is almost doping independent for hole doping, showing an anisotropy of around 2.7 in very good agreement with experiment (circle and triangles in Fig. 3 from Refs. 47–49). In this case, no anisotropic relaxation times had to be assumed. For electron doping, the ratio $\sigma_{\parallel}/\sigma_{\perp}$ is clearly higher, evolving values of 3.5 to 6 for rising in-plane conductivity. The dependence of the anisotropy ratio on the applied doping, i.e., changing σ_{\parallel} , can be directly linked to the functional behaviour of the TDF near band edges, which is crucially influenced by the topology of the band structure.²²

IV. ANISOTROPIC THERMOELECTRIC PROPERTIES OF STRAINED Bi_2Te_3 AND Sb_2Te_3

Before the influence of in-plane strain on the resulting power factor will be discussed, we will first note on the strain-induced changes of the components electrical conductivity and thermopower. In Fig. 4, the anisotropy of the electrical conductivity $\sigma_{\parallel}/\sigma_{\perp}$ is shown for both Bi_2Te_3 in the lattice constant of Sb_2Te_3 , i.e., under biaxial compressive in-plane strain [Fig. 4(a)], and Sb_2Te_3 in the lattice constant of Bi_2Te_3 , i.e., under biaxial tensile in-plane strain [Fig. 4(b)].

For Bi_2Te_3 , the compressive in-plane strain causes an increase of the the band gap by around 23% yielding $E_g = 129$ meV. While the anisotropy $\sigma_{\parallel}/\sigma_{\perp}$ for hole doping [red lines in Fig. 4(a)] decreases to around four and is almost constant under varying doping level, the ratio rises considerably under electron doping to values up to 13 for $\sigma_{\parallel} \sim 100\text{--}1000$ ($\Omega\text{ cm}$)⁻¹, corresponding to electron charge carrier concentrations of $N = 3\text{--}30 \times 10^{19}$ cm⁻³. This concludes, that the cross-plane electrical conductivity of Bi_2Te_3 under compressive in-plane strain will be noticeably enhanced for *p* doping, but drastically suppressed for *n* doping. Such a compressive in-plane strain could be introduced by either a substrate with smaller in-plane lattice constant, e.g.,

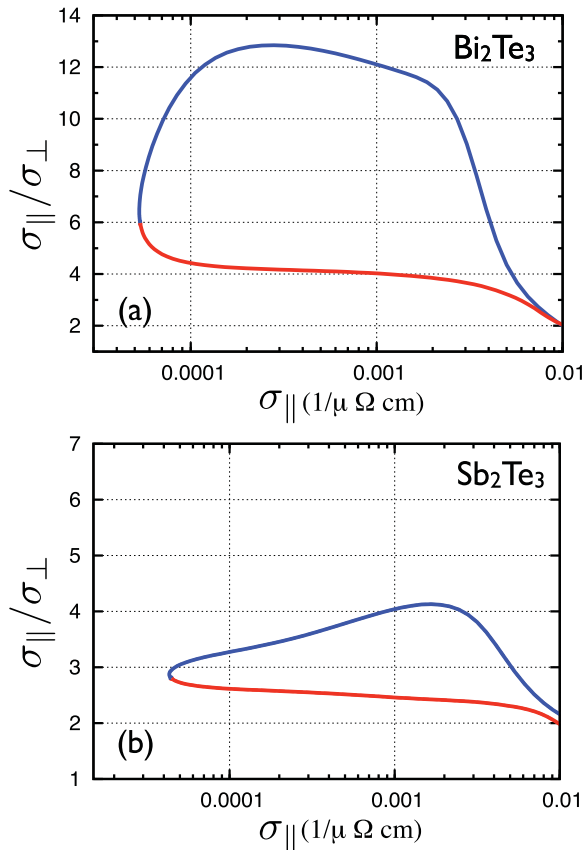


FIG. 4. (Color online) Conductivity ratio $\sigma_{\parallel}/\sigma_{\perp}$ of the electrical conductivities at 300 K for bulk (a) Bi_2Te_3 in the Sb_2Te_3 structure and (b) Sb_2Te_3 in the Bi_2Te_3 structure. Electron doping refers to blue lines, while red lines refer to hole doping. Isotropic relaxation times of $\tau = 1.1 \times 10^{-14}$ and 1.2×10^{-14} s for σ_{\parallel} and σ_{\perp} are assumed for Bi_2Te_3 and Sb_2Te_3 , respectively.

GaAs-[111] with $a = 3.997$ Å, or by a considerable amount of Sb_2Te_3 in the $\text{Bi}_2\text{Te}_3/\text{Sb}_2\text{Te}_3$ SLs. For tensile in-plane strained Sb_2Te_3 , the impact on the electrical conductivity ratio $\sigma_{\parallel}/\sigma_{\perp}$ is less prominent. As shown in Fig. 4(b), at hole doping, $\sigma_{\parallel}/\sigma_{\perp} \sim 2.5$ is only marginally altered compared to the unstrained case [compare Fig. 3(b)]. Meanwhile $\sigma_{\parallel}/\sigma_{\perp}$ decreases noticeably for *n*-type doping yielding about three at low σ_{\parallel} and low electron charge carrier concentrations, and slightly higher values of $\sigma_{\parallel}/\sigma_{\perp} \sim 4$ for higher doping. Overall, the tensile strain reduces the electrical conductivity anisotropy by a factor of about 1.5, directly leading to an enhanced electrical conductivity along the *z* axis of single-crystal Sb_2Te_3 . We note that tensile in-plane strain opens the gap remarkably by around 56% compared to the unstrained case to a value of $E_g = 140$ meV. Furthermore, such tensile strain could be incorporated by using either a substrate with larger in-plane lattice constant, e.g., PbTe-[111] with $a = 4.567$ Å, or a higher fractional amount of Bi_2Te_3 in $\text{Bi}_2\text{Te}_3/\text{Sb}_2\text{Te}_3$ SLs.

In Fig. 5(a) and 5(d) [5(b) and 5(c)], the doping-dependent anisotropic thermopower of unstrained (strained) Bi_2Te_3 and Sb_2Te_3 at room temperature are shown, respectively. Blue thick (red thin) solid lines represent the in-plane thermopower S_{\parallel} under electron doping (hole doping). The corresponding cross-plane thermopower S_{\perp} is shown as a dashed line. The black dashed-dotted lines in Fig. 5(d) emphasize the expected doping-dependent behavior of the thermopower for parabolic bands, following the Pisarenko relation.⁵² For both tellurides, we found that the anisotropy of the thermopower shows a weak dependence on the strain state. However, for strained Bi_2Te_3 [see Fig. 5(b)], the thermopower anisotropy under hole doping almost vanishes, leading to $S_{\parallel} \sim S_{\perp}$. It is worth noting that the anisotropy of the thermopower is less pronounced for hole doping, than for electron doping for Bi_2Te_3 and Sb_2Te_3 in both strain states. As shown by the black dashed-dotted lines in Fig. 5(d), the dependence of the thermopower on the charge carrier concentration differs from the Pisarenko relation⁵² under sufficient high electron doping. This indicates that the nonparabolicity of the energy bands has a noticeable impact in the investigated doping regime and should not be omitted by applying parabolic band models.

Actually, changes for the absolute values of the thermopower can be found for both telluride systems under applied strain. In Fig. 6, the relative change for the in-plane component S_{\parallel} for both tellurides under in-plane strain is given. To compare the changes with the lattice constant, we relate the in-plane thermopower S_{\parallel} at the smaller lattice constant a_{SbTe} to the value at the larger lattice constant a_{BiTe} for both compounds. The doping was fixed to $N = 1 \times 10^{19}$ cm⁻³ for Bi_2Te_3 and $N = 1 \times 10^{20}$ cm⁻³ for Sb_2Te_3 as done for Fig. 2. Figure 6(a) shows that in the relevant temperature range between 350 and 450 K, the thermopower increases for Bi_2Te_3 under compressive strain for both *p* and *n* doping by about 15–20%. For Sb_2Te_3 , a decrease is expected under tensile strain at electron doping and nearly no change under hole doping [see Fig. 6(b)]. With nearly all values above one for Bi_2Te_3 as well as for Sb_2Te_3 it is obvious that higher values of the thermopower require a smaller unit cell volume. One can expect that the volume decrease causes a larger density of states and thus a shift of the chemical potential toward the corresponding band edge, connected with an increase of the thermopower S .

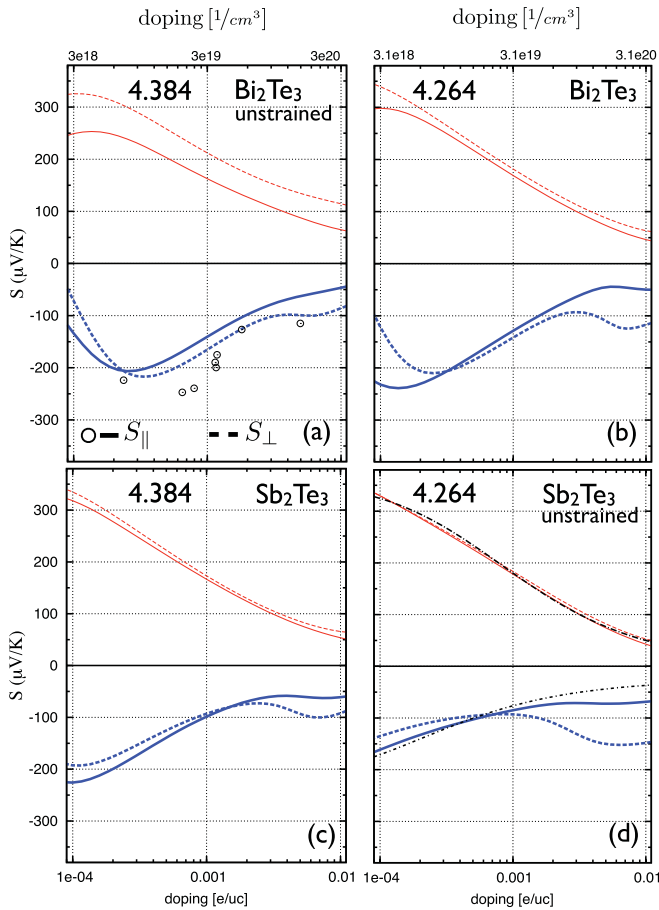


FIG. 5. (Color online) In-plane (solid lines) and cross-plane (dashed lines) doping-dependent thermopower at 300 K for (a) Bi_2Te_3 in the Bi_2Te_3 , (b) Bi_2Te_3 in the Sb_2Te_3 , (c) Sb_2Te_3 in the Bi_2Te_3 , and (d) Sb_2Te_3 in the Sb_2Te_3 structures. Electron (hole) doping is presented as blue thick (red thin) line. The black (dashed-dotted) line in panel (d) shows the Pisarenko dependence of the thermopower expected for parabolic bands. Experimental data (circles) from Ref. 51 are given for comparison. The charge carrier concentration is stated in units of electron per unit cell (e/uc) ($1/\text{cm}^3$) at the bottom (top) x axis.

However, Park *et al.*¹⁴ reported an unexpected increase of 16% for the in-plane thermopower S_{\parallel} of Sb_2Te_3 under p doping ($T = 300$ K and $N = 1.32 \times 10^{19} \text{ cm}^{-3}$) if the material is strained into the Bi_2Te_3 structure. In the same doping and temperature regime, we find a slight decrease of 4% for S_{\parallel} .

Comprising the statements on the electrical conductivity and the thermopower, the related power factor for both tellurides in their bulk lattice and in the strained state are compared in Fig. 7. It is well known that optimizing the power factor σS^2 of a thermoelectric always involves a compromise on the electrical conductivity σ and the thermopower S .⁵³ Due to the interdependence of σ and S , it is not advisable to optimize the power factor by optimizing its parts.

In Figs. 7(a) and 7(d), the doping-dependent anisotropic power factor of unstrained Bi_2Te_3 and Sb_2Te_3 at room temperature is shown, respectively. Blue thick (red thin) solid lines represent the in-plane power factor PF_{\parallel} under electron doping (hole doping). The corresponding cross-plane power factor PF_{\perp} is shown as a dashed line. Under p

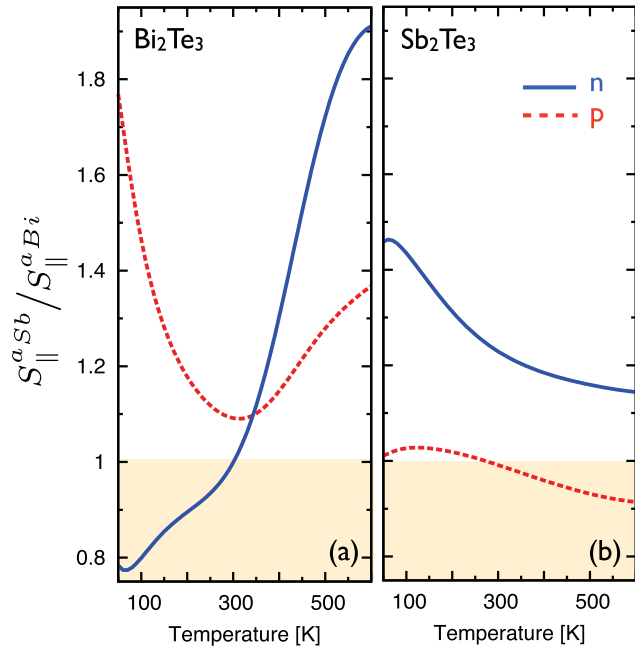


FIG. 6. (Color online) Change of the in-plane thermopower S_{\parallel} under applied strain for (a) Bi_2Te_3 and (b) Sb_2Te_3 . Given is the ratio of S_{\parallel} in the “smaller” lattice of Sb_2Te_3 divided by S_{\parallel} in the “larger” lattice of Bi_2Te_3 . The doping was fixed to $N = 1 \times 10^{19} \text{ cm}^{-3}$ for Bi_2Te_3 and $N = 1 \times 10^{20} \text{ cm}^{-3}$ for Sb_2Te_3 . Solid blue (dashed red) lines refer to electron (hole) doping, respectively.

doping, both unstrained materials show a maximum power factor near carrier concentrations of $N \sim 4 \times 10^{19} \text{ cm}^{-3}$. Absolute values of 35 and $33 \mu\text{W}/\text{cm K}^2$ were found for unstrained Bi_2Te_3 and Sb_2Te_3 , respectively, which is in good agreement with experimental and theoretical findings.^{9,14,51} Under electron doping, the absolute values of PF_{\parallel} (thick blue lines in Fig. 7) were found to be distinctly smaller. This is due to smaller absolute values of the thermopower for electron doping compared to hole doping (see Fig. 2) and apparently smaller in-plane electrical conductivities σ_{\parallel} at fixed carrier concentrations. As a result, a power factor of 18 and $8 \mu\text{W}/\text{cm K}^2$ can be stated for unstrained Bi_2Te_3 and Sb_2Te_3 , respectively, under optimal electron doping. We notice that the power factor for unstrained Sb_2Te_3 is monotonically increasing for electron carrier concentrations of $N \sim 6\text{--}30 \times 10^{19} \text{ cm}^{-3}$. This behavior can be linked to a deviation of S_{\parallel} from the Pisarenko relation under electron doping. While it is expected that the thermopower will decrease for increasing carrier concentration, S_{\parallel} was found to be almost constant in an electron doping range of $N \sim 6\text{--}30 \times 10^{19} \text{ cm}^{-3}$ [see Fig. 5(d)]. For the investigated electron doping range of $N \sim 6\text{--}30 \times 10^{19} \text{ cm}^{-3}$, the chemical potential μ at 300 K is located around 300–450 meV above the VBM. As can be seen from the band structure for unstrained Sb_2Te_3 in Fig. 1(b) (black, solid lines), flat nonparabolic bands near the high-symmetry point Z dominate in this energy region and most likely lead to an increased thermopower. This feature is more pronounced for unstrained Sb_2Te_3 than for strained Sb_2Te_3 [red, dashed lines in Fig. 1(b)]. Similar statements can be done for strained and unstrained Bi_2Te_3 [see Fig. 1(a)]. We note, even though this picture is convincing, that it is

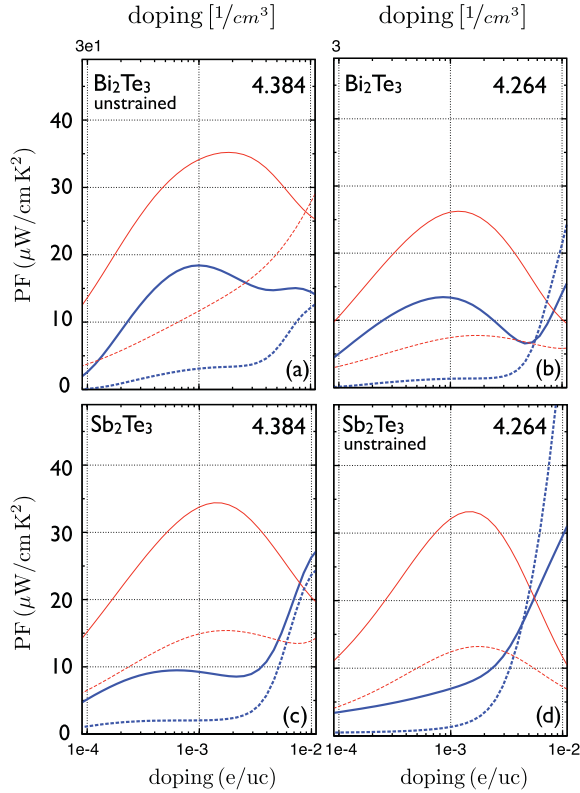


FIG. 7. (Color online) In-plane (solid lines) and cross-plane (dashed lines) doping-dependent power factor at 300 K for (a) Bi_2Te_3 in the Bi_2Te_3 , (b) Bi_2Te_3 in the Sb_2Te_3 , (c) Sb_2Te_3 in the Bi_2Te_3 , and (d) Sb_2Te_3 in the Sb_2Te_3 structures. Electron (hole) doping is presented as blue thick (red thin) line. The charge carrier concentration is stated in units of electron per unit cell (e/uc) ($1/\text{cm}^3$) at the bottom (top) x axis.

difficult to link such specific anomalies to the band structure on high-symmetry lines, as the underlying TDF is an integral quantity over all occupied states in the BZ.

Under applied in-plane compressive strain for Bi_2Te_3 [see Fig. 7(b)] and tensile strain for Sb_2Te_3 [see Fig. 7(c)] the obtained changes in the power factor are noticeably different for both tellurides. While for Bi_2Te_3 a decrease of the maximal power factor PF_{\parallel} of about 27% and 23% for n and p doping, respectively, was found, the strain shows nearly no influence on the power factor for Sb_2Te_3 . At a carrier concentration of about $N \sim 3 \times 10^{19} \text{ cm}^{-3}$, the decrease in PF_{\parallel} for Bi_2Te_3 is about 17% and 28% for n and p doping, respectively, while in the work of Park *et al.*,¹⁴ a slight increase of PF_{\parallel} under strain and hole doping is reported. Obviously, this tendency has to be understood by analyzing the constituent parts σ_{\parallel} and S_{\parallel} . For compressively strained Bi_2Te_3 , at a hole carrier concentration of about $N \sim 3 \times 10^{19} \text{ cm}^{-3}$, the electrical conductivity decreases by about 39% to $330 (\Omega \text{ cm s})^{-1}$. At the same time, S_{\parallel} increases by about 9%, as shown in Fig. 6(a). This results in the overall decrease of about 28% for PF_{\parallel} . Under electron doping of $N \sim 3 \times 10^{19} \text{ cm}^{-3}$, no influence of strain could be found for S_{\parallel} at room temperature [see solid blue lines in Fig. 6(a)]. Thus the decrease of PF_{\parallel} under electron doping can be largely related to a decrease of the electrical conductivity under applied compressive strain. By detailed evaluation of

the effective mass eigenvalues and eigenvectors, we found a decrease of about 15% for the in-plane electrical conductivity of Bi_2Te_3 under applied strain in the low-temperature and low-doping limit.^{22,37} The discussion can be made in the same manner for Sb_2Te_3 .^{22,37} The fact that strain-induced effects in σ and S tend to compensate each other was already reported for the case of silicon.²⁵

As mentioned before (summarized in Figs. 3 and 4), we found a strong anisotropy in the electrical conductivity with $\sigma_{\parallel}/\sigma_{\perp} \gg 1$. The clearly preferred in-plane transport in both bulk tellurides is also reflected in the cross-plane power factor PF_{\perp} (dashed lines in Fig. 7), which is clearly suppressed for all strain states. It is obvious that PF_{\perp} is more suppressed for electron than for hole doping.

Nonetheless, we want to include experimental findings for the thermal conductivity to our calculations, to give an estimation for the figure of merit ZT in plane and cross plane. In Ref. 49, $\kappa_{\parallel} = 2.2 \text{ W/m K}$, $\kappa_{\perp} = 1.0 \text{ W/m K}$ and $\kappa_{\parallel} = 7.5 \text{ W/m K}$, $\kappa_{\perp} = 1.6 \text{ W/m K}$ for unstrained Bi_2Te_3 and Sb_2Te_3 are given, respectively. With this, we find maximal values for the figure of merit at room temperature and optimal hole doping of $ZT_{\parallel} \sim 0.48$ and $ZT_{\perp} \sim 0.41$ for unstrained Bi_2Te_3 and $ZT_{\parallel} \sim 0.13$ and $ZT_{\perp} \sim 0.23$ for unstrained Sb_2Te_3 . We note that the figure of merit ZT maximizes at slightly lower carrier concentration than the power factor σS^2 shown in Fig. 7. This can be linked directly to an increasing electronic part of the thermal conductivity κ_{el} with increasing carrier concentration.^{25,53}

V. CONCLUSION

In the present paper, the influence of in-plane strain on the thermoelectric transport properties of Bi_2Te_3 and Sb_2Te_3 is investigated. A focused view on the influence of strain on the anisotropy of the electrical conductivity σ , thermopower S , and the related power factor σS^2 could help to understand in-plane and cross-plane thermoelectric transport in nanostructured $\text{Bi}_2\text{Te}_3/\text{Sb}_2\text{Te}_3$ superlattices. Based on detailed *ab initio* calculations, we focused mainly on band structure effects and their influence on the thermoelectric transport. For both tellurides, no reasonable decrease of the anisotropy for σ and S could be found under strain, while, in principle, the anisotropy for σ and S is more pronounced under electron doping than at hole doping. Thus a favored thermoelectric transport along the z direction of $\text{Bi}_2\text{Te}_3/\text{Sb}_2\text{Te}_3$ heterostructures due to superlattice-induced in-plane strain effects can be ruled out and a clear preference of p -type thermoelectric transport can be stated for Bi_2Te_3 , Sb_2Te_3 , and their related epitaxial heterostructures. The absolute value of the in-plane thermopower S_{\parallel} was increased under reduced cell volume, which is in contrast to recent findings by Park *et al.*¹⁴

We found that even if thermopower or electrical conductivity are enhanced or decreased via applied strain, they tend to compensate each other suppressing more distinct changes of the power factor under strain. We found the thermoelectrically optimal doping to be in the range of $N \sim 3\text{--}6 \times 10^{19} \text{ cm}^{-3}$ for all considered systems. Our assumption of an anisotropic relaxation time for Bi_2Te_3 , states that already in the single crystalline system, strong anisotropic scattering effects should play a role.

ACKNOWLEDGMENTS

This work was supported by the Deutsche Forschungsgemeinschaft, SPP 1386 “Nanostrukturierte Thermoelektrika:

Theorie, Modellsysteme und kontrollierte Synthese.” N. F. Hinsche is member of the International Max Planck Research School for Science and Technology of Nanostructures.

- *nicki.hinsche@physik.uni-halle.de
- ¹B. Sales, *Science* **295**, 1248 (2002).
- ²A. Majumdar, *Science* **303**, 777 (2004).
- ³H. Böttner, G. Chen, and R. Venkatasubramanian, *MRS Bull.* **31**, 211 (2006).
- ⁴H. Goldsmid, A. Sheard, and D. Wright, *Br. J. Appl. Phys.* **9**, 365 (1958).
- ⁵R. Venkatasubramanian, E. Siivola, and T. Colpitts, *Nature (London)* **413**, 597 (2001).
- ⁶R. Venkatasubramanian, T. Colpitts, B. O’Quinn, S. Liu, N. El-Masry, and M. Lamvik, *Appl. Phys. Lett.* **75**, 1104 (1999).
- ⁷R. Venkatasubramanian, *Phys. Rev. B* **61**, 3091 (2000).
- ⁸H. Beyer, J. Nurnus, H. Böttner, A. Lambrecht, E. Wagner, and G. Bauer, *Physica E: Low-dimensional Systems and Nanostructures* **13**, 965 (2002).
- ⁹H. Böttner, J. Nurnus, A. Gavrikov, and G. Kuhner, *J. Microelectromech. Syst.* **13**, 414 (2004).
- ¹⁰J. König, M. Winkler, S. Buller, W. Bensch, U. Schürmann, L. Kienle, and H. Böttner, *J. Electron. Mater.* **40**, 1266 (2011).
- ¹¹C.-N. Liao, C.-Y. Chang, and H.-S. Chu, *J. Appl. Phys.* **107**, 066103 (2010).
- ¹²N. Peranio, O. Eibl, and J. Nurnus, *J. Appl. Phys.* **100**, 114306 (2006).
- ¹³M. N. Touzelbaev, P. Zhou, R. Venkatasubramanian, and K. E. Goodson, *J. Appl. Phys.* **90**, 763 (2001).
- ¹⁴M. S. Park, J.-H. Song, J. E. Medvedeva, M. Kim, I. G. Kim, and A. J. Freeman, *Phys. Rev. B* **81**, 155211 (2010).
- ¹⁵H. Li, D. Bilec, and S. D. Mahanti, *Mat. Res. Soc. Symp. Proc.* **793**, 837 (2004).
- ¹⁶T. Scheidemantel, C. Ambrosch-Draxl, T. Thonhauser, J. V. Badding, and J. Sofo, *Phys. Rev. B* **68**, 125210 (2003).
- ¹⁷T. Thonhauser, T. Scheidemantel, J. O. Sofo, J. Badding, and G. Mahan, *Phys. Rev. B* **68**, 085201 (2003).
- ¹⁸B.-L. Huang and M. Kaviani, *Phys. Rev. B* **77**, 125209 (2008).
- ¹⁹*Landolt-Börnstein New Series, group III/41C* (Springer Verlag, Berlin, 1998).
- ²⁰M. Gradhand, M. Czerner, D. V. Fedorov, P. Zahn, B. Y. Yavorsky, L. Szunyogh, and I. Mertig, *Phys. Rev. B* **80**, 224413 (2009).
- ²¹S. H. Vosko and L. Wilk, *Phys. Rev. B* **22**, 3812 (1980).
- ²²P. Zahn, N. F. Hinsche, B. Y. Yavorsky, and I. Mertig, e-print [arXiv:1108.0023](https://arxiv.org/abs/1108.0023) (unpublished).
- ²³I. Mertig, *Rep. Prog. Phys.* **62**, 237 (1999).
- ²⁴P. Zahn, I. Mertig, M. Richter, and H. Eschrig, *Phys. Rev. Lett.* **75**, 2996 (1995).
- ²⁵N. F. Hinsche, I. Mertig, and P. Zahn, *J. Phys. Condens. Matter* **23**, 295502 (2011).
- ²⁶T. Vojta, I. Mertig, and R. Zeller, *Phys. Rev. B* **46**, 15761 (1992).
- ²⁷J. Yang, H. Li, T. Wu, and W. Zhang, *Adv. Funct. Mater.* **18**, 2880 (2008).
- ²⁸J. Barth, G. H. Fecher, B. Balke, S. Ouardi, T. Graf, C. Felser, A. Shkablo, A. Weidenkaff, P. Klaer, and H. Elmers, *Phys. Rev. B* **81**, 064404 (2010).
- ²⁹D. J. Singh, *Phys. Rev. B* **81**, 195217 (2010).
- ³⁰D. Parker and D. J. Singh, *Phys. Rev. B* **82**, 035204 (2010).
- ³¹A. F. May, D. J. Singh, and G. J. Snyder, *Phys. Rev. B* **79**, 153101 (2009).
- ³²M.-S. Lee, F. Poudeu, and S. D. Mahanti, *Phys. Rev. B* **83**, 085204 (2011).
- ³³S. Lee and P. von Allmen, *Appl. Phys. Lett.* **88**, 022107 (2006).
- ³⁴M. Situmorang and H. Goldsmid, *Phys. Status Solidi B* **134**, K83 (1986).
- ³⁵T. Thonhauser, *Solid State Commun.* **129**, 249 (2004).
- ³⁶G. Mahan and J. Sofo, *Proc. Natl. Acad. Sci. USA* **93**, 7436 (1996).
- ³⁷B. Y. Yavorsky, N. F. Hinsche, I. Mertig, and P. Zahn, e-print [arXiv:1109.0186](https://arxiv.org/abs/1109.0186) (unpublished).
- ³⁸D. M. Rowe, *CRC Handbook of Thermoelectrics* (CRC, London, 1995).
- ³⁹R. Delves, A. Bowley, and D. Hazelden, *Proceedings of the Phys. Society* **78**, 838 (1961).
- ⁴⁰H. Jeon, H. Ha, D. Hyun, and J. Shim, *J. Phys. Chem. Solids* **52**, 579 (1991).
- ⁴¹H. Kaibe, *J. Phys. Chem. Solids* **50**, 945 (1989).
- ⁴²M. Stordeur and W. Kühnberger, *Phys. Status Solidi B* **69**, 377 (1975).
- ⁴³M. Stordeur and W. Heiliger, *Phys. Status Solidi B* **78**, K103 (1976).
- ⁴⁴M. Zhitinskaya, V. Kaidanov, and V. Kondratev, *Sov. Phys. Semicond.* **10**, 1300 (1976).
- ⁴⁵E. Müller, *Bandstruktur und Ladungsträgerstreuung in p-leitenden (Bi_{1-x}Sb_x)₂Te₃-Mischkristallen* (VDI Verlag, Düsseldorf, 1998).
- ⁴⁶M. Cutler and N. Mott, *Phys. Rev.* **181**, 1336 (1969).
- ⁴⁷G. Simon and W. Eichler, *Phys. Status Solidi B* **103**, 289 (1981).
- ⁴⁸H. Langhammer, M. Stordeur, H. Sobotta, and V. Riede, *Phys. Status Solidi B* **109**, 673 (1982).
- ⁴⁹A. Jacquot, N. Farag, M. Jaegle, M. Bobeth, J. Schmidt, D. Ebling, and H. Böttner, *J. Electron. Mater.* **39**, 1861 (2010).
- ⁵⁰S. Cho, Y. Kim, A. Divenere, G. K. Wong, J. B. Ketterson, and J. R. Meyer, *Appl. Phys. Lett.* **75**, 1401 (1999).
- ⁵¹J. Nurnus, Ph.D. thesis, Albert-Ludwigs-Universität Freiburg, 2001.
- ⁵²A. F. Ioffe, *Physics of Semiconductors* (Academic, New York, 1960).
- ⁵³G. J. Snyder and E. Toberer, *Nat. Mater.* **7**, 105 (2008).

Thermoelectric transport in Bi₂Te₃/Sb₂Te₃ superlattices

N. F. Hinsche,^{1,*} B. Yu. Yavorsky,² M. Gradhand,³ M. Czerner,⁴ M. Winkler,⁵ J. König,⁵ H. Böttner,⁵ I. Mertig,^{1,6} and P. Zahn^{1,7}

¹Institut für Physik, Martin-Luther-Universität Halle-Wittenberg, DE-06099 Halle, Germany

²Forschungszentrum Karlsruhe, Herrmann-von-Helmholtz-Platz 1, 76344 Eggenstein-Leopoldshafen, Germany

³H. H. Wills Physics Laboratory, University of Bristol, Bristol BS8 1TH, United Kingdom

⁴I. Physikalisches Institut, Justus-Liebig-Universität Gießen, DE-35392 Gießen, Germany

⁵Fraunhofer Institut für Physikalische Messtechnik, Heidenhofstrasse 8, DE-79110 Freiburg, Germany

⁶Max-Planck-Institut für Mikrostrukturphysik, Weinberg 2, DE-06120 Halle, Germany

⁷Helmholtz-Zentrum Dresden-Rossendorf, P.O. Box 51 01 19, DE-01314 Dresden, Germany

(Received 28 June 2012; published 27 August 2012)

The thermoelectric transport properties of Bi₂Te₃/Sb₂Te₃ superlattices are analyzed by means of first-principles calculations and semiclassical Boltzmann theory. The anisotropy of the thermoelectric transport under electron and hole doping was studied in detail for different superlattice periods at changing temperature and charge carrier concentrations. A clear preference for thermoelectric transport under hole doping, as well as for the in-plane transport direction was found for all superlattice periods. At hole doping the electrical transport anisotropies remain bulklike for all investigated systems, while under electron doping quantum confinement leads to strong suppression of the cross-plane thermoelectric transport at several superlattice periods. In addition, insights on the Lorenz function, the electronic contribution to the thermal conductivity, and the resulting figure of merit are given.

DOI: [10.1103/PhysRevB.86.085323](https://doi.org/10.1103/PhysRevB.86.085323)

PACS number(s): 31.15.A–, 71.15.Mb, 72.20.Pa

I. INTRODUCTION

Solid-state thermoelectric (TE) power generation devices possess the desirable nature of being highly reliable, stable, compact, and integrable and have potential applications in waste-heat recovery and outer space explorations. However, while intensively studied in the last decades, poor energy conversion efficiencies below a few percent at room temperature prohibited the success of TE devices as promising alternative energy sources. The conversion performance of a thermoelectric material is quantified by the figure of merit

$$ZT = \frac{\sigma S^2}{\kappa_{\text{el}} + \kappa_{\text{ph}}} T, \quad (1)$$

where σ is the electrical conductivity, S is the thermopower, and κ_{el} and κ_{ph} are the electronic and lattice contribution to the thermal conductivity, respectively. From Eq. (1) it is obvious that a higher ZT is obtained by decreasing the denominator or by increasing the numerator, the latter being called power factor $\text{PF} = \sigma S^2$. While σ , S , κ_{el} , and κ_{ph} can individually be tuned by several orders of magnitude, the interdependence between these properties impedes high values for ZT .^{1,2} Bi₂Te₃, Sb₂Te₃, and their related alloys dominate the field of thermoelectrics with ZT around unity from the 1950s until now.^{3–5}

The idea of thermoelectric superlattices (SL) allows for concepts, which could enable both the suppression of the cross-plane thermal conductivity^{6–8} and the increase of the electronic power factor.⁹ It suggests that cross-plane transport along the direction perpendicular to the artificial interfaces of the SL reduces phonon heat conduction while maintaining or even enhancing the electron transport.¹⁰ In 2001 a break-through experiment by Venkatasubramanian *et al.* reported a record apparent $ZT = 2.4$ for p -type Bi₂Te₃/Sb₂Te₃ and $ZT = 1.4$ for n -type Bi₂Te₃/Bi₂Te_{2.83}Se_{0.17} superlattices,^{8,11,12} although

these values have not yet been reproduced to the best of our knowledge.

With the availability of materials with $ZT \geq 3$ thermoelectric materials could compete with conventional energy conversion methods and new applications could emerge.¹³ Besides thermal conductivities below the alloy limit, the investigations of Venkatasubramanian *et al.*¹² found a strong decrease of the mobility anisotropy and the related electronic thermoelectric properties for the SLs at certain periods. This is counterintuitive since superlattices are anisotropic by definition and even the telluride bulk materials show intrinsic anisotropic structural and electronic properties.^{14–18} While considerable effort was undertaken in experimental research,^{19–26} theoretical investigations on Bi₂Te₃/Sb₂Te₃ SLs are rare. Available theoretical works concentrate on the electronic structure and transport properties of the bulk materials,^{17,27–29} with some of them discussing the influence of strain, which could occur at the SL interfaces.^{18,30,31} To our knowledge, only a single theoretical paper discussed the possible transport across such telluride SL structures. Based on density functional theory, Li *et al.*^{32,33} focused on the calculation of the electronic structure for two distinct Bi₂Te₃/Sb₂Te₃ SLs, stating changes of the mobility anisotropy estimated from effective masses. To extend this work and to clarify the open questions on the reduced mobility anisotropy and the enhanced thermoelectric efficiency, we are going to discuss in this paper the anisotropic thermoelectric electronic transport of seven different Bi₂Te₃/Sb₂Te₃ SLs, including the bulk materials, on the basis of density functional theory and semiclassical transport calculations.

For this purpose the paper is organized as follows. In Sec. II we introduce our first-principle electronic structure calculations based on density functional theory and the semiclassical transport calculations based on the solution of the linearized Boltzmann equation. A brief discussion of the obtained band structures, including the dependence of the band

gap on different SL periods, is shown in Sec. III. With this, we present in Sec. IV the electronic thermoelectric transport properties, that is, electrical conductivity, thermopower, and the related power factor of the $\text{Bi}_2\text{Te}_3/\text{Sb}_2\text{Te}_3$ SLs at different SL periods with a focus on their directional anisotropies. The discussions cover a broad temperature and doping range and will include the bulk materials. Even though only p -type conduction was found in SLs stacked out of pure Bi_2Te_3 and Sb_2Te_3 , n -type conduction will be studied too, as being possible at appropriate extrinsic doping. For the latter case strong quantum confinement effects were found, which will be discussed in detail in Sec. IV B. To estimate possible values for the figure of merit, in Sec. IV C results for the electronic contribution to the thermal conductivity, the Lorenz function, as well as existing experimental results for the lattice part of the thermal conductivity will be presented. Most of the discussions are presented in a comparative manner considering the experimental findings of Ref. 12.

II. METHODOLOGY

For both bismuth and antimony telluride, as well as for the composed heterostructures, we used the experimental lattice parameters and relaxed atomic positions³⁴ as provided for the hexagonal Bi_2Te_3 crystal structure with 15 atomic layers. The layered structure itself is composed out of three formula units, Te_1 -Bi- Te_2 -Bi- Te_1 , often called quintuples. The hexagonal lattice parameters are chosen to be $a_{\text{BiTe}}^{\text{hex}} = 4.384 \text{ \AA}$ and $c_{\text{BiTe}}^{\text{hex}} = 30.487 \text{ \AA}$ for Bi_2Te_3 , Sb_2Te_3 , and the $\text{Bi}_2\text{Te}_3/\text{Sb}_2\text{Te}_3$ SLs, respectively. In fact, the main difference between the lattices of Bi_2Te_3 and Sb_2Te_3 is a decrease of the in-plane lattice constant with an accompanied decrease in cell volume. So, a change between the two lattice constants can be related to either compressive or tensile in-plane strain. Previous studies revealed that a larger in-plane lattice constant, for example, $a_{\text{BiTe}}^{\text{hex}} > a_{\text{SbTe}}^{\text{hex}}$, is favorable for an enhanced cross-plane TE transport.^{18,29,35} For this purpose, the experimental lattice parameters of Bi_2Te_3 were chosen for the studied heterostructures. Structural relaxations revealed only minor influences on the bulk electronic structure²⁹⁻³² and are beyond the scope of this work. To study SLs with different layer periods comparable to the experiments of Venkatasubramanian *et al.*¹² we subsequently substituted the Bi site by Sb, starting with six Bi sites in hexagonal bulk Bi_2Te_3 [see Fig. 1(a)]. For instance, substituting two atomic layers of Bi with Sb leads to a $(\text{Bi}_2\text{Te}_3)_x/(\text{Sb}_2\text{Te}_3)_{1-x}$ SL with $x = 2/3$, that is, two quintuples Bi_2Te_3 and one quintuple Sb_2Te_3 [see Fig. 1(b)]. The latter case coincides with a $(20 \text{ \AA}/10 \text{ \AA})$ - $(\text{Bi}_2\text{Te}_3/\text{Sb}_2\text{Te}_3)$ superlattice in the experimental notation of Ref. 12.

Our thermoelectric transport calculations are performed in two steps. In a first step, the detailed electronic structure of the $\text{Bi}_2\text{Te}_3/\text{Sb}_2\text{Te}_3$ SLs were obtained by first-principles density functional theory calculations (DFT), as implemented in the fully relativistic screened Korringa-Kohn-Rostoker Greens-function method (KKR).³⁶ Within this approach the Dirac equation is solved self-consistently and with that spin-orbit-coupling (SOC) is included. Exchange and correlation effects were described within the local density approximation (LDA) parametrized by Vosco *et al.*³⁷ Detailed studies on

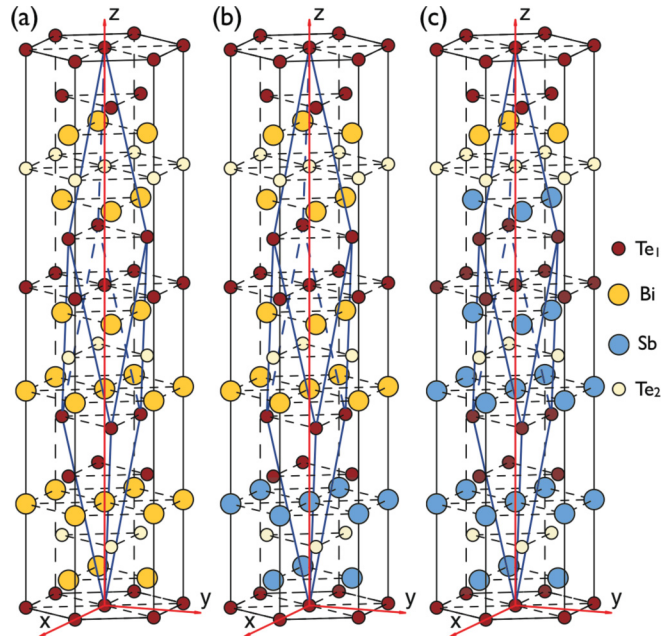


FIG. 1. (Color online) Shown are three possible hexagonal unit cells of the $(\text{Bi}_2\text{Te}_3)_x/(\text{Sb}_2\text{Te}_3)_{1-x}$ superlattices. (a) $x = 1$ which is bulk Bi_2Te_3 , (b) $x = 2/3$, and (c) $x = 1/6$. A concentration of $x = 0$ would coincide with bulk Sb_2Te_3 in the lattice of Bi_2Te_3 .

the electronic structure and transport anisotropy of the bulk tellurides Bi_2Te_3 and Sb_2Te_3 were published before^{18,35} and show very good agreement with experimental results and other theoretical findings.

With the well-converged results from the first step we obtain the thermoelectric transport properties by solving the linearized Boltzmann equation in relaxation time approximation (RTA) within an in-house developed Boltzmann transport code.^{38,39} Boltzmann transport calculations for thermoelectrics have been carried out for quite a long time and show reliable results for wide- and narrow-gap semiconductors.³⁹⁻⁴³ Calculations on the electronic structure and TE transport for bulk Bi_2Te_3 ^{17,31,44,45} and Sb_2Te_3 ^{28,31,46} were presented before. Here the relaxation time τ is assumed to be isotropic and constant with respect to wave vector \mathbf{k} and energy on the scale of $k_B T$. This assumption is widely accepted for degenerately doped semiconductors. Within the RTA, from comparison of the calculated electrical and electronic thermal conductivities [Eqs. (3) and (4)] with experiment, it is possible to conclude on the absolute relaxation time and a possible directional anisotropy of τ . We emphasized that electron-impurity scattering effects could lead to such anisotropic relaxation times at least for bulk Bi_2Te_3 .¹⁸ Previously, anisotropic relaxation times were experimentally stated for both n - and p -doped Bi_2Te_3 at small carrier concentrations and low temperatures from galvanomagnetic and de Haas-van Alphen measurements.⁴⁷ However, to focus on band structure effects and exclude scattering anisotropies τ is set to 10 fs for all bulk and heterostructure systems. The optimized τ is only slightly apart, stating 11 and 12 fs for bulk Bi_2Te_3 and Sb_2Te_3 , respectively.¹⁸ An energy dependence of the relaxation time was found to be neglectable for charge carrier concentrations of $N \sim 5\text{--}500 \times 10^{18} \text{ cm}^{-3}$.

Within the RTA the TDF $\mathcal{L}_{\perp,\parallel}^{(0)}(\mu,0)$ ⁴⁸ and with this the generalized conductance moments $\mathcal{L}_{\perp,\parallel}^{(n)}(\mu,T)$ are defined as

$$\mathcal{L}_{\perp,\parallel}^{(n)}(\mu,T) = \frac{\tau}{(2\pi)^3} \sum_{\nu} \int d^3k (v_{k,(\perp,\parallel)}^{\nu})^2 \times (E_k^{\nu} - \mu)^n \left[-\frac{\partial f(\mu,T)}{\partial E} \right]_{E=E_k^{\nu}}. \quad (2)$$

E_k^{ν} denotes the band structure of band ν , v_k^{ν} is the group velocity, and $f(\mu,T)$ is the Fermi-Dirac distribution. $v_{k,(\parallel)}$, $v_{k,(\perp)}$ denote the group velocities in the directions in the hexagonal basal plane and perpendicular to it, respectively. Within here the group velocities were obtained as derivatives along the lines of the Blöchl mesh in the whole Brillouin zone (BZ).³⁵ The directions of these lines are parallel to the reciprocal space vectors and so the anisotropy of the real lattice is reflected in these vectors. A detailed analysis of the numerical accuracy of the group velocities in highly anisotropic materials was published elsewhere.⁴⁹ The temperature- and doping-dependent electrical conductivity σ and thermopower S in the in- and cross-plane directions are defined as

$$\sigma_{\perp,\parallel} = e^2 \mathcal{L}_{\perp,\parallel}^{(0)}(\mu,T), \quad S_{\perp,\parallel} = \frac{1}{eT} \frac{\mathcal{L}_{\perp,\parallel}^{(1)}(\mu,T)}{\mathcal{L}_{\perp,\parallel}^{(0)}(\mu,T)} \quad (3)$$

and the electronic part to the total thermal conductivity can be written as

$$\kappa_{el\perp,\parallel} = \frac{1}{T} \left\{ \mathcal{L}_{\perp,\parallel}^{(2)}(\mu,T) - \frac{[\mathcal{L}_{\perp,\parallel}^{(1)}(\mu,T)]^2}{\mathcal{L}_{\perp,\parallel}^{(0)}(\mu,T)} \right\}. \quad (4)$$

The second term in Eq. (4) introduces corrections due to the Peltier heat flow that can occur when bipolar conduction takes place.⁵⁰

The chemical potential μ at temperature T and extrinsic carrier concentration N is determined by an integration over the density of states (DOS) $n(E)$,

$$N = \int_{-\infty}^{\text{VBM}} dE n(E)[f(\mu,T) - 1] + \int_{\text{CBM}}^{\infty} dE n(E)f(\mu,T), \quad (5)$$

where CBM is the conduction band minimum and VBM is the valence band maximum. The k -space integration of Eq. (2) for a system with an intrinsic anisotropic texture, for example, in rhombohedral and hexagonal structures, is quite challenging. In previous publications we have highlighted the importance of using adaptive integration methods to converge the energy dependent TDF.^{35,49} Especially in regions close to the band edges, which are important for transport, the anisotropy of the TDF requires a high density of the k mesh. Here, convergence tests for the transport properties showed that at least 150 000 k points in the entire BZ had to be included for sufficiently high doping rates ($N \geq 1 \times 10^{19} \text{ cm}^{-3}$), while for energies near the band edges even more than 56 million k points were required to reach the analytical effective mass values and the corresponding conductivity anisotropies at the band edges.

III. ELECTRONIC STRUCTURE

In Figs. 2(a)–2(g) the electronic band structures on the hexagonal high symmetry lines for all $(\text{Bi}_2\text{Te}_3)_x/(\text{Sb}_2\text{Te}_3)_{1-x}$ SLs are shown, starting with (a) $x = 0$ which is tensile strained bulk Sb_2Te_3 and ending at (g) $x = 1$, which is bulk Bi_2Te_3 . For the case of (b) $x = 1/6$, (d) $x = 1/2$, and (f) $x = 5/6$ a further band splitting is found. The band degeneracy is lifted because of missing space inversion symmetry. This situation occurs if the Bi(Sb) sites in each quintuple are not uniformly occupied.

For increasing number of Bi layers in the SLs no drastic change in the band structure topology was obtained. Only slight variations were found for the in-plane band directions. Stronger impact can be expected from the change of band dispersion which occurs for the lowest-lying conduction band in the cross-plane direction ΓA . Here a continuous change of the bands slope is found for increasing amount of Bi layers in the SL. An almost vanishing dispersion and very flat bands in cross-plane direction are found for the SL with $x = 0.5$, which is three Bi-like layers and three Sb-like layers. Further amount of Bi layers in the system leads to an increase in the bands slope, while showing different signs compared to bulk Sb_2Te_3 .

In Fig. 2(h) the calculated band gap in dependence on the superlattice period is shown. Applying an extended tetrahedron method^{52,53} and very dense k meshes in the BZ, the band gap values were determined within an uncertainty below 1%. While for Sb_2Te_3 at the experimental lattice parameters, we previously found a direct band gap located at the center of the BZ,³⁵ an indirect gap of $E_g = 140 \text{ meV}$ can be stated for the in-plane tensile strained Sb_2Te_3 . For Bi_2Te_3 as well as for all $\text{Bi}_2\text{Te}_3/\text{Sb}_2\text{Te}_3$ SLs indirect band gaps are obtained, too. A known difficulty within standard DFT is the general underestimation of the semiconductors band gaps at zero temperature,⁵⁴ as well as the missing temperature dependence of $E_g(T)$.⁵⁵ For small band gap thermoelectrics, such as Bi_2Te_3 and Sb_2Te_3 , this could affect the TE transport. The thermopower might be reduced at high temperature and low doping due to bipolar conduction.^{17,40} This effect would be overestimated if the band gap is underestimated. With $E_g(T)$ being considered for TE bulk materials^{17,39} lack of knowledge on the absolute size of the gap, as well as its temperature dependence, permits such gap corrections for the strained bulk materials as well as for the SLs. However, the calculated bulk band gap of $E_g = 105 \text{ meV}$ for unstrained bulk Bi_2Te_3 is in better agreement with the experimental value of $E_g = 130 \text{ meV}$,⁵¹ than for unstrained Sb_2Te_3 where a calculated value of $E_g = 90 \text{ meV}$ faces experimental values between $E_g = 150\text{--}230 \text{ meV}$.^{51,56}

As is well known, Bi_2Te_3 and Sb_2Te_3 exhibit band inversion at certain areas in the BZ.⁵⁷ Within LDA the strength of band inversion is most likely underestimated.⁵⁸ At a given band inversion the strength of the spin-orbit interaction then controls the size of the band gap. Fortunately, overestimated SOC effects and underestimated band inversion tend to cancel each other leading to good results for the band gap size and wave function character. The band gaps used for the following thermoelectric transport calculations are summarized in Fig. 2(h). The band gap difference between

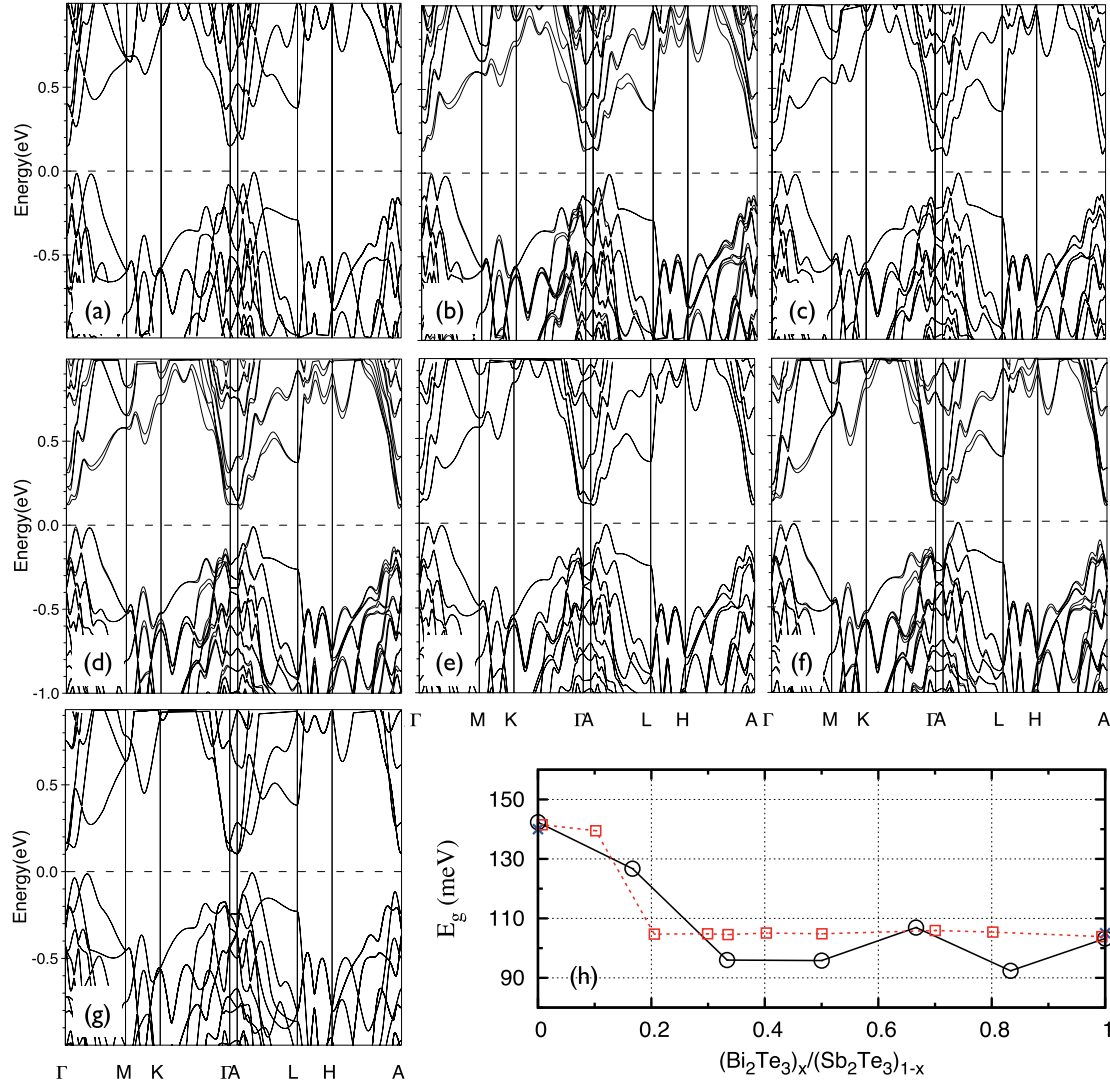


FIG. 2. (Color online) Electronic band structures for $(\text{Bi}_2\text{Te}_3)_x/(\text{Sb}_2\text{Te}_3)_{1-x}$ superlattices in the hexagonal unit cell with different superlattice periods. (a) $x = 0$, (b) $x = 1/6$, (c) $x = 1/3$, (d) $x = 1/2$, (e) $x = 2/3$, (f) $x = 5/6$, and (g) $x = 1$. In (h) black circles show the calculated fundamental energy gap in dependence on the superlattice period. Red squares show experimental findings⁵¹ for $(\text{Bi}_2\text{Te}_3)_x/(\text{Sb}_2\text{Te}_3)_{1-x}$ alloys, which were adapted to the bulk values to allow for comparison with our LDA results.

unstrained Bi_2Te_3 and strained Sb_2Te_3 accounts for about 35 meV in very good agreement to the proposed experimental value.¹² This is of particular importance for the discussion of quantum well effects as done in Sec. IV B. An inclusion of temperature-dependent experimental band gaps will only have a minor influence, shifting the maxima of the thermopower, power factor, and resulting ZT (cf. Figs. 6 and 9) to slightly larger values of the temperature.

While our calculated bulk band gaps are in very good agreement with other calculations,^{59–61} data on the SL are rare. We can only compare the $\text{Bi}_2\text{Te}_3/\text{Sb}_2\text{Te}_3$ SL with $x = 1/3$ [see Fig. 2(c)] with previous results of Li *et al.*³² While they applied a full-potential linearized augmented plane wave (FLAPW) method and treated spin-orbit coupling as a second-order perturbation, the results on the bands topology are in good agreement. However, our band gap is substantially larger with

$E_g = 95$ meV neglecting any structural relaxations, compared to their value of $E_g = 27$ meV.

IV. THERMOELECTRIC TRANSPORT

A. Effects of superlattice period composition

The knowledge of the electronic structure enables us to calculate the thermoelectric transport properties of the $\text{Bi}_2\text{Te}_3/\text{Sb}_2\text{Te}_3$ SLs. As a starting point the in-plane transport properties at room temperature for the electron-doped [cf. Figs. 3(a)–3(c)] and hole-doped [cf. Figs. 3(d)–3(f)] heterostructures are chosen, while afterwards the anisotropy referring to the transport in cross-plane direction is discussed in detail. Preliminary studies revealed the optimal charge carrier concentration for the SLs to be in the range of

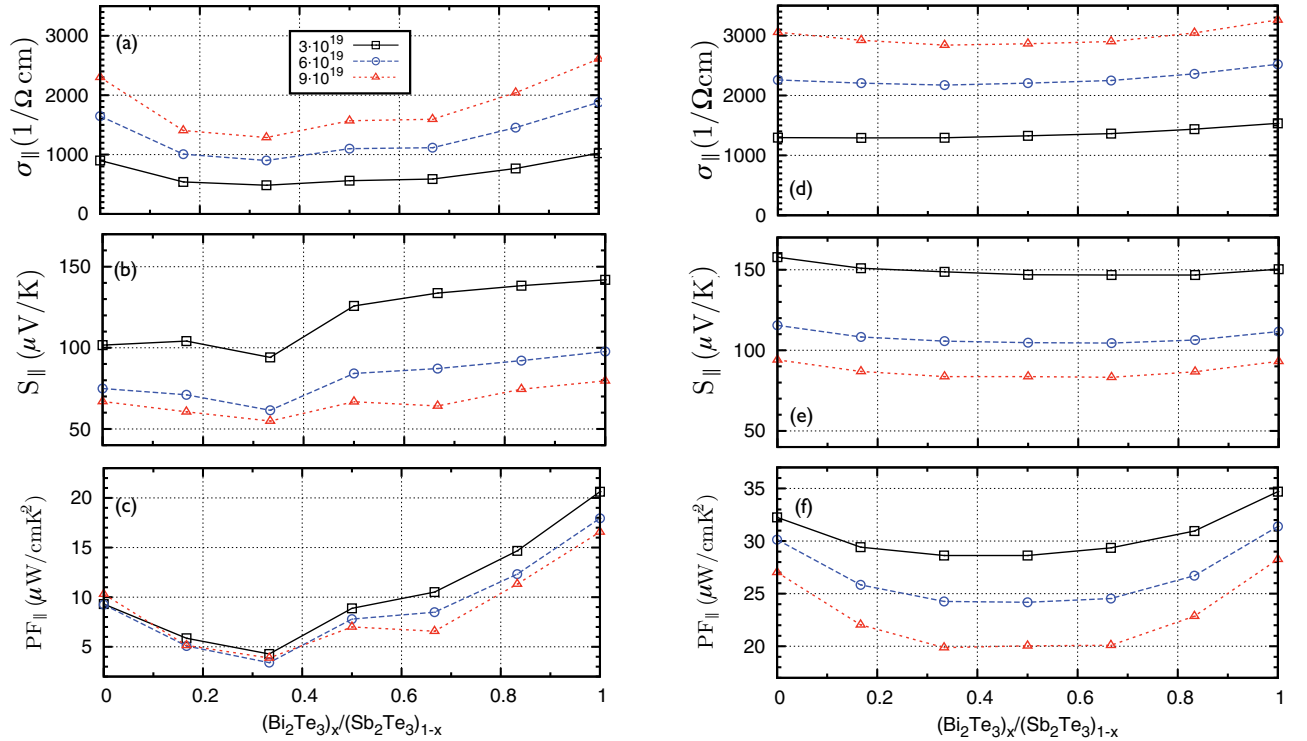


FIG. 3. (Color online) Absolute values of in-plane thermoelectric transport properties for $(\text{Bi}_2\text{Te}_3)_x/(\text{Sb}_2\text{Te}_3)_{1-x}$ superlattices in dependence on the superlattice period. Shown are (a) and (d) electrical conductivity σ_{\parallel} , (b) and (e) thermopower S_{\parallel} , and (c) and (f) power factor PF_{\parallel} . The temperature is fixed to 300 K and results for three different charge carrier concentrations (in units of cm^{-3}) are presented. (a), (b), and (c) refer to electron doping, while (d), (e), and (f) refer to hole doping.

$3\text{--}6 \times 10^{19} \text{ cm}^{-3}$.¹⁸ For the sake of clarity results are presented for three relevant charge carrier concentrations of 3, 6, and $9 \times 10^{19} \text{ cm}^{-3}$ (cf. solid, dashed, and dotted lines in Fig. 3, respectively).

Under electron doping [cf. Fig. 3(a)] a decrease of the in-plane electrical conductivity for the superlattices compared to the bulk materials is found. This decrease is more pronounced at higher charge carrier concentrations, while only slightly depending on the SL period. Assuming a constant relaxation time $\tau = 10 \text{ fs}$, we find very good agreement with experiment^{62,63} for bulk Bi_2Te_3 with $\sigma_{\parallel} = 1030 (\Omega \text{ cm})^{-1}$ at $N = 3 \times 10^{19} \text{ cm}^{-3}$.

The absolute value of the n -type in-plane thermopower is shown in Fig. 3(b). At a carrier concentration of $N = 3 \times 10^{19} \text{ cm}^{-3}$ a higher amount of Bi_2Te_3 in the superlattices leads to a monotone increase of the thermopower from $S_{\parallel} = 103 \mu\text{V/K}$ (bulk Sb_2Te_3) to $S_{\parallel} = 141 \mu\text{V/K}$ (bulk Bi_2Te_3), while showing a dip at a composition of $x = 2/6$ with S_{\parallel} below $100 \mu\text{V/K}$. The latter anomaly is linked to confinement effects and is discussed in detail in Sec. IV B. This overall behavior of S_{\parallel} is retained for higher charge carrier concentrations at reasonable smaller absolute values. Summarizing the previous results, the power factor PF_{\parallel} under relevant electron doping is shown in Fig. 3(c). Clearly the reduction of in-plane electrical conductivity σ_{\parallel} , as well as the dip of S_{\parallel} at a SL period of $x = 2/6$, lead to a minimal power factor of about $4 \mu\text{W/cm K}^2$ at the named SL period. We find PF_{\parallel} for the SLs always below the linear interpolation of the bulk absolute values. Furthermore, due to compensation effects of σ_{\parallel} and S_{\parallel} the dependence

on the amount of doping is less pronounced for PF_{\parallel} than for its constituents. The best power factor was found for bulk Bi_2Te_3 being $\text{PF}_{\parallel} = 21 \mu\text{W/cm K}^2$, while experimentally thin films and single crystals show $\text{PF}_{\parallel} = 8\text{--}27 \mu\text{W/cm K}^2$ and $\text{PF}_{\parallel} = 45 \mu\text{W/cm K}^2$, respectively.^{25,64} We note here that in experiment n -type conduction was only apparent for $\text{Bi}_2\text{Te}_3/\text{Bi}_2\text{Te}_{2.83}\text{Se}_{0.17}$ -SL. Nevertheless, to get more insight into the physical mechanisms in thermoelectric SL transport, n -type transport in $\text{Bi}_2\text{Te}_3/\text{Sb}_2\text{Te}_3$ SLs is of interest as well.

Highest power factors and ZT were experimentally found for p -type $\text{Bi}_2\text{Te}_3/\text{Sb}_2\text{Te}_3$ SLs. The preference of hole conduction is dedicated to the large number of inherent defects introduced by the Sb_2Te_3 layers. In Figs. 3(d)–3(f) the in-plane thermoelectric transport properties under hole doping are displayed in the same manner as done before. Compared to the electron-doped case [cf. Fig. 3(a)] the hole electrical conductivity σ_{\parallel} is higher at the same charge carrier concentration. Furthermore, almost no decrease of σ_{\parallel} could be found for the SLs, which is more pronounced at lower charge carrier concentrations. For the in-plane thermopower the values at different superlattice compositions are again only slightly suppressed compared to the bulk systems. For a $(\text{Bi}_2\text{Te}_3)_x/(\text{Sb}_2\text{Te}_3)_{1-x}$ SL at $x = 3/6$ we state $S_{\parallel} = 149 \mu\text{V/K}$, while $S_{\parallel} = 154 \mu\text{V/K}$ and $S_{\parallel} = 150 \mu\text{V/K}$ were found for bulk Sb_2Te_3 and Bi_2Te_3 at the lowest charge carrier concentration, respectively. This reduction of the thermopower at different superlattice periods is reflected and enhanced for PF_{\parallel} . From Fig. 3(f) it can be seen that the in-plane power factor PF_{\parallel} for the various superlattices is decreased compared to the

TABLE I. Theoretical and experimental in-plane thermoelectric properties of p -type $(\text{Bi}_2\text{Te}_3)_x/(\text{Sb}_2\text{Te}_3)_{1-x}$ SLs at room temperature. The materials composition amounts in all considered systems to about $x = 1/6$. See text for additional details.

N (10^{19} cm^{-3})	σ_{\parallel} ($\Omega \text{ cm}$) $^{-1}$	S_{\parallel} ($\mu\text{V/K}$)	PF_{\parallel} ($\mu\text{W/cm K}^2$)	Ref.
3.0	1300	151	30	this work
3.1	1818	~ 200	~ 72	12,66–68
3.2	761–1160	172–189	27–34	26 ^a
5.8	3050	115	40	69 ^b

^aSputtered $(\text{Bi}_{0.2}\text{Sb}_{0.8})_2\text{Te}_3/\text{Sb}_2\text{Te}_3$ SL.

^b $(\text{Bi}_x\text{Sb}_{1-x})_2\text{Te}_3$ mixed crystal.

bulk materials. The largest reduction ($x = 2/6$ and $x = 3/6$) is found to be about 20% below to the bulk values, but still offers thermoelectrically feasible values of $\text{PF}_{\parallel} = 30 \mu\text{W/cm K}^2$.

To give a reference, in Table I the calculated in-plane thermoelectric properties are compared to experimental results. In the original paper of Venkatasubramanian *et al.*¹² very large values of σ_{\parallel} and S_{\parallel} result in a huge power factor PF_{\parallel} about $72 \mu\text{W/cm K}^2$ at room temperature.⁶⁵ These reported values are way larger than found for bulk or thin film Bi_2Te_3 , Sb_2Te_3 , or their related alloys.²⁵ However, in a more recent study Winkler *et al.*²⁶ reported values for the in-plane electrical conductivity and thermopower of a comparable $(\text{Bi}_{0.2}\text{Sb}_{0.8})_2\text{Te}_3/\text{Sb}_2\text{Te}_3$ sputtered SL (cf. Table I), which are in very good agreement to our theoretical calculations and

combine to an in-plane power factor PF_{\parallel} above $30 \mu\text{W/cm K}^2$. This is similar to values for bulk single crystals with comparable compositions. In contrast to the original experiments,^{12,66} which used low-temperature metal-organic chemical vapor deposition (MOCVD), Winkler *et al.* applied the concept of “nanoalloying.”²¹ Here the elemental layers Bi, Sb, and Te are deposited by sputtering and subsequently annealed to induce interdiffusion and a solid-state reaction to form the SLs. The pronounced periodicity and c orientation of the SLs have been demonstrated by secondary ion mass spectrometry (SIMS) and x-ray diffraction (XRD), respectively.

While up to now we considered only in-plane transport, in the following the cross-plane transport of the superlattices will be discussed. The transport direction is therefore along the SL direction, perpendicular to the hexagonal basal plane of the bulk materials. In detail the directional anisotropy of the transport properties at room temperature are depicted in Figs. 4(a)–4(c) and 4(d)–4(f), for electron and hole doping, respectively. To get the absolute values for cross-plane transport, the in-plane values previously shown in Fig. 3 should be divided by the anisotropies presented hereinafter. Anisotropies larger than unity represent suppressed thermoelectric transport in cross-plane direction and are therefore less desirable. As previously proven by experiment^{14–16,45,62} and theory,^{17,18,27,28} already the bulk thermoelectrics Bi_2Te_3 and Sb_2Te_3 show large anisotropies for the electrical conductivity, thermopower, and the related power factor.

The thermoelectric transport anisotropies under influence of hole doping will be considered first. In Fig. 4(d) the anisotropy

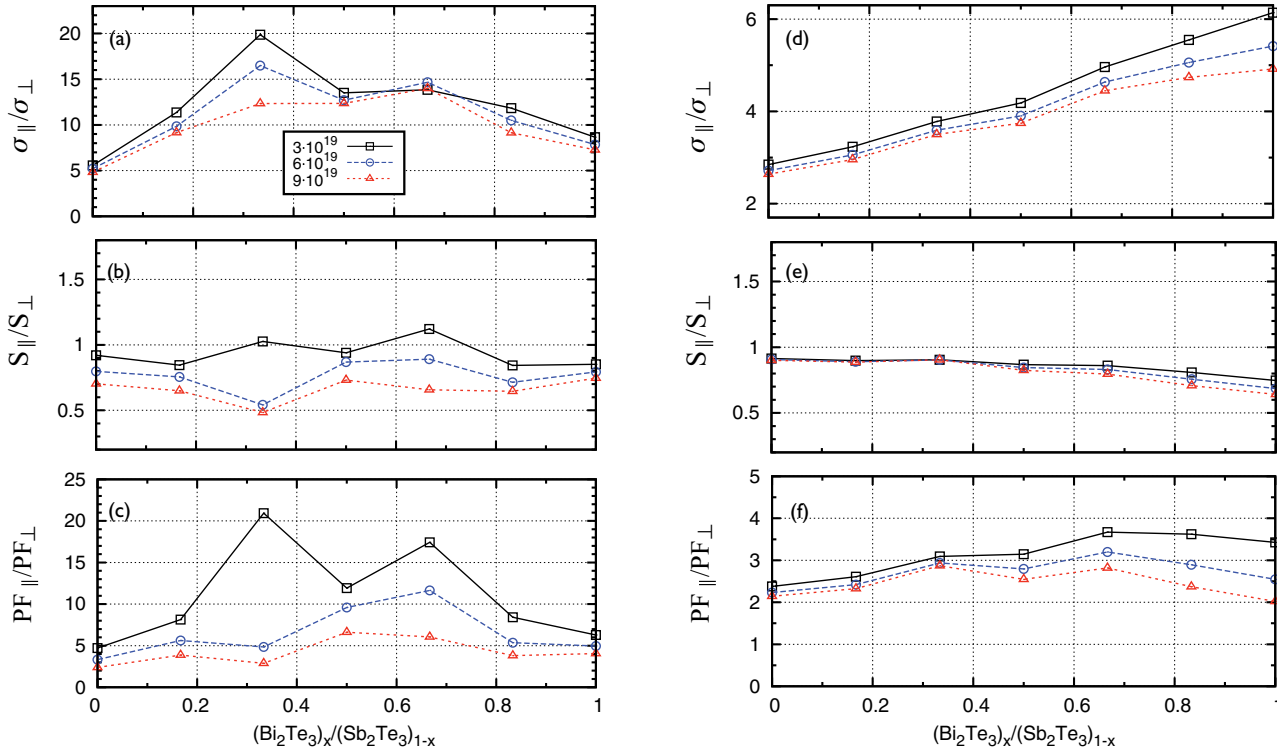


FIG. 4. (Color online) Directional anisotropies of thermoelectric transport properties for $(\text{Bi}_2\text{Te}_3)_x/(\text{Sb}_2\text{Te}_3)_{1-x}$ superlattices in dependence on the superlattice period. Shown are (a) and (d) electrical conductivity ratio $\sigma_{\parallel}/\sigma_{\perp}$, (b) and (e) thermopower ratio S_{\parallel}/S_{\perp} , and (c) and (f) power factor ratio $\text{PF}_{\parallel}/\text{PF}_{\perp}$. The temperature is fixed to 300 K and results for three different charge carrier concentrations (in units of cm^{-3}) are compared. (a), (b), and (c) refer to electron doping, while (d), (e), and (f) refer to hole doping.

ratio of the electrical conductivity for various SL periods is illustrated at a temperature of 300 K. The anisotropy $\sigma_{\parallel}/\sigma_{\perp}$ develops smoothly and monotonously between the bulk limits of $\sigma_{\parallel}/\sigma_{\perp} = 2.7$ and about $\sigma_{\parallel}/\sigma_{\perp} = 5\text{--}6$ for bulk Sb_2Te_3 and Bi_2Te_3 , respectively. With increasing amount of Bi_2Te_3 in the superlattices the dependence of $\sigma_{\parallel}/\sigma_{\perp}$ on the charge carrier concentration is more pronounced. This is in accordance to previous findings for the bulk materials.¹⁸ For the thermopower anisotropy S_{\parallel}/S_{\perp} this picture holds, too. While for Sb_2Te_3 only a slight anisotropy of about $S_{\parallel}/S_{\perp} = 0.9$ is found, the asymmetry increases for increasing amount of Bi in the SLs, saturating at $S_{\parallel}/S_{\perp} = 0.75$ for bulk Bi_2Te_3 , in agreement to earlier investigations on the bulk materials.^{15,16,18,45} The fact of the cross-plane thermopower being enhanced compared to the in-plane part is well known for the two bulk tellurides and compensates the high electrical conductivity anisotropy $\sigma_{\parallel}/\sigma_{\perp}$ to result in a slightly reduced cross-plane power factor.^{18,45} The anisotropy for the latter is shown in Fig. 4(f). Obviously, $\text{PF}_{\parallel}/\text{PF}_{\perp}$ is well above unity for all systems indicating a less preferred cross-plane electronic transport. Compared to the bulk values of $\text{PF}_{\parallel}/\text{PF}_{\perp} = 2.2$ and $\text{PF}_{\parallel}/\text{PF}_{\perp} = 2\text{--}3.5$ for bulk Sb_2Te_3 and Bi_2Te_3 , respectively, the power factor anisotropy is only slightly enhanced for the SLs with different periods. For example, $x = 1/6$, which refers to a $5 \text{ \AA}/25 \text{ \AA}$ $\text{Bi}_2\text{Te}_3/\text{Sb}_2\text{Te}_3$ SL, the cross-plane power flow $\text{PF}_{\parallel}/\text{PF}_{\perp}$ is only suppressed by 13% with respect to bulk Sb_2Te_3 , while being enhanced by 26% compared to bulk Bi_2Te_3 at the optimal charge carrier concentration of $N = 3 \times 10^{19} \text{ cm}^{-3}$. For the thermal conductivity in the SLs a reduction compared to bulk and the related alloys by about a factor of 5 is expected.^{8,12} This would clearly lead to a benefit for the resulting ZT in comparison to bulk, which is discussed in more detail in Sec. IV C. However, we want to mention that in the experiments of Venkatasubramanian *et al.* a further decrease of the electrical conductivity anisotropy was found for thin SLs at various SL periods.¹² It was stated that $\sigma_{\parallel}/\sigma_{\perp}$ under hole doping is about 0.8–1.4 for the $\text{Bi}_2\text{Te}_3/\text{Sb}_2\text{Te}_3$ SLs at different SL periods and therefore electrical cross-plane transport is strongly improved compared to bulk. Our calculations do not confirm this trend.

In Fig. 4(a) the electrical conductivity anisotropy $\sigma_{\parallel}/\sigma_{\perp}$ under electron doping is shown. Bulk Bi_2Te_3 and bulk Sb_2Te_3 show anisotropies around $\sigma_{\parallel}/\sigma_{\perp} = 8$ and $\sigma_{\parallel}/\sigma_{\perp} = 5$, respectively, in good agreement with earlier studies.¹⁸ One easily recognizes the anisotropy ratios being larger than expected from the two bulk limits, while obtaining substantially large values of about $\sigma_{\parallel}/\sigma_{\perp} = 20$ at $N = 3 \times 10^{19} \text{ cm}^{-3}$ for a SL period of $x = 2/6$, that is a $10 \text{ \AA}/20 \text{ \AA}$ $\text{Bi}_2\text{Te}_3/\text{Sb}_2\text{Te}_3$ SL, or one quintuple of Bi_2Te_3 and two quintuples of Sb_2Te_3 . For the considered case the anisotropy strongly depends on the amount of doping, decreasing rapidly with increasing charge carrier concentration and reaching $\sigma_{\parallel}/\sigma_{\perp} \geq 10$ at $N = 9 \times 10^{19} \text{ cm}^{-3}$. At the same time the thermopower anisotropy shows a clear cross-plane preference at $S_{\parallel}/S_{\perp} \approx 0.5$. Nevertheless, the resulting power factor anisotropy shows disappointing high values of about $\text{PF}_{\parallel}/\text{PF}_{\perp} \gg 5$ for the distinct SLs, while even showing $\text{PF}_{\parallel}/\text{PF}_{\perp}$ about 20 for the SL at a composition of $x = 2/6$. The reduced cross-plane thermoelectric transport is clearly related to the large electrical conductivity anisotropies found for the *n*-type $\text{Bi}_2\text{Te}_3/\text{Sb}_2\text{Te}_3$ SLs caused by quantum well effects in the conduction band,

which are evoked by a conduction band offset between Bi_2Te_3 and Sb_2Te_3 in the SLs.

B. Quantum well effects

In the early 1990s concepts were presented to enhance in-plane thermoelectric properties by quantum-confinement effects in SLs.^{70,71} While huge enhancements on the in-plane figure of merit were predicted, the authors neglected electron tunneling and thermal currents between the layers by introducing infinite potential barriers weights at zero widths. Later on it was shown that for realistic barrier heights and widths the enhancement is rather moderate, predicting ZT values that at their best are a few percent larger than corresponding bulk materials.^{72,73}

It is known for the considered tellurides that due to spin-orbit driven band inversion near the Γ point the CBM is related to states localized at the Te atoms, whereas the VBM is formed by Bi or Sb states.^{57,74} Nevertheless, contributions from other areas in the BZ lead to the fact that the valence band conduction contribution is mainly determined by Te states at appropriate charge concentrations. Consequently, a substitution of Bi and Sb in Bi_2Te_3 or Sb_2Te_3 affects the character of the valence band states only marginally and almost bulklike electronic structure and transport properties can be expected in the SLs.

Venkatasubramanian *et al.*¹² argued that in the SLs due to weak confinement and near zero band offset there is minimal anisotropy between in-plane and cross-plane electrical conductivities. While we can confirm that the valence band offset is almost vanishing in all SLs, the argumentation of Ref. 12 would conclude that in bulk Bi_2Te_3 and Sb_2Te_3 $\sigma_{\parallel}/\sigma_{\perp} = 1$ since the band offsets in bulk materials are zero by definition.⁷⁵ The latter conclusion is obviously wrong.

Bi_2Te_3 and Sb_2Te_3 show a theoretical band gap difference of about 35 meV, thus a band offset in the SL is expected. Our calculations reveal that this difference is mostly located in the conduction bands. The offset in the conduction band edges of Bi_2Te_3 and Sb_2Te_3 sets up potential barriers in the superlattice, which leads to confinement of the electrons in the well regions. Therefore, the site resolved probability amplitude for the two bulk tellurides, as well as for the superlattice which showed the highest conductivity anisotropy, that is, $10 \text{ \AA}/20 \text{ \AA}$ $\text{Bi}_2\text{Te}_3/\text{Sb}_2\text{Te}_3$ SL ($x = 2/6$), is shown in Figs. 5(a)–5(c).

For Bi_2Te_3 the conduction band edge is dominated by contributions of the Te_1 followed by the Bi sites. A localization of states nearby the van der Waals gap is already visible in the bulk system. The fact that the band inversion does not heavily affect the orbital character at the CBM is caused by the indirect band gap character of Bi_2Te_3 . Areas of the BZ where no band inversion occurs dominate the CBM.

For Sb_2Te_3 this is quite different. Even though Sb_2Te_3 changes from direct to an indirect semiconductor under applied in-plane tensile strain,³⁵ the CBM remains nearby the Γ point in the BZ. Therefore, most of the contributions to the conductivity arise from an area around the Γ point, where the band inversion favors the Sb character. As can be seen from Fig. 5(b) the contributions to the DOS are equally distributed over all positions in the unit cell, while slightly being enlarged

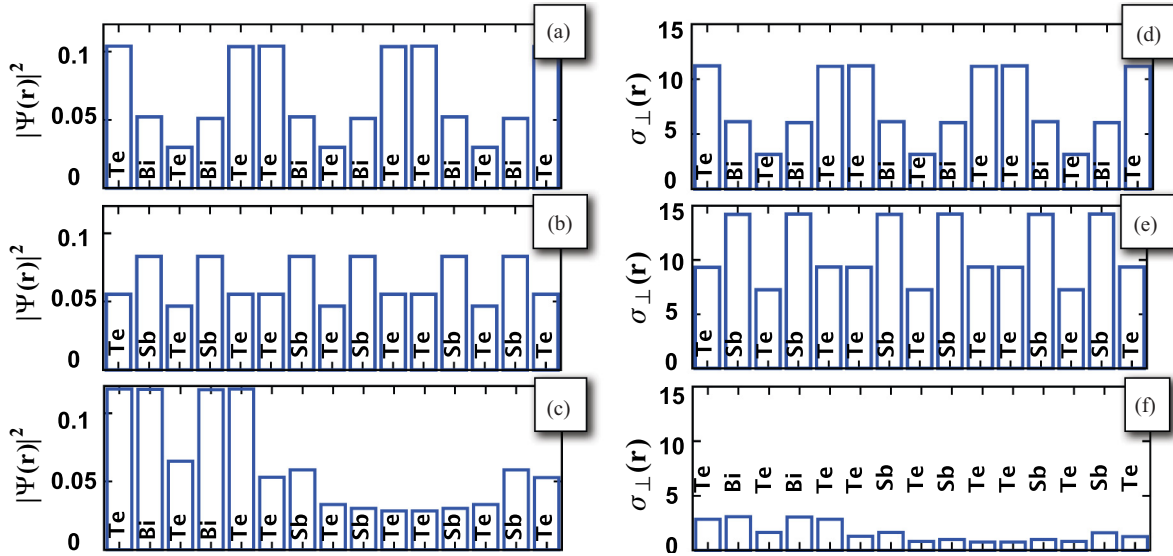


FIG. 5. (Color online) Site resolved probability amplitude for (a) bulk Bi_2Te_3 , (b) bulk Sb_2Te_3 , and (c) a $(\text{Bi}_2\text{Te}_3)_x/(\text{Sb}_2\text{Te}_3)_{1-x}$ superlattice with $x = 2/6$. In the same manner the site resolved cross-plane electrical conductivity σ_{\perp} [in units of $(\Omega \text{ cm})^{-1}$] is shown for (d) bulk Bi_2Te_3 , (e) bulk Sb_2Te_3 , and (f) a $(\text{Bi}_2\text{Te}_3)_x/(\text{Sb}_2\text{Te}_3)_{1-x}$ superlattice with $x = 2/6$. The temperature is fixed at 300 K and the charge carrier concentration is set to $N = 3 \times 10^{19} \text{ cm}^{-3}$.

on the Sb sites. For the $(\text{Bi}_2\text{Te}_3)_x/(\text{Sb}_2\text{Te}_3)_{1-x}$ SL at $x = 2/6$ [cf. Fig. 5(c)] we found quantum well states, which localize about half of the density in the Bi_2Te_3 quintuple, while the density in the two Sb_2Te_3 quintuples is strongly depleted. We obtain similar results if two quintuples ($x = 4/6$) are occupied by Bi_2Te_3 .

As shown in Fig. 5(f) the quantum confinement is reflected in the contribution to the cross-plane electrical conductivity. Here the local contribution to the cross-plane conductivity $\sigma_{\perp}(\mathbf{r})$ is calculated as introduced in Ref. 76 by weighting the contributions to $\mathcal{L}_{\perp,\parallel}^{(0)}(\mu, T)$ with the normalized probability amplitude $|\Psi(\mathbf{r})|^2$ of the electronic states at chemical potential μ . Summing up $\sigma_{\perp}(\mathbf{r})$ over all sites gives the total electrical conductivity σ_{\perp} [cf. Figs. 3(a) and 4(a)]. Weighting the DOS $n(\mu)$ with the normalized probability amplitude $|\Psi(\mathbf{r})|^2$ refers to the local DOS $n(\mu, \mathbf{r})$ (LDOS).

Nevertheless, sites in the Bi_2Te_3 quintuple with more accumulated density carry a larger contribution to the conductivity σ_{\perp} , the total contribution compared to the bulk tellurides is strongly suppressed [cf. Figs. 5(d) and 5(e)]. This can be affirmed by a picture that electrons traveling in the cross-plane direction are governed by a suppression of the probability amplitude in the Sb_2Te_3 quintuples. This clearly leads to a diminished cross-plane group velocity of the electronic states. Comparing Figs. 5(d) and 5(e) we see, furthermore, that even the localization inside the quintuple in bulk Bi_2Te_3 can lead to reduced cross-plane electronic transport, reflected in larger total anisotropies about $\sigma_{\parallel}/\sigma_{\perp} = 8$ for bulk Bi_2Te_3 compared to $\sigma_{\parallel}/\sigma_{\perp} = 5$ for bulk Sb_2Te_3 .

In Fig. 6 the temperature dependence of the in-plane and cross-plane thermopower and power factor are presented at an electron/hole charge carrier concentration of $N = 3 \times 10^{19} \text{ cm}^{-3}$. The p -type thermopower shows only moderate variations with the SL period at all temperatures with the anisotropy slightly favoring the cross-plane thermopower S_{\perp} .

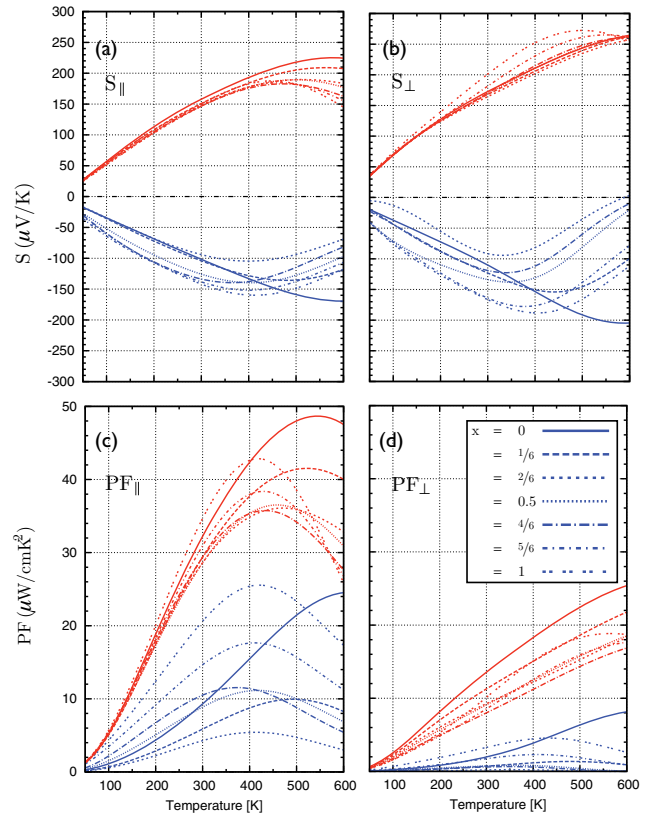


FIG. 6. (Color online) Temperature dependence of thermoelectric transport properties for $(\text{Bi}_2\text{Te}_3)_x/(\text{Sb}_2\text{Te}_3)_{1-x}$ superlattices. Shown are (a) in-plane thermopower S_{\parallel} and (b) cross-plane thermopower S_{\perp} , as well as the corresponding power factors (c) PF_{\parallel} in the in-plane and (d) PF_{\perp} in the cross-plane direction. The charge carrier concentration is fixed to $N = 3 \times 10^{19} \text{ cm}^{-3}$ and different line types correspond to different superlattice periods. Blue lines refer to electron doping, while red lines refer to hole doping.

Under electron doping the dependence of the thermopower on the SL period is more pronounced, which can to some amount be assigned to the quantum well effects which occur in the conduction band. At higher temperatures the thermopower anisotropy increases. The latter was shown before for bulk materials.¹⁸ Due to the fact of the thermopower, as well as the electrical conductivity being clearly smaller under electron doping than hole doping (cf. Fig. 3), we find the largest values of PF for the p -type SLs. Here the largest was found to be $\text{PF}_{\parallel} = 42 \mu\text{W}/\text{cm K}^2$ at 500 K for $(\text{Bi}_2\text{Te}_3)_x/(\text{Sb}_2\text{Te}_3)_{1-x}$ SL with $x = 1/6$. For bulk Bi_2Te_3 and Sb_2Te_3 we state maximum $\text{PF}_{\parallel} = 44$ and $49 \mu\text{W}/\text{cm K}^2$ at 400 and 550 K, respectively. Due to previously discussed conductivity anisotropy $\sigma_{\parallel}/\sigma_{\perp}$, the cross-plane PF is strongly suppressed and the maxima are shifted to higher temperatures.

C. Towards figure of merit

With the electronic transport properties discussed in the previous sections, we are now going to focus on the electronic and lattice part contribution to the thermal conductivity $\kappa_{\text{el}} + \kappa_{\text{ph}}$ to give some estimations for ZT . As has been stated before, the main benefit from a superlattice structure for ZT is expected from a reduction of the cross-plane thermal conductivity at retained electronic transport properties. Today, the reduction of the cross-plane lattice thermal conductivity in thermoelectric superlattices has been widely and successfully proven.⁷⁷⁻⁸⁰

In the past thermal conductivity reduction in crystalline or polycrystalline bulk thermoelectric materials was traditionally achieved by alloying. However, one reaches the so-called alloy limit of thermal conductivity, which has been difficult to surpass by nanostructuring.²

Nevertheless, for $\text{Bi}_2\text{Te}_3/\text{Sb}_2\text{Te}_3$ SLs cross-plane lattice thermal conductivities of $\kappa_{\text{ph}} = 0.22 \text{ W/mK}$ were reported for certain SL periods, which is a factor of 2 below the alloy limit.⁸ It is obvious that at thermoelectric relevant charge carrier concentrations and temperature ranges the electronic contribution κ_{el} can be in the same order of magnitude.

Therefore Fig. 7 shows the room temperature doping-dependent electronic part of the thermal conductivity in the in-plane (thick dashed lines, right scale) and cross-plane direction (thin dashed lines, right scale) for bulk Bi_2Te_3 , to offer insight into the principle dependencies. Furthermore, the Lorenz function defined via Eqs. (3) and (4) as $L_{\perp, \parallel} = \kappa_{\text{el}, \perp, \parallel} \cdot (\sigma_{\perp, \parallel} \cdot T)^{-1}$ is shown for the in-plane (thick solid line, left scale and color code) and cross-plane part (thin solid line, left scale), respectively. As can be seen, κ_{el} minimizes for energies near the band edges. Here, at $N \approx 3 \times 10^{18} \text{ cm}^{-3}$, the thermopower S maximizes at appropriate values for the electrical conductivity σ , hence the second term in Eq. (4) increases leading to small values for κ_{el} . At small intrinsic charge carrier concentrations, the chemical potential shifts into the gap and the total thermopower is strongly reduced due to bipolar diffusion. This leads to an enhanced contribution to the electrical thermal conductivity at intrinsic charge carrier concentrations and is known as the bipolar thermodiffusion effect.⁸¹⁻⁸³ At charge carrier concentrations of $N = 3 \times 10^{19} \text{ cm}^{-3}$ we find $\kappa_{\text{el}, \parallel}$ to be about 0.6–0.8 W/mK for n/p -type bulk Bi_2Te_3 in very good agreement with

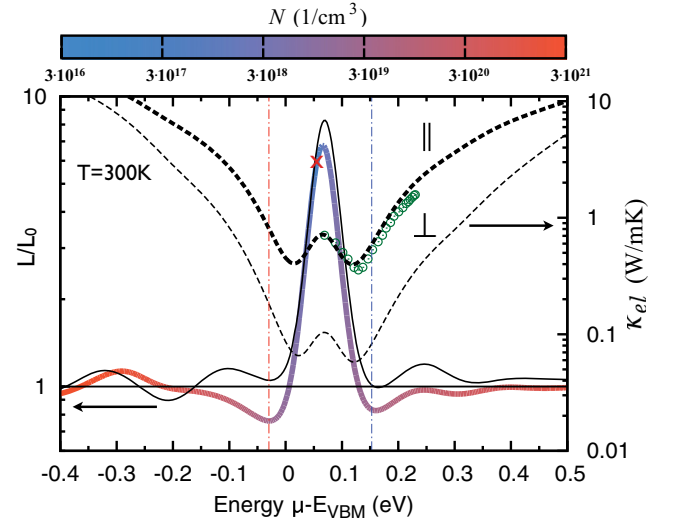


FIG. 7. (Color online) Lorenz function L (solid lines, ref. to left scale) and electronic contribution κ_{el} to the total thermal conductivity (dashed lines, ref. to the right scale) in dependence on position of the chemical potential μ for bulk Bi_2Te_3 for the in-plane (thick lines) and cross-plane (thin lines) transport direction. The Lorenz function is related to the metallic limit $L_0 = 2.44 \times 10^{-8} \text{ W}\Omega/\text{K}^2$. Superimposed onto the Lorenz function in the in-plane direction is a color code referring to the charge carrier concentration given by Eq. (5). The red cross emphasizes the change from n to p doping, respectively. The temperature was fixed at 300 K. Thin vertical dash-dotted lines emphasize the position of the chemical potential for a charge carrier concentration of $N = 3 \times 10^{19} \text{ cm}^{-3}$ under n and p doping (blue and red line, respectively). The CBM is located at 0.105 eV. Green open circles show experimental values from Ref. 81 for $\kappa_{\text{el}, \parallel}$ for an n -type Bi_2Te_3 single crystal.

experimental (cf. green, open circles in Fig. 7) and theoretical results.^{17,23,84} The cross-plane component of κ_{el} is substantially smaller, especially for n -type conduction, reflecting here the electrical conductivity anisotropy discussed earlier. The bipolar thermodiffusion effect is furthermore responsible for the suppression of the Lorenz function to values below the metallic limit L_0 ($L_0 = 2.44 \times 10^{-8} \text{ W}\Omega/\text{K}^2$) for values of the chemical potential near the band edges (cf. Fig. 7 solid lines, right scale). At optimal charge carrier concentrations of $N = 3 \times 10^{19} \text{ cm}^{-3}$ $L_{\parallel} \approx 0.7L_0$ under hole doping (red dashed-dotted lines) and $L_{\parallel} \approx 0.8L_0$ under electron doping (blue dashed-dotted lines) can be found. For the cross-plane Lorenz function $L_{\perp} \approx L_0$ is stated at the same amount of n/p -type doping. Reaching the intrinsic doping regime the Lorenz function reaches substantially large values of $L_{\parallel} \approx 6.5L_0$ and $L_{\perp} \approx 8L_0$. Such a behavior has been described in literature^{17,85} and can have consequences for the determination of the thermal conductivity. The Lorenz factor is generally used to separate κ_{el} and κ_{ph} . At thermoelectric advisable charge carrier concentrations applying the metallic value L_0 to determine the lattice thermal conductivity could lead to an overestimation of the electronic thermal conductivity, and consequently to underestimation of the lattice contribution. The Lorenz function of thermoelectric heterostructures can show further anomalies, which are discussed in detail in a forthcoming publication.⁸⁶

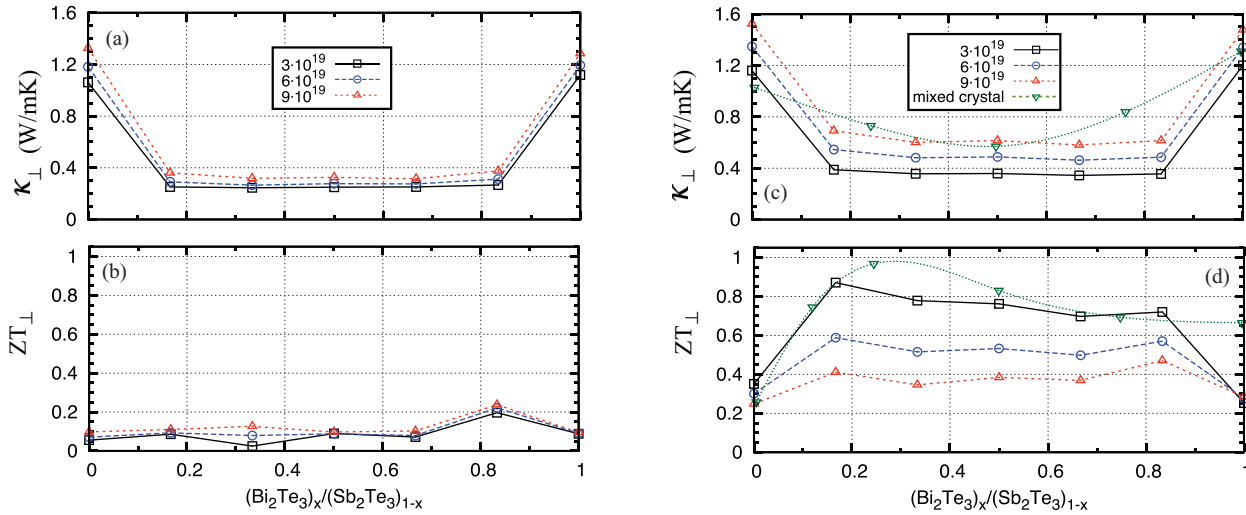


FIG. 8. (Color online) Absolute values of cross-plane thermoelectric transport properties for $(\text{Bi}_2\text{Te}_3)_x/(\text{Sb}_2\text{Te}_3)_{1-x}$ superlattices in dependence on the superlattice period. Shown are (a) and (c) the total thermal conductivity $\kappa_{\text{el}} + \kappa_{\text{ph}}$ and (b) and (d) the cross-plane figure of merit ZT_{\perp} . The temperature is fixed to 300 K and results for three different charge carrier concentrations are compared. (a) and (b) refer to electron doping, while (c) and (d) refer to hole doping. The electronic part κ_{el} was calculated, while the lattice part κ_{ph} was taken from literature.^{8,12} As a reference point experimental results for the mixed single crystal series $(\text{Bi}_x\text{Sb}_{1-x})_2\text{Te}_3$ at comparable material composition are shown as green downward triangles.⁶⁹

Experimental findings for the lattice part κ_{ph} of the thermal conductivity are added to the calculated electronic contribution κ_{el} to present some estimations on the cross-plane ZT_{\perp} . In particular $\kappa_{\text{ph},\perp} = 1.05$ W/mK, $\kappa_{\text{ph},\perp} = 0.96$ W/mK, and $\kappa_{\text{ph},\perp} = 0.22$ W/mK at room temperature were used for bulk Bi_2Te_3 , Sb_2Te_3 , and the $\text{Bi}_2\text{Te}_3/\text{Sb}_2\text{Te}_3$ SLs,⁸ respectively.⁸⁷

Recently Winkler *et al.*²⁶ measured for a *p*-type $(\text{Bi}_{0.2}\text{Sb}_{0.8})_2\text{Te}_3/\text{Sb}_2\text{Te}_3$ SL the total cross-plane thermal conductivity κ_{\perp} to be about 0.45–0.65 W/mK for different annealing temperatures. The values were obtained within a time-domain thermal reflectance (TDTR) measurement and are in very good agreement with our calculations, which are displayed in Fig. 8(c). Compared to the original experiments by Venkatasubramanian *et al.*,¹² the values of the total cross-plane thermal conductivity are smaller. This stems to a large extent from the fact that a strong electrical conductivity anisotropy $\sigma_{\parallel}/\sigma_{\perp}$ is apparent and not vanishing to $\sigma_{\parallel}/\sigma_{\perp} \sim 1$ as proposed in Ref. 12. Hence not only σ_{\perp} but also $\kappa_{\text{el},\perp}$ is noticeably suppressed. Furthermore, in Refs. 8 and 12 it was suggested that mirrorlike SL interfaces lead to potential reflection effects and reduce $\kappa_{\text{ph},\perp}$ very efficiently. Touzelbaev *et al.*²⁴ showed that an existing interface roughness will additionally decrease $\kappa_{\text{ph},\perp}$. Besides the nanocrystallinity of the samples, such an additional interface roughness is most likely provided by interdiffusion effects at the interfaces introduced by the growth of $\text{Bi}_2\text{Te}_3/\text{Sb}_2\text{Te}_3$ SLs within the concept of nanoalloying.^{21,26}

In Fig. 8 the room-temperature cross-plane properties of the total thermal conductivity and the related cross-plane part of ZT are shown for electron (a) and (b) and hole doping (c) and (d), respectively. As could be expected the strong quantum well effects in the conduction band lead to quite small values for $ZT_{\perp} \leq 0.2$ under electron doping. Here a reduction of the SL total thermal conductivity of about a factor 5–6 compared to bulk is impeded by an accompanied reduction of PF_{\perp} by a factor of 10–20 [cf. Fig. 4(c)]. Thus no benefit for

ZT in the cross-plane direction can be revealed under electron doping. At hole doping the situation is more advantageous. Besides the total thermal conductivity [cf. Figs. 8(c) and 7] being somewhat larger than under electron doping, the electronic transport properties remain bulklike for all SL periods [cf. Fig. 4(f)] and hence an enhancement for ZT_{\perp} by a factor of 2–3 can be achieved under hole doping of $N = 3 \times 10^{19} \text{ cm}^{-3}$. We calculated values $ZT_{\perp} \approx 0.7$ –0.9 for different SL periods, while a higher amount of Sb_2Te_3 in the SL leads to larger values for ZT , despite no distinct influence of the SL period on ZT could be found. As a supplement experimental data⁶⁹ for κ_{\perp} and ZT_{\perp} of the mixed single crystal series $(\text{Bi}_x\text{Sb}_{1-x})_2\text{Te}_3$ is shown as green downward triangles in Figs. 8(c) and 8(d). The hole doping varied steadily between $N = 1 \times 10^{19} \text{ cm}^{-3}$ for Bi_2Te_3 to $N = 9 \times 10^{19} \text{ cm}^{-3}$ for Sb_2Te_3 . One easily concludes that ZT_{\perp} values of the optimal doped SLs and the mixed single crystal series show clear similarities considering the dependence on the materials composition, as well as the the absolute values of ZT_{\perp} .

To extend our findings at room temperature, in Figs. 9(a) and 9(b) temperature-dependent results for the total cross-plane thermal conductivity and cross-plane ZT are shown for the $(\text{Bi}_2\text{Te}_3)_x/(\text{Sb}_2\text{Te}_3)_{1-x}$ SLs at an electron/hole concentration of $N = 3 \times 10^{19} \text{ cm}^{-3}$. Within a conventional $1/T$ dependence the lattice thermal conductivity was assumed,⁸⁸ while the calculated electronic part κ_{el} is temperature and doping dependent, per se. We note that for thermoelectric SLs no clear tendency on the temperature dependence of κ_{ph} can be revealed. However, conventional $1/T$ dependence, as well as temperature independent κ_{ph} were found experimentally.^{77,78,89} Models show that κ_{ph} should diminish at low periods,⁹⁰ while experiments reveal a saturation towards the alloy limit for SL periods below 50 Å.⁸

As can be seen from Fig. 9(a) κ_{\perp} takes a minimum at about 300–400 K for the $\text{Bi}_2\text{Te}_3/\text{Sb}_2\text{Te}_3$ SLs. This behavior is

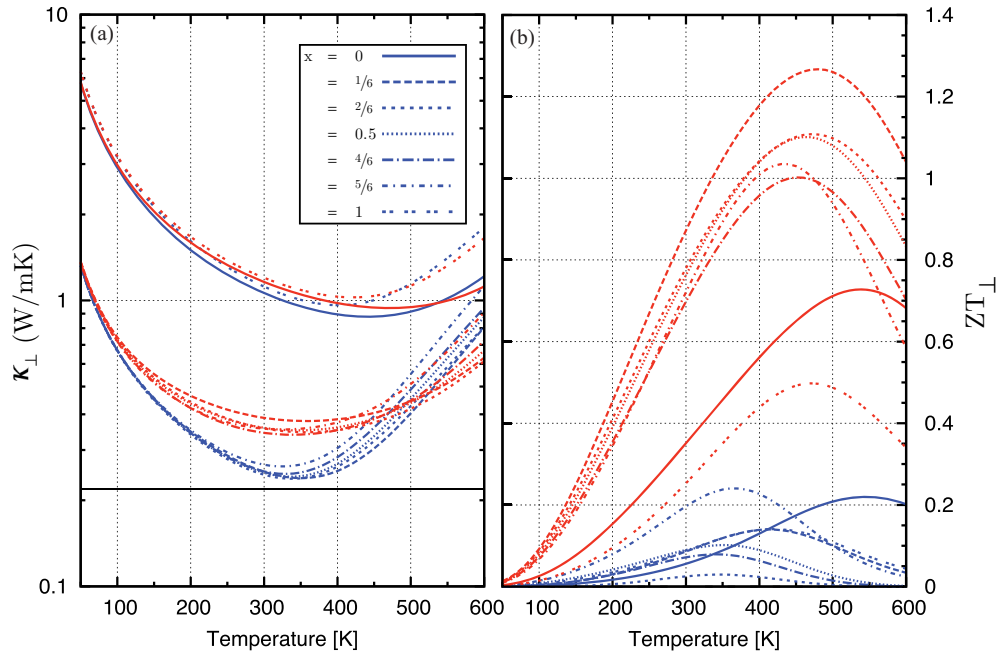


FIG. 9. (Color online) Temperature dependence of the thermal conductivity and figure of merit for the $(\text{Bi}_2\text{Te}_3)_x/(\text{Sb}_2\text{Te}_3)_{1-x}$ SLs. Shown are (a) total cross-plane thermal conductivity $\kappa_{\perp} = \kappa_{\text{el},\perp} + \kappa_{\text{ph},\perp}$ and (b) cross-plane figure of merit. The charge carrier concentration is fixed to $N = 3 \times 10^{19} \text{ cm}^{-3}$ and different line types correspond to different SL periods. Blue lines refer to electron doping, while red lines refer to hole doping. The electronic part κ_{el} was calculated, while the lattice part κ_{ph} was taken from literature.^{8,12}

dictated by the electronic contribution to κ_{\perp} and supported by the $1/T$ dependence of the lattice part of κ . At low temperature the chemical potential is located in the bands and thus a moderate contribution to $\kappa_{\text{el},\perp}$ is obtained. With increasing temperature $\kappa_{\text{el},\perp}$ slightly decreases as the chemical potential shifts towards the band edges, then reaching minimal $\kappa_{\text{el},\perp}$ for chemical potential positions at the band edges (cf. Fig. 7). At elevated temperatures the bipolar contribution leads to an enhanced electronic contribution to κ_{\perp} , which then clearly dominates the $1/T$ dependence of the lattice part of κ leading to large values of the total thermal conductivity. The influence of the electronic contribution is more pronounced in the SLs compared to bulk, as here $\kappa_{\text{el},\perp} \geq \kappa_{\text{ph},\perp}$. Combining these results with the temperature-dependent power factor PF_{\perp} discussed in Fig. 5(d) we find the temperature dependence on the cross-plane ZT as presented in Fig. 9(b). Concentrating on the more promising p -type SLs we state found enhanced values for ZT_{\perp} clearly above unity for temperatures of 400–500 K. The largest cross-plane figure of merit is found to be $ZT_{\perp} = 1.27$ at about 470 K for a $(\text{Bi}_2\text{Te}_3)_x/(\text{Sb}_2\text{Te}_3)_{1-x}$ SL at $x = 1/6$ and a hole concentration of $N = 3 \times 10^{19} \text{ cm}^{-3}$. We want to mention that in the experiments of Ref. 12 the maximal ZT_{\perp} under hole doping was stated at a SL period of $x = 1/6$ too. The best value for an n -type SL is $ZT_{\perp} = 0.25$ at about 360 K at a SL period of $x = 5/6$.

V. CONCLUSION

The anisotropic thermoelectric transport properties of $\text{Bi}_2\text{Te}_3/\text{Sb}_2\text{Te}_3$ superlattices at different superlattice periods are presented to get insight into the physical mechanisms which are responsible for the path-breaking experimental

results with $ZT_{\perp} = 2.4$ at room temperature obtained by Ref. 12. Several aspects added up to obtain those very high ZT values in experiment. (i) In-plane values of the electrical conductivity and thermopower were found to be larger than in the bulk systems at comparable charge carrier concentrations. (ii) An elimination of the electrical conductivity anisotropy $\sigma_{\parallel}/\sigma_{\perp}$, which is apparent in both bulk systems, was found in superlattices at certain periods. (iii) The lattice part of the thermal conductivity was reduced below the alloy limit due to phonon blocking at the superlattice interfaces.^{8,24}

Even though taking into account the most optimistic value $\kappa_{\text{ph},\perp} = 0.22 \text{ W/mK}$ for the lattice part of the thermal conductivity, we found the cross-plane figure of merit for the best p -type superlattice to be $ZT_{\perp} = 0.9$ at room temperature and slightly enhanced to $ZT_{\perp} = 1.27$ at elevated temperature. However, this differs more than a factor of 2 from values experimentally revealed and is caused by the fact that within the presented *ab initio* calculations the findings (i) and (ii) could not be confirmed. We want to add that in first-consistent experiments by Venkatasubramanian *et al.*⁶⁷ a room-temperature $ZT_{\perp} = 1.2$ was proposed for a nonsymmetrical $\text{Bi}_2\text{Te}_3/\text{Sb}_2\text{Te}_3$ superlattice with a period of 30 Å.

For the in-plane transport properties of S , σ , and PF we can present values comparable to bulk for the p -type and n -type superlattices, which is in agreement with recent experiments.^{21,26} Furthermore, for the p -type superlattices a conservation of the bulk transport anisotropies is found, but in no case a reduction, while under electron doping strong quantum well effects due to conduction band offsets lead to large transport anisotropies $\sigma_{\parallel}/\sigma_{\perp} \geq 10$ and suppress the cross-plane thermoelectric transport notably.

Concluding, the remarkable experimentally found thermoelectric transport properties in $\text{Bi}_2\text{Te}_3/\text{Sb}_2\text{Te}_3$ superlattices could not be explained by detailed band structure effects. An ongoing issue will be to clarify whether scattering effects caused by defects and lattice imperfections could give a considerable leap forward to understanding the enhanced thermoelectric efficiency in $\text{Bi}_2\text{Te}_3/\text{Sb}_2\text{Te}_3$ superlattices.

ACKNOWLEDGMENTS

This work was supported by the Deutsche Forschungsgemeinschaft, SPP 1386 ‘Nanostrukturierte Thermoelektrika: Theorie, Modellsysteme und kontrollierte Synthese’. N. F. Hinsche is member of the International Max Planck Research School for Science and Technology of Nanostructures.

*nicki.hinsche@physik.uni-halle.de

- ¹G. J. Snyder and E. Toberer, *Nat. Mater.* **7**, 105 (2008).
- ²C. J. Vineis, A. Shakouri, A. Majumdar, and M. G. Kanatzidis, *Adv. Mater.* **22**, 3970 (2010).
- ³D. A. Wright, *Nature (London)* **181**, 834 (1958).
- ⁴T. Caillat, M. Carle, P. Pierrat, H. Scherrer, and S. Scherrer, *J. Phys. Chem. Solids* **53**, 1121 (1992).
- ⁵B. Poudel, Q. Hao, Y. Ma, Y. Lan, A. Minnich, B. Yu, X. Yan, D. Wang, A. Muto, and D. Vashaee, *Science* **320**, 634 (2008).
- ⁶G. Slack, in *CRC Handbook of Thermoelectrics*, edited by D. M. Rowe, Chap. 34 (CRC, Boca Raton, FL, 1995).
- ⁷G. Chen, *Phys. Rev. B* **57**, 14958 (1998).
- ⁸R. Venkatasubramanian, *Phys. Rev. B* **61**, 3091 (2000).
- ⁹T. Koga, X. Sun, S. Cronin, and M. S. Dresselhaus, in *The 18th International Conference on Thermoelectrics: ICT Symposium Proceedings, Baltimore* (Institute of Electrical and Electronics Engineers, Inc., Piscataway, NJ, 1999), pp. 378–381; *Appl. Phys. Lett.* **75**, 2438 (1999); T. Koga, T. C. Harman, S. B. Cronin, and M. S. Dresselhaus, *Phys. Rev. B* **60**, 14286 (1999); T. Koga, S. Cronin, M. Dresselhaus, and J. Liu, *Appl. Phys. Lett.* **77**, 1490 (2000).
- ¹⁰H. Böttner, G. Chen, and R. Venkatasubramanian, *MRS Bull.* **31**, 211 (2006).
- ¹¹R. Venkatasubramanian, T. Colpitts, B. O’Quinn, S. Liu, N. El-Masry, and M. Lamvik, *Appl. Phys. Lett.* **75**, 1104 (1999).
- ¹²R. Venkatasubramanian, E. Siivola, and T. Colpitts, *Nature (London)* **413**, 597 (2001).
- ¹³A. Majumdar, *Science* **303**, 777 (2004).
- ¹⁴R. Delves, A. Bowley, and D. Hazelden, *Proc. Phys. Soc.* **78**, 838 (1961).
- ¹⁵M. Stordeur and W. Heiliger, *Phys. Status Solidi B* **78**, K103 (1976).
- ¹⁶M. Stordeur and W. Kühnberger, *Phys. Status Solidi B* **69**, 377 (1975).
- ¹⁷B. L. Huang and M. Kaviani, *Phys. Rev. B* **77**, 125209 (2008).
- ¹⁸N. F. Hinsche, B. Y. Yavorsky, I. Mertig, and P. Zahn, *Phys. Rev. B* **84**, 165214 (2011).
- ¹⁹H. Beyer, J. Nurnus, H. Böttner, A. Lambrecht, E. Wagner, and G. Bauer, *Physica E* **13**, 965 (2002).
- ²⁰H. Böttner, J. Nurnus, A. Gavrikov, and G. Kuhner, *J. Micro-electromech. Syst.* **13**, 414 (2004).
- ²¹J. König, M. Winkler, S. Buller, W. Bensch, U. Schürmann, L. Kienle, and H. Böttner, *J. Electron. Mater.* **40**, 1266 (2011).
- ²²C.-N. Liao, C.-Y. Chang, and H.-S. Chu, *J. Appl. Phys.* **107**, 066103 (2010).
- ²³N. Peranio, O. Eibl, and J. Nurnus, *J. Appl. Phys.* **100**, 114306 (2006).
- ²⁴M. N. Touzelbaev, P. Zhou, R. Venkatasubramanian, and K. E. Goodson, *J. Appl. Phys.* **90**, 763 (2010).
- ²⁵N. Peranio, M. Winkler, Z. Aabdin, J. König, H. Böttner, and O. Eibl, *Phys. Status Solidi A* **209**, 289 (2011).
- ²⁶M. Winkler, X. Liu, J. König, L. Kirste, H. Böttner, W. Bensch, and L. Kienle, *J. Electron. Mater.* **41**, 1322 (2012).
- ²⁷T. J. Scheidemantel, C. Ambrosch-Draxl, T. Thonhauser, J. V. Badding, and J. O. Sofo, *Phys. Rev. B* **68**, 125210 (2003).
- ²⁸T. Thonhauser, T. J. Scheidemantel, J. O. Sofo, J. V. Badding, and G. D. Mahan, *Phys. Rev. B* **68**, 085201 (2003).
- ²⁹G. Wang and T. Cagin, *Phys. Rev. B* **76**, 075201 (2007).
- ³⁰G. Wang and T. Cagin, *Appl. Phys. Lett.* **89**, 152101 (2006).
- ³¹M. S. Park, J.-H. Song, J. E. Medvedeva, M. Kim, I. G. Kim, and A. J. Freeman, *Phys. Rev. B* **81**, 155211 (2010).
- ³²H. Li, D. Bilc, and S. D. Mahanti, *MRS Proceedings* **793**, S8.37 (2003).
- ³³S. D. Mahanti, P. M. Larson, and H. Li, in *Chemistry, Physics, and Materials Science of Thermoelectric Materials: Beyond Bismuth Telluride*, edited by M. G. Kanatzidis and T. Hogan (Kluwer Academic/Plenum, New York, 2003), p. 227.
- ³⁴O. Madelung, M. Schulz, and H. Weiss, eds., *Numerical Data and Functional Relationship in Science and Technology* (Springer, Berlin, 1998).
- ³⁵B. Y. Yavorsky, N. F. Hinsche, I. Mertig, and P. Zahn, *Phys. Rev. B* **84**, 165208 (2011).
- ³⁶M. Gradhand, M. Czerner, D. V. Fedorov, P. Zahn, B. Y. Yavorsky, L. Szunyogh, and I. Mertig, *Phys. Rev. B* **80**, 224413 (2009).
- ³⁷S. H. Vosko and L. Wilk, *Phys. Rev. B* **22**, 3812 (1980).
- ³⁸I. Mertig, *Rep. Prog. Phys.* **62**, 237 (1999).
- ³⁹N. Hinsche, I. Mertig, and P. Zahn, *J. Phys.: Condens. Matter* **23**, 295502 (2011).
- ⁴⁰D. J. Singh, *Phys. Rev. B* **81**, 195217 (2010).
- ⁴¹D. Parker and D. J. Singh, *Phys. Rev. B* **82**, 035204 (2010).
- ⁴²A. F. May, D. J. Singh, and G. J. Snyder, *Phys. Rev. B* **79**, 153101 (2009).
- ⁴³M.-S. Lee, F. P. Poudeu, and S. D. Mahanti, *Phys. Rev. B* **83**, 085204 (2011).
- ⁴⁴S. Lee and P. von Allmen, *Appl. Phys. Lett.* **88**, 022107 (2006).
- ⁴⁵M. Situmorang and H. Goldsmid, *Phys. Status Solidi B* **134**, K83 (1986).
- ⁴⁶T. Thonhauser, *Solid State Commun.* **129**, 249 (2004).
- ⁴⁷H. Ashworth, J. Rayne, and R. Ure, *Phys. Rev. B* **3**, 2646 (1971).
- ⁴⁸G. Mahan and J. Sofo, *Proc. Natl. Acad. Sci.* **93**, 7436 (1996).
- ⁴⁹P. Zahn, N. Hinsche, B. Yavorsky, and I. Mertig, *J. Phys.: Condens. Matter* **23**, 505504 (2011).
- ⁵⁰G. Nolas and H. Goldsmid, in *Thermal Conductivity: Theory, Properties, and Applications*, edited by T. Tritt, Chap. 1.4 (Kluwer Academic, New York, 2004).
- ⁵¹R. Sehr, *J. Phys. Chem. Solids* **23**, 1219 (1962).
- ⁵²G. Lehmann and M. Taut, *Phys. Status Solidi B* **54**, 469 (1972).

- ⁵³I. Mertig, E. Mrosan, and P. Ziesche, *Multiple Scattering Theory of Point Defects in Metals: Electronic Properties* (B. G. Teubner, Leipzig, 1987).
- ⁵⁴P. Mori-Sánchez, A. J. Cohen, and W. Yang, *Phys. Rev. Lett.* **100**, 146401 (2008).
- ⁵⁵Y. Varshni, *Physica* **34**, 149 (1967).
- ⁵⁶A. von Middendorff, K. Dietrich, and G. Landwehr, *Solid State Commun.* **13**, 443 (1973).
- ⁵⁷H. Zhang, C. Liu, X. Qi, X. Dai, Z. Fang, and S. Zhang, *Nat. Phys.* **5**, 438 (2009).
- ⁵⁸O. V. Yazyev, E. Kioupakis, J. E. Moore, and S. G. Louie, *Phys. Rev. B* **85**, 161101 (2012).
- ⁵⁹S. Mishra, S. Satpathy, and O. Jepsen, *J. Phys.: Condens. Matter* **9**, 461 (1997).
- ⁶⁰S. J. Youn and A. J. Freeman, *Phys. Rev. B* **63**, 85112 (2001).
- ⁶¹P. Larson, *Phys. Rev. B* **74**, 205113 (2006).
- ⁶²H. Jeon, H. Ha, D. Hyun, and J. Shim, *J. Phys. Chem. Solids* **52**, 579 (1991).
- ⁶³D. M. Rowe, ed., *CRC Handbook of Thermoelectrics* (CRC, Boca Raton, FL, 1995).
- ⁶⁴H. Scherrer and S. Scherrer, in *CRC Handbook of Thermoelectrics*, edited by D. M. Rowe, Chap. 19 (CRC, Boca Raton, FL, 1995).
- ⁶⁵We note that no coherent data of N , σ_{\parallel} , S_{\parallel} , and PF_{\parallel} for the SL is available. N and σ_{\parallel} were concluded from Ref. 12, while S_{\parallel} was estimated from Refs. 66–68 for comparable SLs, but most probably not from the same sample.
- ⁶⁶R. Venkatasubramanian, T. Colpitts, E. Watko, M. Lamvik, and N. El-Masry, *J. Cryst. Growth* **170**, 817 (1997).
- ⁶⁷R. Venkatasubramanian, T. Colpitts, E. Watko, and J. Hutchby, in *Proceedings of 15th International Conference on Thermoelectrics* (IEEE, Piscataway, NJ, 1996), pp. 454–458.
- ⁶⁸R. Venkatasubramanian, *Bi2Te3/Sb2Te3 Superlattice Structures for High-ZT Thermoelectric Cooling Devices*, Tech. Rep. (Office of Naval Research, USA, 1997).
- ⁶⁹M. Stordeur, in *CRC Handbook of Thermoelectrics*, edited by D. M. Rowe, Chap. 20 (CRC, Boca Raton, FL, 1995).
- ⁷⁰L. Hicks, T. Harman, and M. Dresselhaus, *Appl. Phys. Lett.* **63**, 3230 (1993); L. D. Hicks and M. S. Dresselhaus, *Phys. Rev. B* **47**, 12727 (1993).
- ⁷¹M. Dresselhaus, G. Dresselhaus, X. Sun, Z. Zhang, S. Cronin, and T. Koga, *Phys. Solid State* **41**, 679 (1999).
- ⁷²J. Sofo and G. Mahan, *AIP Conf. Proc.* **316**, 239 (1994).
- ⁷³D. A. Broido and T. L. Reinecke, *Phys. Rev. B* **51**, 13797 (1995).
- ⁷⁴S. Eremeev, G. Landolt, T. Menshchikova, B. Slomski, Y. Koroteev, Z. Aliev, M. Babanly, J. Henk, A. Ernst, and L. Patthey, *Nat. Commun.* **3**, 635 (2012).
- ⁷⁵J. Sootsman, D. Chung, and M. Kanatzidis, *Angew. Chem.* **121**, 8768 (2009).
- ⁷⁶P. Zahn, J. Binder, I. Mertig, R. Zeller, and P. H. Dederichs, *Phys. Rev. Lett.* **80**, 4309 (1998).
- ⁷⁷S. Lee, D. Cahill, and R. Venkatasubramanian, *Appl. Phys. Lett.* **70**, 2957 (1997).
- ⁷⁸T. Borca-Tasciuc, W. Liu, J. Liu, T. Zeng, D. W. Song, C. D. Moore, G. Chen, K. L. Wang, M. S. Goorsky, T. Radetic, R. Gronsky, T. Koga, and M. S. Dresselhaus, *Superlattices Microstruct.* **28**, 199 (2000).
- ⁷⁹S. Huxtable, A. Abramson, and C. Tien, *Appl. Phys. Lett.* **80**, 1737 (2002).
- ⁸⁰S. Chakraborty, C. Kleint, A. Heinrich, C. Schneider, J. Schumann, M. Falke, and S. Teichert, *Appl. Phys. Lett.* **83**, 4184 (2003).
- ⁸¹H. Goldsmid, *Adv. Phys.* **14**, 273 (1965).
- ⁸²H. Fröhlich and C. Kittel, *Physica* **3**, 1086 (1954).
- ⁸³C. Uher and H. Goldsmid, *Phys Status Solidi B* **65**, 765 (1974).
- ⁸⁴H. Goldsmid, *Proc. Phys. Soc. London, Sect. B* **69**, 203 (1956).
- ⁸⁵L. Chaput, P. Pêcheur, J. Tobola, and H. Scherrer, *Phys. Rev. B* **72**, 085126 (2005).
- ⁸⁶N. F. Hinsche, I. Mertig, and P. Zahn, [arXiv:1206.6124](https://arxiv.org/abs/1206.6124) [cond-mat.mtrl-sci] (2012).
- ⁸⁷We want to mention that the lattice thermal conductivity was found to be a function of the SL period.⁸ As a lack of further data we assumed the smallest $\kappa_{\text{ph},\perp}$ for all of our SL periods.
- ⁸⁸N. Peranio, Ph.D. thesis, Eberhard-Karls-Universität zu Tübingen, 2008.
- ⁸⁹M. Hase and J. Tominaga, *Appl. Phys. Lett.* **99**, 031902 (2011).
- ⁹⁰A. Pattamatta and C. K. Madnia, *Int. J. Heat Mass Transfer* **52**, 860 (2009).

5.2 Silicon/Germanium heterostructures

Silicon based materials are particularly interesting for TE transport, as conventional TES are often based on environmentally unfriendly lead, tellurium or selenium compounds and are therefore hard to integrate in semiconductor electronics. Silicon, the cradle of modern semiconductor electronics, on the other hand is non-polluting, readily available, cheap, and perfectly integrated in the present electronics infrastructure. While silicon has been stated as an inefficient thermoelectric in the past due to its enormous thermal conductivity, recent experiments and theory revealed that nanostructuring could lead to thermoelectric efficiencies comparable to state-of-the-art commercial thermoelectric materials [Vin08a, CHM⁺08, HCDL08, BBTk⁺08, BBG⁺09].

For successful applications, an optimization of TE electronic properties of silicon, i.e. the power factor, is of utmost interest. Interfacial strain plays an important role in today's silicon-based semiconductor materials. The strain-induced enhancement of the mobility, for either electrons or holes, by strain-engineering is widely applied [FL96, DZMM07, BTN10]. The question whether a significant enhancement of the anisotropic TE transport is achievable by biaxial strain was answered within the two following publications [E8] and [E3]. Two directions of strain were discussed, i.e. [001]-biaxial strain ([E8]) and [111]-biaxial strain ([E3]). Both alter the n-type TE transport due to different physical mechanisms. As shown in figures 5.4(a)-(c), in the case of [001] strain the six-fold electron pocket degeneracy is lifted and a redistribution of states into other areas of the BZ is obtained. These areas are related to other effective masses and FERMI velocities. The gain in the electrical conductivity, which can be obtained by the strain-induced redistribution of states is noticeable. However, the lifting of degeneracy was found to lead to a reduction of the thermopower (cf. figure 5.4(d)). As I showed in an analytical model [E8], which only assumes a lifting of degenerated bands, the absolute value of the thermopower depends directly on the number of carrier pockets

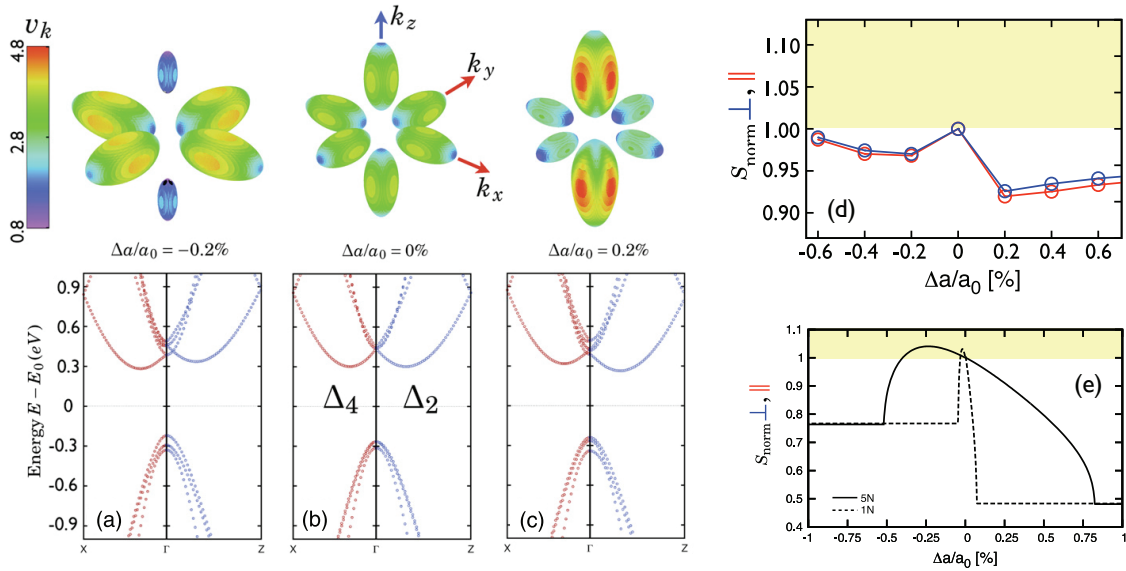


Figure 5.4: FERMI surfaces of electron-doped silicon under (a) compressive strain, (b) no strain, and (c) tensile strain in [001]-direction. The absolute value of the group velocities in units of $0.06 \times 10^6 \text{ ms}^{-1}$ are plotted on the FERMI surfaces. As a reference the band structure on two high-symmetry lines is given below. The doping corresponds to additional 0.01 electrons per unit cell which causes carrier densities of $N = 6.25 \times 10^{19} \text{ cm}^{-3}$. (d) Strain-dependent anisotropic thermopower in relative units (left scale) and absolute units (in $\mu\text{V/K}$, right scale). The temperature was fixed to 100K and the doping amounts to 1.6×10^{-7} electrons per unit cell. (e) Analytical dependence of the thermopower on [001]-biaxial strain for different electron charge carrier concentrations, small charge carrier concentration (dashed lines) and increased charge carrier concentration by a factor of five (solid lines).

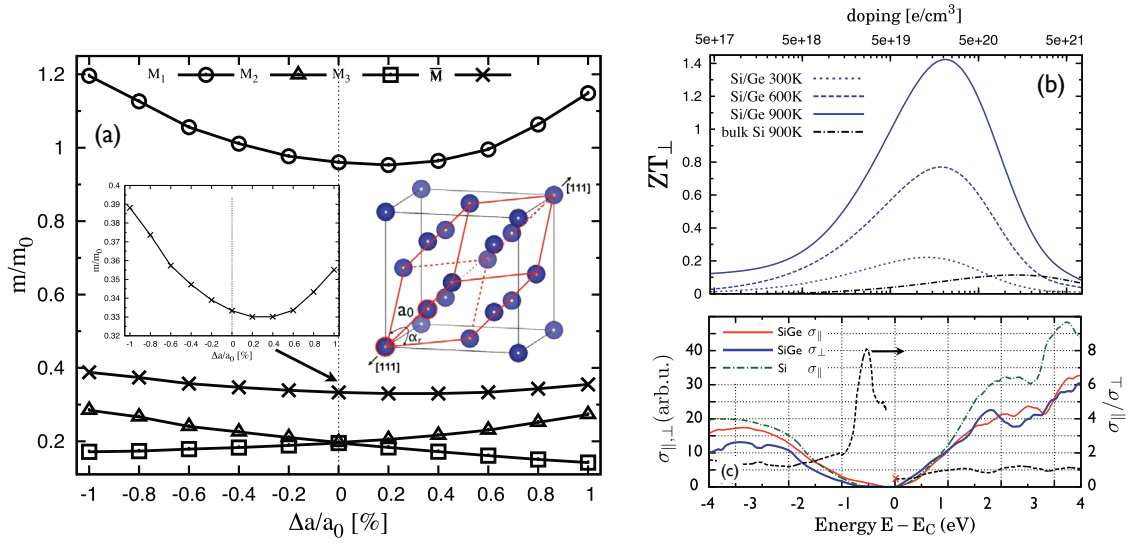


Figure 5.5: (a) Directional effective conduction band masses for silicon under [111]-strain. The insets show in detail the response of the averaged effective mass \bar{M} on the applied strain, as well as the rhombohedral unit cell (red lines). (b) The doping-dependent cross-plane figures of merit ZT (of the Si/Ge-SL (blue lines) and bulk Si (black lines) under electron doping at different temperatures. (c) The electrical conductivity in dependence on the position of the chemical potential μ at zero temperature, shown for bulk silicon (green dashed-dotted line) and the Si/Ge-SL in the in-plane (red solid line) and cross-plane (blue solid line) directions. The conductivity anisotropy (black dashed line referring to the right axis) is stated for the Si/Ge-SL. The cross at the CBM is the value obtained from an analytical effective mass approach.

being occupied. As discussed in [E8], the enhancement obtained in the electrical conductivity is therefore compensated by a reduction in the thermopower, leading to no noticeable optimization of the power factor. This picture holds over a broad temperature and doping range.

In the case of biaxial strain applied in the [111]-direction the situation is different. Here the six-fold degeneracy of the electron carrier pockets is maintained by symmetry. Contrary to the case of [001]-strain, the directional electron effective masses change with applied strain [E3]. This is shown in figure 5.5(a). Due to the retained degeneracy of bands, the thermopower is less sensitive upon applied [111]-strain. In [E3] I found that the thermopower changes proportional to the change in the direction averaged effective mass (cf. inset in figure 5.5(a)), but drops not immediately upon applying strain. Summarizing, at low temperature and low doping an enhancement of the power factor was obtained for compressive and tensile strain in the electron-doped case and for compressive strain in the hole-doped case. For the thermoelectrically more relevant high-temperature and high-doping regime a slight enhancement of the power factor was only found under small compressive strain with the power factor overall being robust against applied strain (see [E3]).

Based upon the previous findings, the TE transport of an archetypical non-symmetrized Si/Ge SL grown on Si-[111] was studied in [E3]. Similar to the case of $\text{Bi}_2\text{Te}_3/\text{Sb}_2\text{Te}_3$ -SLs an evident reduction of the lattice thermal conductivity was found in Si/Ge based SLs and lead to focussed experimental research [LCV97, BT00, YLWC01]. At a first glance it was shown that no degradation of the electronic transport by the heterostructure is expected for electron doping, while even showing an enhancement of about 10% for the cross-plane power factor compared to bulk Si. As shown in figure 5.5(b), assuming a decrease in lattice thermal conductivity, large enhancements in ZT to 0.2 and 1.4 are achieved at 300 K and 900 K, respectively. However, the predictions of an in-plane $ZT \sim 1$ at room temperature stated by KOGA [KSCD99] could not be confirmed. Here, they used parabolic band models neglecting any coupling of adjacent layers, a rather crude assumption. The results of their experimental proof-of-principle for [001] oriented Si/Ge SLs [KCDL00], showing up

$ZT \sim 0.1$ at 300K, are in closer agreement to our first-principles calculations presented in [E3].

Under hole doping the electronic transport in the Si/Ge-SL is heavily suppressed due to quantum-well effects. As shown in figure 5.5(c) the electrical conductivity anisotropy is considerably increased to values of $\sigma_{\parallel}/\sigma_{\perp} \approx 8$ at thermoelectric relevant hole doping rates. The valence states in a broad range around the band gap are formed by germanium states. Consequently, the p -type Si/Ge heterostructure consists of electrical high conducting (Ge) and nearly insulating (Si) material layers. As a result, the cross-plane power factor shows only around 50% of the bulk maximal value, leading to very small ZT values under hole doping.

Effect of strain on the thermoelectric properties of silicon: an *ab initio* study

N F Hinsche^{1,3}, I Mertig^{1,2} and P Zahn¹

¹ Institut für Physik, Martin-Luther-Universität Halle-Wittenberg, D-06099 Halle, Germany

² Max-Planck-Institut für Mikrostrukturphysik, Weinberg 2, D-06120 Halle, Germany

E-mail: nicki.hinsche@physik.uni-halle.de

Received 10 March 2011, in final form 9 June 2011

Published 8 July 2011

Online at stacks.iop.org/JPhysCM/23/295502

Abstract

On the basis of detailed first-principles calculations the anisotropic thermoelectric transport properties of biaxially strained silicon were studied with the focus on a possible enhancement of the power factor. Electron as well as hole doping was examined in a broad doping and temperature range. In the low temperature and low doping regime an enhancement of the power factor was obtained for compressive and tensile strain in the electron-doped case, and for compressive strain in the hole-doped case. In the thermoelectrically more important high temperature and high doping regime a slight enhancement of the power factor was only found for the hole-doped case under small biaxial tensile strain. The results are discussed in terms of band structure effects. An analytical model is presented to understand the fact that the thermopower decreases if degenerate bands are energetically lifted due to a strain-induced redistribution of states.

(Some figures in this article are in colour only in the electronic version)

1. Introduction

Thermoelectrics convert heat into electric current, and vice versa. Known for more than 60 years, thermoelectrics currently attracts a great deal of attention [1–4]. With nearly 90% of the world's power being generated by low efficiency heat engines, thermoelectric modules could potentially convert parts of this wasted heat into electricity. Their conversion efficiency can be stated by the figure of merit:

$$ZT = \frac{\sigma S^2}{\kappa_{\text{el}} + \kappa_{\text{ph}}} T, \quad (1)$$

where σ is the electrical conductivity, S is the thermopower, and κ_{el} and κ_{ph} are the electronic and phononic contributions to the thermal conductivity, respectively. The numerator of equation (1) is called the power factor $\text{PF} = \sigma S^2$.

While $ZT > 1$ was challenging to be reached in the last decades, nowadays nanostructured thermoelectrics enable even larger values of ZT [5–7]. Unfortunately, those materials are often based on environmentally unfriendly lead, tellurium or selenium compounds and are therefore hard to integrate in semiconductor electronics.

³ Author to whom any correspondence should be addressed.

Silicon, the cradle of modern semiconductor electronics, is nonpolluting, readily available, cheap and perfectly integrated in the present electronics infrastructure. While silicon has been stated as an inefficient thermoelectric in the past due to its enormous thermal conductivity [8], recent experiments and theory revealed that nanostructuring could lead to thermoelectric efficiencies comparable to state-of-the-art commercial thermoelectric materials [9–13].

As in nanostructured materials mechanical strain plays an important role; this paper will focus on the influence of biaxial strain on the electronic thermoelectric transport properties of bulk silicon, which might occur in rolled-up and layered Si heterostructures [14–17]. It is well known, that similar strain physics, e.g. band splitting and band deformation, are expected for strained three-dimensional systems, as well as for one and two-dimensional silicon devices in complex strain states. A comprehensive overview on this can be found in [14]. In detail these common strain physics affect the electronic carrier transport depending on the dimensionality, temperature and doping density. The question to be answered in this paper will be whether tensile or compressive strain will lead to an enhancement or reduction of the power factor in silicon under a certain doping and temperature environment. Besides our interest in the high temperature thermoelectric application of

strained silicon we want to emphasize the possible importance of our results in the low temperature regime for the metal-oxide–semiconductor device community, where the knowledge of the thermoelectric properties of silicon under strain could help to understand parasitic effects in these devices. In the low doping regime at low temperature, an enhancement of one part of the power factor, namely the electrical conductivity, under externally applied strain, was found and heavily investigated in the last few decades [18, 19, 14]. For this purpose this paper will be organized as follows. In section 2 we introduce our first-principles electronic structure calculations based on density functional theory and the transport calculations based on the solution of the linearized Boltzmann equation. With this knowledge we start the discussion of the thermoelectric transport properties of unstrained bulk silicon (section 3.1) and present afterwards the influence of biaxial strain on the electron- or hole-doped case of silicon in section 3.2. In the last paragraphs 3.3 and 4 the optimal power factor under strain due to variation of doping is determined and analyzed, while estimations of the possible figure of merit are given.

2. Methodology

Our approach is based on two ingredients: first-principles density functional theory calculations (DFT), as implemented in the QUANTUM ESPRESSO package [20], and an in-house developed Boltzmann transport code [21] to calculate the thermoelectric transport properties.

2.1. Electronic structure

In a first step the band structure of the strained and unstrained Si was calculated using the generalized gradient approximation (GGA) and the PBE (Perdew–Burke–Emzerhof) exchange correlation functional [22]. Fully relativistic and norm-conserving pseudopotentials [23] were used to treat the spin-orbit splitting of the Si valence bands in a correct way. The calculations were performed with the experimental lattice constant $a = 5.434 \text{ \AA}$ for a face-centered tetragonal eight-atom unit cell. The in-plane biaxial strain is simulated by changing the c/a ratio but keeping the cell volume constant. Throughout the paper the biaxial strain will be given in units of the relative change of the in-plane lattice constant as $\Delta a/a_0 = a/a_0 - 1$. That means tensile strain considers changes $\Delta a/a_0 > 0$, while compressive strain means $\Delta a/a_0 < 0$.

As expected, our DFT calculations underestimate the size of the bandgap at zero temperature and do not reproduce the temperature dependence of the gap. For this purpose we included a temperature-dependent scissor operator [24], so that the strain- and temperature-dependent energy gap E_g in electronvolts becomes

$$E_g\left(T, \frac{\Delta a}{a_0}\right) = E_g\left(T = 0, \frac{\Delta a}{a_0}\right) + U_{\text{GGA}} - \frac{4.73 \times 10^{-4} T^2}{T + 636}, \quad (2)$$

where $E_g(T = 0, \frac{\Delta a}{a_0})$ is the zero-temperature gap obtained by our self-consistent DFT calculations and $U_{\text{GGA}} = 0.57 \text{ eV}$ is a static correction to fulfil the experimental low temperature gap. The third part of equation (2) is the correction of

the temperature dependence of the bandgap [25] in a wide temperature range with T given in K.

2.2. Boltzmann transport

With the converged results from the first step we are now able to obtain the thermoelectric transport properties by solving the linearized Boltzmann equation in the relaxation time approximation (RTA) [21]. Boltzmann transport calculations for thermoelectrics have been carried out for quite a long time and show reliable results for metals [26–29] as well as for wide- and narrow-gap semiconductors [30–33]. In here the relaxation time is assumed to be constant with respect to wavevector k and energy on the scale of $k_B T$. This assumption is widely used for metals and doped semiconductors. The constant relaxation time is a big advantage for the calculation of the thermopower S without any adjustable parameter, while lacking any doping or temperature dependence of τ . For unstrained silicon, doping-dependent relaxation times of the order of 15–150 fs for electron doping and 6–65 fs for hole doping could be estimated from experiments in [34]. To concentrate on the band structure effects we assume the relaxation time does not depend on strain, while it was shown that under strain the dominant scattering process varies: for unstrained Si, the room temperature scattering is dominated by optical phonons, i.e. intervalley scattering, whereas for strained Si, this scattering process is less efficient [35, 36].

The temperature- and doping-dependent thermopower in- and cross-plane is defined as

$$S_{\perp, \parallel} = \frac{1}{eT} \frac{\mathcal{L}_{\perp, \parallel}^{(1)}(\mu, T)}{\mathcal{L}_{\perp, \parallel}^{(0)}(\mu, T)}, \quad (3)$$

where

$$\mathcal{L}_{\perp, \parallel}^{(n)}(\mu, T) = \frac{\tau}{(2\pi)^3} \times \sum_v \int d^3k (v_{k, (\perp, \parallel)}^v)^2 (E_k^v - \mu)^n \left(-\frac{\partial f_{(\mu, T)}}{\partial E} \right)_{E=E_k^v} \quad (4)$$

is the transport distribution function as termed by Mahan and Sofo [37], for a given chemical potential μ at temperature T and carrier concentration N determined by an integration over the density of states $n(E)$:

$$N = \int_{\mu - \Delta E}^{\text{VB}^{\text{max}}} dE n(E) [f_{(\mu, T)} - 1] + \int_{\text{CB}^{\text{min}}}^{\mu + \Delta E} dE n(E) f_{(\mu, T)}, \quad (5)$$

where CB^{min} is the conduction band minimum and VB^{max} is the valence band maximum. As can be seen straightforwardly from equations (3) and (4) the electrical conductivity σ is then given by

$$\sigma_{\perp, \parallel} = 2e^2 \mathcal{L}_{\perp, \parallel}^{(0)}(\mu, T). \quad (6)$$

The Fermi surface integration, which is requested in equation (4), is performed within an extended tetrahedron method [38–40] interpolating the calculated eigenvalues E_k^v on a mesh of at least 13 950 k points in the irreducible part of the Brillouin zone. $\mathcal{L}_{\perp, \parallel}^{(0)}(E, T = 0)$ was determined on a fine energy mesh with a step width of 1 meV. Convergence tests

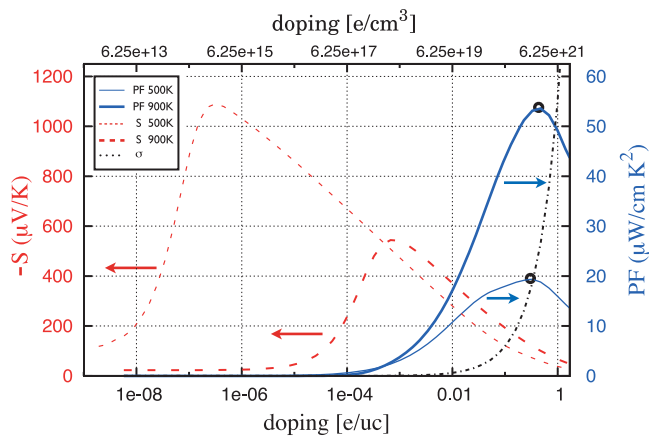


Figure 1. In-plane thermopower (red dashed lines, refer to left scale, red units) and power factor (blue solid lines, refer to right scale, blue units) for unstrained, electron-doped silicon in dependence on the doping level. Furthermore the doping dependence of the electrical conductivity is given as a dashed–dotted line in arbitrary units. The maxima of the power factor are marked by black open circles.

confirmed that the calculation of the electrical conductivity and the thermopower at a given temperature via equations (6) and (3) requires $\mathcal{L}_{\perp,\parallel}^{(0)}(E, T = 0)$ for quite a large range. Convergence of the integrals (4) and (5) was achieved with an adaptive integration method for $2\Delta E \geq 20k_B T$ in the limit of low carrier concentrations $N \leq 1 \times 10^{14} \text{ cm}^{-3}$.

3. Thermoelectric transport

3.1. Unstrained case

Since the thermoelectric transport properties of the strained silicon will always be discussed in comparison with the unstrained case, we will provide an insight into the transport properties of the unstrained silicon. In figure 1, the thermopower and the power factor are shown for two different temperatures (500 and 900 K) in a wide doping range. The qualitative behavior of the electrical conductivity is indicated by the dashed–dotted line to emphasize the trend of the resulting power factor. The picture is well known for the interrelation of electronic transport and the thermoelectric properties of semiconductors [41, 1]. At constant temperature the thermopower (cf the red dashed lines in figure 1) decreases at very low and higher doping levels and reaches a maximum in between [41].

As can be seen from figure 1 the thermopower reaches a maximum around an electron carrier concentration of $1 \times 10^{15} \text{ cm}^{-3}$ at 500 K, while the maximum at 900 K is shifted to a larger doping level of $1 \times 10^{18} \text{ cm}^{-3}$. Besides that, the maximum of the more relevant power factor (cf blue solid lines in figure 1, optimal values indicated by black open circles) is shifted to huge electron carrier concentrations of about $1 \times 10^{21} \text{ cm}^{-3}$. This is determined by the linear increase of the electrical conductivity with increasing charge carrier concentration. Obviously, there is not much space to optimize the power factor with respect to temperature and charge carrier concentration for unstrained silicon. We will

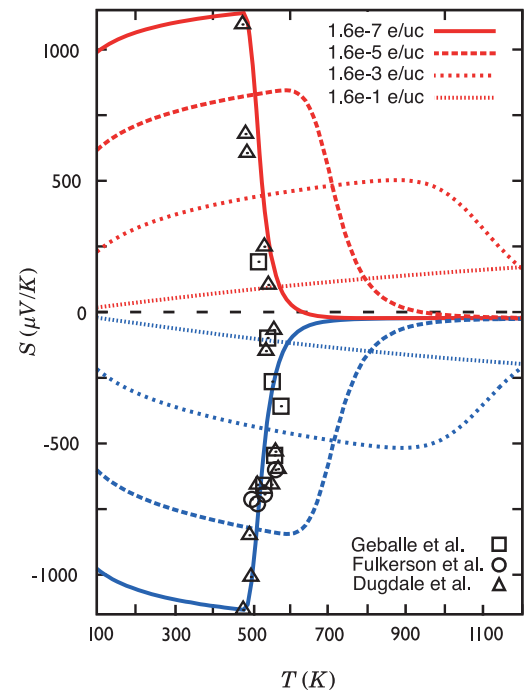


Figure 2. Thermopower for unstrained silicon in dependence on doping and temperature. Electron doping refers to the blue lines in the lower part of the figure, while red lines refer to hole doping and positive values of the thermopower. Experimental data (squares, circles and triangles) from [42–44] are given for comparison.

focus on this optimization in more detail in section 3.3. The complex dependence of the thermopower on temperature and doping is shown in figure 2 for electron- and hole-doped unstrained silicon at different doping concentrations. For low temperatures and doping levels the thermopower reaches values of $1000 \mu\text{V K}^{-1}$ and above, which is caused by the location of the chemical potential near the band edges. The denominator of equation (3), proportional to the electrical conductivity, is small, while the nominator is large and the thermopower becomes maximal. At fixed charge carrier concentration the position of the chemical potential is shifted towards the middle of the gap with increasing temperature. The denominator in equation (3) decreases, because it is mainly determined by the opposite contributions of the tails of the derivative of the Fermi–Dirac distribution function with respect to the valence and conduction bands (equation (4), $n = 1$). At a distinct temperature of about 500 K the thermopower rapidly vanishes. At this temperature the electronic transport enters into the bipolar intrinsic regime. To emphasize the relevance of our calculations experimental results for merely pure silicon in the intrinsic transport regime are added in figure 2. We want to point out that the thermopower does not vanish at all, but converges to small negative values for electron, as well as for hole doping. At large charge carrier concentrations of about 0.16 e/uc (dotted lines in figure 2), where the power factor becomes large, the thermopower grows linearly with temperature up to values of $150 \mu\text{V K}^{-1}$ at 1000 K. In the heavy doped regime the chemical potential is located deep in the bands and equation (3) qualitatively

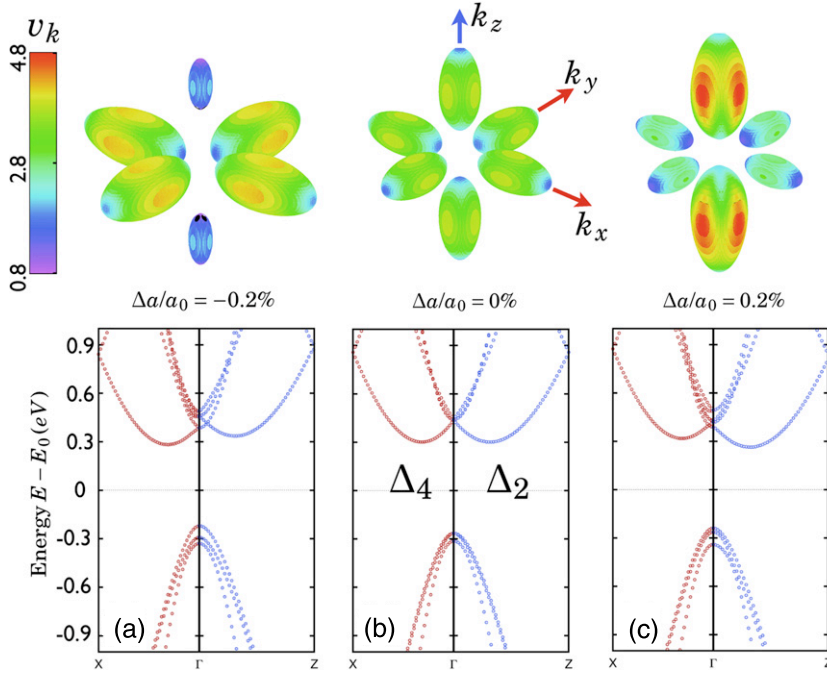


Figure 3. Fermi surfaces of electron-doped silicon under compressive strain (left), no strain (middle) and tensile strain (right). On the Fermi surfaces the absolute value of the group velocities are plotted in units of $0.08 \times 10^6 \text{ m s}^{-1}$. As reference the band structure on two high symmetry lines is given below. The doping corresponds to additionally 0.01 electrons per unit cell which causes carrier densities of $6.25 \times 10^{19} \text{ cm}^{-3}$.

coincides with the well-known MOTT relation $S \propto \frac{d \ln \sigma(E)}{dE} \Big|_{E=\mu}$ for the thermopower in RTA [45].

3.2. Optimization of the power factor by strain

3.2.1. Electron doping. Having provided a general view on the thermoelectric transport properties of unstrained silicon above, we will now focus on the effect of biaxial strain on those properties. The results are presented in comparison to the unstrained case, starting with the electron-doped case, followed by the hole-doped case in section 3.2.2.

In strain-free bulk silicon, as introduced in section 3.1, the conduction band minimum (CBM) consists of six equivalent valleys on the Γ -X high symmetry line as shown in the middle panel of figure 3(b). The Fermi surface pockets corresponding to these valleys are shown on top, with the absolute value of the carrier's group velocity, v_k entering equation (4), plotted in color on the surface. The color code gives v_k in units of $0.08 \times 10^6 \text{ m s}^{-1}$. By applying biaxial in-plane strain, the six CBM valleys are energetically split into two groups: four degenerate in-plane Δ_4 valleys and two degenerate cross-plane Δ_2 valleys (see figures 3(a) and (c)). While the number of electrons is fixed, the different sizes of the ellipsoidal pockets are caused by a change of occupation numbers under strain. The color code indicates the overall smaller Fermi velocities on the small pockets and in particular on the principal axis of the pockets, whereas larger velocities are found for states propagating perpendicular to the principal pocket axis. In figure 4 the thermoelectric transport properties of biaxial strained silicon for two fixed electron doping regimes are shown. First, we consider the left column (figures 4 (a)–(c)),

which shows the electrical conductivity σ , the thermopower S and the resulting power factor $\text{PF} = \sigma S^2$ for a low electron doping of $1.6 \times 10^{-7} \text{ e/uc}$ and a low temperature of 100 K. For this doping and temperature value a large enhancement of up to 35% of the electrical conductivity is obtained for the in-plane component σ_{\parallel} at low tensile strain and for the cross-plane component σ_{\perp} at small compressive strain. σ_{\perp} drops noticeable under small tensile strain up to 30% of the unstrained case, while σ_{\parallel} experiences a slight drop down to 83% under small compressive strain, respectively.

With the conduction bands of silicon behaving parabolically near the band edges, the calculated transport properties can be understood for small charge carrier concentrations and low temperatures in terms of effective masses and occupation number redistributions (see [35]). With increasing tensile strain the Δ_4 bands lift up and the occupied states from the higher bands are transferred to the lowered Δ_2 bands (compare figure 3(c)). At a certain tensile strain the Δ_4 pockets are completely depleted and the maximally occupied Δ_2 states solely contribute to the transport. In a simplified consideration one can estimate the relative change in the electronic conductivity from the relative change in the effective electron mass. As reported earlier [35] it is $m_{\perp, \Delta_2} = m_{\perp, \Delta_4} = 0.205$ and $m_{\parallel, \Delta_2} = m_{\parallel, \Delta_4} = 0.926$, whereas the masses are in units of the free-electron rest mass. For the in-plane component σ_{\parallel} of the electrical conductivity at sufficient tensile strain only the lowered Δ_2 bands contribute with their perpendicular mass m_{\perp, Δ_2} . With the notation

$$\frac{1}{m_0} = \frac{1}{6} \left(\frac{2}{m_{\parallel, \Delta_4}} + \frac{2}{m_{\perp, \Delta_4}} + \frac{2}{m_{\perp, \Delta_2}} \right) = \frac{1}{0.277}, \quad (7)$$

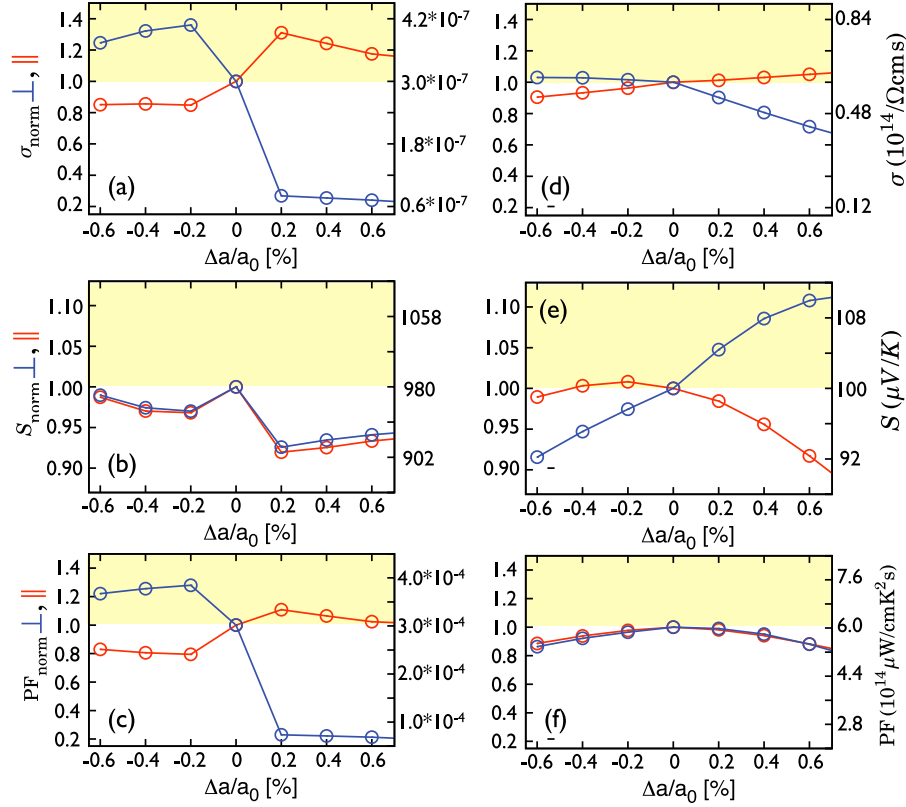


Figure 4. Anisotropic thermoelectric transport properties for fixed temperature and electron doping concentrations in dependence on compressive and tensile strain. Left panels ((a)–(c)) correspond to an electron doping of 1.6×10^{-7} e/uc at a temperature of 100 K, while the right panels refer to an electron doping of 0.48 e/uc at a temperature of 900 K. On the left axis of each figure the relative value compared to the unstrained case is shown, while on the right axis the absolute values are given. Electrical conductivity ((a), (d)) and power factor ((c), (f)) are presented in units of the relaxation time τ .

the normalized asymptotic value becomes

$$\frac{1}{2} \left(\frac{2}{m_{\perp, \Delta_2}} \right) m_0 = 1.35 \quad (8)$$

For the in-plane component σ_{\parallel} of the electrical conductivity at compressive strain only the four pockets of the lowered Δ_4 bands contribute equally with their parallel and perpendicular mass:

$$\frac{1}{4} \left(\frac{2}{m_{\parallel, \Delta_4}} + \frac{2}{m_{\perp, \Delta_4}} \right) m_0 = 0.83. \quad (9)$$

For the cross-plane conductivity σ_{\perp} at tensile strain it is

$$\frac{1}{2} \left(\frac{2}{m_{\parallel, \Delta_2}} \right) m_0 = 0.30, \quad (10)$$

whereas at compressive strain σ_{\perp} becomes

$$\frac{1}{2} \left(\frac{2}{m_{\perp, \Delta_2}} \right) m_0 = 1.35. \quad (11)$$

Since the power factor is composed of σ and S we analyze the influence of strain on the thermopower as well. In the low temperature and doping regime (figure 4 left panel) no enhancement of thermopower at either compressive or tensile strain could be found. It can be seen, that for tensile strain the thermopower decreases by about 10%, while for compressive

strain a drop of about 5% is found. The difference between the in-plane and cross-plane thermopower is marginal. In terms of MOTTs formula [45] it means that the energy dependence of $\mathcal{L}_{\perp, \parallel}^{(0)}(E, T)$ and $\mathcal{L}_{\perp, \parallel}^{(1)}(E, T)$ is almost the same. Nevertheless it is interesting to understand why the thermopower of silicon is reduced under strain and why the decay changes for tensile and compressive strains.

For qualitative understanding of our *ab initio* results we apply a free-electron model to discuss the thermopowers behavior on biaxial strain. The strain-dependent electrical conductivity at zero temperature was modeled as proposed by [35] and then the thermopower was calculated by the MOTTs relation in RTA [45]. Figure 5 shows the resulting thermopower under tensile and compressive strain for a small (dashed line) and a five times larger charge carrier concentration (solid line). For small charge carrier concentration the thermopower rapidly drops to constant values of 48% for tensile and 76% for compressive strain, respectively. We note that the maximum of S which is increased by 4% compared to the unstrained case is not located at zero strain and is shifted to very small values of compressive strain. This behavior is more pronounced for the large charge carrier concentration, where the maximum of the thermopower becomes wider and is shifted to values of -0.25 % compressive strain. Again the enhancement reached for S is about 4% and the asymptotic values remain

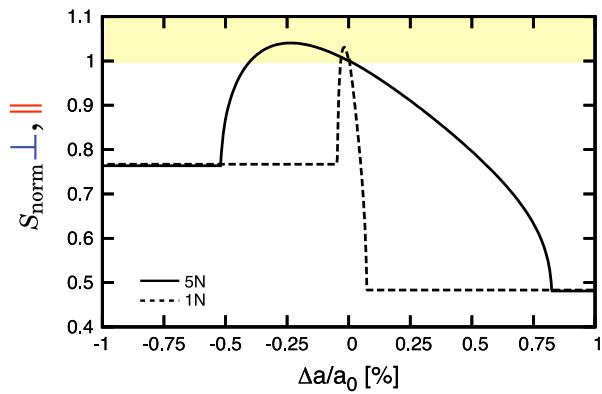


Figure 5. Analytical dependence of the thermopower on biaxial strain for different electron charge carrier concentrations, small charge carrier concentration (dashed lines) and increased charge carrier concentration by a factor of five (solid lines).

unchanged with doping. We note that for the calculation of the thermopower the influence of the effective masses completely cancels. For this reason neither for the *ab initio* nor the analytic calculation was a noticeable difference of the in-plane and cross-plane thermopower found. The different saturation values of the thermopower under tensile and compressive strain again, however, can be explained in terms of a redistribution of electrons. For free electrons at $T = 0$ the electrical conductivity $\sigma \propto E^{3/2}$ and the resulting thermopower $S \propto E^{-1}$. The amount of charge carriers in one spin band is given by $N \propto E^{3/2}$. With the MOTT relation $S \propto N^{-2/3}$. As stated before in this paper under sufficient tensile strain only the twofold-degenerated Δ_2 pockets are occupied compared to the sixfold-degenerated CBM pockets in the unstrained case, so the occupation of every pocket increases by a factor of 3. One directly yields $S_{\text{tens.}}/S_0 = (\frac{6}{2})^{-2/3} = 0.48$. For compressive strain only the fourfold-degenerated Δ_4 pockets contribute, so it is $S_{\text{comp.}}/S_0 = (\frac{6}{4})^{-2/3} = 0.76$. The fact that, for larger charge carrier concentration, larger strain has to be applied to reach these limits, is linked to the fact that higher strain is required to reach a complete redistribution of states into either the Δ_2 or Δ_4 pockets. As a consequence of the discussed results we see in figure 4(c) an enhancement of the power factor in cross-plane direction up to 27% at small compressive strain, while the in-plane power factor is only marginally enhanced by about 5% under low tensile strain. In-plane transport under tensile strain at low doping and low temperature plays an important role in silicon-based devices. Within figure 4(c) it is obvious that the strain-induced influence of the power factor on this transport will play a minor role. We want to point out that the results on the thermopower discussed above are generally valid for all systems with degenerate occupied bands. Lifting of the degeneracy causes redistribution of electrons and reduction of the thermopower. While the low temperature and low doping case was convenient to provide some general findings on an analytical level, we will now focus on the high temperature and high doping regime (see figure 4 left panels) where the power factor might be suitable for thermoelectric application (see also figure 1). At a temperature of 900 K the electronic band structure on a width of at least

$\pm\Delta E = \pm 770$ meV around the position of the chemical potential has to be included, which makes a description of the electronic transport properties within a spherical band picture impossible. Rather than providing analytical quantities a more qualitative description of our *ab initio* calculations will be given instead. The electrical conductivity in figure 4(d) states the same qualitative tendencies for σ_{\parallel} and σ_{\perp} as derived for the low temperature case. As a consequence of the high temperature and the related broadening of the Fermi-Dirac distribution in equations (4) and (5) as well as the high charge carrier concentration the redistribution of states as described before is not completed for the strain values considered here. The analytical limits for the enhancement of σ_{\parallel} and σ_{\perp} for the given high doping and temperature should be achieved for biaxial strains of at least $\Delta a/a_0 = \pm 3\%$, respectively. It is worth mentioning that the absolute value (cf right scales in figures 4(a) and (d)) of the electrical conductivity is raised enormously compared to the low doping case as expected. As a consequence, the power factor rises absolutely but unfortunately no enhancement via strain was obtained. The strain-dependent behavior of the thermopower as shown in figure 4(e) compensates the behavior of the electrical conductivity. In the high-doping-high-temperature regime the thermopower shows a noticeable anisotropy between in-plane and cross-plane components. While the in-plane component S_{\parallel} confirms our analytical predictions for high doping (see the black solid line in figure 5) and even shows the shifted maximum to compressive strain, the cross-plane component S_{\perp} does not follow the analytical model. This might be explained by multiband effects and nonparabolic bands, with the latter being more relevant in the cross-plane direction. The overall resulting power factor summarized in figure 4(f) shows, however, no significant anisotropy. Furthermore no enhancement by biaxial strain could be obtained; in contrast a decrease of about 20% occurs.

3.2.2. Hole doping. We will now focus in more detail on the thermoelectric properties of hole-doped biaxially strained silicon as presented in figure 6. Under full relativistic treatment the three valence bands next to the VBM at the Γ -point are the heavy hole (HH), light hole (LH), and spin-orbit split-off (SO) hole. While the HH and LH are degenerate, the SO lies 44 meV apart (see figure 3 middle panel). Under biaxial tensile or compressive strain, the valence bands become highly anisotropic and a crossover between bands occurs so that they even lose their original meaning [46]. It was shown that mechanical deformation-induced changes in the band structure offers potential for significant enhancement of the hole mobility [47]. Nevertheless, a straightforward explanation of the *ab initio* calculations as done for the electron-doped case is not any longer possible. Actually tensile and compressive biaxial strain does not only cancel the degeneracy of the heavy and light hole bands, which will cause reduced intervalley phonon scattering, but it also leads to a smaller effective conductivity mass and a further depletion of the uppermost hole band [14, 48]. Similarly to the electron-doped case in figure 6 the thermoelectric transport properties for hole-doped silicon under the influence of biaxial strain are shown for

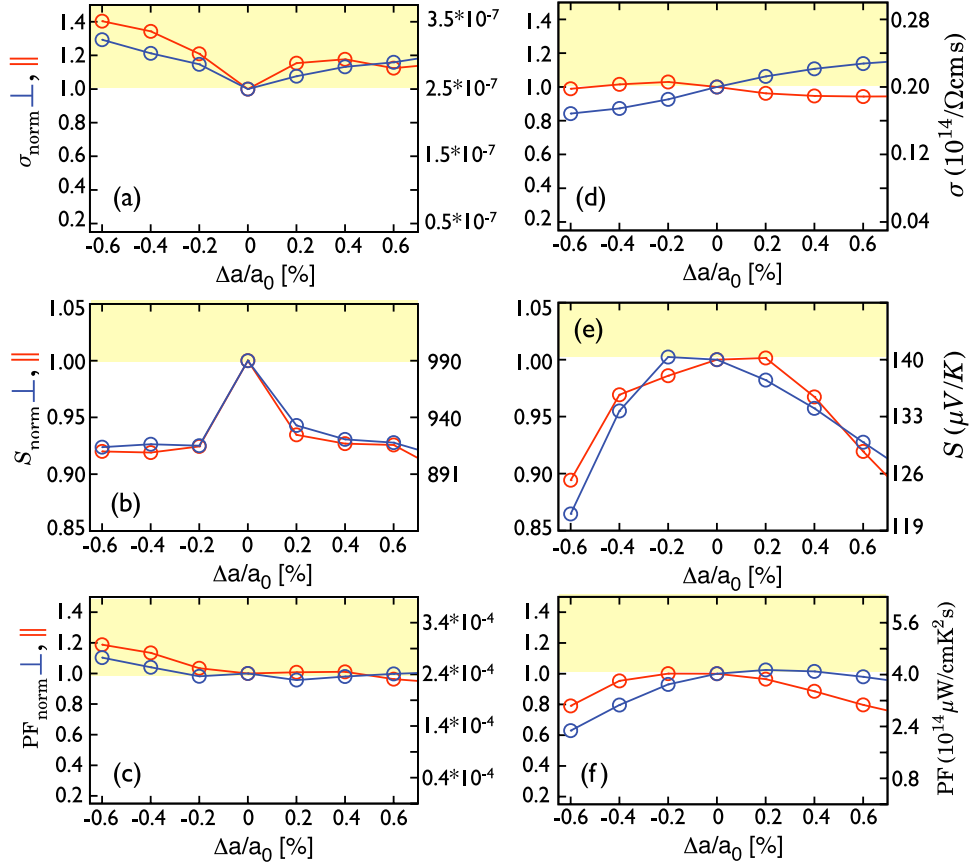


Figure 6. Anisotropic thermoelectric transport properties for fixed temperature and hole doping concentrations in dependence on compressive and tensile strain. Left panels ((a)–(c)) correspond to a hole doping of 1.6×10^{-7} h/uc at a temperature of 100 K, while right panels refer to a hole doping of 0.16 h/uc at a temperature of 900 K. On the left axis of each figure the relative value compared to the unstrained case is shown, while on the right axis absolute values are given. Electrical conductivity ((a),(d)) and power factor ((c),(f)) are presented in units of the relaxation time τ .

a fixed low doping, low temperature in figures 6(a)–(c) and fixed high doping, high temperature regime in figures 6(d)–(f). At low temperature and slight doping an increase of the electrical conductivity was found for tensile as well as for compressive strain for the in-plane component σ_{\parallel} and the cross-plane component σ_{\perp} , while biaxial compressive strain tends to favor the enhancement of σ . As shown in figure 6(b) the thermopower for hole-doped silicon again experiences a drop of nearly 7% under compressive and tensile strain. A possible explanation for the almost symmetric drop of the thermopower under compressive and tensile strain might again be related to the number of bands being occupied. At small doping for compressive and for tensile biaxial strain the primarily occupied HH and LH split and only the upper hole band is depleted and dominates the character of the transport properties [14, 48]. Extending our analytical findings for the electron-doped case one would expect that $S_{\text{tens./compress.}}/S_0 = (\frac{2}{3})^{-2/3} = 0.63$. Through the counteracting behavior of electrical conductivity and thermopower under strain, again no enhancement of the power factor could be found (cf figure 6(c)). Only under strong compressive biaxial strain a significant enhancement is visible in the low temperature/low doping case. In the high doping and temperature regime not only does the upper hole band plays an important role in

transport, but furthermore the former HH, LH and SO have to be mentioned. As shown in figure 6(d) an enhancement of around 10% compared to the unstrained case can be found for the cross-plane component σ_{\perp} under small tensile strain. For the in-plane electrical conductivity σ_{\parallel} under compressive strain only a marginal influence on the strain can be reported. The thermopower shows a small anisotropy of the in-plane and cross-plane components. While the thermopower is mainly decreased for compressive or tensile strain, we again see a broadening of the thermopower drop in dependence on the applied strain with respect to the low doping regime. Besides the absolute values of the power factor being around 30% smaller than in the electron-doped case (compare figures 4(f) and 6 (f)), a slight enhancement under thermoelectrically relevant doping and temperature conditions could be found for the cross-plane power factor PF_{\perp} under small tensile strain (see figure 6(f)).

3.3. Optimization of the power factor by doping

While up to this point the power factor and the incorporated thermoelectric transport properties were studied for fixed temperature and charge carrier concentration in dependence on the applied biaxial strain, we want to gain further insight

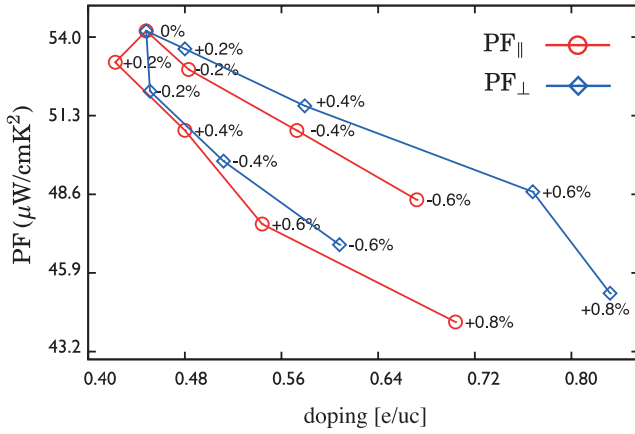


Figure 7. Anisotropic power factor optimized by the carrier concentration at given strain state for electron-doped silicon. The in-plane (cross-plane) power factors are drawn as red circles (blue diamonds). Lines are shown to guide the eyes. The temperature is fixed at 900 K.

into the doping dependence. Therefore the amount of charge carrier concentration to optimize the power factor $PF_{||}$ and PF_{\perp} at given strain and fixed temperature of 900 K was determined. This temperature seems to be a common temperature for thermoelectric application of silicon-based devices. Figures 7 and 8 represent the results for the electron- and hole-doped case, respectively.

From figure 7 it becomes clear that an enhancement of the power factor by sufficiently high electron doping cannot be stated. With increasing biaxial strain the in-plane and cross-plane thermopower decreases compared to the unstrained case. It is worth mentioning that the charge carrier concentration has to be increased for increasing tensile and compressive biaxial strain to achieve the optimal power factor under the certain strain condition. Nevertheless, even for a raised optimal charge carrier concentration the power factor drops to about 80% of the value of the unstrained case for the largest strain values considered here. As an interesting fact one can see that under tensile strain the cross-plane power factor PF_{\perp} is always larger than the in-plane component $PF_{||}$, while under compressive strain it is the other way around and PF_{\perp} is smaller than $PF_{||}$. In contrast to heavily electron-doped silicon an enhancement of the power factor could be found for hole-doped silicon, as shown in figure 8. Nevertheless, the enhancement is limited to the cross-plane contribution PF_{\perp} . Here we find an enhanced PF_{\perp} under small tensile strain of $\Delta a/a_0 = 0.2\% \dots 0.4\%$, while for tensile strain of 0.6% a value of the cross-plane power factor similar to the unstrained case is reached. We note that the charge carrier concentrations, which are necessary to optimize the power factor in the hole doping case, are about three times smaller than in the related electron doping case. Even though an enhancement of the cross-plane power factor under optimized hole doping and tensile strain can be found, unfortunately the absolute values of the power factor are sufficiently smaller than the absolute value of the $PF_{||}$ and PF_{\perp} of electron-doped silicon under all strain conditions examined here.

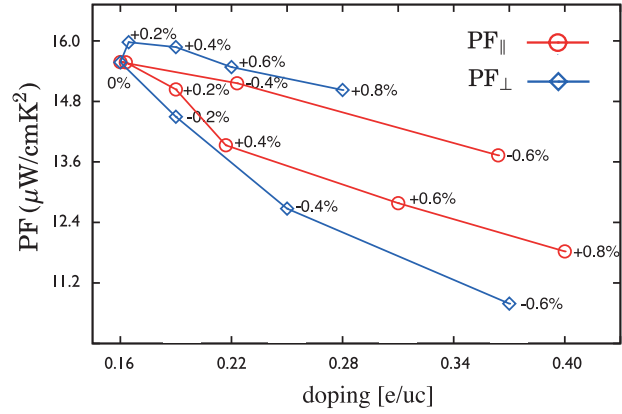


Figure 8. Same as figure 7 but optimized for hole doping.

4. Tendencies on figure of merit

To evaluate tendencies of the figure of merit we are going to include and discuss experimental results for the lattice thermal conductivity κ_{ph} , which adds up to our calculated electronic thermal conductivity κ_{el} for the total thermal conductivity κ . Involving the transport distribution function in equation (4) the electronic contribution to the thermal conductivity is calculated as

$$\kappa_{el} = \frac{1}{T} \left(\mathcal{L}^{(2)} - \frac{(\mathcal{L}^{(1)})^2}{\mathcal{L}^{(0)}} \right). \quad (12)$$

For bulk silicon, porous silicon and thin films, various temperature- and doping-dependent measurements are available [49–51, 12, 52]. It is well known that the lattice thermal conductivity of silicon is strongly dependent on temperature. While at room temperature a value of $87 \text{ W m}^{-1} \text{ K}^{-1}$ was reported, this value decreases to $36 \text{ W m}^{-1} \text{ K}^{-1}$ at 900 K and $23 \text{ W m}^{-1} \text{ K}^{-1}$ at 1200 K [12, 50], making silicon a high temperature thermoelectric. Even at high temperatures and applicable doping the electronic contribution to the thermal conductivity is only a few per cent of the total thermal conductivity. For bulk silicon it is reported that the heat conduction is impeded by higher dopant concentrations [51]. Here the lattice thermal conductivity reduction due to the scattering by dopant ions overbalances the increase of the electronic thermal conductivity. Due to this behavior the total thermal conductivity κ is weakly dependent on doping for temperatures clearly above 300 K [49, 52]. Nevertheless, for nanostructured silicon, e.g. in silicon-based superlattices [11, 53] or nanoparticle bulk silicon [12], with a low lattice thermal conductivity of $\kappa_{ph} < 3 \text{ W m}^{-1} \text{ K}^{-1}$, it may occur that the electronic thermal conductivity contributes remarkably to the total thermal conductivity. At high doping levels above $1 \times 10^{20} \text{ cm}^{-3}$ and temperature of 900 K the electronic contribution κ_{el} can be around $1\text{--}3 \text{ W m}^{-1} \text{ K}^{-1}$ and therefore approx. 25–50% of the total thermal conductivity. While it was recently shown [54, 11], that tensile strain could lead to a reduction of the thermal conductivity by up to 15% in bulk silicon as well as in silicon thin films, we did not

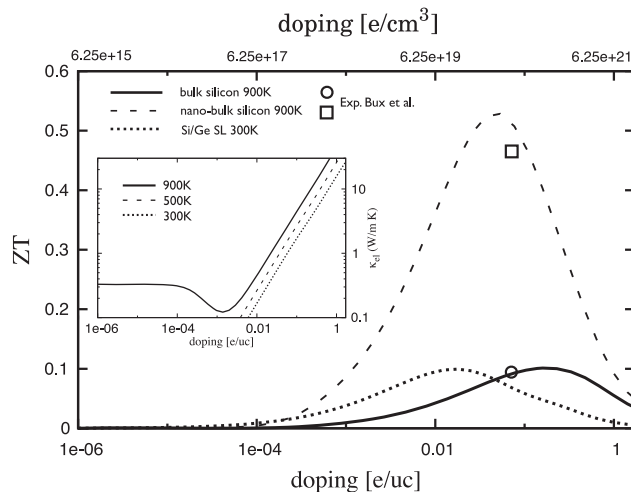


Figure 9. Calculated doping-dependent figure of merit for n-doped bulk silicon at 900 K (solid line), nanobulk silicon at 900 K (dashed line) and strained Si/Ge superlattice at 300 K (dotted line). The inset shows the doping-dependent electronic contribution to the total thermal conductivity for 300, 500 and 900 K. Experimental data (open square and circle) from [12] are given for comparison. Note the logarithmic axes.

include this in our estimation. In figure 9(a) the doping-dependent figure of merit for three silicon-based systems is shown. We assumed doping-independent experimental lattice thermal conductivities, stated for high doping rates, to include the reduction of κ_{ph} by ion scattering. Values of $\kappa_{ph} = 36 \text{ W m}^{-1} \text{ K}^{-1}$ [12], $\kappa_{ph} = 3.8 \text{ W m}^{-1} \text{ K}^{-1}$ [12] and $\kappa_{ph} = 1.9 \text{ W m}^{-1} \text{ K}^{-1}$ [11] were used for single-crystalline bulk silicon, nanostructured bulk silicon and an Si/Ge superlattice, respectively. Here we consider only electron doping, which appeared to be most promising. The calculated doping-dependent electronic part κ_{el} is shown in the inset of figure 9 for three different temperatures. For bulk silicon (solid line in figure 9) we find a broad maximum for the figure of merit $ZT \approx 0.1$ at 900 K and high doping levels of $N \approx 6.5\text{--}18 \times 10^{20} \text{ cm}^{-3}$, which is in good agreement to experiments by Bux *et al* [12]. Compared to the related power factor (see figure 1) the maximum shifts to lower doping concentrations due to the linear increase of κ_{el} at higher doping rates, and therefore a stronger decrease of ZT at high doping rates. If a reduction of the lattice thermal conductivity can be achieved by nano-inclusions as reported in [12] a remarkable ZT of about 0.5 at $N = 3 \times 10^{20} \text{ cm}^{-3}$ at 900 K could be obtained, making silicon an interesting high temperature thermoelectric (dashed line in figure 9). Nevertheless, at room temperature the lowest thermal conductivities have been stated for silicon- and germanium-based superlattices [11, 53]. Therefore the dotted line in figure 9 estimates the figure of merit for an Si/Ge superlattice with a period of 15 nm assuming no degradation of the electronic transport by the heterostructure. Here, at 300 K, the maximum figure of merit is found around doping levels of $7 \times 10^{19} \text{ cm}^{-3}$ with values of about 0.1, which are comparable to single-crystalline silicon at 900 K at ten times larger doping levels.

5. Conclusion

In conclusion, the thermoelectric transport properties of biaxially strained silicon were studied in detail with respect to a possible enhancement of the power factor. Two different doping and temperature regimes were analyzed in detail: a low doping ($N \approx 1 \times 10^{14} \text{ cm}^{-3}$) and low temperature regime ($T = 100 \text{ K}$) suitable for metal-oxide-semiconductor device applications, and a heavy doping ($N \approx 1 \times 10^{20} \text{ cm}^{-3}$) and high temperature regime ($T = 900 \text{ K}$) suitable for silicon-based thermoelectric modules.

It was shown that the electronic transport properties, namely the electrical conductivity σ and the thermopower S , are highly sensitive against strain. Nevertheless it was found that strain-induced effects in σ and S compensate each other, and no remarkable enhancement of the power factor by either compressive or tensile biaxial strain can be reached. On the other hand, a reduction of the power factor of up to 20% (30%) under electron (hole) doping due to the influence of strain was found. The latter was assigned to a large extent to band-structure-related redistribution of electrons. Estimations for the figure of merit under electron doping are given.

As a general result we showed that, when degenerate VBM or CBM exist, the thermopower decreases with deformation due to a redistribution of electrons in energetically lifted valleys. This could be the general explanation of the reduction of the electronic thermoelectric properties in strain-influenced heterostructures.

Acknowledgments

This work was supported by the Deutsche Forschungsgemeinschaft, SPP 1386 ‘Nanostrukturierte Thermoelektrika: Theorie, Modellsysteme und kontrollierte Synthese’. NFH is a member of the International Max Planck Research School for Science and Technology of Nanostructures. We want to thank Florian Rittweger for computational assistance.

References

- [1] Snyder G J and Toberer E S 2008 Complex thermoelectric materials *Nature Mater.* **7** 105–14
- [2] Sales B C 2002 Thermoelectric materials: smaller is cooler *Science* **295** 1248
- [3] Majumdar A 2004 Thermoelectricity in semiconductor nanostructures *Science* **303** 777
- [4] Böttner H, Chen G and Venkatasubramanian R 2006 Aspects of thin-film superlattice thermoelectric materials *MRS Bull.* **31** 211
- [5] Venkatasubramanian R, Siivola E and Colpitts T 2001 Thin-film thermoelectric devices with high room-temperature figures of merit *Nature* **413** 597
- [6] Harman T, Taylor P, Walsh M and LaForge B 2002 Quantum dot superlattice thermoelectric materials and devices *Science* **297** 2229
- [7] Dresselhaus M, Chen G, Tang M and Yang R 2007 New directions for low-dimensional thermoelectric materials *Adv. Mater.* **19** 1
- [8] Vining C B 2008 Materials science: desperately seeking silicon *Nature* **451** 132–3

- [9] Hochbaum A, Chen R, Delgado R and Liang W 2008 Enhanced thermoelectric performance of rough silicon nanowires *Nature* **451** 163
- [10] Boukai A I, Bunimovich Y, Tahir-Kheli J, Yu J K, Goddard W A III and Heath J R 2008 Silicon nanowires as efficient thermoelectric materials *Nature* **451** 168–71
- [11] Lee S, Cahill D and Venkatasubramanian R 1997 Thermal conductivity of Si–Ge superlattices *Appl. Phys. Lett.* **70** 2957
- [12] Bux S K, Blair R G, Gogna P K, Lee H, Chen G, Dresselhaus M S, Kaner R B and Fleurial J-P 2009 Nanostructured bulk silicon as an effective thermoelectric material *Adv. Funct. Mater.* **19** 2445–52
- [13] Hao Q, Zhu G, Joshi G, Wang X, Minnich A, Ren Z and Chen G 2010 Theoretical studies on the thermoelectric figure of merit of nanograined bulk silicon *Appl. Phys. Lett.* **97** 063109
- [14] Baykan M O, Thompson S E and Nishida T 2010 Strain effects on three-dimensional, two-dimensional, and one-dimensional silicon logic devices: predicting the future of strained silicon *J. Appl. Phys.* **108** 093716
- [15] Prinz V and Golod S 2006 Elastic silicon-film-based nanoshells: formation, properties, and applications *J. Appl. Mech. Tech. Phys.* **47** 867
- [16] Schmidt O and Eberl K 2001 Nanotechnology: thin solid films roll up into nanotubes *Nature* **410** 168
- [17] Cho A 2006 Pretty as you please, curling films turn themselves into nanodevices *Science* **313** 164–5
- [18] Jeong M, Doris B, Kedzierski J and Rim K 2004 Silicon device scaling to the sub-10 nm regime *Science* **306** 2057
- [19] Fischetti M and Gamiz F 2002 On the enhanced electron mobility in strained-silicon inversion layers *J. Appl. Phys.* **92** 7320
- [20] Giannozzi P *et al* 2009 QUANTUM ESPRESSO: a modular and open-source software project for quantum simulations of materials *J. Phys.: Condens. Matter* **21** 395502
- [21] Mertig I 1999 Transport properties of dilute alloys *Rep. Prog. Phys.* **62** 237–76
- [22] Perdew J P 1981 Self-interaction correction to density-functional approximations for many-electron systems *Phys. Rev. B* **23** 5048–79
- [23] Corso A and Conte A 2005 Spin–orbit coupling with ultrasoft pseudopotentials: application to Au and Pt *Phys. Rev. B* **71** 115106
- [24] Godby R W, Schlüter M and Sham L J 1988 Self-energy operators and exchange–correlation potentials in semiconductors *Phys. Rev. B* **37** 10159–75
- [25] Varshni Y P 1967 Temperature dependence of the energy gap in semiconductors *Physica* **34** 149–54
- [26] Vojta T, Mertig I and Zeller R 1992 Calculation of the residual resistivity and the thermoelectric power of sp impurities in silver *Phys. Rev. B* **46** 15761
- [27] Thonhauser T, Scheidmantel T J and Sofo J O 2004 Improved thermoelectric devices using bismuth alloys *Appl. Phys. Lett.* **85** 588
- [28] Yang J, Li H, Wu T and Zhang W 2008 Evaluation of half-heusler compounds as thermoelectric materials based on the calculated electrical transport properties *Adv. Funct. Mater.* **18** 2880
- [29] Barth J, Fecher G H, Balke B, Ouardi S, Graf T, Felser C, Shkabko A, Weidenkaff A, Klaer P and Elmers H J 2010 *Phys. Rev. B* **81** 064404
- [30] Singh D J 2010 Doping-dependent thermopower of PbTe from Boltzmann transport calculations *Phys. Rev. B* **81** 195217
- [31] Parker D and Singh D 2010 High-temperature thermoelectric performance of heavily doped PbSe *Phys. Rev. B* **82** 035204
- [32] May A F, Singh D J and Snyder G J 2009 Influence of band structure on the large thermoelectric performance of lanthanum telluride *Phys. Rev. B* **79** 153101
- [33] Lee M-S, Poudeu F and Mahanti S 2011 Electronic structure and thermoelectric properties of Sb-based semiconducting half-Heusler compounds *Phys. Rev. B* **83** 085204
- [34] Jacoboni C, Canali C, Ottaviani G and Quaranta A A 1977 A review of some charge transport properties of silicon *Solid-State Electron.* **20** 77–89
- [35] Dziekan T, Zahn P, Meded V and Mirbt S 2007 Theoretical calculations of mobility enhancement in strained silicon *Phys. Rev. B* **75** 195213
- [36] Roldán J B, Gámiz F, LópezVillanueva J A and Carceller J E 1996 A Monte Carlo study on the electron-transport properties of high-performance strained-Si on relaxed Si–Ge channel MOSFETs *J. Appl. Phys.* **80** 5121
- [37] Mahan G and Sofo J 1996 The best thermoelectric *Proc. Natl Acad. Sci.* **93** 7436
- [38] Lehmann G and Taut M 1972 On the numerical calculation of the density of states and related properties *Phys. Status Solidi b* **54** 469–77
- [39] Zahn P, Mertig I, Richter M and Eschrig H 1995 *Ab initio* calculations of the giant magnetoresistance *Phys. Rev. Lett.* **75** 2996–9
- [40] Mertig I, Mrosan E and Ziesche P 1987 *Multiple Scattering Theory of Point Defects in Metals: Electronic Properties* (Leipzig: B G Teubner)
- [41] Ioffe A F 1960 *Physics of Semiconductors* (New York: Academic)
- [42] Geballe T and Hull G 1955 Seebeck effect in silicon *Phys. Rev.* **98** 940
- [43] Fulkerson W, Moore J, Williams R and Graves R 1968 Thermal conductivity, electrical resistivity, and seebeck coefficient of silicon from *Phys. Rev.* **167** 765
- [44] Dugdale J S 1977 *The Electrical Properties of Metals and Alloys* (London: Edward Arnold)
- [45] Cutler M and Mott N 1969 Observation of Anderson localization in an electron gas *Phys. Rev.* **181** 1336
- [46] Yu D, Zhang Y and Liu F 2008 First-principles study of electronic properties of biaxially strained silicon: effects on charge carrier mobility *Phys. Rev. B* **78** 245204
- [47] Nayak D K and Chun S K 1995 Low field hole mobility of strained Si on (100) Si_{1-x}Ge_x substrate *Appl. Phys. Lett.* **64** 2514
- [48] Sun G, Sun Y, Nishida T and Thompson S E 2007 Hole mobility in silicon inversion layers: stress and surface orientation *J. Appl. Phys.* **102** 084501
- [49] Brinson M and Dunstant W 1970 Thermal conductivity and thermoelectric power of heavily doped n-type silicon *J. Phys. C: Solid State Phys.* **3** 483
- [50] Shanks H, Maycock P, Sidles P and Danielson G 1963 Thermal conductivity of silicon from 300 to 1400 K *Phys. Rev.* **130** 1743–8
- [51] Slack G A 2004 Thermal conductivity of pure and impure silicon, silicon carbide, and diamond *J. Appl. Phys.* **35** 3460
- [52] Ashghi M, Kurabayashi K, Kasnavi R and Goodson K E 2002 Thermal conduction in doped single-crystal silicon films *J. Appl. Phys.* **91** 5079
- [53] Borca-Tasciuc T 2000 Thermal conductivity of symmetrically strained Si/Ge superlattices *Superlatt. Microstruct.* **28** 199–206
- [54] Li X, Maute K, Dunn M and Yang R 2010 Strain effects on the thermal conductivity of nanostructures *Phys. Rev. B* **81** 245318

Thermoelectric transport in strained Si and Si/Ge heterostructures

N F Hinsche¹, I Mertig^{1,2} and P Zahn^{1,3}

¹ Institut für Physik, Martin-Luther-Universität Halle-Wittenberg, D-06099 Halle, Germany

² Max-Planck-Institut für Mikrostrukturphysik, Weinberg 2, D-06120 Halle, Germany

³ Helmholtz-Zentrum Dresden-Rossendorf, PO Box 51 01 19, D-01314 Dresden, Germany

E-mail: nicki.hinsche@physik.uni-halle.de

Received 23 April 2012, in final form 23 May 2012

Published 19 June 2012

Online at stacks.iop.org/JPhysCM/24/275501

Abstract

The anisotropic thermoelectric transport properties of bulk silicon strained in the [111]-direction were studied by detailed first-principles calculations focusing on a possible enhancement of the power factor. Electron and hole doping were examined in a broad doping and temperature range. At low temperature and low doping an enhancement of the power factor was obtained for compressive and tensile strain in the electron-doped case and for compressive strain in the hole-doped case. For the thermoelectrically more important high-temperature and high-doping regime a slight enhancement of the power factor was only found under small compressive strain with the power factor overall being robust against applied strain. To extend our findings the anisotropic thermoelectric transport of a [111]-oriented Si/Ge superlattice was investigated. Here, the cross-plane power factor under hole doping was drastically suppressed due to quantum-well effects, while under electron doping an enhanced power factor was found. For this, we state figures of merit of $ZT = 0.2$ and 1.4 at $T = 300$ and 900 K for the electron-doped [111]-oriented Si/Ge superlattice. All results are discussed in terms of band structure features.

(Some figures may appear in colour only in the online journal)

1. Introduction

Thermoelectric phenomena were first described for metals by Seebeck at the beginning of the 19th century and revived by Ioffe in the late 1950s by the introduction of semiconductors to thermoelectric devices [1, 2]. However, since then thermoelectrics have been restricted to a scientific and economic niche mainly due to their poor conversion efficiency [3, 4]. Nowadays the emerging global need for energy production and conservation has intensified interest and research in more effective alternative energy technologies to reduce our dependence on fossil fuels. Contributing to this, thermoelectric devices could partially convert wasted heat into electricity by their ability to transform heat directly into electric current, and vice versa [5].

The thermoelectric conversion efficiency can be stated by the figure of merit (FOM)

$$ZT = \frac{\sigma S^2}{\kappa_{\text{el}} + \kappa_{\text{ph}}} T, \quad (1)$$

where σ is the electrical conductivity, S is the thermopower, κ_{el} and κ_{ph} are the electronic and phononic contributions to the thermal conductivity, respectively. The numerator of equation (1) is called the power factor $\text{PF} = \sigma S^2$ and characterizes the electric power output.

While thermoelectric devices are extremely facile, have no moving parts, and do not produce greenhouse gases [6], two obstacles limit their applicability. The first, a low efficiency, could be challenged by the nanostructured thermoelectrics of today enabling large values of $ZT \gg 1$ [7–9]. As a second drawback, the materials are based on environmentally hazardous or rare lead, tellurium or selenium compounds and are therefore hard to integrate in semiconductor electronics.

However, current research has achieved tremendous progress in enabling silicon for thermoelectrics. Silicon is non-toxic, readily available, cheap and well integrated in the present electronics infrastructure, so this might be a considerable leap forward. While silicon has been stated as an inefficient thermoelectric in the past due to its enormous

thermal conductivity [10], recent experimental and theoretical attempts have revealed that nanostructuring could lead to thermoelectric efficiencies comparable to state-of-the-art commercial thermoelectric materials [11–14].

Besides the reduction of thermal conductivity, that is the denominator in equation (1), Koga *et al* showed in a seminal work [15, 16] that it should be possible to enhance the power factor, that is the numerator in equation (1). This concept of carrier pocket engineering uses the influence of strain to optimize the band structure of silicon and germanium based superlattices (SLs) regarding their electronic transport. As a main result it was found that the effect of the lattice strain at the Si/Ge interfaces is more relevant for strain in the [111]-direction than in the [001]-direction with respect to a possible enhancement of the power factor. In fact, $ZT = 1.25$ and $ZT = 0.98$ at room temperature were predicted for strain-non-symmetrized and strain-symmetrized [111]-oriented Si/Ge-SLs, respectively, and the ZT values are shown to increase significantly at elevated temperatures [17].

While in a previous study we have already concentrated on the influence of biaxial in-plane strain in the [001]-direction on the thermoelectric properties of silicon [18], we will focus here on the influence of strain along the [111]-direction. For this purpose the paper is organized as follows. In section 2 we introduce our approach based on first principle electronic structure calculations within density functional theory and transport calculations based on the solution of the linearized Boltzmann equation. By this means we start the discussion of the thermoelectric transport properties of bulk silicon strained along the [111]-direction in dependence on the strain and doping to gain insight into the physical mechanisms, which clearly differ from the [001]-strain case. A discussion is given for electron as well as for hole doping in sections 3.1 and 3.2, respectively.

To extend the findings for strained bulk silicon, in section 3.3 results for an exemplary Si/Ge-SL grown on Si in the [111]-direction are presented. Here the influence of tensile strain in the [111]-direction, induced by the lattice mismatch at the Si/Ge interface, is investigated with respect to the thermoelectric transport in-plane and cross-plane in the SL. Again, the temperature and doping dependences of the thermoelectric properties are discussed for electron and hole doping regarding a possible enhancement of the power factor. A further aspect will be the influence of structural relaxation and chemical composition on the transport properties. At the end of the paper, in section 3.4 insights into the FOM will be presented along with the electronic part of the thermal conductivity, to give a clue on optimal charge carrier concentrations to obtain the best FOM.

While focusing our interest on the high-temperature thermoelectric application of strained silicon, our results in the room-temperature regime could be of importance for the metal–oxide–semiconductor device community. Knowledge of the thermoelectric properties of silicon under strain could help in understanding parasitic effects on the electronic transport in those structures. In this low-temperature and low-doping regime we confirm a remarkable influence of externally applied strain on the electrical transport under electron and hole doping.

2. Methodology

Our approach is based on two constituents: first-principles density functional theory calculations (DFT), as implemented in the QuantumEspresso package [19] and an in-house developed Boltzmann transport code [18, 20–22] to calculate the thermoelectric properties.

First, the band structure of the strained and unstrained Si was calculated using the general gradient approximation (GGA) with the Perdew–Burke–Ernzerhof (PBE) flavour of exchange correlation functional [23]. Fully relativistic and norm-conserving pseudopotentials [24] were used to treat the spin–orbit splitting of the Si valence bands appropriately. The calculations for the bulk Si were performed with the rhombohedral experimental lattice constant $a_0 = 5.434 \text{ \AA}/\sqrt{2}$ for a rhombohedral two atom unit cell, which is sketched in the inset of figure 1(c). The strain in the [111]-direction under constant volume is simulated by changing the lattice constant a and the angle α_r . Throughout the paper the biaxial strain will be given in units of the relative change of the in-plane lattice constant, that is the nearest neighbour distance in the [111]-plane as $\Delta a = a_{[111]}$ or a_{\parallel}/a_0 following the notation of previous works [18, 21, 25, 26]. The angle α_r is given by $\cos \alpha_r = 1 - \frac{3(1+\Delta a/a_0)^6}{4+2(1+\Delta a/a_0)^6}$. That means that tensile in-plane strain considers changes $\Delta a/a_0 > 0$ and $\alpha_r > 60^\circ$, while compressive in-plane strain means $\Delta a/a_0 < 0$ and $\alpha_r < 60^\circ$. As used previously in the literature, tensile strain along the [111]-direction coincides with compressive in-plane strain as denoted here.

By this trigonal deformation an atomic relaxation of the atomic positions inside the unit cell is possible, as the displacement of the two sublattices along the [111]-direction is no longer given by symmetry. To obtain the atomic positions of the strained silicon we performed structural relaxations using VASP [27]. The atomic positions were optimized such that the Hellmann–Feynman forces on them were below 0.1 meV \AA^{-1} . At the same time the given deformed lattice parameters were not allowed to relax and conservation of the unit cell volume was assumed. A volume relaxation at the maximum strain $\Delta a/a_0 \pm 1\%$ resulted in a volume reduction by 0.2% which corresponds to a lattice constant change by less than 0.1%.

As expected, our DFT calculations underestimate the size of the bandgap at zero temperature and do not reproduce the temperature dependence of the gap. For this purpose we implemented a temperature-dependent scissor operator [28], so that the strain- and temperature-dependent energy gap E_g becomes

$$E_g \left(T, \frac{\Delta a}{a_0} \right) = E_g \left(T = 0, \frac{\Delta a}{a_0} \right) + U_{\text{GGA}} - \frac{\alpha T^2}{T + \beta}, \quad (2)$$

where $E_g(T = 0, \frac{\Delta a}{a_0})$ is the zero temperature gap obtained by our self-consistent DFT calculations, $U_{\text{GGA}} = 0.57 \text{ eV}$ is a static correction to reproduce the experimental low-temperature gap and the third part of equation (2) is the correction of the temperature dependence of the bandgap in a wide temperature range [29], with $\alpha = 4.73 \times 10^{-4} \text{ eV K}^{-1}$, T the absolute temperature and $\beta = 636 \text{ K}$ for bulk silicon.

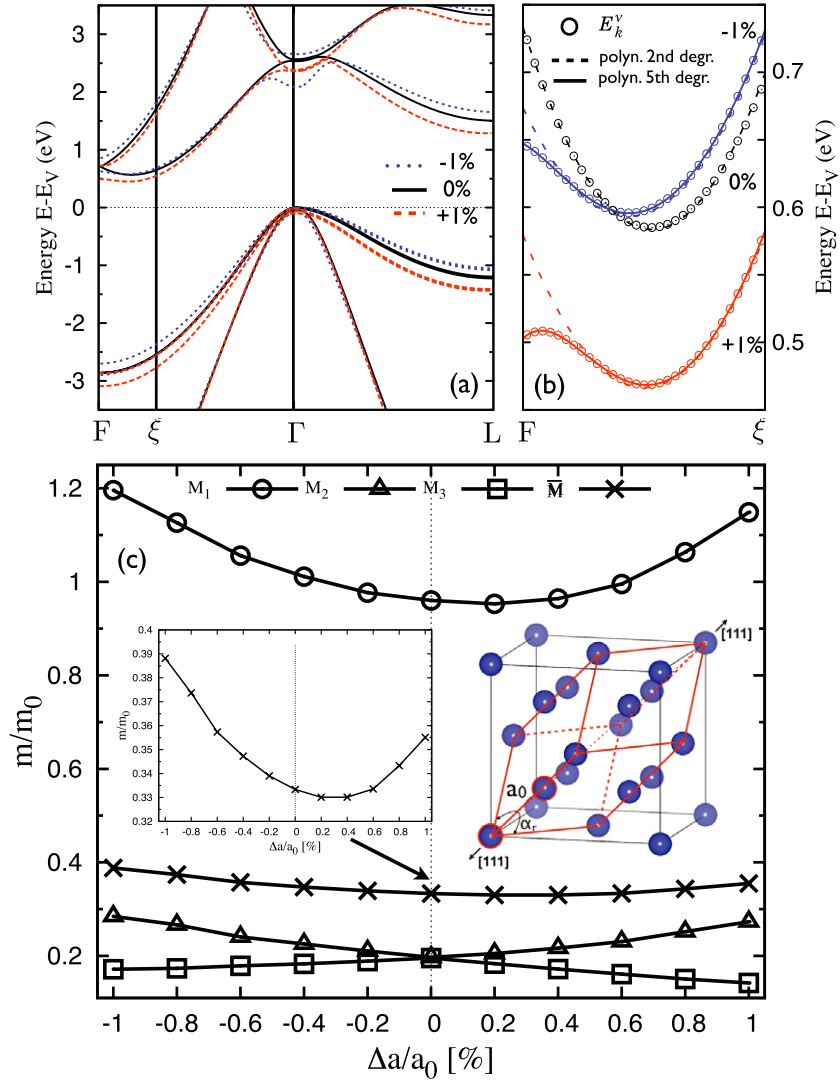


Figure 1. The band structure of bulk silicon in the rhombohedral unit cell. In the unstrained case, the F point coincides with the X point of the fcc Brillouin zone. (a) The bands for the unstrained case (black solid line), under 1% compressive strain (blue dotted line) and under 1% tensile strain (red dashed line) are shown. In (b) a zoom near the conduction band minimum elucidates the nonparabolicity of the bands under applied strain. (c) Directional effective conduction band masses for silicon under [111]-strain. The insets show in detail the response of the averaged effective mass \bar{M} on the applied strain, as well as the rhombohedral unit cell [41] (red lines). More details are given in the text.

Converged results from the first step are the basis to obtain the thermoelectric transport properties by solving the linearized Boltzmann equation in the relaxation time approximation (RTA) [20]. Boltzmann transport calculations for thermoelectrics have been carried out for quite a long time and show reliable results for metals [30, 31] as well as for wide- and narrow-gap semiconductors [18, 21, 32, 33] in the diffusive limit of transport. Here the relaxation time is assumed to be constant with respect to the wavevector k and energy on the scale of $k_B T$. The constant relaxation time allows for the calculation of the thermopower S without any free parameters. To reproduce experimental findings we parametrized the doping-dependent relaxation times from mobility measurements on unstrained silicon according to [34] by

$$\tau(N) = ((-c/\pi \arctan[a \lg(N/N_0)] + c/2) + 2 \lg(N/N_1)^2) d, \quad (3)$$

with $a = 1.8$, $N_0 = 10^{17} \text{ cm}^{-3}$, $N_1 = 10^{17.5} \text{ cm}^{-3}$, $c = 1500$, $d = 0.15 \text{ fs}$ ($a = 1.3$, $N_0 = 10^{16.8} \text{ cm}^{-3}$, $N_1 = 10^{17.5} \text{ cm}^{-3}$, $c = 550$, $d = 0.13 \text{ fs}$) for electron (hole) doping and charge carrier concentrations of N between 10^{14} and 10^{22} cm^{-3} . Nevertheless, we state that our relaxation time is not strain-dependent, while it is known that under strain the dominant scattering process alters: for unstrained Si, the room-temperature scattering is dominated by optical phonons, i.e., intervalley scattering, whereas for strained Si, the scattering by optical phonons is reduced [35, 36].

With the transport distribution function (TDF) as termed by Mahan and Sofo [37]

$$\mathcal{L}_{\perp, \parallel}^{(n)}(\mu, T) = \frac{\tau}{(2\pi)^3} \sum_v \int d^3 \mathbf{k} (v_{\mathbf{k}, (\perp, \parallel)}^v)^2 \times (E_{\mathbf{k}}^v - \mu)^n \left(-\frac{\partial f(\mu, T)}{\partial E} \right)_{E=E_{\mathbf{k}}^v} \quad (4)$$

the temperature- and doping-dependent electrical conductivity σ and thermopower S are defined as

$$\sigma_{\perp,\parallel} = e^2 \mathcal{L}_{\perp,\parallel}^{(0)}(\mu, T), \quad S_{\perp,\parallel} = \frac{1}{eT} \frac{\mathcal{L}_{\perp,\parallel}^{(1)}(\mu, T)}{\mathcal{L}_{\perp,\parallel}^{(0)}(\mu, T)}. \quad (5)$$

Here \parallel denotes the in-plane direction parallel to the a -axis and \perp the cross-plane direction. The electronic part of the total thermal conductivity amounts to

$$\kappa_{e\perp,\parallel} = \frac{1}{T} \left(\mathcal{L}_{\perp,\parallel}^{(2)}(\mu, T) - \frac{(\mathcal{L}_{\perp,\parallel}^{(1)}(\mu, T))^2}{\mathcal{L}_{\perp,\parallel}^{(0)}(\mu, T)} \right). \quad (6)$$

$E_{\mathbf{k}}^v$ denotes the band structure of band v , $v_{\mathbf{k}}^v$ the group velocity and $f_{(\mu,T)}$ the Fermi–Dirac-distribution with chemical potential μ . The chemical potential μ at temperature T and extrinsic carrier concentration N is determined by an integration over the density of states $n(E)$,

$$N = \int_{\mu-\Delta E}^{\text{VBM}} dE n(E) [f_{(\mu,T)} - 1] + \int_{\text{CBM}}^{\mu+\Delta E} dE n(E) f_{(\mu,T)}, \quad (7)$$

where CBM is the conduction band minimum and VBM is the valence band maximum. The necessary size of ΔE will be discussed below.

In a recent work we showed that the determination of surface integrals in anisotropic Brillouin zones is demanding with respect to convergence of the transport property anisotropy [22]. Therefore the constant energy-surface integrations, which are required in equation (4), are performed within an extended tetrahedron method [38–40] interpolating the calculated eigenvalues $E_{\mathbf{k}}^v$ on an adaptive \mathbf{k} -mesh corresponding to a density of at least 44 000 \mathbf{k} points in the irreducible part of the Brillouin zone. $\mathcal{L}_{\perp,\parallel}^{(0)}(E, T = 0)$ was determined on a dense energy mesh with a step width of 1 meV. At vanishing strain $\Delta a/a_0 = 0$ the numerical errors of $\sigma_{\parallel}/\sigma_{\perp}$ and S_{\parallel}/S_{\perp} were constantly below 0.1%. In the limit of low carrier concentrations $N \leq 1 \times 10^{14} \text{ cm}^{-3}$ and for larger carrier concentrations in the bipolar conduction regimes at high temperatures, convergence of the integrals (4) and (7) was achieved with an adaptive integration method for ΔE of at least $10k_{\text{B}}T$.

3. Thermoelectric transport

3.1. [111]-strained silicon: electron doping

In figure 1(a) the uncorrected band structure of bulk silicon in the rhombohedral unit cell is shown for the unstrained case (black solid line), under 1% tensile strain (red dashed line) and for –1% compressive strain (blue-dotted line) on relevant high symmetry lines. Unstrained silicon has an indirect bandgap with conduction band minimum (CBM) near the F high symmetry point. The CBM consists of sixfold degenerate (Δ_6) prolate spheroidal isoenergetic surfaces along six equivalent Γ –F directions. Due to symmetry of the lattice distortion in the [111]-direction this degeneracy holds under applied strain in contrast to strain applied along the [001]-direction [18].

In the unstrained case, for each Δ_6 -valley the effective masses along the major and the minor axis are $M_1 = 0.91m_0$ and $M_2 = 0.19m_0$, respectively. As can be seen from figure 1(b) the idea of an effective mass determined by a second order polynomial fit (dashed lines in figure 1(b)) is valid for the unstrained case, but band warping leads to deviations for silicon under strain already for small band occupations. Here, a fifth order polynomial fit (solid lines in figure 1(b)) is necessary to reproduce the band dispersion, which occurs under applied biaxial [111]-strain. It is therefore advisable to go beyond a simplified effective mass model. In contrast to the conduction bands, the [111]-strain leads to a splitting of the degenerate valence bands, the heavy-hole (HH) and light-hole (LH) bands, similarly to the case of [001]-strain [18, 42]. While the spin–orbit-split-off band is 40 meV away from the band edge, the HH band lifts up energetically under tensile strain, while the LH band lowers in energy. This picture reverses under opposite strain conditions [43]. While the indirect gap closes linearly under tensile in-plane strain from 0.58 eV in equilibrium to about 0.45 eV at $\Delta a/a_0 = 1\%$, the gap size is almost constant within 0.01 eV under compressive strain within the considered range [26, 44, 45] (cf figure 1(b)). The direct gap at Γ decreases slightly under applied strain, in a more pronounced way under compressive in-plane strain.

The influence of biaxial in-plane strain on the fitted effective masses is summarized in figure 1(c). The change of the effective mass M_1 along the major axis is almost symmetric to the applied strain and increases up to 130% of the unstrained value. In contrast, the transverse effective masses behave drastically differently. While the transverse effective mass M_2 increases under tensile strain, the effective mass M_3 perpendicular to M_2 decreases. This behaviour is reversed under applied compressive strain. These results are in good agreement with other findings [44, 45], but add up to GW calculations where only one transverse mass with an almost constant value was found [26]. The strain-dependent averaged effective mass $\bar{M} = \prod_{i=1}^3 (M_i)^{1/3}$, often referred to as the density-of-states effective mass, is shown additionally as an inset in figure 1(c).

In the following the influence of trigonal distortion on the thermoelectric transport of Si under electron doping will be discussed. For this purpose two doping and temperature regimes are considered. The first, at a low temperature of $T = 100 \text{ K}$ and low charge carrier concentration of $N = 1 \times 10^{15} \text{ cm}^{-3}$, is suitable for metal–oxide–semiconductor device applications. The results for the electrical conductivity, thermopower and power factor in dependence on the in-plane strain are shown in figures 2(a)–(c), respectively. Under tensile strain the in-plane electrical conductivity σ_{\parallel} increases almost linearly, while the cross-plane component σ_{\perp} decreases almost comparably. For compressive strain the behaviour reverses, with the cross-plane conductivity being enhanced up to 23% at 1% compressive strain, while the in-plane conductivity decreases to nearly 23% of the unstrained value under 1% tensile strain. In the limit of a degenerate semiconductor at low temperatures and small charge carrier concentrations these results can be completely

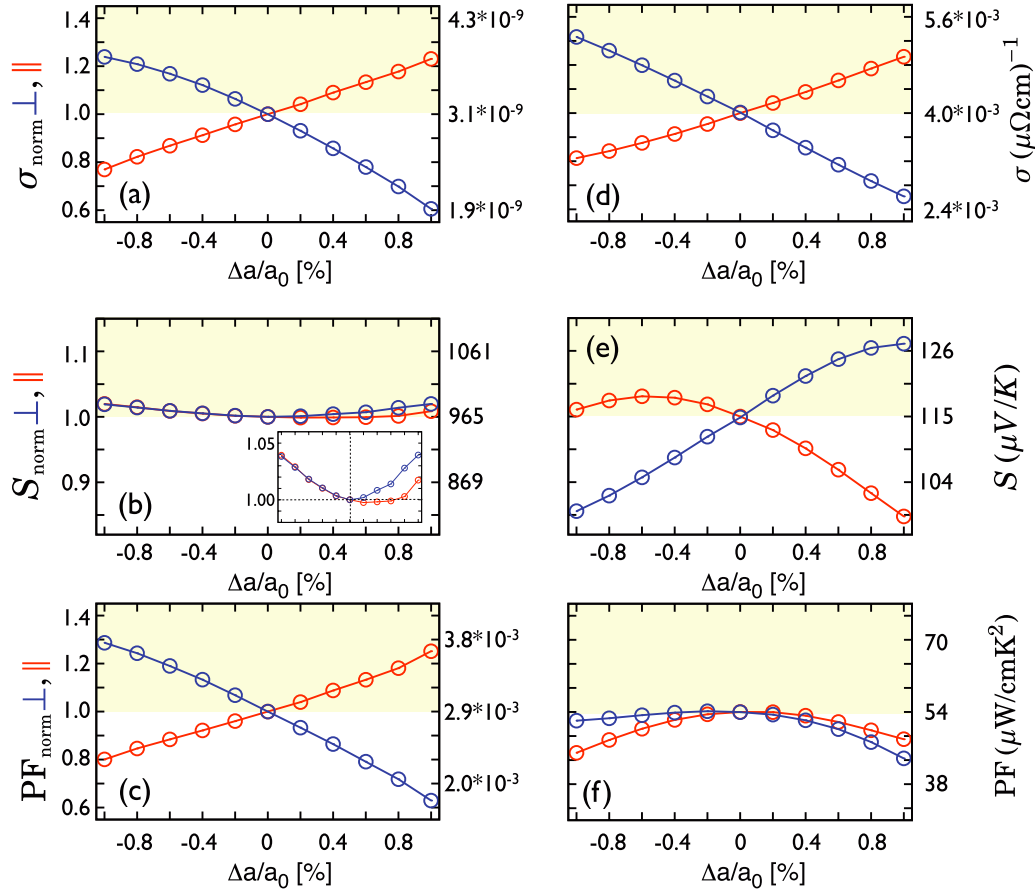


Figure 2. The anisotropic thermoelectric transport properties of Si for fixed temperature and electron doping concentrations in dependence on the compressive and tensile strain in the [111]-direction. The left panels ((a)–(c)) correspond to an electron doping of 2×10^{21} e/atom ($N = 1 \times 10^{15}$ cm $^{-3}$) at a temperature of 100 K, while the right panels ((d)–(f)) refer to an electron doping of 0.04 e/atom ($N = 2 \times 10^{21}$ cm $^{-3}$) at a temperature of 900 K. On the left axis of each figure the relative value compared to the unstrained case is shown, while on the right axis the absolute values are given.

understood within an effective mass calculation [22]. With noticeable variation of the electrical conductivity under applied strain, the thermopower is almost unaffected. At low temperatures only a small energy window near the band edges plays an important role for the determination of the thermopower. As the functional change of the coefficients $\mathcal{L}_{\perp, \parallel}^{(0,1)}(\mu, T)$ is determined by parabolic bands and a strain-dependent shift of the chemical potential, a strong change in the thermopower cannot be expected. However, a slight upward tendency for the thermopower under compressive and tensile strain can be stated. As $S \propto (E_{\text{CBM/VBM}} - \mu)^{-1} \propto \bar{M}$, this can be directly linked to the strain dependence of \bar{M} (cf figure 1(c)). For tensile strain an anisotropy of the thermopower is apparent, which seems to be suppressed for compressive strain. This could be linked to stronger deviations from the isotropic effective mass for tensile strain as shown in figure 1(b).

The strain dependence of the resulting power factor PF is shown in figure 2(c). Due to the weak impact of the thermopower, the behaviour of the power factor is dominated by the electrical conductivity dependence on the applied strain. At low temperatures and small charge carrier concentrations, such a behaviour has already been observed for biaxially strained silicon [18]. However, the

additional power output described by the power factor is enhanced by 30% under 1% applied compressive strain for PF_{\perp} and by 25% under 1% applied tensile strain for PF_{\parallel} . We note that this low temperature and small doping case is not feasible for thermoelectric power generation, but could give insight into the parasitic effects which play a role in metal–oxide–semiconductor devices.

The usual conditions for silicon-based thermoelectric applications, such as a high temperature of 900 K and large charge carrier concentrations $N = 2 \times 10^{21}$ cm $^{-3}$ are assumed in figures 2(d)–(f). At a temperature of 900 K the electronic band structure on a width $\pm\Delta E = \pm 800$ meV around the position of the chemical potential has to be considered, which makes a simplified description of the electronic transport properties within a spherical band picture inaccurate. However, the dependence of the electrical conductivity (cf figure 2(d)) on the applied [111]-strain is almost preserved, even if accidentally. This is in contrast to biaxial strain in the [001]-direction, where the strain dependence induced by reoccupation of bands is suppressed under higher temperatures and dopings [18, 35].

In figure 2(e) the anisotropic thermopower under trigonal distortion is shown. The cross-plane thermopower shows a monotonic increase from 85% to 110% of the unstrained

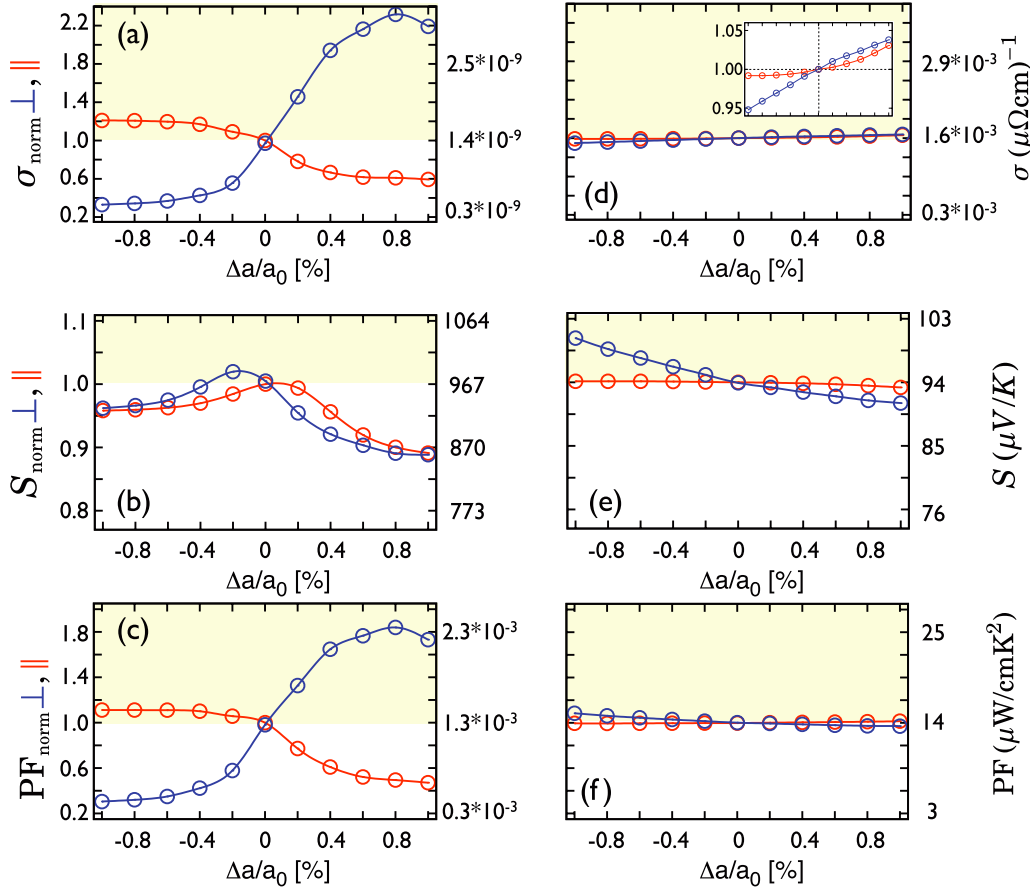


Figure 3. The anisotropic thermoelectric transport properties of Si for fixed temperature and hole doping concentrations in dependence on the compressive and tensile strain in the [111]-direction. The left panels ((a)–(c)) correspond to a hole doping of 2×10^{-8} e/atom ($N = 1 \times 10^{15}$ cm $^{-3}$) at a temperature of 100 K, while the right panels ((d)–(f)) refer to a hole doping of 0.04 e/atom ($N = 2 \times 10^{21}$ cm $^{-3}$) at a temperature of 900 K. On the left axis of each figure the relative value compared to the unstrained case is shown, while on the right axis the absolute values are given.

thermopower value of $S_{\perp} = 115$ μ V K $^{-1}$ varying from compressive to tensile strain. The in-plane component S_{\parallel} decreases to 85% of the unstrained thermopower value under 1% tensile strain. A very similar behaviour was found for the thermopower of biaxially strained silicon in the [001]-direction [18]. The compensation effects of the enhanced thermopower and decreased electrical conductivity, and vice versa, are well known for thermoelectrics under strain [18, 21, 46]. This scenario holds for [111]-strained silicon, too. In figure 2(f) the anisotropic power factor shown in the in-plane and cross-plane directions is always smaller than the power factor of the undistorted system, with PF_{\perp} being at least stable under small values of compressive strain. We mention that the absolute values (cf the right scales in figures 2(a) and (d)) of the electrical conductivity are increased remarkably compared to the low-doping case as expected. Due to this, the absolute value of the power factor increases its absolute value, but unfortunately does not show an enhancement due to mechanical strain in the [111]-direction. Furthermore, compared to the low-doping/low-temperature regime (figure 2(c)) the power factor does not show noticeable anisotropy between the in-plane and cross-plane components.

3.2. [111]-strained silicon: hole doping

As is well known, thermoelectric devices use two types of semiconductor, namely n-type and p-type, which are connected in series [6]. Therefore, the influence of biaxial [111]-strain on hole-doped silicon is presented in figure 3 in the same way as was done for the electron-doped case. In the low-doping/low-temperature regime an enormous enhancement for the cross-plane electrical conductivity σ_{\perp} under sufficient tensile strain can be found (cf figure 3(a)), while the in-plane component σ_{\parallel} decreases more slightly under the same strain conditions. This behaviour can be linked to a changed subband structure. As mentioned before, strain lifts the degeneracy of the LH and HH bands around the Γ point and alters the curvature, that is the effective mass, of both bands. Under applied strain, the valence bands become highly anisotropic and a crossover between bands occurs so that they even lose their original LH and HH meanings [18, 25]. Extended discussions on this can be found in [43, 47].

The thermopower of p-type silicon is shown in figure 3(b). The thermopower in-plane and cross-plane decreases slightly under tensile as well as under compressive strain. The anisotropy of the thermopower is moderate. As previously reported [18, 48], the thermopower depends

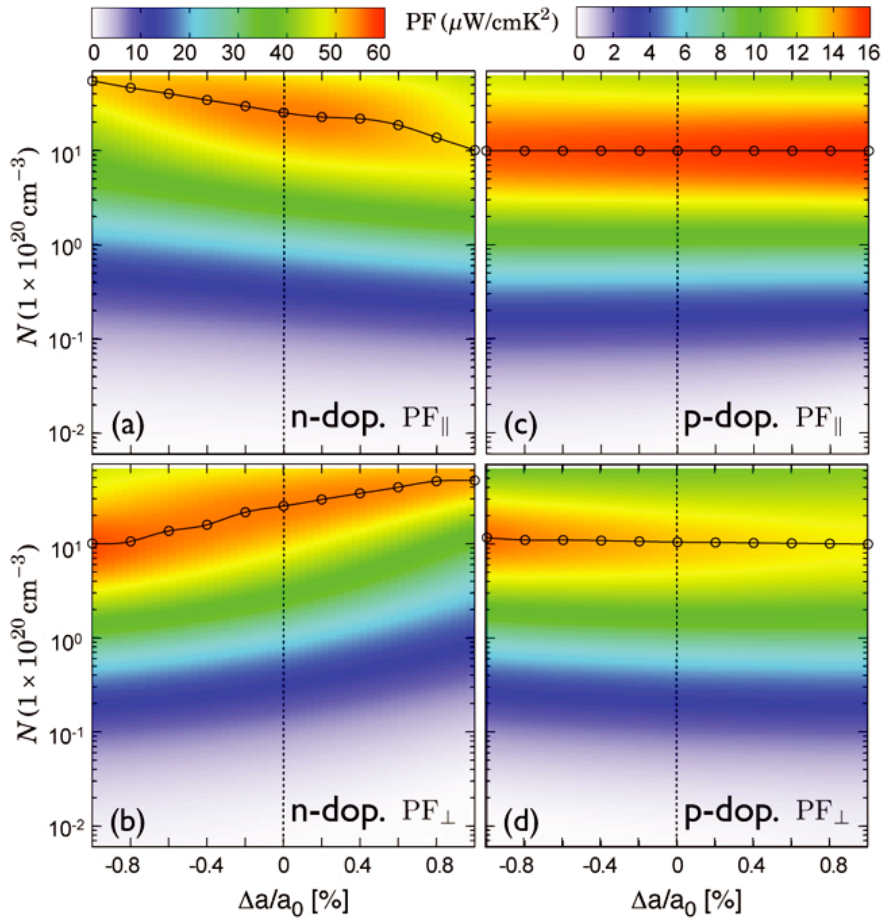


Figure 4. In-plane and cross-plane power factor of Si at a fixed temperature of 900 K under electron ((a), (b)) and hole doping ((c), (d)) for varying charge carrier concentration and applied [111]-strain. The black circles emphasize the position of optimal doping at a certain strain state to maximize the power factor. Note the different scales for electron and hole doping.

strongly on the number of occupied carrier pockets. A higher valley degeneracy at a fixed charge carrier concentration leads to an increased thermopower. As already mentioned, the formerly degenerate HH and LH bands split under tensile and compressive strain. At low hole concentrations and low temperatures only the former HH (LH) band is occupied. This leads directly to a reduction of S_{\parallel} and S_{\perp} . Consequently, the accompanied power factor (cf figure 3(c)) is also reduced in its maximal possible enhancement, but follows in principle the behaviour given by the electrical conductivity.

For high temperatures and high hole concentrations the results are shown in figures 3(d)–(f). As the carrier concentration is raised by nearly six orders of magnitude with respect to the low-doping case, the absolute value of the electrical conductivity increases in the same order (note the right scale of figure 3(d)). Unfortunately, due to the higher band occupation and the broader smearing of the Fermi–Dirac-distribution, the effects of redistribution in strain-split bands do not play a role any more. Moreover, the effects of reduced and increased effective masses cancel each other leading to negligible change, in absolute values as well as in anisotropy, of the hole electrical conductivity.

For the hole thermopower shown in figure 3(e) this behaviour is still valid. For the in-plane thermopower S_{\parallel} no

significant influence of either compressive or tensile strain could be found. A minor dependence on applied [111]-strain is observed for S_{\perp} . Here, the cross-plane thermopower decreases from 100 to 91 $\mu\text{V K}^{-1}$ for strain values varying from 1% compressive to 1% tensile strain.

Comprising the results for the electrical conductivity and thermopower, the resulting power factor under hole doping is shown in figure 3(f). No evident influence of [111]-strain on the power factor could be found in the thermoelectrically relevant temperature and hole doping regime. Furthermore, the absolute value of the power factor is about 3–4 times smaller than in the comparable electron-doped case, which is mainly caused by the higher hole scattering rate as assumed in equation (3). At varying strain not only do the absolute values of the thermoelectric properties change, but also the optimal charge carrier concentrations to obtain these maximized values. For biaxially [001]-strained silicon it was found that the optimal doping range can change by a factor of two, while reducing the power factor by up to 20% if not adapting the charge carrier concentration [18]. Therefore, the in-plane and cross-plane power factor under varying electron and hole doping, as well as varying [111]-strain is shown in figure 4. The maximized power factor at optimal charge carrier concentration at a given strain state is emphasized by a

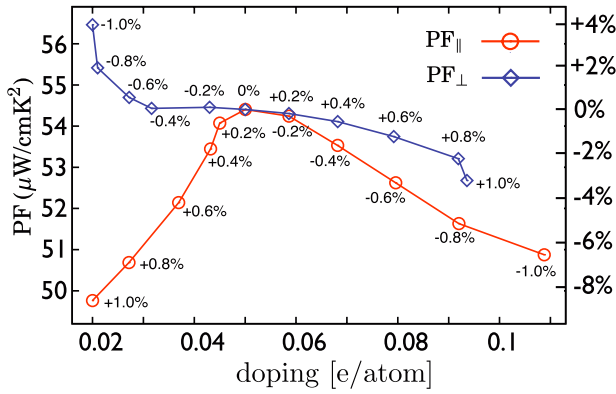


Figure 5. Maximized in-plane and cross-plane power factors of [111]-strained Si at a fixed temperature of 900 K under optimal electron doping. The figure highlights the path of the black circles in figures 4(a) and (b). $N = 0.01$ e/atom corresponds to $N = 5 \times 10^{20}$ cm⁻³.

black-dotted line in figures 4(a)–(d). Comparing silicon under electron doping (cf figures 4(a) and (b)) and hole doping (cf figures 4(c) and (d)), it is obvious that electron-doped silicon shows a much stronger variation of the optimal doping range. For the in-plane component $PF_{||}$ and electron doping the optimal carrier concentration decreases by about a factor of 5, from $N = 5 \times 10^{21}$ to 1×10^{21} cm⁻³, with the strain changing from 1% compressive to 1% tensile strain. For the corresponding cross-plane power factor PF_{\perp} the optimal carrier concentration is about $N = 1 \times 10^{21}$ cm⁻³ at 1% compressive strain and increases by about a factor of 5 under the same strain conditions. For hole doping no evident change of the optimal doping could be found for varying strain, while the absolute value depends only weakly on the applied strain (cf figure 3(f)).

To summarize our findings, sections along the path of optimal electron doping are shown in figure 5. With this, it is obvious that even with optimized doping no enhancement by tensile or compressive [111]-strain can be obtained for the in-plane power factor $PF_{||}$. For the cross-plane component PF_{\perp} , which is more relevant for possible SLs, an increase of the power factor of about 4% at 1% compressive strain was found. To obtain this rather small enhancement the electron charge carrier concentration has to be reduced by about a factor of 2.5 compared to the unstrained case.

3.3. Strained Si/Ge-SL on Si[111]

By introducing the concepts of carrier pocket engineering [15–17] and phonon–glass/electron–crystal [49, 50] to semiconducting SLs an enormous leap forward to maximize the thermoelectric FOM was proposed. Indeed, several proofs-of-principle showed a remarkable enhancement of the FOM for thermoelectric semiconducting heterostructures [7, 8, 17, 51]. With the thermal conductivity of SLs far below their alloy limit [52–55] and their constituents’ bulk values, a main task in optimizing the FOM is to enhance or at least to retain advantageous electronic properties of the bulk materials, that is the power factor. For silicon-based SLs,

carrier pocket engineering can be triggered by lattice strain. Using Si_{1-x}/Ge_x substrates in [111] and [100] orientations ZT values of 0.96 and 0.24, respectively, were predicted for strain-symmetrized⁴ $Si(20 \text{ \AA})/Ge(20 \text{ \AA})$ SLs at room temperature. The latter case was experimentally confirmed with $ZT = 0.1$ at $N \approx 1 \times 10^{19}$ cm⁻³ [17], which is nevertheless about a sevenfold enhancement relative to bulk Si [13, 18]. These experimental findings encourage further research for strain-non-symmetrized $Si(20 \text{ \AA})/Ge(20 \text{ \AA})$ SLs in [001]-orientation and $Si(15 \text{ \AA})/Ge(40 \text{ \AA})$ SLs in [111]-orientation, with $ZT = 0.78$ and 1.25, respectively, predicted at $T = 300$ K [15].

While being in principle possible for very thin films [58, 59], to the best of our knowledge state-of-the-art thin film technology has not enabled strain-non-symmetrized SLs with satisfactory structural qualities and thicknesses for thermoelectric applications so far [56, 57, 60, 61]. Nevertheless, in the following the thermoelectric transport properties of a strain-non-symmetrized $Si(5 \text{ \AA})/Ge(5 \text{ \AA})$ SL in [111]-orientation will be discussed, as the largest enhancement of the FOM is expected here [15].

The $Si(5 \text{ \AA})/Ge(5 \text{ \AA})$ SL used is represented by a hexagonal six-atom unit cell (see the inset in figure 7(a)) with point group symmetry C_{3v} and a fixed in-plane lattice constant of $a = 5.434 \text{ \AA}$ was used to simulate the bulk silicon substrate. Structural optimization of the atomic positions and the c -axis elongation of the unit cell was obtained using VASP [27]. The distinct interlayer distances δ in the [111]-direction were determined as $\delta_{Si_1-Si_2} = 2.359 \text{ \AA}$, $\delta_{Si_2-Si_3} = 0.784 \text{ \AA}$, $\delta_{Si_3-Ge_4} = 2.409 \text{ \AA}$, $\delta_{Ge_4-Ge_5} = 0.929 \text{ \AA}$, $\delta_{Ge_5-Ge_6} = 2.470 \text{ \AA}$, $\delta_{Ge_6-Si_1} = 0.851 \text{ \AA}$ and are in good agreement with previous calculations [62]. The ratio $c/a = 2.551$ shows an increase of the lattice constant in the c -direction by about 4% compared to bulk Si. This is clearly dictated by the fixed in-plane Si lattice constant and the larger volume of Ge. Due to this, the Ge layer can be seen as compressively strained in the [111]-direction.

As has already been mentioned in the literature [62, 63], the face centred cubic (fcc) L high symmetry point in the [111] direction folds onto the hexagonal A high symmetry point at a c/a -ratio of 2.449. In addition, the fcc X point is equivalent to the hexagonal M point, while the symmetry directions fcc ΓX and hexagonal ΓM are inequivalent. This is due the fcc X point lying in an adjoining Brillouin zone. Under biaxial [111]-strain two inequivalent sets of the eight L points occur. There are two points along the c -axis in the [111] direction of growth which fold onto the A point and those in the six directions equivalent to $[11\bar{1}]$ hereafter denoted as L.

In figure 6 the band structure for the fully relaxed Si/Ge-SL in the hexagonal unit cell is shown. While in figure 6(a) the site-resolved bands for the Si/Ge-SL are depicted, in figure 6(b) the bands for pure Si on the fully relaxed Si/Ge positions are shown (blue dashed lines), as well as all sites occupied by Ge (red dotted lines) and the bands referring to the original Si/Ge-SL bands as shown in

⁴ For an introduction to strain-symmetrized and strain-non-symmetrized Si/Ge superlattices we refer to the publications of Kasper *et al* [56, 57].

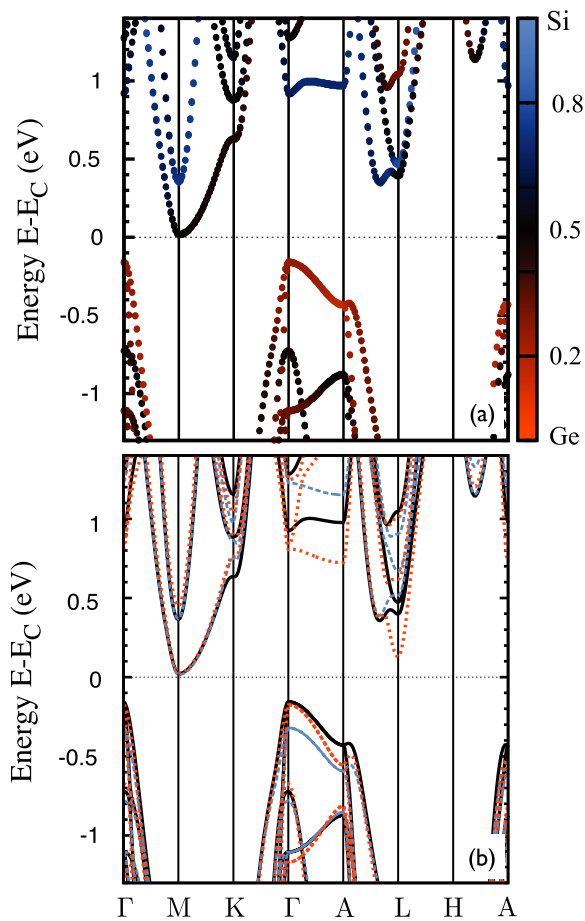


Figure 6. (a) The band structure of the Si/Ge-SL. The colour code of the bands refers to the atomic character of the bands. The red dots refer to the wavefunction character of pure germanium, while the blue dots refer to pure silicon like character. (b) The band structures of silicon (blue dashed lines), germanium (red dotted lines) and Si/Ge (black solid line). All three configurations are calculated in the lattice of Si/Ge. To allow comparison with (a), the bands are energetically matched at the CBM. The figure has not been corrected for the bandgap error.

figure 6(a) (black solid lines). Two main insights can be drawn. First, the VBM is located around the Γ point and has an almost pure Ge character, given by the red dots in figure 6(a). This is mainly due to the smaller bandgap of Ge and the accompanied band offset between Ge and Si. Furthermore, the compressive biaxial strain in the Ge layers decreases the gap size and favours a direct bandgap at Γ instead of an indirect one between Γ and L [64, 45, 65]. Valence bands of mixed Si/Ge character come into play around 0.65 eV below the CBM and suggest the local indirect Si bandgap between Γ and M to be almost retained bulk like. Second, the CBM is located at the M point and shows a strong mixing of Si and Ge character. Furthermore a strain-induced lifting of degeneracy occurs at the M point lowering a band of mixed character to the band edge and lifting a Si like band upwards in energy. As only the Ge layers in the SL are compressively strained while the Si layers are nearly unstrained, the Ge L-point CBM valleys split into A valleys located higher in energy and L valleys lower in energy [15,

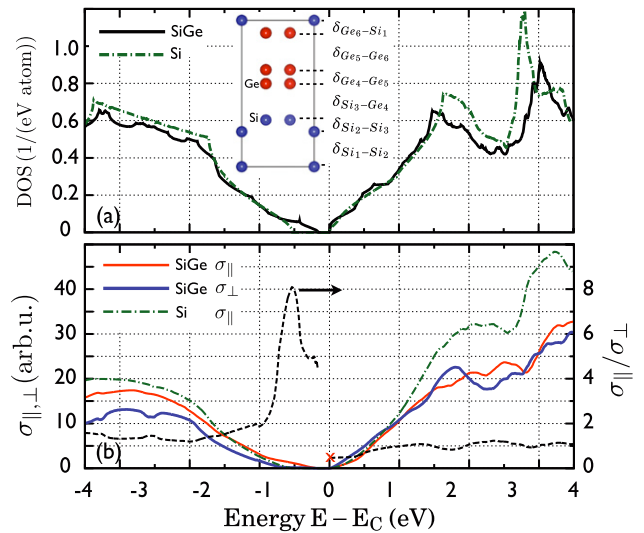


Figure 7. (a) The densities of states for bulk silicon (green dashed-dotted line) and the Si/Ge-SL (black solid line). As an inset the hexagonal unit cell of the Si/Ge-SL is shown [41]. Furthermore the interlayer distances are labelled, as referred to in the text. (b) The electrical conductivity in dependence on the position of the chemical potential μ at zero temperature, shown for bulk silicon (green dashed-dotted line) and the Si/Ge-SL in the in-plane (red solid line) and cross-plane (blue solid line) directions. The conductivity anisotropy (black dashed line referring to the right axis) is stated for the Si/Ge-SL. The cross at the CBM is the value obtained from an analytical effective mass approach.

65, 66]. These findings on the CBM and VBM characteristics are in agreement with experimental studies [59]. With this the uncorrected bandgap decreases to around 178 meV, which is about 30% of the uncorrected GGA gap for unstrained bulk Si. Furthermore, the effective masses at the CBM decrease to $M_1 = 0.125m_0$, $M_2 = 0.026m_0$ and $M_3 = 0.010m_0$.⁵ Applying an effective mass approach [22] we find the conductivity anisotropy for energies near the CBM to be $\sigma_{\parallel}/\sigma_{\perp} = 0.6$, which clearly prefers cross-plane transport under electron doping.

The energy-dependent transport distribution functions in the in-plane and cross-plane directions and their ratio are displayed in figure 7(b) for the Si/Ge-SL and isotropic unstrained bulk Si. For the same systems the densities of states are shown in figure 7(a). As can be seen from figure 7(b) unfortunately the conductivity anisotropy near the valence band edge strongly increases to a value of 8 around 0.58 eV below the CBM, clearly suppressing cross-plane electronic transport under p-type doping. This behaviour is largely due to the localization of the Ge like VBM states, in space as well as energy. As can be deduced from figure 6(a) bands in the cross-plane direction (here ΓA) show pure Ge band character in an energy range of 0.18–0.74 eV below the CBM. Clearly, in this energy range cross-plane conduction is suppressed by states localized in the Ge layers and almost vanishing in the Si layers leading to a strongly increased conductivity anisotropy. At an energy of 0.38 eV below the CBM at Γ a light band with

⁵ The corresponding eigenvectors were determined as $e_1 = (0.8, 0, 0.6)$, $e_2 = (0, 1, 0)$ and $e_3 = (0.6, 0, -0.8)$.

strong Si/Ge mixed character appears (cf the black solid line in figure 6(b)) leading to cross-plane transport through the Si and Ge layer forcing $\sigma_{\parallel}/\sigma_{\perp}$ to decrease, while saturating for values above 1, still indicating a preferred in-plane transport under hole doping.

In figures 8(a), (b) the doping-dependent thermopower and power factor for the Si/Ge-SL are shown, respectively. As a comparison the reference values for bulk silicon are stated as black dashed–dotted lines. We note that a temperature dependence of the energy gap was introduced by applying equation (2). For the Si/Ge-SL the⁶ parameters are chosen as $U_{\text{GGA}} = 0.78$ eV, $\alpha = 4.76 \times 10^{-4}$ eV K⁻¹ and $\beta = 395$ K. However, in the highly degenerate limit ($N > 1 \times 10^{20}$ cm⁻³) the temperature dependence of the gap plays a negligible role even for temperatures above 900 K.

From figure 8(a) it can be seen that the thermopower in the Si/Ge-SL under electron doping (blue lines in the lower panel) is comparable to that of bulk silicon and follows a Pisarenko relation [68]. Under hole doping (red lines in the upper panel) the thermopower is suppressed compared to bulk silicon by about $80 \mu\text{V K}^{-1}$ for S_{\parallel} and S_{\perp} in the relevant doping regime, which might be linked to a changed functional behaviour of the TDF $\mathcal{L}_{\perp,\parallel}^{(0,1)}(\mu, T)$. The latter can be deduced from figure 7(b) where apparent differences in the functional behaviour of $\sigma_{\perp,\parallel}$, which is proportional to $\mathcal{L}_{\perp,\parallel}^{(0)}(\mu, T)$, are visible especially in the valence bands of bulk Si and the Si/Ge-SL. The clear deviation of S_{\perp} from the Pisarenko relation in the vicinity of $N \approx 3 \times 10^{21}$ cm⁻³ is related to the strongly increased conductivity anisotropy 0.58 eV below the VBM as shown in figure 7(b). Here, the strong suppression of σ_{\perp} causes a larger S_{\perp} . Nevertheless, this slight enhancement of S_{\perp} is not reflected in the power factor of the p-type Si/Ge-SL. As shown in figure 8(b) S_{\parallel} and S_{\perp} are always smaller than the values for bulk Si under hole doping (red lines). Obviously, the suppressed electrical conductivity, especially in the cross-plane direction, is responsible for this result. A power factor of about $9 \mu\text{W cm}^{-1} \text{K}^{-2}$ is found for PF_{\parallel} at $N \approx 3 \times 10^{20}$ cm⁻³, while in the cross-plane direction the same value can be stated at huge values of $N \approx 3 \times 10^{21}$ cm⁻³, clearly evoked by the anomaly in the thermopower. More interesting is the case of electron doping (blue lines in figure 8(a)). With the thermopower's behaviour almost bulk like and conductivity anisotropies $\sigma_{\parallel}/\sigma_{\perp}$ below 1 an enhanced power factor in the required cross-plane direction is found. Compared to bulk silicon the PF_{\perp} is enhanced by 10% and reaches a value of $60 \mu\text{W cm}^{-1} \text{K}^{-2}$ at an electron concentration of $N \approx 7 \times 10^{20}$ cm⁻³. With that the optimal charge carrier concentration is four times smaller compared to bulk Si. For the in-plane component PF_{\parallel} almost no reduction can be seen, while the maximal value of $53 \mu\text{W cm}^{-1} \text{K}^{-2}$ is shifted to slightly larger charge carrier concentrations.

3.4. Towards the figure of merit

In figure 9(a) the FOM in the cross-plane direction for the Si/Ge-SL (blue lines) and the more promising electron-doped case is shown. Different temperatures are chosen to

⁶ Here we adapted experimental data for Si_{0.5}Ge_{0.5} alloys from [67].

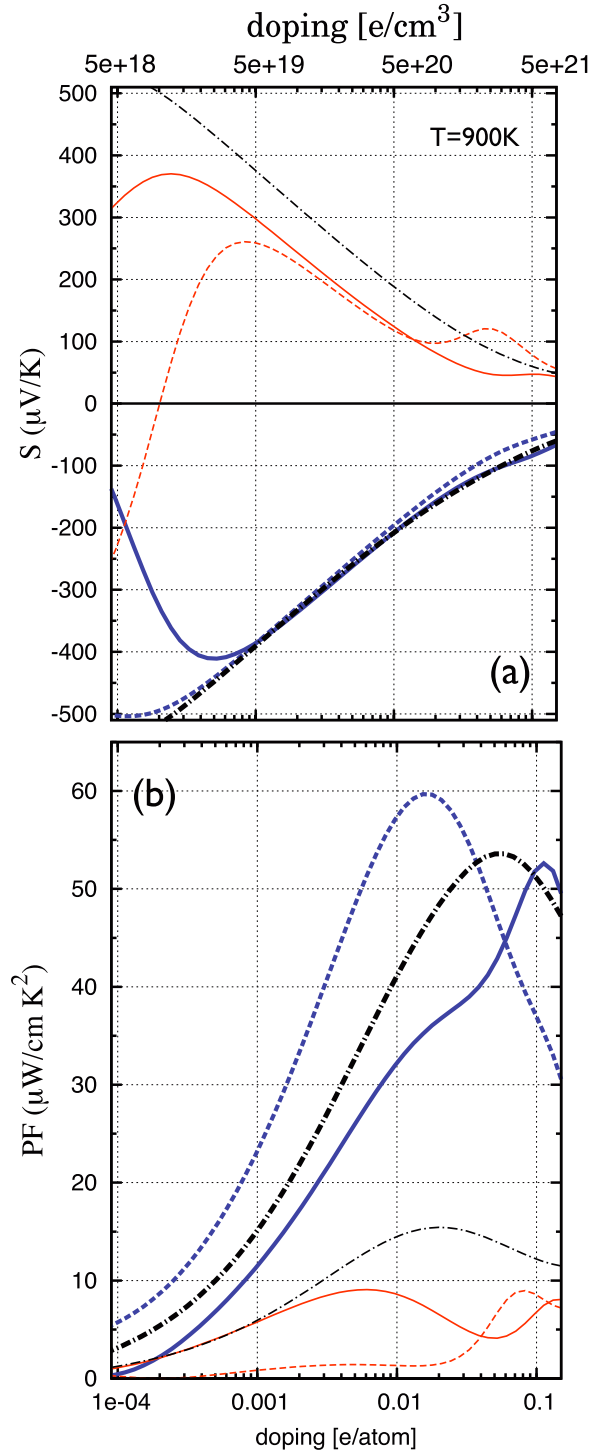


Figure 8. (a) The in-plane (solid lines) and cross-plane (dashed lines) doping-dependent thermopowers at 900 K for the Si/Ge-SL under electron (thick blue lines) and hole doping (thin red lines). For comparison the values for bulk silicon are given (black dashed–dotted lines). (b) The in-plane (solid lines) and cross-plane (dashed lines) doping-dependent power factors at 900 K for the Si/Ge-SL under electron (thick blue lines) and hole doping (thin red lines). Again, for comparison the values for bulk silicon are given (black dashed–dotted lines).

demonstrate the evaluation of maximal ZT and the range of optimal charge carrier concentration. As a comparison the FOM for bulk Si is shown as a black dashed–dotted

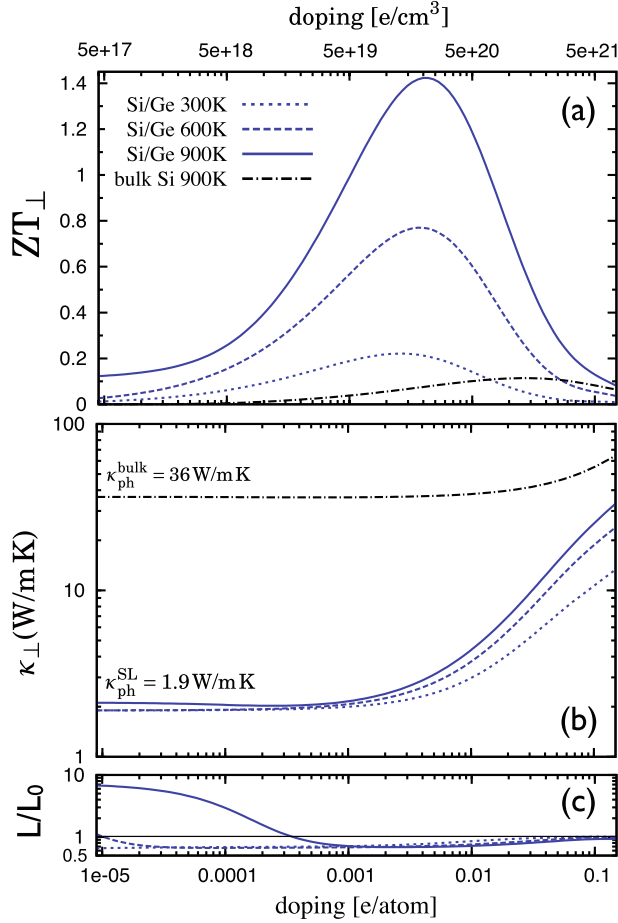


Figure 9. (a) The doping-dependent cross-plane figures of merit ZT_{\perp} of the Si/Ge-SL (blue lines) and bulk Si (black lines) under electron doping at different temperatures. (b) The total thermal conductivities κ_{\perp} in the cross-plane direction for the Si/Ge-SL (blue lines) and bulk Si (black lines) under electron doping at different temperatures. While the electronic part $\kappa_{el\perp}$ was calculated, the lattice part $\kappa_{ph\perp}$ was estimated from experiments [13, 55] and is constant for varying charge carrier concentration. (c) The calculated cross-plane Lorenz function $L_{\perp} = \kappa_{el\perp}(\sigma_{\perp}T)^{-1}$ is related to the metallic limit $L_0 = 2.44 \times 10^{-8} \text{ W } \Omega \text{ K}^{-2}$.

line too. To present results for the FOM, knowledge of the thermal conductivity is relevant. For this purpose, the electronic part of the thermal conductivity $\kappa_{el\perp}$ was calculated applying equation (6), while the lattice part $\kappa_{ph\perp}$ was taken from experiment. Here, $\kappa_{ph\perp} = 36 \text{ W m}^{-1} \text{ K}^{-1}$ [13] was used for bulk Si at 900 K, while $\kappa_{ph\perp} = 1.9 \text{ W m}^{-1} \text{ K}^{-1}$ was used for the Si/Ge-SL [55], with the latter being rather optimistic, since it is smaller than the expected nano-alloy limit of $2.5 \text{ W m}^{-1} \text{ K}^{-1}$ [69], but achievable in Si/Ge-SL [53, 55, 70]. However, from figure 9(b) one can deduce that for thermoelectric reliable charge carrier concentrations above $4 \times 10^{20} \text{ cm}^{-3}$ the electronic contribution to the total thermal conductivity dominates over its lattice part. At 900 K for $N \approx 1.5 \times 10^{20} \text{ cm}^{-3}$ the electronic part amounts to $0.73 \text{ W m}^{-1} \text{ K}^{-1}$, clearly smaller than the lattice part. This contribution increases significantly at higher temperatures and charge carrier concentrations omitting higher absolute values

of the FOM. However, ZT_{\perp} above unity can be reached for operating temperatures higher than 750 K and electron-doping $N \approx 1.5\text{--}3 \times 10^{20} \text{ cm}^{-3}$.

At room temperature a $ZT_{\perp} \approx 0.2$ is achieved in a broad doping range of $N \approx 5\text{--}25 \times 10^{19} \text{ cm}^{-3}$. Although this value is an order of magnitude higher than the bulk Si value of $ZT \approx 0.01$ [13, 15, 18], it is still less than the postulated values of $ZT_{\perp} = 0.96$ and $ZT_{\perp} = 1.25$ by Koga *et al* [15] for strain-symmetrized and strain-non-symmetrized Si/Ge-SL, respectively. With these values, and using a rather conservative value of $\kappa_{ph\perp} = 7.3 \text{ W m}^{-1} \text{ K}^{-1}$ for their estimations, they expect enormous power factors of $PF_{\perp} \approx 250 \mu\text{W cm}^{-1} \text{ K}^{-2}$ and $PF_{\perp} \approx 340 \mu\text{W cm}^{-1} \text{ K}^{-2}$ for the strain-optimized Si/Ge-SL in the [111]-direction. We found $PF_{\perp} \approx 15 \mu\text{W cm}^{-1} \text{ K}^{-2}$ at 300 K and $N \approx 1 \times 10^{20} \text{ cm}^{-3}$ for the Si/Ge-SL. Even though a convergence of carrier pockets is not fully achieved in our superlattice, power factors beyond $200 \mu\text{W cm}^{-1} \text{ K}^{-2}$ seem to be very high, as state-of-the-art power factors near or above room temperature are well below $100 \mu\text{W cm}^{-1} \text{ K}^{-2}$ [7, 71, 72]. A benefit from thermionic emission even at moderate temperatures cannot be expected in Si/Ge-SL [73–75]. We note that at very low temperatures below 10 K huge PFs of about $100\text{--}1000 \mu\text{W cm}^{-1} \text{ K}^{-2}$ were reported for bulk Fe_2Sb_2 and $\text{ZnO}_{1-x}\text{Se}_x$ [76, 77].

As an addition, in figure 9(c) the doping-dependent Lorenz function $L_{\perp} = \kappa_{el\perp}(\sigma_{\perp}T)^{-1}$ as defined via equations (5) and (6) is presented. From figure 9(c) it is obvious that the Lorenz number L_{\perp} can be substantially different from the metallic limit L_0 . Nevertheless, for very large charge carrier concentrations and the chemical potential located deep inside the conduction band, L_{\perp} almost coincides with L_0 . At intermediate and thermoelectrically relevant charge carrier concentrations of $N \approx 5\text{--}50 \times 10^{19} \text{ cm}^{-3}$ L_{\perp} can be much smaller than L_0 . For 900 K and $N \approx 1.25 \times 10^{20} \text{ cm}^{-3}$ we find a minimal value of $L_{\perp} \approx 0.7L_0$. At smaller charge carrier concentrations L_{\perp} rapidly increases and reaches $L_{\perp} \approx 7L_0$ for electron charge carrier concentrations of $N < 1 \times 10^{18} \text{ cm}^{-3}$ in the intrinsic doping regime. At decreasing temperatures minimal values of the Lorenz function are obtained at much smaller charge carrier concentrations. Furthermore, the maximal values of L shift to smaller charge carrier concentrations too, and can reach huge values of L at very low temperatures and charge carrier concentrations. The effect, which is responsible for the suppression of the Lorenz function to values below the metallic limit L_0 , is termed the bipolar thermodiffusion effect [78–80] and is maximized for positions of the chemical potential near the band edges. However, a Lorenz function $L \neq L_0$ can have consequences for the determination of the thermal conductivity. The Lorenz factor is generally used to separate κ_{el} and κ_{ph} . At thermoelectrically advisable charge carrier concentrations applying the metallic value L_0 to determine the lattice thermal conductivity could lead to an overestimation of the electronic thermal conductivity, and consequently to an underestimation of the lattice contribution.

4. Conclusions and outlook

With the presented results we have shown, that strain in the [111]-direction is not sufficient to significantly enhance the thermoelectric transport properties in bulk Si for energy harvesting applications. In the low-temperature and low-doping case large enhancements were found under tensile strain for PF_{\parallel} (electron doping) and PF_{\perp} (hole doping) and under compressive strain for PF_{\perp} (electron doping). This could have a negative impact for metal–oxide–semiconductor devices involving [111]-strained Si. Here, in the low-temperature and low-doping regime, small temperature gradients in the devices could lead to an additional parasitic electrical power, which could be far larger than expected from unstrained bulk.

The enhancements found in the high-temperature and high-doping regime were distinctly smaller. Here slight enhancements of 5% for PF_{\perp} were found under compressive strain. It is more interesting that the power factor is robust against [111]-strain, especially under hole doping. Thus, thermoelectric SLs based on [111]-strained Si could provide an enhanced FOM, as κ_{ph} is most likely reduced in SLs. We note that due to the high bulk thermal conductivity and the only modest gain in the power factor by [111]-strain engineering, bulk silicon remains an unfavourable thermoelectric, even if the electronic transport properties are strain optimized. However, from comparison with earlier studies on biaxially [001]-strained silicon [18], we confirm that strain in the [111]-direction, e.g. in silicon-based SLs, should be preferred, as the carrier pocket degeneracy is retained and therefore the thermopower and power factor can be maximized.

To deal with this, we investigated the anisotropic thermoelectric transport of a [111]-oriented Si/Ge superlattice. At a first glance we have shown that no degradation of the electronic transport by the heterostructure is expected for electron doping, while even showing an enhancement of 10% in PF_{\perp} compared to bulk Si. Assuming a decrease in lattice thermal conductivity large enhancements in ZT to 0.2 and 1.4 are achieved at 300 K and 900 K, respectively. Under hole doping the electronic transport in the Si/Ge-SL is heavily suppressed due to quantum-well effects. Here the cross-plane power factor PF_{\perp} is expected to show only around 50% of the bulk maximal value, leading to small ZT values.

Acknowledgments

This work was supported by the Deutsche Forschungsgemeinschaft, SPP 1386 ‘Nanostrukturierte Thermoelektrika: Theorie, Modellsysteme und kontrollierte Synthese’. N F Hinsche is a member of the International Max Planck Research School for Science and Technology of Nanostructures.

References

[1] Seebeck T J 1826 Über die magnetische Polarisation der Metalle und Erze durch Temperatur-Differenz *Ann. Phys., Lpz.* **82** 253–86

- [2] Ioffe A F 1958 The revival of thermoelectricity *Sci. Am.* **199** 31–7
- [3] Majumdar A 2004 Thermoelectricity in semiconductor nanostructures *Science* **303** 777
- [4] Böttner H, Chen G and Venkatasubramanian R 2006 Aspects of thin-film superlattice thermoelectric materials, devices, and applications *MRS Bull.* **31** 211
- [5] Tritt T M and Subramanian M A 2006 Thermoelectric materials, phenomena, and applications: a bird’s eye view *MRS Bull.* **31** 188–98
- [6] Sales B C 2002 Thermoelectric materials: smaller is cooler *Science* **295** 1248
- [7] Venkatasubramanian R, Siivola E and Colpitts T 2001 Thin-film thermoelectric devices with high room-temperature figures of merit *Nature* **413** 597
- [8] Harman T, Taylor P, Walsh M and LaForge B 2002 Quantum dot superlattice thermoelectric materials and devices *Science* **297** 2229
- [9] Dresselhaus M, Chen G, Tang M and Yang R 2007 New directions for low-dimensional thermoelectric materials *Adv. Mater.* **19** 1
- [10] Vining C B 2008 Materials science: desperately seeking silicon *Nature* **451** 132–3
- [11] Hochbaum A, Chen R, Delgado R and Liang W 2008 Enhanced thermoelectric performance of rough silicon nanowires *Nature* **451** 163
- [12] Boukai A I, Bunimovich Y, Tahir-Kheli J, Yu J K, Goddard Iii W A and Heath J R 2008 Silicon nanowires as efficient thermoelectric materials *Nature* **451** 168–71
- [13] Bux S K, Blair R G, Gogna P K, Lee H, Chen G, Dresselhaus M S, Kaner R B and Fleurial J-P 2009 Nanostructured bulk silicon as an effective thermoelectric material *Adv. Funct. Mater.* **19** 2445–52
- [14] Tang J, Wang H T, Lee D H, Fardy M, Huo Z, Russell T P and Yang P 2010 Holey silicon as an efficient thermoelectric material *Nano Lett.* **10** 4279
- [15] Koga T, Sun X, Cronin S B and Dresselhaus M S 1999 Carrier pocket engineering applied to strained Si/Ge superlattices to design useful thermoelectric materials *Appl. Phys. Lett.* **75** 2438
- [16] Koga T, Harman T, Cronin S and Dresselhaus M 1999 Mechanism of the enhanced thermoelectric power in (111)-oriented n-type PbTe/Pb_{1-x}Eu_xTe multiple quantum wells *Phys. Rev. B* **60** 14286
- [17] Koga T, Cronin S, Dresselhaus M and Liu J 2000 Experimental proof-of-principle investigation of enhanced ZT in (001) oriented Si/Ge superlattices *Appl. Phys. Lett.* **77** 1490
- [18] Hinsche N, Mertig I and Zahn P 2011 Effect of strain on the thermoelectric properties of silicon: an *ab initio* study *J. Phys.: Condens. Matter* **23** 295502
- [19] Giannozzi P *et al* 2009 Quantum espresso: a modular and open-source software project for quantum simulations of materials *J. Phys.: Condens. Matter* **21** 395502
- [20] Mertig I 1999 Transport properties of dilute alloys *Rep. Prog. Phys.* **62** 237–76
- [21] Hinsche N, Yavorsky B, Mertig I and Zahn P 2011 Influence of strain on anisotropic thermoelectric transport in Bi₂Te₃ and Sb₂Te₃ *Phys. Rev. B* **84** 165214
- [22] Zahn P, Hinsche N, Yavorsky B and Mertig I 2011 Bi₂Te₃: implications of the rhombohedral *k*-space texture on the evaluation of the in-plane/out-of-plane conductivity anisotropy *J. Phys.: Condens. Matter* **23** 505504
- [23] Perdew J P, Burke K and Ernzerhof M 1996 Generalized gradient approximation made simple *Phys. Rev. Lett.* **77** 3865–8
- [24] Corso A and Conte A 2005 Spin–orbit coupling with ultrasoft pseudopotentials: application to Au and Pt *Phys. Rev. B* **71** 115106

- [25] Yu D, Zhang Y and Liu F 2008 First-principles study of electronic properties of biaxially strained silicon: effects on charge carrier mobility *Phys. Rev. B* **78** 245204
- [26] Bouhassoune M and Schindlmayr A 2009 Electronic structure and effective masses in strained silicon *Phys. Status Solidi c* **7** 460–3
- [27] Kresse G and Furthmüller J 1996 Efficient iterative schemes for *ab initio* total-energy calculations using a plane-wave basis set *Phys. Rev. B* **54** 11169
- [28] Godby R W, Schlüter M and Sham L J 1988 Self-energy operators and exchange–correlation potentials in semiconductors *Phys. Rev. B* **37** 10159–75
- [29] Varshni Y P 1967 Temperature dependence of the energy gap in semiconductors *Physica* **34** 149–54
- [30] Vojta T, Mertig I and Zeller R 1992 Calculation of the residual resistivity and the thermoelectric power of sp impurities in silver *Phys. Rev. B* **46** 16761
- [31] Thonhauser T, Scheidemantel T J and Sofo J O 2004 Improved thermoelectric devices using bismuth alloys *Appl. Phys. Lett.* **85** 588
- [32] Singh D J 2010 Doping-dependent thermopower of PbTe from Boltzmann transport calculations *Phys. Rev. B* **81** 195217
- [33] Scheidemantel T J, Ambrosch-Draxl C, Thonhauser T, Badding J V and Sofo J O 2003 Transport coefficients from first-principles calculations *Phys. Rev. B* **68** 125210
- [34] Jacoboni C, Canali C, Ottaviani G and Quaranta A A 1977 A review of some charge transport properties of silicon *Solid-State Electron.* **20** 77–89
- [35] Dziekan T, Zahn P, Meded V and Mirbt S 2007 Theoretical calculations of mobility enhancement in strained silicon *Phys. Rev. B* **75** 195213
- [36] Roldán J B, Gámiz F, LópezVillanueva J A and Carceller J E 1996 A Monte Carlo study on the electron transport properties of high performance strained Si on relaxed Si_{1-x}Ge_x channel MOSFETs *J. Appl. Phys.* **80** 5121
- [37] Mahan G and Sofo J O 1996 The best thermoelectric *Proc. Natl Acad. Sci.* **93** 7436
- [38] Lehmann G and Taut M 1972 On the numerical calculation of the density of states and related properties *Phys. Status Solidi b* **54** 469–77
- [39] Zahn P, Mertig I, Richter M and Eschrig H 1995 *Ab initio* calculations of the giant magnetoresistance *Phys. Rev. Lett.* **75** 2996–9
- [40] Mertig I, Mrosan E and Ziesche P 1987 *Multiple Scattering Theory of Point Defects in Metals: Electronic Properties* (Leipzig: B G Teubner)
- [41] Momma K and Izumi F 2011 VESTA3 for three-dimensional visualization of crystal, volumetric and morphology data *J. Appl. Crystallogr.* **44** 1272–6
- [42] Baykan M O, Thompson S E and Nishida T 2010 Strain effects on three-dimensional, two-dimensional, and one-dimensional silicon logic devices: predicting the future of strained silicon *J. Appl. Phys.* **108** 093716
- [43] Sun G, Sun Y, Nishida T and Thompson S E 2007 Hole mobility in silicon inversion layers: stress and surface orientation *J. Appl. Phys.* **102** 084501
- [44] Boykin T, Kharche N and Klimeck G 2007 Brillouin-zone unfolding of perfect supercells having nonequivalent primitive cells illustrated with a SiGe tight-binding parameterization *Phys. Rev. B* **76** 035310
- [45] Niquet Y, Rideau D, Tavernier C, Jaouen H and Blase X 2009 Onsite matrix elements of the tight-binding Hamiltonian of a strained crystal: application to silicon, germanium, and their alloys *Phys. Rev. B* **79** 245201
- [46] Park M S, Song J-H, Medvedeva J E, Kim M, Kim I G and Freeman A J 2010 Electronic structure and volume effect on thermoelectric transport in p-type Bi and Sb tellurides *Phys. Rev. B* **81** 155211
- [47] Thompson S E, Sun G, Choi Y S and Nishida T 2006 Uniaxial-process-induced strained-Si: extending the CMOS roadmap *IEEE Trans. Electron Devices* **53** 1010–20
- [48] Pei Y, Shi X, LaLonde A, Wang H, Chen L and Jeffrey Snyder G 2011 Convergence of electronic bands for high performance bulk thermoelectrics *Nature* **473** 66–9
- [49] Slack G A 1995 *CRC Handbook of Thermoelectrics* (Boca Raton, FL: CRC Press) chapter 34, p 407
- [50] Poudel B, Hao Q, Ma Y, Lan Y, Minnich A, Yu B, Yan X, Wang D, Muto A and Vashaee D 2008 High-thermoelectric performance of nanostructured bismuth antimony telluride bulk alloys *Science* **320** 634
- [51] Hicks L, Harman T, Sun X and Dresselhaus M 1996 Experimental study of the effect of quantum-well structures on the thermoelectric figure of merit *Phys. Rev. B* **53** R10493
- [52] Venkatasubramanian R 2000 Lattice thermal conductivity reduction and phonon localizationlike behavior in superlattice structures *Phys. Rev. B* **61** 3091–7
- [53] Borca-Tasciuc T 2000 Thermal conductivity of symmetrically strained Si/Ge superlattices *Superlattices Microstruct.* **28** 199–206
- [54] Chakraborty S, Kleint C A, Heinrich A, Schneider C M, Schumann J, Falke M and Teichert S 2003 Thermal conductivity in strain symmetrized Si/Ge superlattices on Si(111) *Appl. Phys. Lett.* **83** 4184
- [55] Lee S, Cahill D and Venkatasubramanian R 1997 Thermal conductivity of Si–Ge superlattices *Appl. Phys. Lett.* **70** 2957
- [56] Kasper E, Kibbel H, Jorke H, Brugger H, Friess E and Abstreiter G 1988 Symmetrically strained Si/Ge superlattices on Si substrates *Phys. Rev. B* **38** 3599–601
- [57] Kasper E 1986 Growth and properties of Si/SiGe superlattices *Surf. Sci.* **174** 630–9
- [58] Pearsall T, Bevk J, Feldman L, Bonar J, Mannaerts J and Ourmazd A 1987 Structurally induced optical transitions in Ge–Si superlattices *Phys. Rev. Lett.* **58** 729–32
- [59] Pearsall T, Bevk J, Bean J, Bonar J, Mannaerts J and Ourmazd A 1989 Electronic structure of Ge/Si monolayer strained-layer superlattices *Phys. Rev. B* **39** 3741–57
- [60] Brunner K 2002 Si/Ge nanostructures *Rep. Prog. Phys.* **65** 27
- [61] Kuan T S and Iyer S S 1991 Strain relaxation and ordering in SiGe layers grown on (100), (111), and (110) Si surfaces by molecular-beam epitaxy *Appl. Phys. Lett.* **59** 2242
- [62] Bass J M and Matthai C C 1990 Electronic structure of (111) Si/Ge superlattices *J. Phys.: Condens. Matter* **2** 7841
- [63] Salehpour M R and Satpathy S 1990 Comparison of electron bands of hexagonal and cubic diamond *Phys. Rev. B* **41** 3048
- [64] Tahini H, Chronopoulos A, Grimes R W, Schwingenschlögl U and Dimoulas A 2012 Strain-induced changes to the electronic structure of germanium *J. Phys.: Condens. Matter* **24** 195802
- [65] Zhang F, Crespi V and Zhang P 2009 Prediction that uniaxial tension along 111 produces a direct band gap in germanium *Phys. Rev. Lett.* **102** 156401
- [66] Rideau D, Feraille M, Ciampolini L, Minondo M, Tavernier C, Jaouen H and Ghetti A 2006 Strained Si, Ge, and Si_{1-x}Ge_x alloys modeled with a first-principles-optimized full-zone kp method *Phys. Rev. B* **74** 195208
- [67] Braunstein R, Moore A R and Herman F 1958 Intrinsic optical absorption in germanium–silicon alloys *Phys. Rev.* **109** 695–710
- [68] Ioffe A F 1960 *Physics of Semiconductors* (New York: Academic)
- [69] Wang X W, Lee H, Lan Y C, Zhu G H, Joshi G, Wang D Z, Yang J, Muto A J, Tang M Y and Klatsky J 2008 Enhanced thermoelectric figure of merit in nanostructured n-type silicon germanium bulk alloy *Appl. Phys. Lett.* **93** 193121

- [70] Pernot G, Stoffel M, Savic I, Pezzoli F, Chen P, Savelli G, Jacquot A, Schumann J, Denker U and Mönch I 2010 Precise control of thermal conductivity at the nanoscale through individual phonon-scattering barriers *Nature Mater.* **9** 491
- [71] Jalan B and Stemmer S 2010 Large seebeck coefficients and thermoelectric power factor of La-doped SrTiO₃ thin films *Appl. Phys. Lett.* **97** 3
- [72] Okinaka N and Akiyama T 2006 Latent property of defect-controlled metal oxide: nonstoichiometric titanium oxides as prospective material for high-temperature thermoelectric conversion *Japan. J. Appl. Phys.* **45** 7009–10
- [73] Vashaee D and Shakouri A 2007 Thermionic power generation at high temperatures using SiGe/Si superlattices *J. Appl. Phys.* **101** 053719
- [74] Shakouri A and Bowers J E 1997 Heterostructure integrated thermionic coolers *Appl. Phys. Lett.* **71** 1234
- [75] Vashaee D and Shakouri A 2004 Improved thermoelectric power factor in metal-based superlattices *Phys. Rev. Lett.* **92** 106103
- [76] Sun P, Oeschler N, Johnsen S, Iversen B B and Steglich F 2009 Huge thermoelectric power factor: FeSb₂ versus FeAs₂ and RuSb₂ *Appl. Phys. Express* **2** 091102
- [77] Lee J-H, Wu J and Grossman J C 2010 Enhancing the thermoelectric power factor with highly mismatched isoelectronic doping *Phys. Rev. Lett.* **104** 016602
- [78] Nolas G S and Goldsmid H J 2004 *Thermal Conductivity: Theory, Properties, and Applications* (New York: Kluwer Academic) chapter 1.4, p 110
- [79] Chaput L, Pécheur P, Tobola J and Scherrer H 2005 Transport in doped skutterudites: *ab initio* electronic structure calculations *Phys. Rev. B* **72** 085126
- [80] Flage-Larsen E and Prytz O 2011 The Lorenz function: its properties at optimum thermoelectric figure-of-merit *Appl. Phys. Lett.* **99** 202108

SUMMARY & OUTLOOK

The major goal of this thesis was to strengthen the theoretical understanding of anisotropic thermoelectric transport in semiconducting heterostructures and to elucidate details of the electronic structure, which could be the origin for high thermoelectric conversion efficiency in the cross-plane transport direction of these systems. Motivated by state-of-the-art experiments, superlattices based on $\text{Bi}_2\text{Te}_3/\text{Sb}_2\text{Te}_3$ or Si/Ge were of major interest.

For this purpose, *ab initio* calculations footing on a KORRINGA-KOHN-ROSTOKER and a pseudopotential method were carried out. Here, it was accounted for all important relativistic effects, by solving the DIRAC equation. The macroscopic thermoelectric transport properties were then described by a linearized BOLTZMANN equation.

The interdependence of the thermoelectric transport properties remains a big obstacle in thermoelectric superlattices and bulk materials. Optimizing the electronic transport properties by tuning the charge carrier concentration seems to remain the only efficient and promising approach.

As an alternative *ansatz* it was suggested to enhance the thermoelectric transport by strain, or in other words, to understand whether strain could be the reason for enhanced cross-plane thermoelectric transport, even at the expense of a possibly less efficient in-plane transport. In both material systems, no pronounced enhancement could be found, while the transport properties were robust against strain, especially in the thermoelectric desirable high-doping and high-temperature regime. While for Bi_2Te_3 a decrease of the maximal power factor of about 27% and 23% for *n* and *p*-doping, respectively, was found, the strain shows nearly no influence on the power factor for Sb_2Te_3 .

For Si/Ge -based superlattices, strain along the [111]-direction was found to be preferable. Under biaxial strain in [001]-direction lifting of the band's degeneracy causes reoccupation of states in the BRILLOUIN zone, which can enhance the electrical conductivity in some cases, but is always related to a decrease of the thermopower. Both effects tend to compensate each other. The degeneracy of the conduction bands is preserved by symmetry in the case of strain along the [111]-direction. Therefore, a reduction of the thermopower is not expected a priori.

The studies on the thermoelectric transport of the superlattices revealed distinct similarities, too. For both superlattice systems, the band gap differences between the bulk materials caused band offsets in the heterostructures. These band offsets tend to localize entirely at either the valence band edge or the conduction band edge, causing strong quantum confinement effects of the carriers in the cross-plane transport direction. For $\text{Bi}_2\text{Te}_3/\text{Sb}_2\text{Te}_3$ -SLs, quantum confinement leads to a strong reduction of the cross-plane transport under *n*-doping, while for the Si/Ge superlattice the *p*-type transport was diminished. The remaining other *n* or *p*-type transport properties were found to be bulk-like, or could only be slightly enhanced, as shown for the Si/Ge superlattice. The remarkable experimental findings of a strongly enhanced cross-plane transport in the $\text{Bi}_2\text{Te}_3/\text{Sb}_2\text{Te}_3$ -SLs could not be confirmed.

Nevertheless, for at least one carrier-type (electron or hole transport) bulk-like electronic transport can be expected in thermoelectric superlattices, enabling to benefit from the reduction of the lattice thermal conductivity for an enhanced figure of merit.

Further studies could account additionally for interfacial disorder or the detailed influence of scattering effects, like electron-impurity or electron-phonon scattering, as already proposed in this thesis, to get more insight into the complexity of thermoelectric heterostructures.

List of publications

- [E1] **N. F. Hinsche, I. Mertig, and P. Zahn**, *Lorenz function of $\text{Bi}_2\text{Te}_3/\text{Sb}_2\text{Te}_3$ superlattices*, *Journal of Electronic Materials* **42** (7), 1406 (2013), [DOI: [10.1007/s11664-012-2279-z](https://doi.org/10.1007/s11664-012-2279-z)]. (Cited on pages 34, 35, and 47.)
- [E2] **N. F. Hinsche, B. Y. Yavorsky, M. Gradhand, M. Czerner, M. Winkler, J. König, H. Böttner, I. Mertig, and P. Zahn**, *Thermoelectric transport in $\text{Bi}_2\text{Te}_3/\text{Sb}_2\text{Te}_3$ superlattices*, *Physical Review B* **86** (8), 085323 (2012), [DOI: [10.1103/PhysRevB.86.085323](https://doi.org/10.1103/PhysRevB.86.085323)]. (Cited on pages 34, 35, 45, 46, and 47.)
- [E3] **N. F. Hinsche, I. Mertig, and P. Zahn**, *Thermoelectric transport in strained Si and Si/Ge heterostructures*, *J. Phys.: Condens. Matter* **24** (27), 275501 (2012), [DOI: [10.1088/0953-8984/24/27/275501](https://doi.org/10.1088/0953-8984/24/27/275501)]. (Cited on pages 14, 21, 43, 45, 71, 72, and 73.)
- [E4] **J. Boor, D. S. Kim, X. Ao, M. Becker, N. F. Hinsche, I. Mertig, P. Zahn, and V. Schmidt**, *Thermoelectric properties of porous silicon*, *Appl. Phys. A* **107** (4), 789–794 (2012), [DOI: [10.1007/s00339-012-6879-5](https://doi.org/10.1007/s00339-012-6879-5)]. (Cited on pages 8 and 14.)
- [E5] **N. F. Hinsche, B. Yavorsky, I. Mertig, and P. Zahn**, *Influence of strain on anisotropic thermoelectric transport in Bi_2Te_3 and Sb_2Te_3* , *Physical Review B* **84** (16), 165214 (2011), [DOI: [10.1103/PhysRevB.84.165214](https://doi.org/10.1103/PhysRevB.84.165214)] and *Publisher’s note: Influence of strain on anisotropic thermoelectric transport in Bi_2Te_3 and Sb_2Te_3* , *Physical Review B* **85** (8), 089902 (2012), [DOI: [10.1103/PhysRevB.85.089902](https://doi.org/10.1103/PhysRevB.85.089902)]. (Cited on pages 6, 21, 34, 41, 45, and 46.)
- [E6] **Peter Zahn, N. F. Hinsche, B. Yavorsky, and I. Mertig**, *Bi_2Te_3 : implications of the rhombohedral k -space texture on the evaluation of the in-plane / out-of-plane conductivity anisotropy*, *J. Phys.: Condens. Matter* **23** (50), 505504 (2011), [DOI: [10.1088/0953-8984/23/50/505504](https://doi.org/10.1088/0953-8984/23/50/505504)]. (Cited on pages 25, 26, 32, and 46.)
- [E7] **B. Yu Yavorsky, N. F. Hinsche, I. Mertig, and P. Zahn**, *Electronic structure and transport anisotropy of Bi_2Te_3 and Sb_2Te_3* , *Physical Review B* **84** (16), 165208 (2011), [DOI: [10.1103/PhysRevB.84.165208](https://doi.org/10.1103/PhysRevB.84.165208)]. (Cited on pages 21, 25, 26, 32, 33, 41, and 45.)
- [E8] **N. F. Hinsche, I. Mertig, and P. Zahn**, *Effect of strain on the thermoelectric properties of silicon: an ab initio study*, *J. Phys.: Condens. Matter* **23** (29), 295502 (2011), [DOI: [10.1088/0953-8984/23/29/295502](https://doi.org/10.1088/0953-8984/23/29/295502)]. (Cited on pages 6, 14, 21, 37, 45, 71, and 72.)
- [E9] **N. F. Hinsche, M. Fechner, P. Bose, S. Ostanin, J. Henk, I. Mertig, and P. Zahn**, *Strong influence of complex band structure on tunneling electroresistance: A combined model and ab initio study*, *Phys. Rev. B* **82** (21), 214110 (2010), [DOI: [10.1103/PhysRevB.82.214110](https://doi.org/10.1103/PhysRevB.82.214110)]. (Not cited.)
- [E10] **N. F. Hinsche, A. Moskalenko, and J. Berakdar**, *High-order harmonic generation by a driven mesoscopic ring with a localized impurity*, *Phys. Rev. A* **79** (2), 023822 (2009). (Not cited.)

Bibliography

- [AAL97] **V. I. Anisimov, F. Aryasetiawan, and A. I. Lichtenstein**, *First-principles calculations of the electronic structure and spectra of strongly correlated systems: the LDA+U method*, J. Phys.: Condens. Matter **9** (4), 767 (1997), [DOI: [10.1088/0953-8984/9/4/002](https://doi.org/10.1088/0953-8984/9/4/002)]. (Cited on page [14](#).)
- [AG98] **F. Aryasetiawan and O. Gunnarsson**, *The GW method*, Reports on Progress in Physics **61** (3), 237 (1998), [DOI: [10.1088/0034-4885/61/3/002](https://doi.org/10.1088/0034-4885/61/3/002)]. (Cited on page [14](#).)
- [AJ84] **O. K. Andersen and O. Jepsen**, *Explicit, First-Principles Tight-Binding Theory*, Physical Review Letters **53** (27), 2571–2574 (1984), [DOI: [10.1103/PhysRevLett.53.2571](https://doi.org/10.1103/PhysRevLett.53.2571)]. (Cited on page [18](#).)
- [All72] **P. Allen**, *Neutron Spectroscopy of Superconductors*, Phys. Rev B **6** (7), 2577–2579 (1972), [DOI: [10.1103/PhysRevB.6.2577](https://doi.org/10.1103/PhysRevB.6.2577)]. (Cited on page [42](#).)
- [AM98] **N. Argaman and G. Makov**, *Density Functional Theory: an introduction*, American Journal of Physics **68** (1), 69–79 (1998), [DOI: [10.1119/1.19375](https://doi.org/10.1119/1.19375)]. (Cited on page [14](#).)
- [ASH⁺99] **M. Asato, A. Settels, T. Hoshino, T. Asada, S. Blügel, R. Zeller, and P. Dederichs**, *Full-potential KKR calculations for metals and semiconductors*, Physical Review B **60** (8), 5202–5210 (1999), [DOI: [10.1103/PhysRevB.60.5202](https://doi.org/10.1103/PhysRevB.60.5202)]. (Cited on page [16](#).)
- [Ask94] **B. Askerov**, *Electron transport phenomena in semiconductors*, World Scientific Pub., Singapore, 1994, [ISBN: [9810212836](https://www.worldscientific.com/9810212836)]. (Cited on pages [29](#) and [30](#).)
- [Bai67] **M. Bailyn**, *Phonon-Drag Part of the Thermoelectric Power in Metals*, Physical Review **157** (3), 480–485 (1967), [DOI: [10.1103/PhysRev.157.480](https://doi.org/10.1103/PhysRev.157.480)]. (Cited on page [43](#).)
- [BBG⁺09] **S. K. Bux, R. G. Blair, P. K. Gogna, H. Lee, G. Chen, M. S. Dresselhaus, R. B. Kaner, and J.-P. Fleurial**, *Nanostructured Bulk Silicon as an Effective Thermoelectric Material*, Adv. Funct. Mater. **19** (15), 2445–2452 (2009), [DOI: [10.1002/adfm.200900250](https://doi.org/10.1002/adfm.200900250)]. (Cited on pages [8](#) and [71](#).)
- [BBTK⁺08] **A. Boukai, Y. Bunimovich, J. Tahir-Kheli, J. Yu, W. G. Iii, and J. Heath**, *Silicon nanowires as efficient thermoelectric materials*, Nature **451** (7175), 168–171 (2008), [DOI: [10.1038/nature06458](https://doi.org/10.1038/nature06458)]. (Cited on pages [5](#), [7](#), and [71](#).)
- [BCB⁺04] **A. Bientien, M. Christensen, J. Bryan, A. Sanchez, S. Paschen, F. Steglich, G. Stucky, and B. Iversen**, *Thermal conductivity of thermoelectric clathrates*, Physical Review B **69** (4), 045107 (2004), [DOI: [10.1103/PhysRevB.69.045107](https://doi.org/10.1103/PhysRevB.69.045107)]. (Cited on page [7](#).)
- [BCV06] **H. Böttner, G. Chen, and R. Venkatasubramanian**, *Aspects of Thin-Film Superlattice Thermoelectric Materials, Devices, and Applications*, MRS bulletin **31** (3), 211 (2006), [DOI: [10.1557/mrs2006.47](https://doi.org/10.1557/mrs2006.47)]. (Cited on pages [9](#) and [10](#).)
- [Bec93] **A. D. Becke**, *A new mixing of Hartree–Fock and local density-functional theories*, J. Chem. Phys. **98** (2), 1372–1377 (1993), [DOI: [10.1063/1.464304](https://doi.org/10.1063/1.464304)]. (Cited on page [14](#).)

- [Bee67] **J. L. Beeby**, *The Density of Electrons in a Perfect or Imperfect Lattice*, Proceedings of the Royal Society A: Mathematical, Physical and Engineering Sciences **302 (1468)**, 113–136 (1967), [DOI: [10.1098/rspa.1967.0230](https://doi.org/10.1098/rspa.1967.0230)]. (Cited on page 15.)
- [Bel08] **L. Bell**, Science **321 (5895)**, 1457 (2008), [DOI: [10.1126/science.1158899](https://doi.org/10.1126/science.1158899)]. (Cited on pages 1, 2, and 35.)
- [BGC01] **S. Baroni, S. D. Gironcoli, and A. D. Corso**, *Phonons and related crystal properties from density-functional perturbation theory*, Reviews of Modern Physics **73 (2)**, 515–562 (2001), [DOI: [10.1103/RevModPhys.73.515](https://doi.org/10.1103/RevModPhys.73.515)]. (Cited on pages 21 and 42.)
- [BGI10] **S. Baroni, P. Giannozzi, and E. Isaev**, *Density-Functional Perturbation Theory for Quasi-Harmonic Calculations*, Reviews in Mineralogy and Geochemistry **71 (1)**, 39–57 (2010), [DOI: [10.2138/rmg.2010.71.3](https://doi.org/10.2138/rmg.2010.71.3)]. (Cited on page 21.)
- [BGT87] **S. Baroni, P. Giannozzi, and A. Testa**, *Green's-function approach to linear response in solids*, Physical Review Letters **58 (18)**, 1861–1864 (1987), [DOI: [10.1103/PhysRevLett.58.1861](https://doi.org/10.1103/PhysRevLett.58.1861)]. (Cited on page 21.)
- [BHS82] **G. Bachelet, D. Hamann, and M. Schlüter**, *Pseudopotentials that work: From H to Pu*, Physical Review B **26 (8)**, 4199–4228 (1982), [DOI: [10.1103/PhysRevB.26.4199](https://doi.org/10.1103/PhysRevB.26.4199)]. (Cited on page 20.)
- [Blo25] **A. Bloch**, *Les théorèmes de M. Valiron sur les fonctions entières et la théorie de l'uniformisation*, Annales de la faculté des sciences de Toulouse **17 (3)**, 22 (1925), [DOI: [10.5802/afst.335](https://doi.org/10.5802/afst.335)]. (Cited on page 18.)
- [BNB⁺02a] **H. Beyer, J. Nurnus, H. Böttner, A. Lambrecht, T. Roch, and G. Bauer**, *PbTe based superlattice structures with high thermoelectric efficiency*, Applied Physics Letters **80 (7)**, 1216 (2002), [DOI: [10.1063/1.1448388](https://doi.org/10.1063/1.1448388)]. (Cited on page 9.)
- [BNB⁺02b] **H. Beyer, J. Nurnus, H. Böttner, A. Lambrecht, E. Wagner, and G. Bauer**, *High thermoelectric figure of merit ZT in PbTe and Bi₂Te₃-based superlattices by a reduction of the thermal conductivity*, Physica E: Low-dimensional Systems and Nanostructures **13 (2-4)**, 965–968 (2002), [DOI: [10.1016/S1386-9477\(02\)00246-1](https://doi.org/10.1016/S1386-9477(02)00246-1)]. (Cited on page 9.)
- [BNSV07] **H. Böttner, J. Nurnus, A. Schubert, and F. Volkert**, *New high density micro structured thermogenerators for stand alone sensor systems*, Proceedings of the XXVI International Conference on Thermoelectrics, 306–309 (2007), [DOI: [10.1109/ICT.2007.4569484](https://doi.org/10.1109/ICT.2007.4569484)]. (Cited on page 1.)
- [BR95a] **D. Broido and T. Reinecke**, *Effect of superlattice structure on the thermoelectric figure of merit*, Physical Review B **51 (19)**, 13797–13800 (1995), [DOI: [10.1103/PhysRevB.51.13797](https://doi.org/10.1103/PhysRevB.51.13797)]. (Cited on page 6.)
- [BR95b] **D. Broido and T. Reinecke**, *Thermoelectric figure of merit of quantum wire superlattices*, Applied Physics Letters **67 (1)**, 100–102 (1995), [DOI: [10.1063/1.115495](https://doi.org/10.1063/1.115495)]. (Cited on page 6.)
- [BT00] **T. Borca-Tasciuc**, *Thermal conductivity of symmetrically strained Si/Ge superlattices*, Superlattices and Microstructures **28 (3)**, 199–206 (2000), [DOI: [10.1006/spmi.2000.0900](https://doi.org/10.1006/spmi.2000.0900)]. (Cited on pages 9 and 72.)

-
- [BTKC01] **T. Borca-Tasciuc, A. Kumar, and G. Chen**, *Data reduction in 3ω method for thin-film thermal conductivity determination*, *Rev. Sci. Instrum.* **72** (4), 2139 (2001), [DOI: [10.1063/1.1353189](https://doi.org/10.1063/1.1353189)]. (Cited on pages 35 and 47.)
- [BTN10] **M. O. Baykan, S. E. Thompson, and T. Nishida**, *Strain effects on 3D, 2D, and 1D silicon logic devices: Predicting the future of strained silicon*, *Journal of Applied Physics* **108** (9), 093716 (2010), [DOI: [10.1063/1.3488635](https://doi.org/10.1063/1.3488635)]. (Cited on page 71.)
- [BZLD84] **P. Braspennig, R. Zeller, A. Lodder, and P. Dederichs**, *Self-consistent cluster calculations with correct embedding for 3d, 4d, and some sp impurities in copper*, *Physical Review B* **29** (2), 703–718 (1984), [DOI: [10.1103/PhysRevB.29.703](https://doi.org/10.1103/PhysRevB.29.703)]. (Cited on page 17.)
- [BZS⁺07] **Z. Bian, M. Zebarjadi, R. Singh, Y. Ezzahri, A. Shakouri, G. Zeng, J.-H. Bahk, J. Bowers, J. Zide, and A. Gossard**, *Cross-plane Seebeck coefficient and Lorenz number in superlattices*, *Physical Review B* **76** (20), 205311 (2007), [DOI: [10.1103/PhysRevB.76.205311](https://doi.org/10.1103/PhysRevB.76.205311)]. (Cited on page 35.)
- [CA86] **D. Ceperley and B. Alder**, *Quantum Monte Carlo*, *Science* **231** (4738), 555–560 (1986), [DOI: [10.1126/science.231.4738.555](https://doi.org/10.1126/science.231.4738.555)]. (Cited on page 14.)
- [CAC⁺08] **M. Christensen, A. B. Abrahamsen, N. B. Christensen, F. Juranyi, N. H. Andersen, K. Lefmann, J. Andreasson, C. R. H. Bahl, and B. B. Iversen**, *Avoided crossing of rattler modes in thermoelectric materials*, *Nature Materials* **7** (10), 811 (2008), [DOI: [doi:10.1038/nmat2273](https://doi.org/10.1038/nmat2273)]. (Cited on page 7.)
- [Cal59] **J. Callaway**, *Model for Lattice Thermal Conductivity at Low Temperatures*, *Physical Review* **113** (4), 1046–1051 (1959), [DOI: [10.1103/PhysRev.113.1046](https://doi.org/10.1103/PhysRev.113.1046)]. (Cited on pages 37, 38, and 40.)
- [Cap06] **K. Capelle**, *A bird's-eye view of density-functional theory*, *Brazilian Journal of Physics* **36** (4A), 1318–1343 (2006), [DOI: [10.1590/S0103-97332006000700035](https://doi.org/10.1590/S0103-97332006000700035)]. (Cited on page 14.)
- [CC05] **A. D. Corso and A. Conte**, *Spin-orbit coupling with ultrasoft pseudopotentials: Application to Au and Pt*, *Physical Review B* **71**, 115106 (2005), [DOI: [10.1103/PhysRevB.71.115106](https://doi.org/10.1103/PhysRevB.71.115106)]. (Cited on pages 19, 20, and 24.)
- [CCHL08] **C. Chiritescu, D. Cahill, C. Heideman, and Q. Lin**, *Low thermal conductivity in nanoscale layered materials synthesized by the method of modulated elemental reactants*, *J. Appl. Phys* **104** (3), 033533 (2008), [DOI: [10.1063/1.2967722](https://doi.org/10.1063/1.2967722)]. (Cited on page 10.)
- [CCN⁺07] **C. Chiritescu, D. G. Cahill, N. Nguyen, D. Johnson, A. Bodapati, P. Keblinski, and P. Zschack**, *Ultralow Thermal Conductivity in Disordered, Layered WSe₂ Crystals*, *Science* **315** (5810), 351–353 (2007), [DOI: [10.1126/science.1136494](https://doi.org/10.1126/science.1136494)]. (Cited on page 10.)
- [CCP⁺92] **T. Caillat, M. Carle, P. Pierrat, H. Scherrer, and S. Scherrer**, *Thermoelectric properties of (Bi_xSb_{1-x})₂Te₃ single crystal solid solutions grown by the THM method*, *Journal of Physics and Chemistry of Solids* **53** (8), 1121–1129 (1992), [DOI: [10.1016/0022-3697\(92\)90087-T](https://doi.org/10.1016/0022-3697(92)90087-T)]. (Cited on page 5.)
- [CD68] **J. Carbotte and R. Dynes**, *Superconductivity in Simple Metals*, *Physical Review* **172** (2), 476–484 (1968), [DOI: [10.1103/PhysRev.172.476](https://doi.org/10.1103/PhysRev.172.476)]. (Cited on page 43.)
-

- [Cep80] **D. M. Ceperley**, *Ground State of the Electron Gas by a Stochastic Method*, Physical Review Letters **45** (7), 566–569 (1980), [DOI: [10.1103/PhysRevLett.45.566](https://doi.org/10.1103/PhysRevLett.45.566)]. (Cited on page 14.)
- [Cer88] **C. Cercignani**, *The Boltzmann equation and its applications*, Springer, New York, 1988, [ISBN: [0387966374](https://www.isbn-international.org/product/0387966374)]. (Cited on page 28.)
- [CFB97] **T. Caillat, J. Fleurial, and A. Borshchevsky**, *Preparation and thermoelectric properties of semiconducting Zn_4Sb_3* , Journal of Physics and Chemistry of Solids **58** (7), 1119–1125 (1997), [DOI: [10.1016/S0022-3697\(96\)00228-4](https://doi.org/10.1016/S0022-3697(96)00228-4)]. (Cited on page 8.)
- [CG52] **H. Callen and R. Greene**, *On a Theorem of Irreversible Thermodynamics*, Physical Review **86** (5), 702–710 (1952), [DOI: [10.1103/PhysRev.86.702](https://doi.org/10.1103/PhysRev.86.702)]. (Cited on page 37.)
- [Che98] **G. Chen**, *Thermal conductivity and ballistic-phonon transport in the cross-plane direction of superlattices*, Physical Review B **57** (23), 14958 (1998), [DOI: [10.1103/PhysRevB.57.14958](https://doi.org/10.1103/PhysRevB.57.14958)]. (Cited on page 10.)
- [CHM⁺08] **R. Chen, A. I. Hochbaum, P. Murphy, J. Moore, P. Yang, and A. Majumdar**, *Thermal Conductance of Thin Silicon Nanowires*, Physical Review Letters **101** (10), 105501 (2008), [DOI: [10.1103/PhysRevLett.101.105501](https://doi.org/10.1103/PhysRevLett.101.105501)]. (Cited on pages 7 and 71.)
- [CKH⁺03] **S. Chakraborty, C. Kleint, A. Heinrich, C. Schneider, J. Schumann, M. Falke, and S. Teichert**, *Thermal conductivity in strain symmetrized Si/Ge superlattices on Si (111)*, Applied Physics Letters **83**, 4184 (2003), [DOI: [10.1063/1.1628819](https://doi.org/10.1063/1.1628819)]. (Cited on page 10.)
- [CKY⁺01] **S. Cho, Y. Kim, S. Youn, A. DiVenere, and G. Wong**, *Artificially ordered Bi/Sb superlattice alloys: Fabrication and transport properties*, Physical Review B **64** (23), 235330 (2001), [DOI: [10.1103/PhysRevB.64.235330](https://doi.org/10.1103/PhysRevB.64.235330)]. (Cited on page 9.)
- [CM69] **M. Cutler and N. Mott**, *Observation of Anderson localization in an electron gas*, Phys. Rev. **181** (3), 1336 (1969), [DOI: [10.1103/PhysRev.181.1336](https://doi.org/10.1103/PhysRev.181.1336)]. (Cited on page 6.)
- [CM95] **J. Costella and B. McKellar**, *The Foldy-Wouthuysen transformation*, American Journal of Physics **63** (12), 1119 (1995), [DOI: [10.1119/1.18017](https://doi.org/10.1119/1.18017)]. (Cited on page 23.)
- [CP87] **D. Cahill and R. Pohl**, *Thermal conductivity of amorphous solids above the plateau*, Physical Review B **35** (8), 4067–4073 (1987), [DOI: [10.1103/PhysRevB.35.4067](https://doi.org/10.1103/PhysRevB.35.4067)]. (Cited on pages 7 and 35.)
- [CQK⁺10] **S. Chadov, X. Qi, J. Kübler, G. H. Fecher, C. Felser, and S. C. Zhang**, *Tunable multifunctional topological insulators in ternary Heusler compounds*, Nature Materials **9** (7), 541 (2010), [DOI: [doi:10.1038/nmat2770](https://doi.org/10.1038/nmat2770)]. (Cited on page 24.)
- [CR11] **J. Cornett and O. Rabin**, *Thermoelectric figure of merit calculations for semiconducting nanowires*, Applied Physics Letters **98** (18), 182104 (2011), [DOI: [10.1063/1.3585659](https://doi.org/10.1063/1.3585659)]. (Cited on pages 6 and 7.)
- [CSS⁺01] **J. Caylor, M. Sander, A. Stacy, J. Harper, R. Gronsky, and T. Sands**, *Epitaxial growth of skutterudite $CoSb_3$ thin films on (001) InSb by pulsed laser deposition*, Journal of Materials Research **16** (9), 2467 (2001), [DOI: [10.1557/JMR.2001.0337](https://doi.org/10.1557/JMR.2001.0337)]. (Cited on page 9.)

-
- [CW04] **P. Carrier and S.-H. Wei**, *Calculated spin-orbit splitting of all diamondlike and zinc-blende semiconductors: Effects of $p_{1/2}$ local orbitals and chemical trends*, *Physical Review B* **70** (3), 035212 (2004), [DOI: [10.1103/PhysRevB.70.035212](https://doi.org/10.1103/PhysRevB.70.035212)]. (Cited on page 23.)
- [Cze09] **M. Czerner**, *Beiträge zur Theorie des Elektronentransports in Systemen mit nichtkollinearer magnetischer Ordnung*, PhD Thesis, (2009), URL: <http://digital.bibliothek.uni-halle.de/hs/urn/urn:nbn:de:gbv:3:4-1796>. (Cited on pages 18 and 23.)
- [Dän08] **M. Däne**, *Beschreibung der elektronischen Struktur korrelierter Systeme mittels lokaler Selbstwechselwirkungskorrekturen im Rahmen der Vielfachstreuungstheorie*, Ph.D. thesis, Martin-Luther-Universität Halle-Wittenberg, 2008, URL: http://sundoc.bibliothek.uni-halle.de/diss-online/08/08H021/of_index.htm. (Cited on page 16.)
- [DDS⁺99] **M. Dresselhaus, G. Dresselhaus, X. Sun, Z. Zhang, S. Cronin, and T. Koga**, *Low-dimensional thermoelectric materials*, *Phys. Solid State* **41** (5), 679–682 (1999), [DOI: [10.1134/1.1130849](https://doi.org/10.1134/1.1130849)]. (Cited on page 6.)
- [DES⁺64] **J. Dismukes, L. Ekstrom, E. Steigmeier, I. Kudman, and D. Beers**, *Thermal and Electrical Properties of Heavily Doped Ge-Si Alloys up to 1300K*, *Journal of Applied Physics* **35** (10), 2899–2907 (1964), [DOI: [10.1063/1.1713126](https://doi.org/10.1063/1.1713126)]. (Cited on page 5.)
- [DGW58] **J. R. Drabble, R. D. Groves, and R. Wolfe**, *Galvanomagnetic Effects in n -type Bismuth Telluride*, *Proceedings of the Physical Society* **71** (3), 430 (1958), [DOI: [10.1088/0370-1328/71/3/317](https://doi.org/10.1088/0370-1328/71/3/317)]. (Cited on page 45.)
- [Dir28] **P. A. M. Dirac**, *The quantum theory of the electron*, *Proceedings of the Royal Society of London. Series A, Containing Papers of a Mathematical and Physical Character* **117** (778), 610–624 (1928), [DOI: [10.1098/rspa.1928.0023](https://doi.org/10.1098/rspa.1928.0023)]. (Cited on page 22.)
- [Dir30] ———, *Note on Exchange Phenomena in the Thomas Atom*, *Mathematical Proceedings of the Cambridge Philosophical Society* **26** (03), 376–385 (1930), [DOI: [10.1017/S0305004100016108](https://doi.org/10.1017/S0305004100016108)]. (Cited on pages 12 and 14.)
- [DJ69] **P. D. DeCicco and F. A. Johnson**, *The Quantum Theory of Lattice Dynamics. IV*, *Proceedings of the Royal Society of London. A. Mathematical and Physical Sciences* **310** (1500), 111–119 (1969), [DOI: [10.1098/rspa.1969.0066](https://doi.org/10.1098/rspa.1969.0066)]. (Cited on page 21.)
- [DLZ06] **P. H. Dederichs, S. Lounis, and R. Zeller**, *The Korringa-Kohn-Rostoker (KKR) Green Function Method II. Impurities and Clusters in the Bulk and on Surfaces*, in *Computational Nanoscience: Do It Yourself*, Jülich **31**, (2006), [ISBN: [3-00-017350-1](https://www.isbn-international.org/product/3-00-017350-1)]. (Cited on page 15.)
- [DSM01] **J. Dong, O. Sankey, and C. Myles**, *Theoretical study of the lattice thermal conductivity in Ge framework semiconductors*, *Physical Review Letters* **86** (11), 2361 (2001), [DOI: [10.1103/PhysRevLett.86.2361](https://doi.org/10.1103/PhysRevLett.86.2361)]. (Cited on page 7.)
- [Dup61] **T. Dupree**, *Electron scattering in a crystal lattice*, *Annals of Physics* **15** (1), 63–78 (1961), [DOI: [10.1016/0003-4916\(61\)90166-X](https://doi.org/10.1016/0003-4916(61)90166-X)]. (Cited on pages 15 and 17.)
-

- [DWZD91] **B. Drittler, M. Weinert, R. Zeller, and P. H. Dederichs**, *Vacancy formation energies of fcc transition metals calculated by a full potential Green's function method*, Solid State Communications **79** (1), 31–35 (1991), [DOI: [10.1016/0038-1098\(91\)90474-A](https://doi.org/10.1016/0038-1098(91)90474-A)]. (Cited on page 16.)
- [DZMM07] **T. Dziekan, P. Zahn, V. Meded, and S. Mirbt**, *Theoretical calculations of mobility enhancement in strained silicon*, Physical Review B **75** (19), 195213 (2007), [DOI: [10.1103/PhysRevB.75.195213](https://doi.org/10.1103/PhysRevB.75.195213)]. (Cited on page 71.)
- [EBB⁺10] **H. Ebert, S. Bornemann, J. Braun, D. Ködderitzsch, S. Lowitzer, S. Mankovsky, J. Minár, M. Offenberger, S. Polesya, and V. Popescu**, *Recent Developments in KKR Theory, Ψ_k - Scientific highlight of the month (97)*, (2010), "URL: http://www.psi-k.org/newsletters/News_97/Highlight_97.pdf". (Cited on page 15.)
- [EGR⁺07] **Y. Ezzahri, S. Grauby, J. Rampnoux, H. Michel, G. Pernot, W. Claeys, S. Dilhaire, C. Rossignol, G. Zeng, and A. Shakouri**, *Coherent phonons in Si/SiGe superlattices*, Physical Review B **75** (19), 195309 (2007), [DOI: [10.1103/PhysRevB.75.195309](https://doi.org/10.1103/PhysRevB.75.195309)]. (Cited on page 10.)
- [EKM11] **H. Ebert, D. Ködderitzsch, and J. Minár**, *Calculating condensed matter properties using the KKR-Green's function method—recent developments and applications*, Reports on Progress in Physics **74**, 096501 (2011), [DOI: [10.1088/0034-4885/74/9/096501](https://doi.org/10.1088/0034-4885/74/9/096501)]. (Cited on pages 15, 16, and 17.)
- [Éli60] **G. M. Éliashberg**, *Interactions between electrons and lattice vibrations in a superconductor*, Soviet Physics JETP **11** (3), 696 (1960), URL: <http://www.w2agz.com/Library/>. (Cited on page 42.)
- [Fau77] **J. S. Faulkner**, *Scattering theory and cluster calculations*, Journal of Physics C: Solid State Physics **10** (23), 4661 (1977), [DOI: [10.1088/0022-3719/10/23/003](https://doi.org/10.1088/0022-3719/10/23/003)]. (Cited on page 17.)
- [Fer27] **E. Fermi**, *Statistical method to determine some properties of atoms*, Rend. R. Acc. Naz. dei Lincei **6** (1), 602–607 (1927), URL: <http://ricerca.mat.uniroma3.it/ipparco/pagine/deposito/2011/TF.pdf>. (Cited on pages 12 and 14.)
- [Fer28] ———, *Eine statistische Methode zur Bestimmung einiger Eigenschaften des Atoms und ihre Anwendung auf die Theorie des periodischen Systems der Elemente*, Z. Physik **48** (1-2), 73–79 (1928), [DOI: [10.1007/BF01351576](https://doi.org/10.1007/BF01351576)]. (Cited on pages 12 and 14.)
- [Fey39] **R. Feynman**, *Forces in Molecules*, Physical Review **56** (4), 340–343 (1939), [DOI: [10.1103/PhysRev.56.340](https://doi.org/10.1103/PhysRev.56.340)]. (Cited on page 21.)
- [FK54] **H. Fröhlich and C. Kittel**, *Remark on the paper by Prof. G. Busch*, Physica **3**, 1086–1086 (1954), [DOI: [10.1016/S0031-8914\(54\)80240-0](https://doi.org/10.1016/S0031-8914(54)80240-0)]. (Cited on page 34.)
- [FKBK00] **J. Furthmüller, P. Käckell, F. Bechstedt, and G. Kresse**, *Extreme softening of Vanderbilt pseudopotentials: General rules and case studies of first-row and d-electron elements*, Physical Review B **61** (7), 4576–4587 (2000), [DOI: [10.1103/PhysRevB.61.4576](https://doi.org/10.1103/PhysRevB.61.4576)]. (Cited on page 18.)

-
- [FL96] **M. Fischetti and S. Laux**, *Band structure, deformation potentials, and carrier mobility in strained Si, Ge, and SiGe alloys*, *Journal of Applied Physics* **80** (4), 2234–2252 (1996), [DOI: [10.1063/1.363052](https://doi.org/10.1063/1.363052)]. (Cited on page 71.)
- [Fog63] **B. Fogarassy**, *On the Solution of the Boltzmann Transport Equation with Relaxation Time Approximation*, *Physica status solidi (b)* **3** (12), 2347–2355 (1963), [DOI: [10.1002/pssb.19630031217](https://doi.org/10.1002/pssb.19630031217)]. (Cited on page 29.)
- [FRA83] **R. Feder, F. Rosicky, and B. Ackermann**, *Relativistic multiple scattering theory of electrons by ferromagnets*, *Zeitschrift für Physik B: Condensed Matter* **52** (1), 31–36 (1983), [DOI: [10.1007/BF01305895](https://doi.org/10.1007/BF01305895)]. (Cited on page 23.)
- [FS99a] **J. Fabian and S. D. Sarma**, *Phonon-Induced Spin Relaxation of Conduction Electrons in Aluminum*, *Physical Review Letters* **83** (6), 1211–1214 (1999), [DOI: [10.1103/PhysRevLett.83.1211](https://doi.org/10.1103/PhysRevLett.83.1211)]. (Cited on page 43.)
- [FS99b] **M. Fuchs and M. Scheffler**, *Ab initio pseudopotentials for electronic structure calculations of poly-atomic systems using density-functional theory*, *Computer Physics Communications* **119** (1), 67–98 (1999), [DOI: [10.1016/S0010-4655\(98\)00201-X](https://doi.org/10.1016/S0010-4655(98)00201-X)]. (Cited on pages 20 and 24.)
- [FT64] **H. Fröhlich and A. Taylor**, *The Boltzmann equations in electron-phonon systems*, *Proceedings of the Physical Society* **83**, 739 (1964), [DOI: [10.1088/0370-1328/83/5/305](https://doi.org/10.1088/0370-1328/83/5/305)]. (Cited on page 42.)
- [FW50] **L. Foldy and S. Wouthuysen**, *On the Dirac theory of spin 1/2 particles and its non-relativistic limit*, *Physical Review* **78** (1), 29 (1950), [DOI: [10.1103/PhysRev.78.29](https://doi.org/10.1103/PhysRev.78.29)]. (Cited on page 23.)
- [GC52] **R. Greene and H. Callen**, *On a Theorem of Irreversible Thermodynamics. II*, *Physical Review* **88** (6), 1387–1391 (1952), [DOI: [10.1103/PhysRev.88.1387](https://doi.org/10.1103/PhysRev.88.1387)]. (Cited on page 37.)
- [GCF⁺09] **M. Gradhand, M. Czerner, D. V. Fedorov, P. Zahn, B. Y. Yavorsky, L. Szunyogh, and I. Mertig**, *Spin polarization on Fermi surfaces of metals by the KKR method*, *Physical Review B* **80** (22), 224413 (2009), [DOI: [10.1103/PhysRevB.80.224413](https://doi.org/10.1103/PhysRevB.80.224413)]. (Cited on pages 18 and 23.)
- [GFP⁺11] **M. Gradhand, D. V. Fedorov, F. Pientka, P. Zahn, I. Mertig, and B. L. Györfy**, *Calculating the Berry curvature of Bloch electrons using the KKR method*, *Physical Review B* **84** (7), 075113 (2011), [DOI: [10.1103/PhysRevB.84.075113](https://doi.org/10.1103/PhysRevB.84.075113)]. (Cited on page 25.)
- [GFZM10a] **M. Gradhand, D. V. Fedorov, P. Zahn, and I. Mertig**, *Extrinsic Spin Hall Effect from First Principles*, *Physical Review Letters* **104** (18), 186403 (2010), [DOI: [10.1103/PhysRevLett.104.186403](https://doi.org/10.1103/PhysRevLett.104.186403)]. (Cited on pages 40 and 41.)
- [GFZM10b] ———, *Fully relativistic ab initio treatment of spin-flip scattering caused by impurities*, *Physical Review B* **81** (2), 020403 (2010), [DOI: [10.1103/PhysRevB.81.020403](https://doi.org/10.1103/PhysRevB.81.020403)]. (Cited on page 41.)
- [GGPB91] **P. Giannozzi, S. D. Gironcoli, P. Pavone, and S. Baroni**, *Ab initio calculation of phonon dispersions in semiconductors*, *Physical Review B* **43** (9), 7231 (1991), [DOI: [10.1103/PhysRevB.43.7231](https://doi.org/10.1103/PhysRevB.43.7231)]. (Cited on page 21.)
-

- [GK66] **R. Guyer and J. Krumhansl**, *Solution of the Linearized Phonon Boltzmann Equation*, Physical Review **148** (2), 766–778 (1966), [DOI: [10.1103/PhysRev.148.766](https://doi.org/10.1103/PhysRev.148.766)]. (Cited on page 37.)
- [GKE12] **S. Giraud, A. Kundu, and R. Egger**, *Electron-phonon scattering in topological insulator thin films*, Physical Review B **85** (3), 035441 (2012), [DOI: [10.1103/PhysRevB.85.035441](https://doi.org/10.1103/PhysRevB.85.035441)]. (Cited on page 43.)
- [Gmo09] **P. Giannozzi and many others**, *QUANTUM ESPRESSO: a modular and open-source software project for quantum simulations of materials*, J. Phys.: Condens. Matter **21**, 395502 (2009), [DOI: [10.1088/0953-8984/21/39/395502](https://doi.org/10.1088/0953-8984/21/39/395502)]. (Cited on pages 19, 22, and 43.)
- [God11] **J. Goddard**, *On the Thermoelectricity of W. Thomson: Towards a Theory of Thermoelastic Conductors*, Journ. of Elasticity **104** (1-2), 267–280 (2011), [DOI: [10.1007/s10659-011-9309-6](https://doi.org/10.1007/s10659-011-9309-6)]. (Cited on page 1.)
- [Gol56] **H. Goldsmid**, *The Thermal Conductivity of Bismuth Telluride*, Proceedings of the Physical Society. Section B **69**, 203 (1956), [DOI: [10.1088/0370-1301/69/2/310](https://doi.org/10.1088/0370-1301/69/2/310)]. (Cited on pages 6, 34, and 35.)
- [Gol65] **H. Goldsmid**, *Transport effects in semi-metals and narrow-gap semiconductors*, Advances in Physics **14** (55), 273 (1965), [DOI: [10.1080/00018736500101061](https://doi.org/10.1080/00018736500101061)]. (Cited on page 34.)
- [Gol09] **H. Goldsmid**, *Porous Thermoelectric Materials*, Materials 2009, Vol. 2, Pages 903-910 **2** (3), 903–910 (2009), [DOI: [10.3390/ma2030903](https://doi.org/10.3390/ma2030903)]. (Cited on page 8.)
- [Gon92] **A. Gonis**, *Green functions for ordered and disordered systems*, Nort Holland, Amsterdam, 1992, [ISBN: [0444889868](https://www.isbn-international.org/product/0444889868)]. (Cited on pages 16 and 17.)
- [Gon95a] **X. Gonze**, *Adiabatic density-functional perturbation theory*, Physical Review A **52** (2), 1096–1114 (1995), [DOI: [10.1103/PhysRevA.52.1096](https://doi.org/10.1103/PhysRevA.52.1096)]. (Cited on page 21.)
- [Gon95b] ———, *Perturbation expansion of variational principles at arbitrary order*, Physical Review A **52** (2), 1086–1095 (1995), [DOI: [10.1103/PhysRevA.52.1086](https://doi.org/10.1103/PhysRevA.52.1086)]. (Cited on page 21.)
- [Goo07] **K. E. Goodson**, *Materials Science: Ordering up the minimum thermal conductivity of solids*, Science **315** (5810), 342–343 (2007), [DOI: [10.1126/science.1138067](https://doi.org/10.1126/science.1138067)]. (Cited on page 10.)
- [Gra10] **M. Gradhand**, *The extrinsic spin Hall effect*, Ph.D. thesis, Martin-Luther-Universität Halle, 2010, URL: <http://digital.bibliothek.uni-halle.de/hs/content/titleinfo/777648>. (Cited on pages 18, 23, 25, and 41.)
- [GS64] **C. Glassbrenner and G. Slack**, *Thermal Conductivity of Silicon and Germanium from 3°K to the Melting Point*, Physical Review **134** (4A), A1058–A1069 (1964), [DOI: [10.1103/PhysRev.134.A1058](https://doi.org/10.1103/PhysRev.134.A1058)]. (Cited on page 39.)
- [GS73] **B. L. Györffy and M. J. Stott**, in *Band structure spectroscopy of metals and alloys*, p. 753, Academic Press, London-New York, 1973, [ISBN: [0122474406](https://www.isbn-international.org/product/0122474406)]. (Cited on page 16.)

-
- [GSS88] **R. Godby, M. Schlüter, and L. Sham**, *Self-energy operators and exchange-correlation potentials in semiconductors*, Physical Review B **37** (17), 10159–10175 (1988), [DOI: [10.1103/PhysRevB.37.10159](https://doi.org/10.1103/PhysRevB.37.10159)]. (Cited on page 14.)
- [GSS91] **X. Gonze, R. Stumpf, and M. Scheffler**, *Analysis of separable potentials*, Physical Review B **44** (16), 8503–8513 (1991), [DOI: [10.1103/PhysRevB.44.8503](https://doi.org/10.1103/PhysRevB.44.8503)]. (Cited on page 20.)
- [GSW58] **H. Goldsmid, A. Sheard, and D. Wright**, *The performance of bismuth telluride thermojunctions*, British Journal of Applied Physics **9** (9), 365 (1958), [DOI: [10.1088/0508-3443/9/9/306](https://doi.org/10.1088/0508-3443/9/9/306)]. (Cited on pages 5, 6, and 45.)
- [GSZ⁺11] **C. Goupil, W. Seifert, K. Zabrocki, E. Müller, and G. Snyder**, *Thermodynamics of Thermoelectric Phenomena and Applications*, Entropy **13** (8), 1481–1517 (2011), [DOI: [10.3390/e13081481](https://doi.org/10.3390/e13081481)]. (Cited on pages 33, 36, and 37.)
- [GYN05] **G. Guo, Y. Yao, and Q. Niu**, *Ab initio Calculation of the Intrinsic Spin Hall Effect in Semiconductors*, Physical Review Letters **94** (22), 226601 (2005), [DOI: [10.1103/PhysRevLett.94.226601](https://doi.org/10.1103/PhysRevLett.94.226601)]. (Cited on page 25.)
- [HAT02] **S. Huxtable, A. Abramson, and C. Tien**, *Thermal conductivity of Si/SiGe and SiGe/SiGe superlattices*, Applied Physics Letters **80** (10), 1737 (2002), [DOI: [10.1063/1.1455693](https://doi.org/10.1063/1.1455693)]. (Cited on page 10.)
- [HCDL08] **A. Hochbaum, R. Chen, R. Delgado, and W. Liang**, *Enhanced thermoelectric performance of rough silicon nanowires*, Nature **451** (7175), 163 (2008), [DOI: [10.1038/nature06381](https://doi.org/10.1038/nature06381)]. (Cited on pages 7 and 71.)
- [HCTH98] **F. A. Hamprecht, A. J. Cohen, D. J. Tozer, and N. C. Handy**, *Development and assessment of new exchange-correlation functionals*, J. Chem. Phys. **109** (15), 6264–6271 (1998), [DOI: [10.1063/1.477267](https://doi.org/10.1063/1.477267)]. (Cited on page 13.)
- [HD93] **L. Hicks and M. Dresselhaus**, *Effect of quantum-well structures on the thermoelectric figure of merit*, Physical Review B **47** (19), 12727–12731 (1993), [DOI: [10.1103/PhysRevB.47.12727](https://doi.org/10.1103/PhysRevB.47.12727)]. (Cited on pages 5 and 6.)
- [HEC02] **B. Hellsing, A. Eiguren, and E. V. Chulkov**, *Electron-phonon coupling at metal surfaces*, J. Phys.: Condens. Matter **14** (24), 5959 (2002), [DOI: [10.1088/0953-8984/14/24/306](https://doi.org/10.1088/0953-8984/14/24/306)]. (Cited on page 42.)
- [Hel37] **H. Hellmann**, *Einführung in die Quantenchemie*, Franz Deuticke, Leipzig, 1937, [DOI: [10.1002/ange.19410541109](https://doi.org/10.1002/ange.19410541109)]. (Cited on page 21.)
- [Hen09] **J. Henk**, *Lecture notes on "Concepts and Methods in Electronic Structure Calculations"*, Max-Planck Institute of Microstructure Physics, 2009. (Cited on page 19.)
- [Her40] **C. Herring**, *A New Method for Calculating Wave Functions in Crystals*, Physical Review **57** (12), 1169–1177 (1940), [DOI: [10.1103/PhysRev.57.1169](https://doi.org/10.1103/PhysRev.57.1169)]. (Cited on page 19.)
- [HHD93] **L. Hicks, T. Harman, and M. Dresselhaus**, *Use of quantum-well superlattices to obtain a high figure of merit from nonconventional thermoelectric materials*, Applied Physics Letters **63** (23), 3230–3232 (1993), [DOI: [10.1063/1.110207](https://doi.org/10.1063/1.110207)]. (Cited on page 6.)

- [HHSD96] **L. Hicks, T. Harman, X. Sun, and M. Dresselhaus**, *Experimental study of the effect of quantum-well structures on the thermoelectric figure of merit*, *Physical Review B* **53** (16), R10493–R10496 (1996), [DOI: [10.1103/PhysRevB.53.R10493](https://doi.org/10.1103/PhysRevB.53.R10493)]. (Cited on pages 5 and 6.)
- [HJT⁺08] **J. P. Heremans, V. Jovovic, E. S. Toberer, A. Saramat, K. Kurosaki, A. Charoiphakdee, S. Yamanaka, and G. J. Snyder**, *Enhancement of thermoelectric efficiency in PbTe by distortion of the electronic density of states*, *Science* **321** (5888), 554 (2008), [DOI: [10.1126/science.1159725](https://doi.org/10.1126/science.1159725)]. (Cited on pages 5 and 7.)
- [HK64] **P. Hohenberg and W. Kohn**, *Inhomogeneous Electron Gas*, *Phys. Rev.* **136** (3B), B864–B871 (1964), [DOI: [10.1103/PhysRev.136.B864](https://doi.org/10.1103/PhysRev.136.B864)]. (Cited on pages 11 and 12.)
- [HK10] **M. Z. Hasan and C. L. Kane**, *Colloquium: Topological insulators*, *Reviews of Modern Physics* **82** (4), 3045 (2010), [DOI: [10.1103/RevModPhys.82.3045](https://doi.org/10.1103/RevModPhys.82.3045)]. (Cited on page 24.)
- [HLG⁺04] **K. Hsu, S. Loo, F. Guo, W. Chen, and J. Dyck**, *Cubic AgPb_mSbTe_{2+m}: Bulk thermoelectric materials with high figure of merit*, *Science* **303** (5659), 818–821 (2004), [DOI: [10.1126/science.1092963](https://doi.org/10.1126/science.1092963)]. (Cited on pages 5 and 8.)
- [HM97] **P. Hyldgaard and G. Mahan**, *Phonon superlattice transport*, *Physical Review-Section B-Condensed Matter* **56** (17), 10754–10757 (1997), [DOI: [10.1103/PhysRevB.56.10754](https://doi.org/10.1103/PhysRevB.56.10754)]. (Cited on page 10.)
- [Hol75] **N. A. W. Holzwarth**, *Theory of impurity scattering in dilute metal alloys based on the muffin-tin model*, *Physical Review B* **11** (10), 3718 (1975), [DOI: [10.1103/PhysRevB.11.3718](https://doi.org/10.1103/PhysRevB.11.3718)]. (Cited on page 15.)
- [HSC79] **D. Hamann, M. Schlüter, and C. Chiang**, *Norm-Conserving Pseudopotentials*, *Physical Review Letters* **43** (20), 1494–1497 (1979), [DOI: [10.1103/PhysRevLett.43.1494](https://doi.org/10.1103/PhysRevLett.43.1494)]. (Cited on pages 19 and 20.)
- [HSRC09] **P. Hofmann, I. Y. Sklyadneva, E. D. L. Rienks, and E. V. Chulkov**, *Electron-phonon coupling at surfaces and interfaces*, *New Journal of Physics* **11** (12), 125005 (2009), [DOI: [10.1088/1367-2630/11/12/125005](https://doi.org/10.1088/1367-2630/11/12/125005)]. (Cited on pages 42 and 43.)
- [HTSW00] **T. C. Harman, P. J. Taylor, D. L. Spears, and M. P. Walsh**, *Thermoelectric quantum-dot superlattices with high ZT*, *Journal of Electronic Materials* **29** (1), L1–L2 (2000), [DOI: [10.1007/s11664-000-0117-1](https://doi.org/10.1007/s11664-000-0117-1)]. (Cited on pages 6, 7, 9, and 10.)
- [HTWL02] **T. Harman, P. Taylor, M. Walsh, and B. LaForge**, *Quantum dot superlattice thermoelectric materials and devices*, *Science* **297** (5590), 2229 (2002), [DOI: [10.1126/science.1072886](https://doi.org/10.1126/science.1072886)]. (Cited on pages 5, 6, 9, and 10.)
- [HWLT05] **T. C. Harman, M. P. Walsh, B. E. Laforge, and G. W. Turner**, *Nanostructured thermoelectric materials*, *Journal of Electronic Materials* **34** (5), L19–L22 (2005), [DOI: [10.1007/s11664-005-0083-8](https://doi.org/10.1007/s11664-005-0083-8)]. (Cited on pages 2, 5, 6, 7, 9, and 10.)
- [HXQ⁺09] **D. Hsieh, Y. Xia, D. Qian, L. Wray, F. Meier, J. Dil, J. Osterwalder, L. Patthey, A. Fedorov, H. Lin, A. Bansil, D. Grauer, Y. Hor, R. Cava, and M. Hasan**, *Observation of Time-Reversal-Protected Single-Dirac-Cone Topological-Insulator States in Bi₂Te₃ and Sb₂Te₃*, *Physical Review Letters* **103** (14), 146401 (2009), [DOI: [10.1103/PhysRevLett.103.146401](https://doi.org/10.1103/PhysRevLett.103.146401)]. (Cited on page 24.)

-
- [HZE⁺98] **T. Huhne, C. Zecha, H. Ebert, P. Dederichs, and R. Zeller**, *Full-potential spin-polarized relativistic Korringa-Kohn-Rostoker method implemented and applied to bcc Fe, fcc Co, and fcc Ni*, *Physical Review B* **58** (16), 10236 (1998), [DOI: [10.1103/PhysRevB.58.10236](https://doi.org/10.1103/PhysRevB.58.10236)]. (Cited on pages 16, 22, and 23.)
- [Iof57] **A. F. Ioffe**, *Semiconductor thermoelements, and Thermoelectric cooling*, Infosearch, London, 1957, [ISBN: [0850860393](https://www.isbn-international.org/product/0850860393)]. (Cited on pages 2, 5, 6, and 7.)
- [Iof58] ———, *The Revival of Thermoelectricity*, *Scientific American* **199** (5), 31 (1958), [DOI: [10.1038/scientificamerican1158-31](https://doi.org/10.1038/scientificamerican1158-31)]. (Cited on page 5.)
- [JKH09] **C. Jaworski, V. Kulbachinskii, and J. Heremans**, *Resonant level formed by tin in Bi₂Te₃ and the enhancement of room-temperature thermoelectric power*, *Physical Review B* **80** (23), 233201 (2009), [DOI: [10.1103/PhysRevB.80.233201](https://doi.org/10.1103/PhysRevB.80.233201)]. (Cited on page 7.)
- [JNC⁺11] **J. Jeffers, K. Namjou, Z. Cai, P. McCann, and L. Olona**, *Cross-plane thermal conductivity of a PbSnSe/PbSe superlattice material*, *Applied Physics Letters* **99** (4), 041903 (2011), [DOI: [10.1063/1.3615797](https://doi.org/10.1063/1.3615797)]. (Cited on page 9.)
- [JS10] **B. Jalan and S. Stemmer**, *Large Seebeck coefficients and thermoelectric power factor of La-doped SrTiO₃ thin films*, *Applied Physics Letters* **97** (4), 3 (2010), [DOI: [10.1063/1.3471398](https://doi.org/10.1063/1.3471398)]. (Cited on page 6.)
- [Kai89] **H. Kaibe**, *Anisotropic galvanomagnetic and thermoelectric properties of n-type Bi₂Te₃ single crystal with the composition of a useful thermoelectric cooling material*, *Journal of Physics and Chemistry of Solids* **50** (9), 945–950 (1989), [DOI: [10.1016/0022-3697\(89\)90045-0](https://doi.org/10.1016/0022-3697(89)90045-0)]. (Cited on page 37.)
- [KB82] **L. Kleinman and D. Bylander**, *Efficacious Form for Model Pseudopotentials*, *Physical Review Letters* **48** (20), 1425–1428 (1982), [DOI: [10.1103/PhysRevLett.48.1425](https://doi.org/10.1103/PhysRevLett.48.1425)]. (Cited on page 20.)
- [KCDL00] **T. Koga, S. Cronin, M. Dresselhaus, and J. Liu**, *Experimental proof-of-principle investigation of enhanced ZT in (001) oriented Si/Ge superlattices*, *Applied Physics Letters* **77** (10), 1490 (2000), [DOI: [10.1063/1.1308271](https://doi.org/10.1063/1.1308271)]. (Cited on page 72.)
- [KDL09] **R. Kim, S. Datta, and M. S. Lundstrom**, *Influence of dimensionality on thermoelectric device performance*, *Journal of Applied Physics* **105** (3), 034506 (2009), [DOI: [10.1063/1.3074347](https://doi.org/10.1063/1.3074347)]. (Cited on page 7.)
- [KHCD99] **T. Koga, T. Harman, S. Cronin, and M. S. Dresselhaus**, *Mechanism of the enhanced thermoelectric power in (111)-oriented n-type PbTe/Pb_{1-x}Eu_xTe*, *Physical Review B* **60** (20), 14286 (1999), [DOI: [10.1103/PhysRevB.60.14286](https://doi.org/10.1103/PhysRevB.60.14286)]. (Cited on page 6.)
- [KKKI12] **M. Kim, C. H. Kim, H. S. Kim, and J. Ihm**, *Topological quantum phase transitions driven by external electric fields in Sb₂Te₃ thin films*, *Proceedings of the National Academy of Sciences* **109** (3), 671–674 (2012), [DOI: [10.1073/pnas.1119010109](https://doi.org/10.1073/pnas.1119010109)]. (Cited on page 24.)
- [Kle80] **L. Kleinman**, *Relativistic norm-conserving pseudopotential*, *Physical Review B* **21** (6), 2630–2631 (1980), [DOI: [10.1103/PhysRevB.21.2630](https://doi.org/10.1103/PhysRevB.21.2630)]. (Cited on page 24.)
-

- [KNG⁺11] **J. König, M. Nielsen, Y.-B. Gao, M. Winkler, A. Jacquot, H. Böttner, and J. Heremans**, *Titanium forms a resonant level in the conduction band of PbTe*, *Physical Review B* **84** (20), 205126 (2011), [DOI: [10.1103/PhysRevB.84.205126](https://doi.org/10.1103/PhysRevB.84.205126)]. (Cited on page 7.)
- [Koh99] **W. Kohn**, *Nobel Lecture: Electronic structure of matter—wave functions and density functionals*, *Reviews of Modern Physics* **71** (5), 1253–1266 (1999), [DOI: [10.1103/RevModPhys.71.1253](https://doi.org/10.1103/RevModPhys.71.1253)]. (Cited on page 11.)
- [Kor47] **J. Korryng**, *On the calculation of the energy of a Bloch wave in a metal*, *Physica* **13** (6), 392–400 (1947), [DOI: [10.1016/0031-8914\(47\)90013-X](https://doi.org/10.1016/0031-8914(47)90013-X)]. (Cited on pages 15 and 17.)
- [Kor12] **P. Kordt**, *Single-Site Green Function of the Dirac Equation for Full-Potential Electron Scattering*, *Schriften des Forschungszentrums Jülich*, Jülich, 2012, [ISBN: [9783893367603](https://www.isbn-international.org/product/9783893367603)]. (Cited on page 23.)
- [KPP93] **G. S. Kumar, G. Prasad, and R. O. Pohl**, *Experimental determinations of the Lorenz number*, *Journal of Materials Science* **28** (16), 4261–4272 (1993), [DOI: [10.1007/BF01154931](https://doi.org/10.1007/BF01154931)]. (Cited on page 35.)
- [KR54] **W. Kohn and N. Rostoker**, *Solution of the Schrödinger Equation in Periodic Lattices with an Application to Metallic Lithium*, *Physical Review* **94** (5), 1111–1120 (1954), [DOI: [10.1103/PhysRev.94.1111](https://doi.org/10.1103/PhysRev.94.1111)]. (Cited on page 15.)
- [KRR⁺04] **V. D. Kagan, N. A. Red’ko, N. A. Rodionov, V. I. Pol’shin, and O. V. Zotova**, *Phonon drag thermopower in doped bismuth*, *Phys. Solid State* **46** (8), 1410–1419 (2004), [DOI: [10.1134/1.1788771](https://doi.org/10.1134/1.1788771)]. (Cited on page 43.)
- [KS65] **W. Kohn and L. J. Sham**, *Self-Consistent Equations Including Exchange and Correlation Effects*, *Physical Review* **140** (4), A1133 (1965), [DOI: [10.1103/PhysRev.140.A1133](https://doi.org/10.1103/PhysRev.140.A1133)]. (Cited on pages 11, 12, and 14.)
- [KSCD99] **T. Koga, X. Sun, S. Cronin, and M. Dresselhaus**, *Carrier pocket engineering applied to strained Si/Ge superlattices to design useful thermoelectric materials*, *Applied Physics Letters* **75**, 2438 (1999), [DOI: [10.1063/1.125040](https://doi.org/10.1063/1.125040)]. (Cited on page 72.)
- [Kud72] **I. Kudman**, *Thermoelectric properties of p-type PbTe-PbSe alloys*, *Journal of Materials Science* **7** (9), 1027–1029 (1972), [DOI: [10.1007/BF00550066](https://doi.org/10.1007/BF00550066)]. (Cited on page 5.)
- [KWB⁺11] **J. König, M. Winkler, S. Buller, W. Bensch, U. Schürmann, L. Kienle, and H. Böttner**, *Bi₂Te₃-Sb₂Te₃ Superlattices Grown by Nanoalloying*, *Journal of Electronic Materials* **40** (5), 1266 (2011), [DOI: [10.1007/s11664-011-1578-0](https://doi.org/10.1007/s11664-011-1578-0)]. (Cited on pages 9 and 47.)
- [KZG⁺06] **W. Kim, J. Zide, A. Gossard, D. Klenov, S. Stemmer, A. Shakouri, and A. Majumdar**, *Thermal conductivity reduction and thermoelectric figure of merit increase by embedding nanoparticles in crystalline semiconductors*, *Physical Review Letters* **96** (4), 45901 (2006), [DOI: [10.1103/PhysRevLett.96.045901](https://doi.org/10.1103/PhysRevLett.96.045901)]. (Cited on page 8.)
- [LCV97] **S. Lee, D. Cahill, and R. Venkatasubramanian**, *Thermal conductivity of Si-Ge superlattices*, *Appl. Phys. Lett.* **70** (22), 2957 (1997), [DOI: [10.1063/1.118755](https://doi.org/10.1063/1.118755)]. (Cited on pages 9, 10, and 72.)
- [LD03] **Y.-M. Lin and M. Dresselhaus**, *Thermoelectric properties of superlattice nanowires*, *Physical Review B* **68** (7), 075304 (2003), [DOI: [10.1103/PhysRevB.68.075304](https://doi.org/10.1103/PhysRevB.68.075304)]. (Cited on page 7.)

-
- [LED⁺05] **M. Lüders, A. Ernst, M. Däne, Z. Szotek, A. Svane, D. Ködderitzsch, W. Hergert, B. Györffy, and W. Temmerman**, *Self-interaction correction in multiple scattering theory*, *Physical Review B* **71** (20), 205109 (2005), [DOI: [10.1103/PhysRevB.71.205109](https://doi.org/10.1103/PhysRevB.71.205109)]. (Cited on page 14.)
- [Leh54] **H. Lehmann**, *Über Eigenschaften von Ausbreitungsfunktionen und Renormierungskonstanten quantisierter Felder*, *Il Nuovo Cimento* **11** (4), 342–357 (1954), [DOI: [10.1007/BF02783624](https://doi.org/10.1007/BF02783624)]. (Cited on page 15.)
- [Lev82] **M. Levy**, *Electron densities in search of Hamiltonians*, *Physical Review A* **26** (3), 1200–1208 (1982), [DOI: [10.1103/PhysRevA.26.1200](https://doi.org/10.1103/PhysRevA.26.1200)]. (Cited on page 12.)
- [LG09] **J. Lee and J. Grossman**, *Thermoelectric properties of nanoporous Ge*, *Applied Physics Letters* **95** (1), 013106 (2009), [DOI: [10.1063/1.3159813](https://doi.org/10.1063/1.3159813)]. (Cited on page 8.)
- [LS50] **B. Lippmann and J. Schwinger**, *Variational Principles for Scattering Processes. I*, *Physical Review* **79** (3), 469–480 (1950), [DOI: [10.1103/PhysRev.79.469](https://doi.org/10.1103/PhysRev.79.469)]. (Cited on page 16.)
- [LSX⁺12] **H. Liu, X. Shi, F. Xu, L. Zhang, W. Zhang, L. Chen, Q. Li, C. Uher, T. Day, and G. J. Snyder**, *Copper ion liquid-like thermoelectrics*, *Nature Materials* **11** (5), 422 (2012), [DOI: [doi:10.1038/nmat3273](https://doi.org/10.1038/nmat3273)]. (Cited on page 9.)
- [LT72] **G. Lehmann and M. Taut**, *On the Numerical Calculation of the Density of States and Related Properties*, *Physica status solidi (b)* **54** (2), 469–477 (1972), [DOI: [10.1002/pssb.2220540211](https://doi.org/10.1002/pssb.2220540211)]. (Cited on page 25.)
- [LWG10] **J.-H. Lee, J. Wu, and J. C. Grossman**, *Enhancing the Thermoelectric Power Factor with Highly Mismatched Isoelectronic Doping*, *Physical Review Letters* **104** (1), 016602 (2010), [DOI: [10.1103/PhysRevLett.104.016602](https://doi.org/10.1103/PhysRevLett.104.016602)]. (Cited on page 7.)
- [LWK⁺03] **D. Li, Y. Wu, P. Kim, L. Shi, P. Yang, and A. Majumdar**, *Thermal conductivity of individual silicon nanowires*, *Applied Physics Letters* **83** (14), 2934–2936 (2003), [DOI: [10.1063/1.1616981](https://doi.org/10.1063/1.1616981)]. (Cited on page 7.)
- [Mah90] **G. D. Mahan**, *Many particle physics*, Plenum Press, New York, 1990, [ISBN: [0-306-43423-7](https://www.worldscientific.com/9780306434237)]. (Cited on page 42.)
- [Mat02] **A. E. Mattsson**, *In Pursuit of the "Divine" Functional*, *Science* **298** (5594), 759–760 (2002), [DOI: [10.1126/science.1077710](https://doi.org/10.1126/science.1077710)]. (Cited on page 13.)
- [McK76] **N. L. McKay**, *A Theoretical Calculation of Quasiparticle Properties in Aluminum*, Ph.D. thesis, McMaster University, 1976, URL: <http://digitalcommons.mcmaster.ca/opensdissertations/412/>. (Cited on page 43.)
- [Mer99] **I. Mertig**, *Transport properties of dilute alloys*, *Reports on Progress in Physics* **62**, 237–276 (1999), [DOI: [10.1088/0034-4885/62/2/004](https://doi.org/10.1088/0034-4885/62/2/004)]. (Cited on pages 27, 28, 33, and 40.)
- [Mic12] **Micropelt GmbH**, *Thin Film Thermogenerators and Sensing Devices: MPG-D651*, accessed in September 2012, URL: http://www.micropelt.com/download/datasheet_mpg_d651_d751.pdf. (Cited on page 2.)
-

- [Mig58] **A. B. Migdal**, *Interactions between electrons and lattice vibrations in a normal metal*, Soviet Physics JETP **34**(7) (6), 996 (1958), URL: <http://www.w2agz.com/Library/>. (Cited on page 42.)
- [Mil60] **D. G. Miller**, *Thermodynamics of Irreversible Processes. The Experimental Verification of the Onsager Reciprocal Relations.*, Chem. Rev. **60** (1), 15 (1960), [DOI: [10.1021/cr60203a003](https://doi.org/10.1021/cr60203a003)]. (Cited on page 36.)
- [MMZ87] **I. Mertig, E. Mrosan, and P. Ziesche**, *Multiple scattering theory of point defects in metals: electronic properties*, Teubner-Texte zur Physik, Band 11, B. G. Teubner Verlagsgesellschaft, Leipzig, 1987, [ISBN: [3322004406](https://www.isbn-international.org/product/3322004406)]. (Cited on pages 15, 25, 26, and 40.)
- [Mot67] **N. Mott**, *Electrons in disordered structures*, Advances in Physics **16** (61), 49–144 (1967), [DOI: [10.1080/00018736700101265](https://doi.org/10.1080/00018736700101265)]. (Cited on page 6.)
- [MP06] **P. Mavropoulos and N. Papanikolaou**, *The Korringa-Kohn-Rostoker (KKR) Green Function Method I. Electronic Structure of Periodic Systems*, in Computational Nanoscience: Do It Yourself, Jülich **31**, 131–158 (2006), [ISBN: [3-00-017350-1](https://www.isbn-international.org/product/3-00-017350-1)]. (Cited on pages 15 and 17.)
- [MS96] **G. Mahan and J. O. Sofo**, *The best thermoelectric*, Proceedings of the National Academy of Sciences **93** (15), 7436 (1996), URL: <http://www.pnas.org/content/93/15/7436.abstract>. (Cited on pages 7 and 32.)
- [MS06] **G. Madsen and D. J. Singh**, BOLTZTRAP. *A code for calculating band-structure dependent quantities*, Computer Physics Communications **175** (1), 67–71 (2006), [DOI: [10.1016/j.cpc.2006.03.007](https://doi.org/10.1016/j.cpc.2006.03.007)]. (Cited on page 25.)
- [MSS09] **A. May, D. J. Singh, and G. J. Snyder**, *Influence of band structure on the large thermoelectric performance of lanthanum telluride*, Physical Review B **79** (15), 153101 (2009), [DOI: [10.1103/PhysRevB.79.153101](https://doi.org/10.1103/PhysRevB.79.153101)]. (Cited on page 5.)
- [MV64] **A. Matthiessen and C. Vogt**, *On the Influence of Temperature on the Electric Conducting-power of Alloys*, Philosophical Transactions of the Royal Society of London **154**, 167–200 (1864), URL: <http://www.jstor.org/stable/108867>. (Cited on page 40.)
- [MV79] **A. H. MacDonald and S. H. Vosko**, *A relativistic density functional formalism*, Journal of Physics C: Solid State Physics **12** (15), 2977 (1979), [DOI: [10.1088/0022-3719/12/15/007](https://doi.org/10.1088/0022-3719/12/15/007)]. (Cited on page 22.)
- [MW98] **G. Mahan and L. Woods**, *Multilayer Thermionic Refrigeration*, Physical Review Letters **80** (18), 4016–4019 (1998), [DOI: [10.1103/PhysRevLett.80.4016](https://doi.org/10.1103/PhysRevLett.80.4016)]. (Cited on page 10.)
- [NCS98] **G. S. Nolas, J. L. Cohn, and G. A. Slack**, *Effect of partial void filling on the lattice thermal conductivity of skutterudites*, Physical Review B **58** (1), 164 (1998), [DOI: [10.1103/PhysRevB.58.164](https://doi.org/10.1103/PhysRevB.58.164)]. (Cited on page 7.)
- [NCSS98] **G. Nolas, J. Cohn, G. Slack, and S. Schujman**, *Semiconducting Ge clathrates: Promising candidates for thermoelectric applications*, Applied Physics Letters **73** (2), 178–180 (1998), [DOI: [10.1063/1.121747](https://doi.org/10.1063/1.121747)]. (Cited on page 7.)

- [NG04] **G. S. Nolas and H. J. Goldsmid**, in *Thermal conductivity: Theory, Properties and Applications*, ch. 1.4, p. 306, Kluwer Academic, New York, 2004, [ISBN: 0306483270]. (Cited on page 40.)
- [Nie07] **K. Nielsch**, *Thermoelektrische Multitalente*, Physik Journal **6** (5), 35 (2007), URL: <http://www.pro-physik.de/details/articlePdf/1105003/issue.html>. (Cited on page 2.)
- [NMT99] **G. Nolas, D. Morelli, and T. Tritt**, *Skutterudites: A phonon-glass-electron crystal approach to advanced thermoelectric energy conversion applications*, Annual Review of Materials Science **29**, 89–116 (1999), [DOI: 10.1146/annurev.matsci.29.1.89]. (Cited on page 7.)
- [NPK06] **G. Nolas, J. Poon, and M. Kanatzidis**, *Recent developments in bulk thermoelectric materials*, MRS bulletin **31** (3), 199–205 (2006), [DOI: 10.1557/mrs2006.45]. (Cited on pages 7 and 8.)
- [NSM⁺96] **G. S. Nolas, G. A. Slack, D. T. Morelli, T. M. Tritt, and A. C. Ehrlich**, *The effect of rare-earth filling on the lattice thermal conductivity of skutterudites*, Journal of Applied Physics **79** (8), 4002–4008 (1996), [DOI: 10.1063/1.361828]. (Cited on page 7.)
- [Oht07] **H. Ohta**, *Thermoelectrics based on strontium titanate*, Materials today **10** (10), 44–49 (2007), [DOI: 10.1016/S1369-7021(07)70244-4]. (Cited on pages 6 and 7.)
- [OKM⁺07] **H. Ohta, S. Kim, Y. Mune, T. Mizoguchi, K. Nomura, S. Ohta, T. Nomura, Y. Nakanishi, Y. Ikuhara, M. Hirano, H. Hosono, and K. Koumoto**, *Giant thermoelectric Seebeck coefficient of a two-dimensional electron gas in SrTiO₃*, Nature Materials **6** (2), 129 (2007), [DOI: doi:10.1038/nmat1821]. (Cited on pages 6 and 7.)
- [OMK⁺08] **H. Ohta, Y. Mune, K. Koumoto, T. Mizoguchi, and Y. Ikuhara**, *Critical thickness for giant thermoelectric Seebeck coefficient of 2DEG confined in SrTiO₃/SrTi_{0.8}Nb_{0.2}O₃ superlattices*, Thin Solid Films **516** (17), 5916–5920 (2008), [DOI: 10.1016/j.tsf.2007.10.034]. (Cited on pages 6 and 7.)
- [Ons31a] **L. Onsager**, *Reciprocal Relations in Irreversible Processes. I.*, Physical Review **37** (4), 405 (1931), [DOI: 10.1103/PhysRev.37.405]. (Cited on pages 33 and 36.)
- [Ons31b] ———, *Reciprocal Relations in Irreversible Processes. II.*, Physical Review **37** (12), 2265 (1931), [DOI: 10.1103/PhysRev.38.2265]. (Cited on pages 33 and 36.)
- [Pau27] **W. Pauli**, *Zur Quantenmechanik des magnetischen Elektrons*, Z. Physik **43** (9-10), 601–623 (1927), [DOI: 10.1007/BF01397326]. (Cited on page 23.)
- [PBE96] **J. Perdew, K. Burke, and M. Ernzerhof**, *Generalized gradient approximation made simple*, Physical Review Letters **77** (18), 3865–3868 (1996), [DOI: 10.1103/PhysRevLett.78.1396]. (Cited on pages 14 and 19.)
- [PBT⁺98] **L. Petit, S. V. Beiden, W. M. Temmerman, Z. Szotek, G. M. Stocks, and G. A. Gehring**, *Screened real-space study of the magnetic properties of Ni*, Philosophical Magazine B **78** (5/6), 449–456 (1998), [DOI: 10.1080/014186398257691]. (Cited on page 17.)
- [Pei29] **R. Peierls**, *Zur kinetischen Theorie der Wärmeleitung in Kristallen*, Annalen der Physik **395** (8), 1055–1101 (1929), [DOI: 10.1002/andp.19293950803]. (Cited on page 40.)

- [Pel34] **J. C. A. Peltier**, *Nouvelles expériences sur la calorité des courants électrique*, Ann. Chim. Phys. **56**, 371 (1834), [ISBN: 9781179117317]. (Cited on page 1.)
- [Per81] **J. P. Perdew**, *Self-interaction correction to density-functional approximations for many-electron systems*, Physical Review B **23** (10), 5048–5079 (1981), [DOI: 10.1103/PhysRevB.23.5048]. (Cited on page 14.)
- [Per85] ———, *Density functional theory and the band gap problem*, International Journal of Quantum Chemistry **28** (S19), 497–523 (1985), [DOI: 10.1002/qua.560280846]. (Cited on page 14.)
- [PHM⁺08] **B. Poudel, Q. Hao, Y. Ma, Y. Lan, A. Minnich, B. Yu, X. Yan, D. Wang, A. Muto, and D. Vashaee**, *High-thermoelectric performance of nanostructured bismuth antimony telluride bulk alloys*, Science **320** (5876), 634 (2008), [DOI: 10.1126/science.1156446]. (Cited on pages 5 and 45.)
- [Pic89] **W. Pickett**, *Pseudopotential methods in condensed matter applications*, Computer Physics Reports **9** (3), 115–197 (1989), [DOI: 10.1016/0167-7977(89)90002-6]. (Cited on pages 19 and 20.)
- [PJP⁺92] **J. P. Perdew, K. A. Jackson, M. R. Pederson, D. J. Singh, and C. Fiolhais**, *Atoms, molecules, solids, and surfaces: Applications of the generalized gradient approximation for exchange and correlation*, Physical Review B **46** (11), 6671–6687 (1992), [DOI: 10.1103/PhysRevB.46.6671]. (Cited on page 14.)
- [PK59] **J. Phillips and L. Kleinman**, *New Method for Calculating Wave Functions in Crystals and Molecules*, Physical Review **116** (2), 287–294 (1959), [DOI: 10.1103/PhysRev.116.287]. (Cited on page 19.)
- [PLIS11] **Y. Pei, A. LaLonde, S. Iwanaga, and G. Snyder**, *High thermoelectric figure of merit in heavy hole dominated PbTe*, Energy Environ. Sci. **4** (6), 2085–2089 (2011), [DOI: 10.1039/C0EE00456A]. (Cited on page 5.)
- [Pri56a] **P. J. Price**, *Anomalous Lorenz Numbers in Mixed Semiconductors*, Proceedings of the Physical Society. Section B **69** (8), 851 (1956), [DOI: 10.1088/0370-1301/69/8/117]. (Cited on pages 6, 34, and 35.)
- [Pri56b] ———, *Theory of Transport Effects in Semiconductors: Thermoelectricity*, Physical Review **104** (5), 1223–1239 (1956), [DOI: 10.1103/PhysRev.104.1223]. (Cited on pages 6 and 31.)
- [Pyy88] **P. Pyykko**, *Relativistic effects in structural chemistry*, Chemical Reviews **88** (3), 563–594 (1988), [DOI: 10.1021/cr00085a006]. (Cited on page 24.)
- [PZD02] **N. Papanikolaou, R. Zeller, and P. Dederichs**, *Conceptual improvements of the KKR method*, J. Phys.: Condens. Matter **14** (11), 2799 (2002), [DOI: 10.1088/0953-8984/14/11/304]. (Cited on page 15.)
- [QZ10] **X. Qi and S. Zhang**, *The quantum spin Hall effect and topological insulators*, Physics Today **63** (1), 33–38 (2010), [DOI: 10.1063/1.3293411]. (Cited on page 24.)
- [RK73] **M. Roufosse and P. Klemens**, *Thermal Conductivity of Complex Dielectric Crystals*, Physical Review B **7** (12), 5379–5386 (1973), [DOI: 10.1103/PhysRevB.7.5379]. (Cited on page 9.)

-
- [Ros61] **M. E. Rose**, *Relativistic electron theory*, 1 ed., John Wiley & Sons, New York, 1961, [ISBN: [10.1119/1.1937653](#)]. (Cited on page 24.)
- [Row06] **D. M. Rowe**, *Thermoelectrics Handbook: Macro to Nano*, CRC Press, Boca Raton, 2006, [ISBN: [0-8493-2264-2](#)]. (Cited on page 1.)
- [RR79] **M. V. Ramana and A. K. Rajagopal**, *Relativistic spin-polarised electron gas*, Journal of Physics C: Solid State Physics **12** (22), L845 (1979), [DOI: [10.1088/0022-3719/12/22/005](#)]. (Cited on page 22.)
- [Sav96] **S. Y. Savrasov**, *Electron-phonon interactions and related physical properties of metals from linear-response theory*, Physical Review B **54** (23), 16487–16501 (1996), [DOI: [10.1103/PhysRevB.54.16487](#)]. (Cited on page 43.)
- [SB97] **A. Shakouri and J. Bowers**, *Heterostructure integrated thermionic coolers*, Applied Physics Letters **71** (9), 1234 (1997), [DOI: [10.1063/1.119861](#)]. (Cited on page 10.)
- [SBPP11] **J. Smith, S. Banerjee, V. Pardo, and W. Pickett**, *Dirac Point Degenerate with Massive Bands at a Topological Quantum Critical Point*, Physical Review Letters **106** (5), 056401 (2011), [DOI: [10.1103/PhysRevLett.106.056401](#)]. (Cited on page 24.)
- [SCNC04] **G. J. Snyder, M. Christensen, E. Nishibori, and T. Caillat**, *Disordered zinc in Zn_4Sb_3 with phonon-glass and electron-crystal thermoelectric properties*, Nature Materials **3** (7), (2004), [DOI: [10.1038/nmat1154](#)]. (Cited on page 8.)
- [See26] **T. J. Seebeck**, *Über die magnetische Polarisation der Metalle und Erze durch Temperaturdifferenz*, Annalen der Physik **82** (3), 253–286 (1826), [DOI: [10.1002/andp.18260820302](#)]. (Cited on pages 1 and 35.)
- [SESG89] **P. Strange, H. Ebert, J. B. Staunton, and B. L. Györfy**, *A relativistic spin-polarised multiple-scattering theory, with applications to the calculation of the electronic structure of condensed matter*, J. Phys.: Condens. Matter **1** (18), 2959 (1989), [DOI: [10.1088/0953-8984/1/18/002](#)]. (Cited on page 23.)
- [SH76] **M. Stordeur and W. Heiliger**, *Anisotropy of the thermopower of p - Sb_2Te_3* , Physica status solidi (b) **78** (2), K103–K106 (1976), [DOI: [10.1002/pssb.2220780255](#)]. (Cited on page 46.)
- [Sha11] **A. Shakouri**, *Recent Developments in Semiconductor Thermoelectric Physics and Materials*, Annual Review of Materials Research **41**, 399–431 (2011), [DOI: [10.1146/annurev-matsci-062910-100445](#)]. (Cited on pages 6, 9, and 10.)
- [SJ89] **H. Smith and H. H. Jensen**, *Transport phenomena*, Clarendon Press, Oxford, 1989, [ISBN: [0198519850](#)]. (Cited on page 37.)
- [SK75] **M. Stordeur and W. Kühnberger**, *Nichtparabolizität des Valenzbandes von Bi_2Te_3 gefolgert aus Transporteigenschaften*, Physica status solidi (b) **69** (2), 377–387 (1975), [DOI: [10.1002/pssb.2220690208](#)]. (Cited on page 37.)
- [SKL⁺08] **X. Shi, H. Kong, C. Li, C. Uher, J. Yang, J. Salvador, H. Wang, L. Chen, and W. Zhang**, *Low thermal conductivity and high thermoelectric figure of merit in n -type $BaYbCoSb$ double-filled skutterudites*, Applied Physics Letters **92**, 182101 (2008), [DOI: [10.1063/1.2920210](#)]. (Cited on page 7.)
-

- [SKS62] **M. Smith, R. Knight, and C. Spencer**, *Properties of Bi_2Te_3 - Sb_2Te_3 Alloys*, *Journal of Applied Physics* **33** (7), 2186–2190 (1962), [DOI: [10.1063/1.1728925](https://doi.org/10.1063/1.1728925)]. (Cited on page 6.)
- [Sla79] **G. Slack**, *The thermal conductivity of nonmetallic crystals*, *Solid state physics*, vol. 34, Academic Press, New York, 1979, [DOI: [10.1016/S0081-1947\(08\)60359-8](https://doi.org/10.1016/S0081-1947(08)60359-8)], pp. 1–71. (Cited on page 7.)
- [Sla95] **G. A. Slack**, in *CRC Handbook of thermoelectrics*, ch. 34, p. 701, CRC Press, Boca Raton, 1995, [ISBN: [0849301467](https://www.isbn-international.org/product/0849301467)]. (Cited on pages 5 and 7.)
- [SLT⁺10] **D. Sellan, E. Landry, J. Turney, A. McGaughey, and C. Amon**, *Size effects in molecular dynamics thermal conductivity predictions*, *Physical Review B* **81** (21), 214305 (2010), [DOI: [10.1103/PhysRevB.81.214305](https://doi.org/10.1103/PhysRevB.81.214305)]. (Cited on page 40.)
- [SN06] **D. Singh and L. Nordström**, *Planewaves, Pseudopotentials, and the LAPW method*, 2 ed., Springer, New York, 2006, [ISBN: [0387287809](https://www.isbn-international.org/product/0387287809)]. (Cited on pages 19, 20, and 21.)
- [SS05] **G. Scuseria and V. Staroverov**, *Progress in the development of exchange-correlation functionals*, *Theory and Applications of Computational Chemistry: The First Forty Years* **24**, 669–724 (2005), [DOI: [10.1016/B978-044451719-7/50067-6](https://doi.org/10.1016/B978-044451719-7/50067-6)]. (Cited on page 13.)
- [SST⁺12] **W. Seifert, G. Snyder, E. Toberer, C. Goupil, K. Zabrocki, and E. Müller**, *The self-compatibility effect in graded thermoelectric cooler elements*, unpublished, 1–16 (2012). (Cited on pages 36 and 37.)
- [ST08] **G. J. Snyder and E. Toberer**, *Complex thermoelectric materials*, *Nature Materials* **7** (2), 105–114 (2008), [DOI: [10.1038/nmat2090](https://doi.org/10.1038/nmat2090)]. (Cited on page 2.)
- [Ste10] **S. Stepanow**, *Relativistische Quantentheorie*, 1 ed., Springer-Verlag, Berlin-Heidelberg, 2010, [ISBN: [9783642120497](https://www.isbn-international.org/product/9783642120497)]. (Cited on page 23.)
- [STKS12] **G. Snyder, E. Toberer, R. Khanna, and W. Seifert**, *Improved thermoelectric cooling based on the Thomson effect*, *Physical Review B* **86** (4), 045202 (2012), [DOI: [10.1103/PhysRevB.86.045202](https://doi.org/10.1103/PhysRevB.86.045202)]. (Cited on pages 36 and 37.)
- [STMA10] **D. P. Sellan, J. E. Turney, A. J. H. McGaughey, and C. H. Amon**, *Cross-plane phonon transport in thin films*, *Journal of Applied Physics* **108** (11), 113524 (2010), [DOI: [10.1063/1.3517158](https://doi.org/10.1063/1.3517158)]. (Cited on page 40.)
- [Sto80] **M. Stordeur**, *Anisotropie des Seebeck-Koeffizienten, der Lorenz-Zahl und des Hall-Koeffizienten von Halbleitern, verursacht durch anisotrop gemischte Streuung*, *Physica status solidi (b)* **98** (1), 199–206 (1980), [DOI: [10.1002/pssb.2220980119](https://doi.org/10.1002/pssb.2220980119)]. (Cited on page 46.)
- [Str98] **P. Strange**, *Relativistic quantum mechanics*, University Press, Cambridge, 1998, [ISBN: [9787506292580](https://www.isbn-international.org/product/9787506292580)]. (Cited on pages 22, 24, and 40.)
- [SUWK94] **L. Szunyogh, B. Ujfalussy, P. Weinberger, and J. Kollár**, *Self-consistent localized KKR scheme for surfaces and interfaces*, *Physical Review B* **49** (4), 2721–2729 (1994), [DOI: [10.1103/PhysRevB.49.2721](https://doi.org/10.1103/PhysRevB.49.2721)]. (Cited on page 18.)

- [SVG01] **J. Sharp, E. Volckmann, and H. Goldsmid**, *The Thermal Conductivity of Polycrystalline $\text{Bi}_{88}\text{Sb}_{12}$* , *Physica status solidi (a)* **185** (2), 257–265 (2001), [DOI: [10.1002/1521-396X\(200106\)185:2<257::AID-PSSA257>3.0.CO;2-D](https://doi.org/10.1002/1521-396X(200106)185:2<257::AID-PSSA257>3.0.CO;2-D)]. (Cited on pages 35 and 47.)
- [SW01] **G. Springholz and K. Wiesauer**, *Nanoscale Dislocation Patterning in $\text{PbTe}/\text{PbSe}(001)$ Lattice-Mismatched Heteroepitaxy*, *Physical Review Letters* **88** (1), 015507 (2001), [DOI: [10.1103/PhysRevLett.88.015507](https://doi.org/10.1103/PhysRevLett.88.015507)]. (Cited on page 8.)
- [SYB⁺10] **X. Shi, J. Yang, S. Bai, J. Yang, H. Wang, M. Chi, J. Salvador, W. Zhang, L. Chen, and W. Wong-Ng**, *On the Design of High-Efficiency Thermoelectric Clathrates through a Systematic Cross-Substitution of Framework Elements*, *Adv. Funct. Mater.* **20** (5), 755–763 (2010), [DOI: [10.1002/adfm.200901817](https://doi.org/10.1002/adfm.200901817)]. (Cited on page 7.)
- [TB09] **F. Tran and P. Blaha**, *Accurate band gaps of semiconductors and insulators with a semilocal exchange-correlation potential*, *Physical Review Letters* **102** (22), 226401 (2009), [DOI: [10.1103/PhysRevLett.102.226401](https://doi.org/10.1103/PhysRevLett.102.226401)]. (Cited on page 14.)
- [TBC08] **T. Tritt, H. Böttner, and L. Chen**, *Thermoelectrics: Direct solar thermal energy conversion*, *MRS bulletin* **33** (4), 366–368 (2008), URL: <http://publica.fraunhofer.de/documents/N-117914.html>. (Cited on page 10.)
- [TBD62] **L. Testardi, J. Bierly, and F. Donahoe**, *Transport properties of p-type Bi_2Te_3 - Sb_2Te_3 alloys in the temperature range 80-370K*, *Journal of Physics and Chemistry of Solids* **23** (9), 1209 (1962), [DOI: [10.1016/0022-3697\(62\)90168-3](https://doi.org/10.1016/0022-3697(62)90168-3)]. (Cited on page 5.)
- [TCB⁺08] **E. S. Toberer, C. A. Cox, S. R. Brown, T. Ikeda, A. F. May, S. M. Kauzlarich, and G. J. Snyder**, *Traversing the Metal-Insulator Transition in a Zintl Phase: Rational Enhancement of Thermoelectric Efficiency in $\text{Yb}_{14}\text{Mn}_{1-x}\text{Al}_x\text{Sb}_{11}$* , *Adv. Funct. Mater.* **18** (18), 2795–2800 (2008), [DOI: [10.1002/adfm.200800298](https://doi.org/10.1002/adfm.200800298)]. (Cited on pages 8 and 9.)
- [Tel47] **M. Telkes**, *The Efficiency of Thermoelectric Generators. I.*, *Journal of Applied Physics* **18** (12), 1116–1127 (1947), [DOI: [10.1063/1.1697593](https://doi.org/10.1063/1.1697593)]. (Cited on pages 5 and 6.)
- [Tho27] **L. Thomas**, *The calculation of atomic fields*, *Mathematical Proceedings of the Cambridge Philosophical Society* **23** (05), 542–548 (1927), [DOI: [10.1017/S0305004100011683](https://doi.org/10.1017/S0305004100011683)]. (Cited on pages 12 and 14.)
- [Tiw78] **M. Tiwari**, *Contribution of optical phonons in lattice thermal conductivity of NaCl*, *Il Nuovo Cimento B* **48** (1), 102–108 (1978), [DOI: [10.1007/BF02748652](https://doi.org/10.1007/BF02748652)]. (Cited on page 9.)
- [TMS09] **E. S. Toberer, A. F. May, and G. J. Snyder**, *Zintl Chemistry for Designing High Efficiency Thermoelectric Materials*, *Chemistry of Materials* **22** (3), 624–634 (2009), [DOI: [10.1021/cm901956r](https://doi.org/10.1021/cm901956r)]. (Cited on pages 8 and 9.)
- [TPPT07] **M. Tanatar, J. Paglione, C. Petrovic, and L. Taillefer**, *Anisotropic violation of the Wiedemann-Franz law at a quantum critical point*, *Science* **316** (5829), 1320–1322 (2007), [DOI: [10.1126/science.1140762](https://doi.org/10.1126/science.1140762)]. (Cited on page 43.)
- [TPSS03] **J. Tao, J. Perdew, V. Staroverov, and G. Scuseria**, *Climbing the Density Functional Ladder: Nonempirical Meta-Generalized Gradient Approximation Designed for Molecules and Solids*, *Physical Review Letters* **91** (14), 146401 (2003), [DOI: [10.1103/PhysRevLett.91.146401](https://doi.org/10.1103/PhysRevLett.91.146401)]. (Cited on pages 13 and 14.)

- [TPZ72] **R. Tubino, L. Piseri, and G. Zerbi**, *Lattice Dynamics and Spectroscopic Properties by a Valence Force Potential of Diamondlike Crystals: C, Si, Ge, and Sn*, *J. Chem. Phys.* **56** (3), 1022–1039 (1972), [DOI: [10.1063/1.1677264](https://doi.org/10.1063/1.1677264)]. (Cited on page 22.)
- [TTM99] **S. Tamura, Y. Tanaka, and H. Maris**, *Phonon group velocity and thermal conduction in superlattices*, *Physical Review B* **60** (4), 2627 (1999), [DOI: [10.1103/PhysRevB.60.2627](https://doi.org/10.1103/PhysRevB.60.2627)]. (Cited on page 10.)
- [TWL⁺10] **J. Tang, H. Wang, D. Lee, M. Fardy, Z. Huo, T. Russell, and P. Yang**, *Holey Silicon as an Efficient Thermoelectric Material*, *Nano Lett* **10**, 4279 (2010), [DOI: [10.1021/nl102931z](https://doi.org/10.1021/nl102931z)]. (Cited on page 8.)
- [TZG08] **G. Tai, B. Zhou, and W. Guo**, *Structural characterization and thermoelectric transport properties of uniform single-crystalline lead telluride nanowires*, *The Journal of Physical Chemistry C* **112** (30), 11314–11318 (2008), [DOI: [10.1021/jp8041318](https://doi.org/10.1021/jp8041318)]. (Cited on page 7.)
- [TZVG01] **M. N. Touzelbaev, P. Zhou, R. Venkatasubramanian, and K. E. Goodson**, *Thermal characterization of Bi₂Te₃/Sb₂Te₃ superlattices*, *Journal of Applied Physics* **90** (2), 763 (2001), [DOI: [doi:10.1063/1.1374458](https://doi.org/10.1063/1.1374458)]. (Cited on pages 9 and 10.)
- [UG74] **C. Uher and H. Goldsmid**, *Separation of electronic and lattice thermal conductivities in bismuth crystals*, *Phys. Status Solidi B* **65** (2), 765–772 (1974), [DOI: [10.1002/pssb.2220650237](https://doi.org/10.1002/pssb.2220650237)]. (Cited on pages 34 and 35.)
- [Uhe04] **C. Uher**, in *Thermal conductivity: Theory, Properties and Applications*, ch. 1.2, p. 306, Kluwer Academic, New York, 2004, [ISBN: [0306483270](https://www.kluweronline.com/ISBN/978-1-4020-3270-0)]. (Cited on pages 30, 31, 35, and 43.)
- [Van90] **D. Vanderbilt**, *Soft self-consistent pseudopotentials in a generalized eigenvalue formalism*, *Physical Review B* **41** (11), 7892–7895 (1990), [DOI: [10.1103/PhysRevB.41.7892](https://doi.org/10.1103/PhysRevB.41.7892)]. (Cited on pages 20 and 24.)
- [Var67] **Y. Varshni**, *Temperature dependence of the energy gap in semiconductors*, *Physica* **34** (1), 149–154 (1967), [DOI: [10.1016/0031-8914\(67\)90062-6](https://doi.org/10.1016/0031-8914(67)90062-6)]. (Cited on page 14.)
- [vBH72] **U. von Barth and L. Hedin**, *A local exchange-correlation potential for the spin polarized case. i*, *Journal of Physics C: Solid State Physics* **5** (13), 1629–1642 (1972), [DOI: [10.1088/0022-3719/5/13/012](https://doi.org/10.1088/0022-3719/5/13/012)]. (Cited on page 12.)
- [VCO⁺99] **R. Venkatasubramanian, T. Colpitts, B. O’Quinn, S. Liu, N. El-Masry, and M. Lamvik**, *Low-temperature organometallic epitaxy and its application to superlattice structures in thermoelectrics*, *Applied Physics Letters* **75** (8), 1104–1106 (1999), [DOI: [10.1063/1.124610](https://doi.org/10.1063/1.124610)]. (Cited on pages 9 and 10.)
- [VCW⁺97] **R. Venkatasubramanian, T. Colpitts, E. Watko, M. Lamvik, and N. El-Masry**, *MOCVD of Bi₂Te₃, Sb₂Te₃ and their superlattice structures for thin-film thermoelectric applications*, *Journal of crystal growth* **170** (1-4), 817–821 (1997), [DOI: [10.1016/S0022-0248\(96\)00656-2](https://doi.org/10.1016/S0022-0248(96)00656-2)]. (Cited on pages 9 and 46.)
- [VCWH96] **R. Venkatasubramanian, T. Colpitts, E. Watko, and J. Hutchby**, *Experimental evidence of high power factors and low thermal conductivity in Bi₂Te₃/Sb₂Te₃ superlattice thin-films*, *Proceedings of the XV International Conference on Thermoelectrics*, 454–458 (1996), [DOI: [10.1109/ICT.1996.553526](https://doi.org/10.1109/ICT.1996.553526)]. (Cited on pages 9 and 46.)

- [Ven97] **R. Venkatasubramanian**, *Bi₂Te₃/Sb₂Te₃ Superlattice Structures for High-ZT Thermoelectric Cooling Devices*, Naval Research Reviews, Special Issue on Thermoelectric, (1997), URL: <http://handle.dtic.mil/100.2/ADA327170>. (Cited on page 9.)
- [Ven00] ———, *Lattice thermal conductivity reduction and phonon localizationlike behavior in superlattice structures*, Physical Review B **61** (4), 3091–3097 (2000), [DOI: [10.1103/PhysRevB.61.3091](https://doi.org/10.1103/PhysRevB.61.3091)]. (Cited on pages 10, 46, and 47.)
- [vG80] **U. von Barth and C. Gelatt**, *Validity of the frozen-core approximation and pseudopotential theory for cohesive energy calculations*, Physical Review B **21** (6), 2222–2228 (1980), [DOI: [10.1103/PhysRevB.21.2222](https://doi.org/10.1103/PhysRevB.21.2222)]. (Cited on page 19.)
- [VHC⁺08] **C. Vineis, T. Harman, S. Calawa, M. Walsh, R. Reeder, R. Singh, and A. Shakouri**, *Carrier concentration and temperature dependence of the electronic transport properties of epitaxial PbTe and PbTe/PbSe nanodot superlattices*, Physical Review B **77** (23), 235202 (2008), [DOI: [10.1103/PhysRevB.77.235202](https://doi.org/10.1103/PhysRevB.77.235202)]. (Cited on pages 7 and 10.)
- [VI98] **M. Vedernikov and E. Iordanishvili**, *AF Ioffe and origin of modern semiconductor thermoelectric energy conversion*, Proceedings of the XVII International Conference on Thermoelectrics, 37–42 (1998), [DOI: [10.1109/ICT.1998.740313](https://doi.org/10.1109/ICT.1998.740313)]. (Cited on pages 5 and 6.)
- [Vin08a] **C. B. Vining**, *Materials science: Desperately seeking silicon*, Nature **451** (7175), 132–133 (2008), [DOI: [10.1038/451132a](https://doi.org/10.1038/451132a)]. (Cited on page 71.)
- [Vin08b] ———, *Thermoelectrics: Half-full glasses*, Nature Materials **7** (10), 765 (2008), [DOI: [doi:10.1038/nmat2271](https://doi.org/10.1038/nmat2271)]. (Cited on page 7.)
- [Vin09] ———, *An inconvenient truth about thermoelectrics*, Nature Materials **8**, 83 (2009), [DOI: [10.1038/nmat2361](https://doi.org/10.1038/nmat2361)]. (Cited on page 2.)
- [vL94] **R. van Leeuwen**, *Kohn-Sham potentials in density functional theory*, Ph.D. thesis, Vrije Universiteit Amsterdam, 1994, URL: <http://www.scm.com/Doc/thesis.leeuwen.pdf>. (Cited on page 14.)
- [VS07] **D. Vashaee and A. Shakouri**, *Thermionic power generation at high temperatures using SiGe/Si superlattices*, Journal of Applied Physics **101** (5), 053719 (2007), [DOI: [10.1063/1.2645607](https://doi.org/10.1063/1.2645607)]. (Cited on page 10.)
- [VSC01] **R. Venkatasubramanian, E. Siivola, and T. Colpitts**, *Thin-film thermoelectric devices with high room-temperature figures of merit*, Nature **413**, 597 (2001), [DOI: [10.1038/35098012](https://doi.org/10.1038/35098012)]. (Cited on pages 2, 5, 9, and 46.)
- [VW80] **S. H. Vosko and L. Wilk**, *Influence of an improved local-spin-density correlation-energy functional on the cohesive energy of alkali metals*, Physical Review B **22** (8), 3812–3815 (1980), [DOI: [10.1103/PhysRevB.22.3812](https://doi.org/10.1103/PhysRevB.22.3812)]. (Cited on page 14.)
- [VWN80] **S. H. Vosko, L. Wilk, and M. Nusair**, *Accurate spin-dependent electron liquid correlation energies for local spin density calculations: a critical analysis*, Canadian Journal of Physics **58** (8), 1200 (1980), [DOI: [10.1139/p80-159](https://doi.org/10.1139/p80-159)]. (Cited on page 14.)
- [WB10] **A. Ward and D. A. Broido**, *Intrinsic phonon relaxation times from first-principles studies of the thermal conductivities of Si and Ge*, Physical Review B **81** (8), 085205 (2010), [DOI: [10.1103/PhysRevB.81.085205](https://doi.org/10.1103/PhysRevB.81.085205)]. (Cited on page 40.)

- [WBSD09] **A. Ward, D. Broido, D. Stewart, and G. Deinzer**, *Ab initio theory of the lattice thermal conductivity in diamond*, *Physical Review B* **80** (12), 125203 (2009), [DOI: [10.1103/PhysRevB.80.125203](https://doi.org/10.1103/PhysRevB.80.125203)]. (Cited on page 40.)
- [Wei35] **C. Weizsäcker**, *Zur Theorie der Kernmassen*, *Z. Physik* **96** (7-8), 431–458 (1935), [DOI: [10.1007/BF01337700](https://doi.org/10.1007/BF01337700)]. (Cited on page 14.)
- [WGG05] **M. Wierzbowska, S. D. Gironcoli, and P. Giannozzi**, *Origins of low-and high-pressure discontinuities of T_c in niobium*, 2005, preprint ArXiv:[cond-mat/0504077v2](https://arxiv.org/abs/cond-mat/0504077v2). (Cited on page 42.)
- [WLG92] **L. Weber, M. Lehr, and E. Gmelin**, *Reduction of the thermopower in semiconducting point contacts*, *Physical Review B* **46** (15), 9511–9514 (1992), [DOI: [10.1103/PhysRevB.46.9511](https://doi.org/10.1103/PhysRevB.46.9511)]. (Cited on page 7.)
- [WLK⁺11] **M. Winkler, X. Liu, J. D. König, L. Kirste, H. Böttner, W. Bensch, and L. Kienle**, *Sputtered p-Type Sb_2Te_3 / $(Bi,Sb)_2Te_3$ Soft Superlattices Created by Nanoalloying*, *Journal of Electronic Materials* **41** (6), 1322 (2011), [DOI: [10.1007/s11664-011-1854-z](https://doi.org/10.1007/s11664-011-1854-z)]. (Cited on pages 9 and 47.)
- [WLK⁺12] **M. Winkler, X. Liu, J. D. König, S. Buller, U. Schürmann, L. Kienle, W. Bensch, and H. Böttner**, *Electrical and structural properties of Bi_2Te_3 and Sb_2Te_3 thin films grown by the nanoalloying method with different deposition patterns and compositions*, *J. Mater. Chem.* **22** (22), 11323–11334 (2012), [DOI: [10.1039/c2jm30363a](https://doi.org/10.1039/c2jm30363a)]. (Cited on pages 9 and 47.)
- [WM74] **K. Wittel and R. Manne**, *Atomic spin-orbit interaction parameters from spectral data for 19 elements*, *Theoret. Chim. Acta* **33** (4), 347–349 (1974), [DOI: [10.1007/BF00551162](https://doi.org/10.1007/BF00551162)]. (Cited on page 23.)
- [Woo88] **C. Wood**, *Materials for thermoelectric energy conversion*, *Reports on Progress in Physics* **51** (4), 459 (1988), [DOI: [10.1088/0034-4885/51/4/001](https://doi.org/10.1088/0034-4885/51/4/001)]. (Cited on page 5.)
- [Wri58] **D. A. Wright**, *Thermoelectric Properties of Bismuth Telluride and its Alloys*, 834 (1958), [DOI: [10.1038/181834a0](https://doi.org/10.1038/181834a0)]. (Cited on pages 5, 6, and 45.)
- [WYSV06] **X. Wang, J. Yates, I. Souza, and D. Vanderbilt**, *Ab initio calculation of the anomalous Hall conductivity by Wannier interpolation*, *Physical Review B* **74** (19), 195118 (2006), [DOI: [10.1103/PhysRevB.74.195118](https://doi.org/10.1103/PhysRevB.74.195118)]. (Cited on page 25.)
- [WZB⁺92] **X. Wang, X.-G. Zhang, W. Butler, G. Stocks, and B. Harmon**, *Relativistic-multiple-scattering theory for space-filling potentials*, *Physical Review B* **46** (15), 9352–9358 (1992), [DOI: [10.1103/PhysRevB.46.9352](https://doi.org/10.1103/PhysRevB.46.9352)]. (Cited on pages 22 and 23.)
- [WZD97] **K. Wildberger, R. Zeller, and P. H. Dederichs**, *Screened KKR-Green's-function method for layered systems*, *Physical Review B* **55** (15), 10074–10080 (1997), [DOI: [10.1103/PhysRevB.55.10074](https://doi.org/10.1103/PhysRevB.55.10074)]. (Cited on page 18.)
- [YBP⁺09] **R. B. Yang, J. Bachmann, E. Pippel, A. Berger, J. Woltersdorf, U. Gösele, and K. Nielsch**, *Pulsed Vapor-Liquid-Solid Growth of Antimony Selenide and Antimony Sulfide Nanowires*, *Advanced Materials* **21** (31), 3170–3174 (2009), [DOI: [10.1002/adma.200803436](https://doi.org/10.1002/adma.200803436)]. (Cited on page 7.)

- [YF05] **Y. Yao and Z. Fang**, *Sign Changes of Intrinsic Spin Hall Effect in Semiconductors and Simple Metals: First-Principles Calculations*, Physical Review Letters **95** (15), 156601 (2005), [DOI: [10.1103/PhysRevLett.95.156601](https://doi.org/10.1103/PhysRevLett.95.156601)]. (Cited on page 25.)
- [YKM⁺04] **Y. Yao, L. Kleinman, A. MacDonald, J. Sinova, T. Jungwirth, D.-S. Wang, E. Wang, and Q. Niu**, *First Principles Calculation of Anomalous Hall Conductivity in Ferromagnetic bcc Fe*, Physical Review Letters **92** (3), 037204 (2004), [DOI: [10.1103/PhysRevLett.92.037204](https://doi.org/10.1103/PhysRevLett.92.037204)]. (Cited on page 25.)
- [YKML12] **O. Yazyev, E. Kioupakis, J. Moore, and S. Louie**, *Quasiparticle effects in the bulk and surface-state bands of Bi₂Se₃ and Bi₂Te₃ topological insulators*, Physical Review B **85** (16), 161101 (2012), [DOI: [10.1103/PhysRevB.85.161101](https://doi.org/10.1103/PhysRevB.85.161101)]. (Cited on page 24.)
- [YLWC01] **B. Yang, J. Liu, K. Wang, and G. Chen**, *Characterization of cross-plane thermoelectric properties of Si/Ge superlattices*, Proceedings of the XX International Conference on Thermoelectrics, 344–347 (2001), [DOI: [10.1109/ICT.2001.979902](https://doi.org/10.1109/ICT.2001.979902)]. (Cited on pages 9 and 72.)
- [Zah98] **P. Zahn**, *Screened Korringa-Kohn-Rostoker-Method für Vielfachschichten*, Ph.D. thesis, Technische Universität Dresden, 1998, URL: <http://nbn-resolving.de/urn:nbn:de:swb:14-1119864864984-42479>. (Cited on pages 18 and 25.)
- [Zah05] ———, *Transport phenomena in metallic nanostructures: an ab initio approach*, Habilitation thesis, Technische Universität Dresden, 2005, URL: <http://nbn-resolving.de/urn:nbn:de:swb:14-1117186073142-40775>. (Cited on pages 30 and 41.)
- [ZB01] **J. Zou and A. Balandin**, *Phonon heat conduction in a semiconductor nanowire*, Journal of Applied Physics **89** (5), 2932–2938 (2001), [DOI: [10.1063/1.1345515](https://doi.org/10.1063/1.1345515)]. (Cited on page 9.)
- [ZBM⁺98] **P. Zahn, J. Binder, I. Mertig, R. Zeller, and P. Dederichs**, *Origin of Giant Magnetoresistance: Bulk or Interface Scattering*, Physical Review Letters **80** (19), 4309–4312 (1998), [DOI: [10.1103/PhysRevLett.80.4309](https://doi.org/10.1103/PhysRevLett.80.4309)]. (Cited on page 41.)
- [ZCS12] **Z. Zhu, Y. Cheng, and U. Schwingenschlögl**, *Band inversion mechanism in topological insulators: A guideline for materials design*, Physical Review B **85** (23), 235401 (2012), [DOI: [10.1103/PhysRevB.85.235401](https://doi.org/10.1103/PhysRevB.85.235401)]. (Cited on page 24.)
- [ZDU⁺95] **R. Zeller, P. H. Dederichs, B. Ujfalussy, L. Szunyogh, and P. Weinberger**, *Theory and convergence properties of the screened Korringa-Kohn-Rostoker method*, Physical Review B **52** (12), 8807–8812 (1995), [DOI: [10.1103/PhysRevB.52.8807](https://doi.org/10.1103/PhysRevB.52.8807)]. (Cited on page 18.)
- [Zim60] **J. M. Ziman**, *Electrons and phonons: the theory of transport phenomena in solids*, Clarendon Press, Oxford, 1960, [ISBN: [0198507798](https://www.isbn-international.org/product/0198507798)]. (Cited on pages 6, 27, 28, 29, 30, 31, 33, 37, 40, and 43.)
- [Zim61] **J. M. Ziman**, *Approximate Calculation of the Anisotropy of the Relaxation Time of the Conduction Electrons in the Noble Metals*, Physical Review **121** (5), 1320–1324 (1961), [DOI: [10.1103/PhysRev.121.1320](https://doi.org/10.1103/PhysRev.121.1320)]. (Cited on page 30.)
- [Zim62] **J. M. Ziman**, *Electrons in metals: A short guide to the Fermi surface*, Contemporary Physics **4** (2), 81–99 (1962), [DOI: [10.1080/00107516208201722](https://doi.org/10.1080/00107516208201722)]. (Cited on page 29.)

- [ZJS⁺05] **J. Zhou, C. Jin, J. Seol, X. Li, and L. Shi**, *Thermoelectric properties of individual electrodeposited bismuth telluride nanowires*, Applied Physics Letters **87** (13), 133109 (2005), [DOI: [10.1063/1.2058217](https://doi.org/10.1063/1.2058217)]. (Cited on page 7.)
- [ZLQ⁺09] **H. Zhang, C. Liu, X. Qi, X. Dai, Z. Fang, and S. Zhang**, *Topological insulators in Bi_2Se_3 , Bi_2Te_3 and Sb_2Te_3 with a single Dirac cone on the surface*, Nature Physics **5** (6), 438–442 (2009), [DOI: [10.1038/NPHYS1270](https://doi.org/10.1038/NPHYS1270)]. (Cited on page 24.)
- [ZMRE95] **P. Zahn, I. Mertig, M. Richter, and H. Eschrig**, *Ab Initio Calculations of the Giant Magnetoresistance*, Physical Review Letters **75** (16), 2996–2999 (1995), [DOI: [10.1103/PhysRevLett.75.2996](https://doi.org/10.1103/PhysRevLett.75.2996)]. (Cited on pages 40 and 41.)
- [ZTIY03] **L. Zhang, M. Tsutsui, K. Ito, and M. Yamaguchi**, *Effects of ZnSb and Zn inclusions on the thermoelectric properties of β - Zn_4Sb_3* , Journal of Alloys and Compounds **358** (1), 252–256 (2003), [DOI: [10.1016/S0925-8388\(03\)00074-4](https://doi.org/10.1016/S0925-8388(03)00074-4)]. (Cited on page 8.)
- [ZZP⁺] **A. Zevalkink, W. G. Zeier, G. Pomrehn, E. Schechtel, W. Tremel, and G. J. Snyder**, *Thermoelectric properties of Sr_3GaSb_3 – a chain-forming Zintl compound*, Energy Environ. Sci. **5** (10), 9121–9128, [DOI: [10.1039/C2EE22378C](https://doi.org/10.1039/C2EE22378C)]. (Cited on pages 8 and 9.)

Acknowledgement

At this stage I would like to express my appreciation to some people who shared time, knowledge and friendliness in the last years with me.

Foremost, I thank my supervisor Prof. Ingrid Mertig for giving me the possibility to do a doctorate in her group and in this very interesting and diverse field. Her commitment to form good scientists was noticeable all the time. Besides, she was always an attentive and caring listener and I am grateful she shared some of her knowledge. The opportunity to attend a lot of conferences, to give many talks and to collaborate with brilliant scientists enriched my scientific understanding immensely.

I am furthermore greatly indebted to Dr. habil. Peter Zahn who guided me through the main part of my thesis. His patience in discussions, his accuracy, as well as his knowledge in condensed matter physics were exhaustless. I hope that I adopted some of his capability of developing plausible physical models to get insight the physics and beyond the numerical clutter of our computational methods.

I am thankful to Dr. habil. Jürgen Henk, who gave me valuable assistance in scientific writing and time management. He always was willing to answer questions immediately. The same accounts to Dr. habil. Arthur Ernst who generously offered his time to discuss physics at a cup of tea.

I am obliged to Dr. “Dima” Fedorov and Dr. Martin Gradhand, who helped me a lot to understand the physics and numerics of the fully relativistic version of the KKR code.

Right now I could just thank all my office neighbours. Truly, I was some kind of office-nomad and I loved to change my working place every few months. To name my office mates and some other nice guys from the floor and the MPI: Dr. Rüdiger S. Achilles, Stephan “LI” Borek, Dr. Michael Fechner, Dr. Guntram Fischer, Markus Flieger, Lord Martin Hölzer, Dr. Christian “KaLeu” Matyssek, Dr. Igor Maznichenko, Florian Rittweger, Dr. Wolfgang Seifert, Michael Strauch and Dr. Bogdan Yavorsky. I am very fortunate that I was able to benefit on the know-how, experience and help of all of you. Thanks a lot.

One should never forget the secretariat. Many thanks to Helgard Meyn and Jurate Claus for storing and delivering my postal packages, feeding me with pens and post-it’s, and correcting my business bills.

Last but not least, this thesis would not have been possible without the support and interest of my family and friends. I am grateful to my parents, who enabled such a worthy path of education for me. Furthermore, I am very glad to have such valuable and warm friends around me. At the top Carsta Langner, who always took care of me and supported me in all my decisions, as stupid as they might have been.

I am deeply impressed by all of you and want to thank you with the words of Sir Isaac NEWTON (or OASIS):

“If I have seen further it is by standing on the shoulders of giants.”

Curriculum vitae

Personal information

Name	Nicki Frank Hinsche
Address	Richard-Wagner-Str. 54 in 06114 Halle (Saale), Germany
Date and place of birth	7th of August, 1982 in Halle (Saale)

Education

since 08/2009	PhD studies at the “Martin-Luther University Halle-Wittenberg” and the “Max Planck Institute of Microstructure Physics”, Halle (Saale)
10/2003–07/2009	Study of Physics at the “Martin-Luther University Halle-Wittenberg”, Halle(Saale) Diploma thesis “Electronic transport of ferroelectric tunnel junctions”, supervisor Priv.-Doz. Dr. habil. Peter Zahn
10/2002–08/2003	Civilian service at “Martin-Luther-University Hospital”, Halle (Saale)
09/1993–07/2002	High school, “Frieden Gymnasium”, Halle (Saale)
08/1989–07/1993	Elementary school, “Walentina-Tereschkowa-Grundschule”, Halle (Saale)

Academic career

since 01/2010	Scientific member at the “International Max Planck Research School for Science and Technology of Nanostructures”, chairman E.K.U. Gross
since 08/2009	Research Assistant at the “Martin-Luther University Halle-Wittenberg”, Halle (Saale) in the group of Prof. Dr. Ingrid Mertig
10/2007–08/2009	Research Assistant at the “Martin-Luther University Halle-Wittenberg”, Halle (Saale) and “Research Centre Dresden-Rossendorf”, Dresden in the groups of Prof. Dr. Reinhard Krause-Rehberg and Prof. Dr. Thomas Cowan
10/2005–02/2009	Student Assistant at the “Martin-Luther University Halle-Wittenberg”, Halle (Saale) in the groups of Prof. Dr. Jamal Berakdar and Prof. Dr. Horst Beige

Eidesstattliche Erklärung

Hiermit erkläre ich, gemäß §5 Abs. 2b der Promotionsordnung der Naturwissenschaftlichen Fakultät II-Chemie und Physik der Martin-Luther-Universität Halle-Wittenberg vom 13.06.2012, dass die vorliegende Arbeit

THERMOELECTRIC TRANSPORT IN SEMICONDUCTING HETEROSTRUCTURES

selbständig und ohne fremde Hilfe verfasst, andere als die von mir angegebenen Quellen und Hilfsmittel nicht benutzt und die den benutzten Werken wörtlich oder inhaltlich entnommenen Stellen als solche kenntlich gemacht habe. Ich erkläre, die Angaben wahrheitsgemäß gemacht und keine Dissertation an einer anderen wissenschaftlichen Einrichtung zur Erlangung eines akademischen Grades eingereicht zu haben.

Halle (Saale), den 27. Juni 2013

Nicki F. Hinsche